Quantitative evaluation of fibroglandular tissue for estimation of tissue-differentiated absorbed energy in breast tomosynthesis

Nausikaa Geeraert

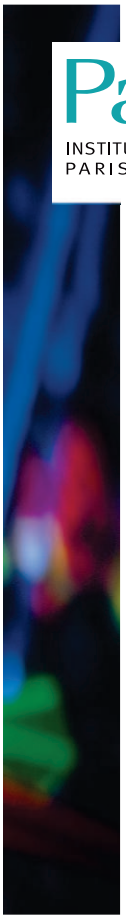

ParisTech
INSTITUT DES SCIENCES ET TECHNOLOGIES
PARIS INSTITUTE OF TECHNOLOGY

TELECOM ParisTech

2014-ENST-0060

KU LEUVEN
DOCTORAL SCHOOL BIOMEDICAL SCIENCES

EDITE - ED 130

Doctorat ParisTech

T H E S E

pour obtenir le grade de docteur délivré par

TELECOM ParisTech

Spécialité « Traitement du Signal et de l'Image »

présentée et soutenue publiquement par

Nausikaä GEERAERT

le 6 octobre 2014

Quantitative evaluation of fibroglandular tissue for estimation of tissue-differentiated absorbed energy in breast tomosynthesis

Jury

Mme. Isabelle BLOCH, Prof., TSI, Télécom ParisTech	Directrice de thèse
Mme. Hilde BOSMANS, Prof., Imaging and Pathology , KU Leuven	Directrice de thèse
M. Rémy KLAUSZ, Ir., GE Healthcare	Encadrant industriel
M. Michel BOURGUIGNON, Prof., Université de Versailles Saint-Quentin en Yvelines	Rapporteur
M. Nathal SEVERIJNS, Prof., IKS, KU Leuven	Rapporteur
M. Francis VERDUN, Prof., Institut de radiophysique - CHUV et Université de Lausanne	Examinateur
M. Madan REHANI, Prof., Harvard Med. School & Mass. Gen. Hosp., Boston, Secretary ICRP Prot. in Medicine	Examinateur
Mme. Chantal VAN ONGEVAL, Prof., Radiology, KU Leuven	Examinateur

T H È S E

TELECOM ParisTech
école de l'Institut Mines-Télécom - membre de ParisTech
46 rue Barrault 75013 Paris - (+33) 1 45 81 77 77 - www.telecom-paristech.fr

KU Leuven
Biomedical Sciences Group
Faculty of Medical Sciences
Department of Radiology

QUANTITATIVE EVALUATION OF FIBROGLANDULAR TISSUE FOR ESTIMATION OF TISSUE-DIFFERENTIATED ABSORBED ENERGY IN BREAST TOMOSYNTHESIS

Nausikaä GEERAERT

Jury

Promoters:	Isabelle Bloch	Dissertation presented
	Hilde Bosmans	in partial fulfilment
Industrial promoter:	Rémy Klausz	of the requirements for
Chair:	Nathal Severijns	the degree of Doctor in
Jury members:	Michel Bourguignon	Biomedical Sciences
	Madan Rehani	
	Chantal Van Ongeval	
	Francis Verdun	

Defense October 6, 2014

Acknowledgment

PhD stands for *Philosophiae Doctor*, an expert in the understanding of things (philosophy here means wisdom), or someone who reasons. Besides the technical knowledge in this text we thus also tried to give a vision for further research and innovation beyond this project. However reasoning also means realising that great things are achieved while working together. Therefore a considerable number of people should be acknowledged for the success of this work.

The main actors are professor Isabelle Bloch, professor Hilde Bosmans and Rémy Klausz, forming a great team of promotors for daily support during the last three years. They provided a good balance between support and encouragements on the one hand, and demanding high(er) quality on the other hand. Supervising someone from a distance is, as I found out when supervising an intern, not an easy task. Isabelle, Hilde and Rémy, you did this successfully, even if you had your own specific motivations. Therefore I express my greatest respect and a sincere thank you for all what you did.
I also would like to thank Serge Muller for making this CIFRE project possible and for welcoming me in his research team.

Thank you to professor Bourguignon, professor Rehani, professor Severijns, professor Van Ongeval and professor Verdun, who accepted to be member of the jury of this thesis and who applied their expertise to read and comment the manuscript. Your critical and valuable inputs helped me to improve this manuscript in a considerable way. Thank you for your interest in our work and your encouraging conclusions.

People providing me technical support and material helped me a lot: the assistents in Buc, Leuven and Paris, planning my trips and preparing documents for the studies, the partnering hospitals, the physicists in Jolimont, the mammography team in UZ Leuven and the GE CT service team, who provided me with data, images and access to the equipment, my colleagues in Buc, Leuven and Paris, helping me when a program wasn't installed or working as expected, ...

I was very welcome in the teams at the different institutions: in GE (BCare, IQ and in general engineering), in Télécom Paristech (TII and the medical imaging group), and at UZ-KU Leuven (the QA and research group for medical physics). The continuous traveling between the different places did not facilitate integration, but with the help of my colleagues it all went well. Humanly speaking, I also learned a lot during extra-professional activities: team buildings, conferences, running and swimming together, the yearly GE football cup, extended lunches, ... You allowed me in a nice way to learn more

about the world and the lives of real people with different backgrounds, habits and cultures.

Finally I want to thank my family and friends: mama, papa, Mario, Naomi, Jorinde, Arvid, grootva, grootmoe, oma, ... for the great life I had until now, Naomi, Geraud, Jorinde and Jeroen for hosting me when I was traveling to Leuven, and mama, Mario and Naomi for reading my texts and discussing my work.

A list of names of people I met during my PhD adventure in Paris or a list of events would never be complete, so I just say:

Thank you all for entering in and
contributing to my life and this work.

Nausikaä GEERAERT
October 6, 2014

Contents

List of abbreviations

AAPM	American Association of Medical Physicists
ABD	Area-based Breast Density
AEC	Automatic Exposure Control
AGD	Average Glandular Dose
AIE	Adipose Imparted Energy
ALARA	As Low As Reasonably Achievable
AOP (CNT, STD, DOSE)	Automatic Optimization of Parameters (CoNTrast mode, STanDard mode, DOSE mode)
BI-RADS	Breast Imaging-Reporting And Data System
CC	Cranio-Caudal
CDRH	Center for Devices and Radiological Health
CIFRE	Convention Industrielle de Formation par la REcherche
CIRS	Phantoms of CIRS Inc., Norfolk, VA
CT	Computed Tomography
DBT	Digital Breast Tomosynthesis
DICOM	Digital Imaging and COmmunications in Medicine
DNA	Desoxyribo-Nucleic Acid
ECR	European Congress of Radiology
FOV	Field Of View
GE (HC)	General Electric (HealthCare)
GIE	Glandular Imparted Energy
GSI	Gemstone Spectral Imaging
HSM	Histogram Segmentation Method
HU	Hounsfield Units
HVL	Half Value Layer
IAEA	International Atomic Energy Agency
iAGD	individualized Average Glandular Dose
ICRP	International Commission on Radiological Protection
LNT	Linear Non Treshold model
LUCMFR	Leuvens Universitair Centrum voor Medische Fysica in de Radiologie
MBD	Massic Breast Density
MC	Monte-Carlo (simulation)
MDEST	Mammographic Density ESTimator
MGD	Mean Glandular Dose
MIE	Muscular Imparted Energy
MLO	Medio-Lateral Oblique

MR(I)	Magnetic Resonance (Imaging)
NIST	National Institute of Standards and Technology
PBD	Peak Breast Density
PMMA	polymethylmethacrylate
QC	Quality Control
QVL	Quarter Value Layer
ROI	Region Of Interest
RSNA	Radiological Society of North-America
SART	Simultaneous Algebraic Reconstruction Technique
SBP	Simple Back-Projection
SPIE	Society of Photo-Optical Instrumentation Engineers
TIE	Total Imparted Energy
VBD	Volumetric Breast Density
VBD_{CT}	Volumetric Breast Density measured from a CT acquisition
VBD_{MX}	Volumetric Breast Density measured from a mammographic acquisition
VGF	Volumetric Glandular Fraction

Abstract

Breast cancer is an important disease, accounting worldwide for 25.2% of all female cancers [7] and for 16% of cancer deaths in adult women [6]. Early detection of suspicious lesions via breast screening increases survival chances [8]. Mammography is the cornerstone of population-based breast cancer screening [116]. The quality of screening tools is strictly controlled [116] and continuously improved. A possible improvement of the current screening programs is an even more specific identification of the population at risk. Today, most screening programs invite women only based on and sometimes on patient or family history [71]. Another improvement could be a better estimation of the associated radiation risk. For both improvements, breast density, a quantitative evaluation of fibroglandular tissue, differing in amount and distribution within the population, is a key parameter.

Breast density has been identified as a risk factor for breast cancer by many studies [108]. In addition an abundant dense tissue tends to mask suspicious lesions and reduces their detection. In this thesis we developed a volumetric breast density computation method in mammographic images, based on calibrating the image chain with breast-equivalent phantoms, and the acquisition data stored in the image-header. We applied and published [57] a new validation method for breast density computation methods based on regular thorax CT images.

In 1979 Hammerstein et al. [66] stated that mammary gland is tissue at high risk for radiation damage, as opposed to skin, fat and connective tissue, which are not at high risk. They concluded with the proposition of total energy absorbed in glandular tissue as the most relevant indicator of risk in mammography. The average glandular dose (AGD), the currently accepted measure of mammographic dose, is not a function of the amount of tissue at risk, and as a consequence is not a good indicator for the radiation risk from a specific mammographic examination. In the individualized evaluation of the radiation related risk in mammography, the different radiation sensitivities of glandular and adipose tissues should be taken into account. This also requires the knowledge of the amount and localization of each of these components of the breast at an individual level. Thanks to methods as the volumetric breast density computation it is possible to assess to the amount of glandular tissue. Thanks to recent developments in breast imaging such as breast tomosynthesis it is possible to partly overcome the problem of the glandular tissue localization [121, 145]. Hence, breast tomosynthesis reconstructs a 3D volume of the breast from a limited number of projections over a small angular range. In this thesis we apply a method to estimate the tissue-differentiated absorbed energy for a Senographe Essential configuration with the SenoClaire Digital Tomosynthesis attachment (GE Healthcare, Chalfont,UK). From the 0° projection image we computed the volumetric breast density.

Contrary to CT scanning that produces Hounsfield units, the pixel values in reconstructed DBT volumes have no physical meaning and therefore segmentation of the glandular versus adipose tissue cannot be readily performed using simple thresholding techniques. We have proposed and worked out a procedure in which the volumetric breast density computation is used to label the local tissue, based on the conservation of glandular tissue percentage between the projection and the 3D volume.
We then computed the locally imparted energy by Monte Carlo simulations applied to the reconstructed volume. Combining the labeled volume and the local imparted energy leads to the total imparted energy to the glandular and adipose tissues separately for the given breast tomosynthesis exam. For daily use more research is necessary to facilitate the calibration of the system, the computation of locally imparted energy avoiding Monte Carlo simulations and an improvement of the reconstructed volume with for goal glandular segmentation.

Résumé

Présentation du projet

Le projet de recherche se situe dans le domaine de l'imagerie médicale, et plus précisément de l'imagerie radiographique du sein et de son application au dépistage du cancer du sein. Le cancer du sein est une maladie à fort impact. Il représente 25,5% des cancers féminins [7] et est responsable de 16% des décès à la suite d'un cancer chez la femme adulte [6]. Grâce au dépistage du cancer du sein, les cancers et les lésions suspectes sont détectés à un stade précoce où le traitement est moins invasif, ce qui augmente les possibilités de survie [8]. Le dépistage du cancer du sein se fait par la mammographie en utilisant des rayons X qui forment une image de projection des tissus mammaires. Comme pour toute exposition aux rayons X le principe de justification s'applique : une exposition est justifiée à condition que les avantages dépassent significativement les préjudices. En d'autres termes, le nombre de cancers détectés doit être significativement supérieur au nombre de cancers susceptibles d'être induits par l'exposition au rayonnement. Bien que dans la plupart des pays développés un programme de dépistage soit développé, le débat sur les bénéfices et les risques est toujours actuel [20, 94, 111, 134]. La qualité des systèmes utilisés en dépistage est vérifiée et contrôlée strictement [116], et les performances des nouveaux équipements s'améliorent progressivement. Une amélioration possible concernant les programmes actuels serait de mieux cibler encore la population à risque, qui est aujourd'hui déterminée seulement sur des critères d'âge et parfois d'antécédents personnels ou familiaux [71]. Une autre amélioration possible serait une meilleure estimation du risque résultant de l'exposition aux rayons X. Pour ces deux améliorations, la *densité du sein*, qui mesure le contenu tissulaire, est un paramètre clé [41, 108].

Le sein normal contient principalement des tissus adipeux et fibroglandulaires, le tissu adipeux apparaissant plus sombre sur l'image mammographique, et le tissu fibroglandulaire plus clair. Ces tissus diffèrent en quantité et en distribution parmi la population. Le pourcentage de tissu fibroglandulaire sur le tissu total est appelé la densité du sein (voir plus bas pour la définition exacte). La densité du sein a été identifiée comme indicateur de risque par de nombreuses études [108]. En outre, un excès de tissu fibroglandulaire a tendance à masquer les lésions et à rendre leur détection plus difficile. Initialement les seins ont été classés selon leur apparence sur les clichés mammographiques par Wolfe en 1976 [152]. L'influence de la densité du sein sur le développement du cancer du sein n'est néanmoins pas bien comprise [26, 106]. Parmi les difficultés rencontrées, nous trouvons notamment un manque de consensus sur la façon de quantifier la densité [54, 73], de caractériser l'impact de sa distribution sur le risque [88, 100, 148] et d'inclure cette mesure dans les modèles de risque [32]. En 1979 Hammerstein et al. [66] ont basé leurs propositions

sur le fait que le risque radique est significativement plus élevé pour la glande mammaire que pour la peau et le tissu adipeux. Ils conclurent en proposant comme le meilleur indicateur de risque l'énergie totale absorbée par le tissu glandulaire. Ils ajoutèrent que la mesure de cette grandeur devra être faite en utilisant la quantité et la distribution du tissu glandulaire.

Densité volumique du sein

Etat de l'art

La classification des mammographies par densité a été développée initialement par Wolfe en 1976 [152]. Il proposa quatre catégories d'après les caractéristiques du parenchyme et les distributions relatives dans les images (voir figure 1). Tabar et al. [64] présentèrent également une classification à cinq catégories (voir figure 1) par risque de cancer, alors que Jeffreys et al. [83] en proposèrent six. Dans la précédente classification de BI-RADS [33], reposant sur la classification de Wolfe, la densité est basée sur la proportion approximative de tissu fibroglandulaires par rapport à l'image du sein (*area-based breast density (ABD)*) comme indiqué sur la figure 2. Il existe deux autres grandeurs décrivant la densité du sein. La densité volumique (*volumetric breast density (VBD)*) est égale au rapport entre le volume fibroglandulaire et le volume total du sein. La densité du sein peut également être considérée localement comme le rapport de l'épaisseur de tissu traversée à l'épaisseur totale. Cerains exposeurs automatiques déterminent la valeur maximale de cette densité locale dans l'imagge pour ajuster l'exposition. La grandeur résultante est la densité pic *peak breast density (PBD)*. Les classifications de Wolfe [152], Tabar et al. [64] BI-RADS [33] sont des critères d'évaluation visuelle de la densité par les radiologues, bien que des méthodes de classification automatiques aient été développées [54]. Des algorithmes (semi)-automatiques ont été conçus pour améliorer cette estimation et reposent sur un seuillage de valeur de pixel [27, 102, 160]. Malgré ces méthodes automatiques, les valeurs de l'ABD pour un même sein peuvent différer, principalement à cause de positionnements différents. On peut penser qu'utiliser la densité volumique évite cet inconvénient [95], sa mesure étant possible en analysant l'image et ses paramètres d'exposition.

La plupart des méthodes récentes pour le calcul de la VBD reposent sur les travaux de Highnam, Brady et Shepstone en 1996 [74]. Ces auteurs ont numérisé les films mammographiques provenant de systèmes qu'ils ont calibrés en utilisant un fantôme connu. Les valeurs de pixels étaient ensuite comparées à celles du fantôme. Une calibration journalière était nécessaire afin de pouvoir gérer les fluctuations de la chaîne d'acquisition.
En 2002, Kaufhold et al. [86, 87] ont publié une méthode de calcul de la VBD pour des images acquises avec un mammographe numérique. Ils ont acquis des images d'un matériau radiologiquement équivalent à des tissus mammaires de VBD 0%, 50% et 100% pour des épaisseurs et des hautes-tensions courantes de l'usage clinique. Les niveaux dans ces images ont été tracés en fonction de l'épaisseur pour chaque valeur de haute-tension, permettant ainsi le calcul de la VBD par interpolation (voir figure 3). En 2006, la méthode de Highnam, Brady et al. [76] a également été adaptée aux systèmes numériques. Cette méthode sert de base à deux produits commerciaux: R2 QUANTRA™ (Hologic, Bedford, MA) et Volpara® (Matakina® Inc., Wellington, New Zealand). La principale difficulté pour ces méthodes est la nécessité de connaître l'épaisseur du sein

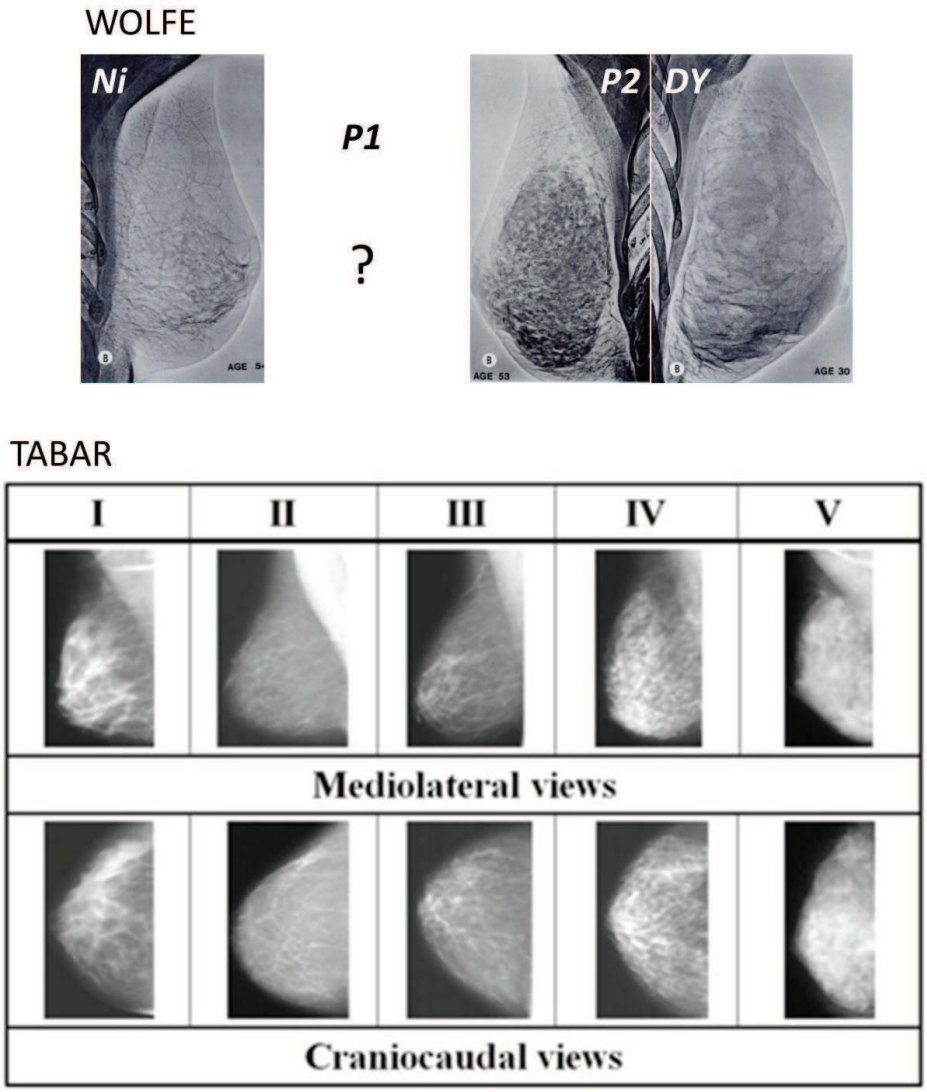

Figure 1: Exemples des catégories de Wolfe [152] et de Tabar [82]. Les images de Wolfe ont été acquises par xérographie et dans sa publication il manque la deuxième catégorie.

en chaque point. Highnam, Brady et al. déterminent l'épaisseur fondée sur le niveau dans une région supposée adipeuse prise dans la bande non-comprimée en bord de sein. Le logiciel R2 QUANTRA^{TM} utilise une méthode de correction d'épaisseur exploitant l'image et la hauteur de la pelote de compression [69]. Le logiciel Volpara® cherche une région adipeuse en utilisant la congruence de phase [75]. Shepherd et al. [130] ont comparé les valeurs de pixel dans le sein aux valeurs de pixel de deux objets de référence dans l'image. Pour surmonter le problème de non-planéité et de non-parallelisme de la pelote de compression, ils plaçaient des repères en plomb sur la pelote de compression [103].

Toutes ces méthodes reposent sur des hypothèses. Il est donc important que le résultat puisse être comparé à des valeurs de densité connues. Les quantités de tissus adipeux et fibroglandulaires sont alors calculées à partir d'images tri-dimensionnelles du même sein.

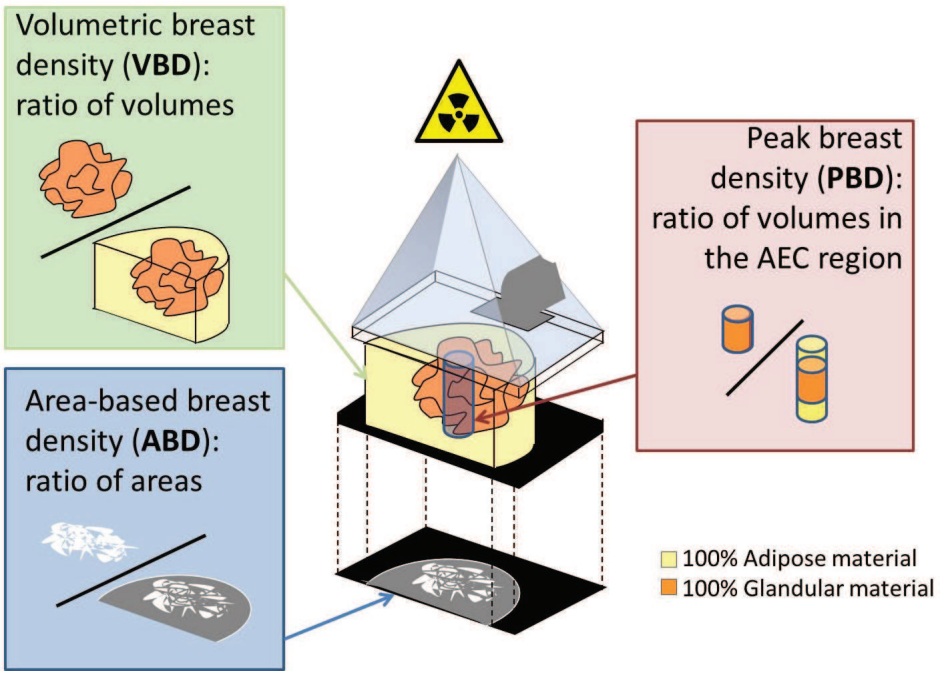

Figure 2: Schéma des différents types de densité du sein: la densité surfacique (ABD), la densité volumique (VBD) et la densité pic (PBD).

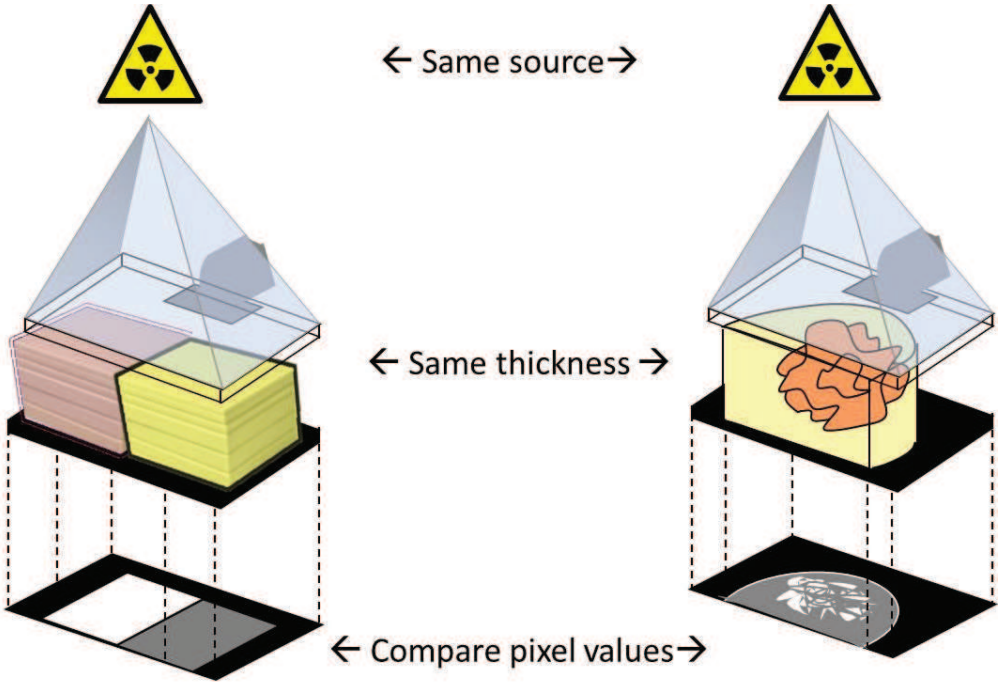

Figure 3: Schéma des méthodes pour calculer la VBD, par la comparaison des valeurs de pixel d'un objet inconnu à un objet connu pour les mêmes paramètres d'exposition.

Malheureusement les limites anatomiques du sein ne sont pas bien définies ce qui rend la détermination du volume difficile en 2D comme en 3D. Par conséquent il est difficile de trouver de bonnes corrélations entre les volumes calculés par différentes modalités [143,147]. Malgré cette difficulté, les corrélations entre les valeurs de VBD calculées dans des images mammographiques et par différentes modalités d'imagerie sont possibles. Pour les méthodes décrites précédemment (Volpara® [75], R2 QUANTRA™ [69]), les auteurs des publications ont comparé leurs résultats à la VBD calculée par segmentation du sein et du tissu glandulaire dans des images de résonance magnétique de la même patiente. Dans ce cas, la segmentation manuelle est nécessaire en raison des inhomogénéités qui empêchent l'utilisation d'un seuillage uniforme. En outre, les bords irréguliers et les petites structures fibreuses du tissu fibroglandulaire le rendent difficile à segmenter manuellement. Enfin, les images utilisées n'ont pas été acquises dans ce but, mais à des fins cliniques avec injection de produit de contraste. Les images qui en résultent peuvent donc ne pas être optimales pour la séparation des tissus suivant les mêmes critères qu'aux rayons X.
Alonzo-Proulx et al. [10] ont ensuite proposé une méthode de validation utilisant un scanner dédié au sein, méthode utilisée également par Vedantham et al. [146]. L'inconvénient principal de cette méthode est que ces équipement ne sont disponibles que dans un nombre limité de centres de recherche. En janvier 2014 Salvatore et al. [125] ont publié une étude montrant une bonne corrélation entre les classifications de BI-RADS et les mesures de VBD par segmentation manuelle d'images de scanner thoracique, indiquant la possibilité de son utilisation pour la validation de la VBD.

Nos contributions

Nous avons étudié une méthode améliorée de calcul de la VBD et nous l'avons validée au moyen d'images de scanner thoracique de routine. On peut ainsi profiter du grand nombre de scanners thoraciques acquis pour des raisons médicales autres que le dépistage du cancer du sein. Cette validation peut être mise en place facilement par d'autres utilisateurs de calcul de VBD.

Méthode de calcul de la VBD

La méthode pour calculer la VBD est schématisée en figure 4. D'après les lois de la physique du rayonnement [18, 25, 97] la formule

$$VBD_{MX} = \frac{ln(p/m)_A - ln(p/m)_x}{ln(p/m)_A - ln(p/m)_G} \tag{1}$$

a été obtenue. Dans cette formule, VBD_{MX} est la densité du sein volumique calculée dans les images mammographiques, p la valeur de pixel dans l'image, m le produit courant temps exprimé en mAs, A le tissu adipeux, G le tissu glandulaire et x le tissu inconnu. Les termes $ln(p/m)_a$ et $(ln(p/m)_a - ln(p/m)_g$ sont décrits par un polynôme d'ordre deux

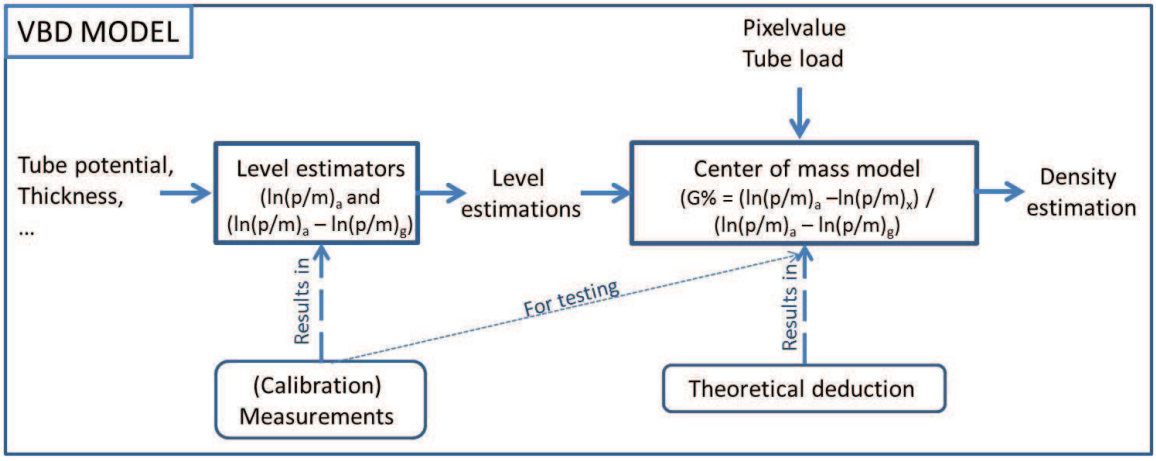

Figure 4: Vue d'ensemble de la méthode proposée de calcul de densité. La relation de type centre de gravité, basé sur la physique, prend comme entrées les modèles dérivés des mesures d'étalonnage (les valeurs prédites de $ln(p/m)_a$ et $(ln(p/m)_a - ln(p/m)_g)$), les paramètres d'acquisition et les valeurs de pixel.

en fonction de l'épaisseur du sein et de la tension du tube.

$$ln(p/m)_A = \begin{pmatrix} 1 & kV & kV^2 \end{pmatrix} \begin{pmatrix} a_{11} & a_{12} & a_{13} \\ a_{21} & a_{22} & a_{23} \\ a_{31} & a_{32} & a_{33} \end{pmatrix} \begin{pmatrix} 1 \\ T \\ T^2 \end{pmatrix}$$

$$ln(p/m)_A - ln(p/m)_G = \begin{pmatrix} 1 & kV & kV^2 \end{pmatrix} \begin{pmatrix} b_{11} & b_{12} & b_{13} \\ b_{21} & b_{22} & b_{23} \\ b_{31} & b_{32} & b_{33} \end{pmatrix} \begin{pmatrix} 1 \\ T \\ T^2 \end{pmatrix}$$

avec kV la tension du tube et T l'épaisseur du sein. Les coefficients a et b sont déterminés par acquisition d'images d'objets test d'épaisseur connue et de composition équivalente à du tissu glandulaire ou adipeux. Pour vérifier cette formule nous avons calculé la VBD pour des images de fantômes pour lesquels la VBD est connue. La corrélation entre les VBD connues et calculées est montrée en figure 5. Les résultats des calculs de VBD sont obtenus avec un écart inférieur à 1,5 point de densité par rapport à la valeur réelle et sont ainsi parmi les meilleurs présentés dans la littérature [75]. La distribution de mesures de densité dans notre base de données est comparée à la distribution publiée par Yaffe al. [156] (voir figure 6).
Pour l'application à des images de sein, l'épaisseur retenue est l'épaisseur de sein comprimé fournie par le mammographe.

Méthode de validation

La validation est basée sur la définition des unités Hounsfield (HU) comme fonction linéaire des coefficients d'atténuation moyens des matériaux. Par conséquent les HU varient linéairement avec la VBD locale sans nécessiter de segmenter les zones glandulaires et

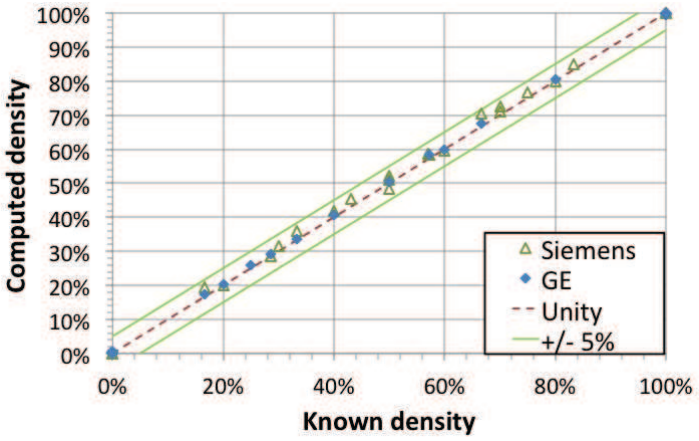

Figure 5: Vérification de l'équation 1 : la corrélation entre les VBD connues et calculées pour des fantômes pour deux mammographes différents.

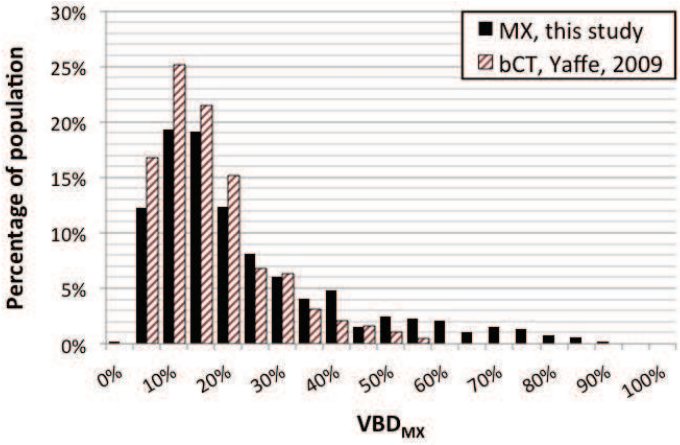

Figure 6: Distribution des VBD pour la population de dépistage. Les résultats de notre étude sont comparés aux résultats de Yaffe et al. [156].

peuvent être calculés par la formule

$$VBD_{CT} = \frac{HU_X - HU_A}{HU_G - HU_A} \tag{2}$$

avec VBD_{CT} la densité calculée en scanner thoracique, HU la valeur Hounsfield, A le tissu adipeux, G le tissu glandulaire et X le tissu inconnu. HU_A et HU_G ont été déterminés à partir d'images de patientes sur lesquelles des zones de tissu purement adipeux et purement glandulaire ont pu être identifiées. Cette formule est valable localement ainsi qu'en moyenne sur l'ensemble du sein.

La mesure qui vient d'être décrite peut être facilement comparée aux résultats de VBD provenant des images mammographiques. En effet il suffit de choisir parmi les patients ayant subi un scanner thoracique, les femmes dont la tranche d'âge correspond au dépistage du cancer du sein, ce qui donne une probabilité élevée qu'elles aient également subi une mammographie dans un intervalle de temps acceptable. Au total nous avons exploité

87 clichés de seins pour lesquels nous avons corrélé la VBD_{MX} et le HU dans la zone identifiée comme étant le sein. La corrélation est présentée en figure 7. La moyenne des

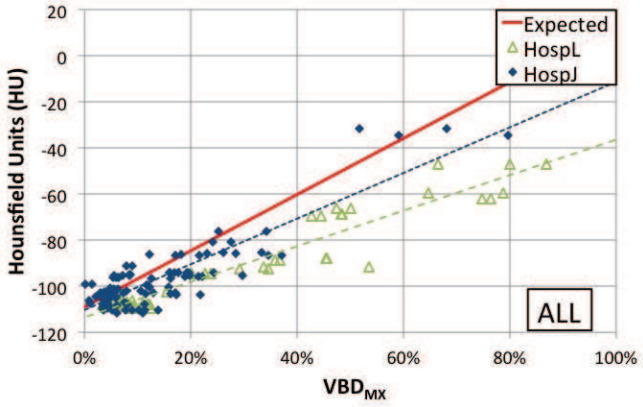

Figure 7: Le HU moyen du volume de sein en CT thoracique rapporté à la VBD_{MX}. Chaque point représente un sein pour lequel le HU moyen est accessible ainsi que la VBD_{MX} estimée. Des cas de deux hôpitaux différents sont représentés séparément avec leur régression linéaire correspondante. Le trait plein représente les HU attendus selon l'équation 2 et la détermination des valeurs de HU_A et de HU_G.

erreurs de l'ensemble des points dans nos deux bases de données, construites à cette fin, est de 10% et 4%. Les différences sont dues à différents facteurs, comme le positionnement du sein par la manipulatrice et l'interprétation des limites du sein par deux physiciens. A nouveau les résultats sur la distribution sont comparables aux meilleures valeurs de la littérature utilisant l'IRM.

Energie déposée dans la glande

Etat de l'art

En général, il est admis que le risque radique lié à un examen de mammographie est limité au sein lui-même. Hammerstein et al. [66] ont étudié la dose absorbée par le sein et ont proposé d'adopter une grandeur qui prendrait en compte la distribution spatiale du tissu à risque. Pour cette raison, l'attention devait se porter sur l'énergie déposée dans le tissu glandulaire, et il était nécessaire de faire des hypothèses sur la quantité et la distribution du tissu glandulaire dans le sein moyen. En conséquence, ils ont proposé "l'énergie totale déposée dans le tissu glandulaire" comme indicateur le plus représentatif du risque en mammographie et la "dose moyenne à la glande pour un sein moyen" comme base de comparaison des doses produites par différentes techniques de radiographie [85]. Cette dernière grandeur avait l'avantage de ne pas nécessiter la connaissance de la distribution du tissu glandulaire.
Par la suite, de nombreux auteurs [22, 39, 124, 132, 153] ont développé des méthodes pour calculer la dose glandulaire moyenne (DGM). La méthode de Dance [41] a été intégrée dans les régulations nationales et internationales et les recommandations de contrôle de qualité comme en Europe [116]. Les méthodes retenues déterminent les valeurs de DGM normalisées par rapport au kerma dans l'air dans le plan d'entrée du sein [21].

Dance et al. [39], Wu et al. [153] et Boone [22] ont construit des tables de DGM normalisée à partir de la méthode de Monte-Carlo pour un fantôme semi-circulaire pour différentes épaisseurs [39, 133] et contenus [41, 153] et pour différents spectres de rayons X [22, 23, 41, 154].
Pourtant la DGM ne correspond pas aux besoin d'une mesure du risque individuel [35, 126] et ces limitations ont été soulignées par Sechopoulos et al. [128].
La limitation principale a été indiquée par Dance et al. [40], qui ont démontré une différence allant jusqu'à 43% en calculant la DGM pour respectivement un fantôme texturé et le fantôme homogène utilisé pour la détermination des tables. Porras-Chaverri et al. [120] ont trouvé également des différences considérables pour des fantômes d'une densité totale de 50%, mais constitués de couches de densités différentes placées dans un ordre différent. Ces différences pouvaient atteindre jusqu'à 50% pour des fantômes de 8 cm d'épaisseur avec la couche la plus dense positionnée à la sortie du fantôme. Sechopoulos et al. [128] en calculant la DGM pour des images de patientes acquises avec un scanner dédié à la mammographie, ont trouvé une surestimation de 27% en moyenne sur la DGM pour le sein structuré par rapport au sein homogène de même densité.
Une autre limitation concerne la quantité de tissu glandulaire du sein moyen. La composition moyenne de 50% de tissu glandulaire a été introduite par Hammerstein [66] en l'absence de connaissance plus précise. Depuis il a été démontré que la densité du sein est plutôt de 20% [93, 146, 156] (voir figure 6).
Les différents auteurs ont traité ce problème en prenant en compte la densité dans les tables de DGM normalisée. Dans l'utilisation de ces tables un problème subsiste, la connaissance de la valeur de densité à utiliser, c'est-à-dire la densité massique en excluant la peau. Cette nécessité est trop souvent négligée par les utilisateurs des tables de DGM normalisée. Dans notre présentation au RSNA 2013 [58], nous avons démontré une différence atteignant 15% pour le même fantôme avec différentes définitions de densité (surfacique, volumique, massique, ...). La densité surfacique surestime la densité massique, ce qui provoque une sous-estimation de la DGM.
Un troisième problème rencontré avec les simulations de Monte-Carlo initiales a été la valeur de l'épaisseur de la peau. Là où Dance [39] et Wu [153] ont utilisé respectivement 5 et 4 mm de tissu adipeux, Huang et al. [78] ont mesuré 1,45 mm en moyenne sur de vraies patientes et avec des densités et compositions plus proches du tissu glandulaire que du tissu adipeux [66]. Par conséquent, en utilisant les tables, l'énergie absorbée dans le cas de vrais seins est sous-estimée.

Nos contributions

La médecine d'aujourd'hui s'oriente vers l'individualisation [15, 138] et donc une alternative à la DGM, mieux représentive du risque individuel, est nécessaire. Nous proposons ici une méthode non pas pour "individualiser la DGM", mais permettant de calculer l'énergie déposée dans la glande (GIE) comme proposé par Hammerstein et al. [66]. En particulier on devra prendre en compte pour chaque patiente la quantité et la localisation des différents tissus mammaires. Des essais utilisant une carte de densité ont déjà eu lieu pour estimer la localisation du tissu glandulaire [119]. L'émergence de la tomosynthèse du sein rend partiellement possible la localisation du tissu glandulaire dans le sein comprimé [121, 123, 145], ce qui permet de calculer l'énergie déposée dans le tissu glandulaire (GIE) et adipeux (AIE) séparément. Dans cette thèse nous présentons une méthode permettant d'estimer la

localisation du tissu glandulaire et d'analyser l'énergie déposée par couche de tissu pour un spectre polyénergétique.

Calcul de l'énergie déposée

Notre but est de calculer l'énergie déposée en chaque point en tenant compte de tous les mécanismes d'interactions. Nous avons donc choisi d'y accéder par des simulations de Monte-Carlo. Pour cela, nous avons utilisé un outil interne de GE, le logiciel CatSim et son modèle de dose CatDose [104]. Ce logiciel ayant été développé pour les applications CT, nous avons validé son extension au calcul de dose en mammographie. Ceci a été fait en recalculant les facteurs de DGM normalisée des tables de Dance [41] et de Boone [23], obtenant un écart inférieur à 10%.
Cet outil a été utilisé pour calculer l'énergie déposée dans des fantômes géométriques connus et d'étudier l'influence de la quantité et de la distribution du tissu glandulaire sur respectivement l'énergie déposée et la DGM [61].

Calcul de l'énergie déposée par couche

La GIE locale a été calculée par des simulations de Monte-Carlo, non-compatibles avec une implementation en routine. Il serait donc préférable de disposer d'une méthode de calcul plus simple et plus rapide. Pour cela nous avons étudié la distribution de l'énergie déposée en fonction de la profondeur dans le tissu, comme déjà décrit pour la radiologie générale par Chan et Doi [31] en segmentant un volume deau par couches dépaisseur finie. Les résultats ont été calculés en normalisant les valeurs par rapport au kerma dans l'air. L'énergie déposée par couche de 1 mm à été calculée par la méthode de Monte-Carlo pour un fantôme homogène de forme identique à celle du fantôme décrit par Dance et al. [39] et de composition uniformément glandulaire ou uniformément adipeuse. Les valeurs obtenues ont été normalisées également par unité de surface. Le résultat est donc la valeur de l'énergie déposée par unité de volume ou énergie volumique déposée (EVD).
La figure 8 montre le résultat des simulations. L'énergie reçue par une couche est la

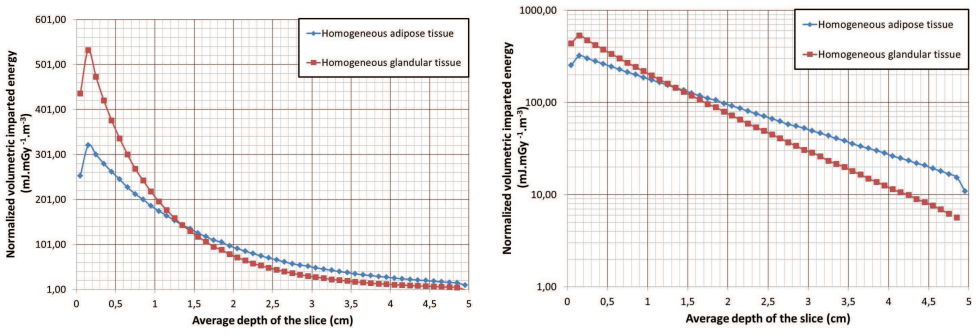

(a) (b)

Figure 8: Énergie volumique déposée normalisée au kerma dans l'aire à l'entrée pour un fantôme de référence uniformément adipeux ou glandulaire.

somme des énergies déposées par le faisceau incident atténué par les couches précédentes, le rayonnement diffusé par les couches précédentes et le rayonnement retro-diffusé par les

couches suivantes. Pour les premières couches l'énergie volumique dpose est inférieure en l'absence de diffusé par les couches précédentes. Le pic initial observé est comparable à l'effet de *build-up*, bien connu en radiothérapie. En régime d'équilibre, après 3 mm, l'énergie volumique déposée varie exponentiellement avec la profondeur. Dans le cas d'un volume constitué de tissu purement glandulaire la valeur extrapolée à l'origine de l'EVD est de 532 mJ.mGy^{-1}.m^{-3} et elle est divisée par deux tous les 7,3 mm (coefficient d'atténuation linéaire 0,95 cm^{-1}). Pour un volume constitué de tissu purement adipeux la valeur extrapolée à l'origine est de 347 mJ.mGy^{-1}.m^{-3} et elle est divisée par deux tous les 10,7 mm (coefficient d'atténuation linéaire 0,64 cm^{-1}). Il en résulte que les deux courbes se croisent à 13 mm, épaisseur pour laquelle l'énergie volumique déposée dans le tissu adipeux devient plus élevée que dans le tissu glandulaire. On retrouve ici le même comportement que pour le calcul de lénergie déposé (ou du kerma) à partir du coefficient datténuation linéaire énergétique en monoénergétique, pour des valeurs correspondant à respectivement 18 keV (tissu adipeux) et 18,5 keV (tissu glandulaire). Une méthode comparable avait déjà été proposée en négligeant lénergie déposée par effet Compton, le diffusé non colinéaire et les diffusions multiples [65]. Elle est ici confirmée sans faire dhypothèse particulière. Il est donc possible de calculer l'énergie déposée dans un volume dont on connait les caractéristiques et la composition locale.

Localisation du tissu glandulaire

Nous proposons une méthode de segmentation des images obtenues en tomosynthèse utilisant la VBD. La VBD peut être calculée pour la projection à 0° comme pour une mammographie normale. Le calcul a été mis au point pour le système de tomosynthèse SenoClaire de GE. Ce système comporte une grille anti-diffusante utilisée aussi bien en mammographie 2D qu'en tomosynthèse, et donc un seul étalonnage suffit. La VBD peut être interprétée comme étant le pourcentage de voxels du sein constitués de tissu glandulaire, les autres étant du tissu adipeux. Contrairement au scanner l'angle de balayage limité de la tomosynthèse ne permet pas d'obtenir des images quantitatives. En particulier la résolution suivant l'axe des rayons X est très inférieure à la résolution dans le plan des images reconstruites, ce qui se traduit par des artefacts qui se propagent en dehors des plans reconstruits, rendant difficile la semgentation des tissus. La méthode de segmentation proposée est basée sur la conservation de la densité entre une projection et le volume reconstruit. Nous calculons l'histogramme du volume reconstruit et fixons un seuil au-dessus duquel la proportion de voxels par rapport au volume total du sein est égale à la VBD. Les voxels dont la valeur est au-dessus du seuil sont classés comme "glandulaires", et les autres comme "adipeux".

Application au calcul de l'énergie déposée en tomosynthèse

Dans un premier temps nous avons défini une série de fantômes géométriques comportant différentes distributions de zones glandulaires sphériques. Nous avons calculé l'énergie déposée dans ces fantômes, la valeur résultante étant considérée comme étant la valeur vraie. Ensuite une tomosynthèse a été simulée et le volume 3D reconstruit. Un deuxième calcul d'énergie déposée a été fait pour le volume 3D reconstruit, et le résultat comparée au résultat précédent. Les valeurs de GIE sont en dessous de 5μJ/mGy pour des masses de glande principalement de 32g. Pour neuf des dix fantômes les écarts entre les valeurs

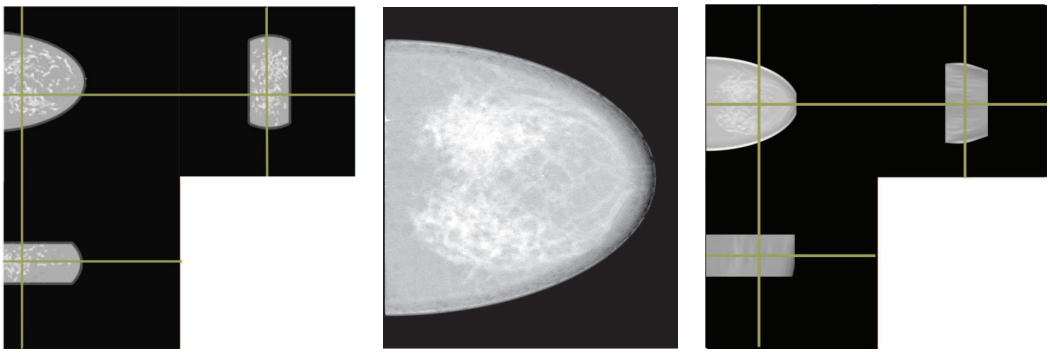

(a) (b) (c)

Figure 9: a) Fantôme texturé, b) une projection de tomosynthèse et c) le volume reconstruit.

de masse glandulaire vraies et reconstruites varient entre 8% et 13%. Pour le dixième fantôme, caractérisé par une faible épaisseur et des sphères glandulaires de diamètre égal à l'épaisseur du fantôme, l'écart est de 83%. Pour la moitié des fantômes l'écart en énergie déposée est inférieur à 20%. Les fantômes présentant les plus grands écarts relatifs sont le fantôme dont la masse a été mal calculée, le fantôme où l'énergie déposée est presque nulle et le fantôme d'épaisseur la plus élevée, pour lequel le rayonnement utilisé est de trop basse énergie.
La méthode a été appliquée à un fantôme texturé généré suivant Carton et al. [30] dont la VBD est de 6%. Le fantôme est présenté en diamètre en figure 9(a), une image de projection en figure 9(b) et le volume reconstruit en figure 9(c).
Après reconstruction, nous avons appliqué la méthode de segmentation par l'histogramme. Les volumes original et reconstruit sont représentés segmentés en figure 10.
La masse totale du fantôme est surestimée de 15% et la masse glandulaire de 23%. L'énergie déposée dans la glande est sous-estimée de 25%. Cette méthode a également été appliquée à une image de tomosynthèse d'une patiente sans possibilité de comparer la valeur trouvée à une valeur vraie.

Conclusion

Ce projet de recherche avait deux buts principaux : a) l'implémentation et l'amélioration d'une méthode de calcul de densité volumique du sein (VBD), et b) la proposition d'une grandeur d'irradiation utilisable pour l'évaluation du risque individuel en mammographie avec une méthode pour l'estimer.

Nous avons développé une méthode de mesure de la VBD et l'avons appliquée à deux équipements de mammographie numérique. Cette méthode repose sur un étalonnage du système avec des fantômes d'épaisseur connue et d'absorption équivalente aux tissus mammaires. Une carte de densité est calculée à partir de l'image numérique acquise en utilisant les paramètres d'acquisition. La précision obtenue est de 1,2%, et comparable à l'état de l'art [75]. Nous avons également mis au point et appliqué une méthode de validation de la VBD par comparaison entre la VBD_{MX} issue d'images mammographiques et la VBD_{CT} calculée dans des images de scanner thoracique. L'écart entre cette méthode

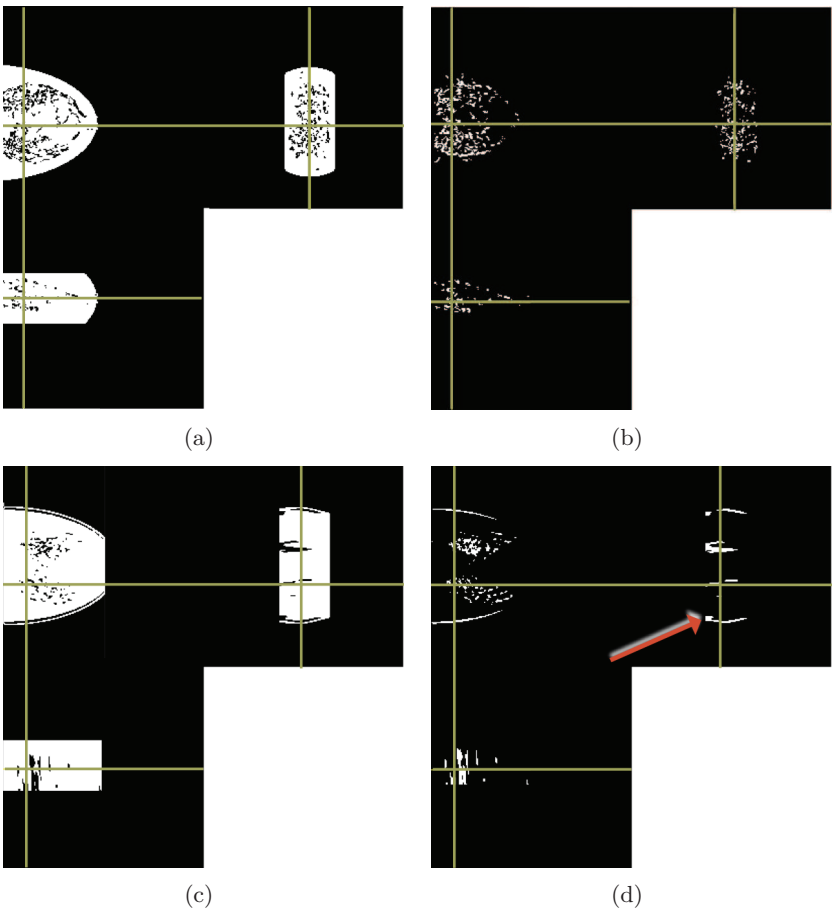

Figure 10: Segmentations du tissu a) adipeux et b) glandulaire du volume original, et du tissu c) adipeux et d) glandulaire du volume reconstruit.

et notre méthode de calcul de VBD est de moins de 10% en moyenne, ce qui est acceptable.

Dans la deuxième partie, nous avons cherché une alternative à la dose glandulaire moyenne (DGM) actuellement utilisée, qui est une bonne mesure collective, mais ne répond pas aux besoins d'une mesure individuelle pour le risque radique [58,61]. A la suite de Hammerstein en 1979 [66] nous avons retenu l'énergie déposée dans la glande (GIE). Cette grandeur demande des calculs plus complexes que la DGM, car elle nécessite la connaissance de la distribution de la glande dans le sein suivi du calcul de l'énergie déposée en chaque point du volume du sein. La tomosynthèse permet d'accéder à une approximation de la distribution de la glande. La méthode présentée est donc une démonstration de faisabilité pour le calcul de la GIE en tomosynthèse du sein. La segmentation du volume obtenu par tomosynthèse se fait de manière à conserver la VBD par rapport à la projection à 0°. Des valeurs typiques de GIE par kerma dans l'air sont en dessous de 20μJ/mGy. Actuellement l'énergie déposée est calculée par simulation de Monte-Carlo. Cependant nous avons montré la possibilité de calculer une fois pour toutes l'énergie volumique déposée pour chaque qualité de faisceau et pour chacun des deux tissus mammaires, rendant possible une implémentation de la méthode proposée pour des examens de tomosynthèse du sein.

Ces travaux ouvrent une nouvelle voie pour des mesures de risque radique individuel, et des études importantes sont encore nécessaires avant que la GIE ne puisse devenir un standard en mammographie.

Avec cette thèse et nos publications, nous avons augmenté les informations qu'il est possible d'obtenir à partir d'une image mammographique en espérant que ces données pourront contribuer à l'amélioration et à l'individualisation du dépistage du cancer du sein.

Samenvatting

Probleemstelling

Het onderzoeksproject situeert zich in het gebied van de medische beeldvorming, meer bepaald van de borst en borstkankerscreening. Borstkanker is een veelvoorkomende aandoening, namelijk 25.5% van de kankers bij vrouwen [7], en is verantwoordelijk voor 16% van de overlijdens door kanker bij volwassen vrouwen [6]. Dankzij borstkanker screening kunnen verdachte letsels vroeg-tijdig worden opgespoord en is hun behandeling minder invasief met hogere overlevingskansen [8]. De borstkanker screening gebeurt via mammografie. Deze modaliteit gebruikt X-stralen om een projectiebeeld vormen van het weefsel binnenin de borst. Zoals voor elke blootstelling aan X-stralen, moet het "ALARA (As low as raisonably achievable)"-principe worden toegepast: een blootstelling is enkel en alleen gerechtvaardigd als het voordeel significant hoger is dan het nadeel, of dus als er meer kankers gevonden worden dan veroorzaakt. Hoewel in de meeste Westerse landen een screeningprogramma opgezet is, blijft het debat over de voor- en nadelen voortduren [20, 94, 111, 134]. De kwaliteit van de screeningstoestellen wordt strict gecontroleerd [116] en continu verbeterd. Een mogelijke verbetering betreft het definiëren van de doelgroep, vandaag enkel gebaseerd op leeftijd en indirect soms op familiale antecedenten [71]. Een tweede mogelijke verbetering zou bestaan uit een verbeterde schatting van de stralingsblootstelling na een onderzoek. Voor beide verbeteringen is de densiteit, m.a.w. de hoeveelheid klierweefsel in de borst, een belangrijke parameter [41,108].

De borst bevat voornamelijk adipeus en fibroglandulair weefsel, waarbij het adipeus weefsel donkerder is in het beeld en het fibroglandulair weefsel lichter. De verhouding van beide weefsels is verschillend van vrouw tot vrouw. Het percentage fibroglandulair weefsel ten opzichte van het totaal borstweefsel wordt densiteit genoemd (zie verder voor een nauwkeurige definitie). De densiteit werd geïdentificeerd als een risico-indicatie voor het ontwikkelen van borstkanker in verschillende studies [108]. Bovendien maakt de aanwezigheid van klierweefsel het moeilijker om letsels op te sporen. Oorspronkelijk werden borsten volgens het projectiebeeld geklasseerd door Wolfe in 1976 [152]. De invloed van de densiteit op de ontwikkeling van borstkanker is tot nu toe echter niet goed begrepen [26,106]. Een van de moeilijkheden is de consensus over de manier waarop densiteit moet berekend worden [54, 73], de afwezigheid van een algemeen erkende methode om de verdeling te karakteriseren [88, 100, 148] en om die gegevens daarna in een risicomodel te integreren [32]. In 1979 beschreven Hammerstein et al. [66] fibroglandulair weefsel als weefsel dat meer gevoelig aan straling dan adipeus en huidweefsel. In hun conclusie stelden ze de totale energie geabsorbeerd door het fibroglandulair weefsel voor als de beste grootheid om het individuele stralingsrisico te bepalen. Ze voegden hieraan toe dat

de kennis van hoeveelheid en verdeling noodzakelijk waren om de grootheid te kunnen berekenen.

Volumetrische borstdensiteit

State of the art

De classificatie van de mammografieën werd initïeel ontwikkeld door Wolfe in 1976 [152]. Hij stelde categoriëen voor volgens de eigenschappen van het parenchym en de relative verdeling ervan in het beeld (zie Figuur 11). Tabar et al. [64] stelden een classificatie voor met vijf categoriëen (zie Figuur 11) en Jeffreys et al. [83] zelfs zes. De BI-RADS-

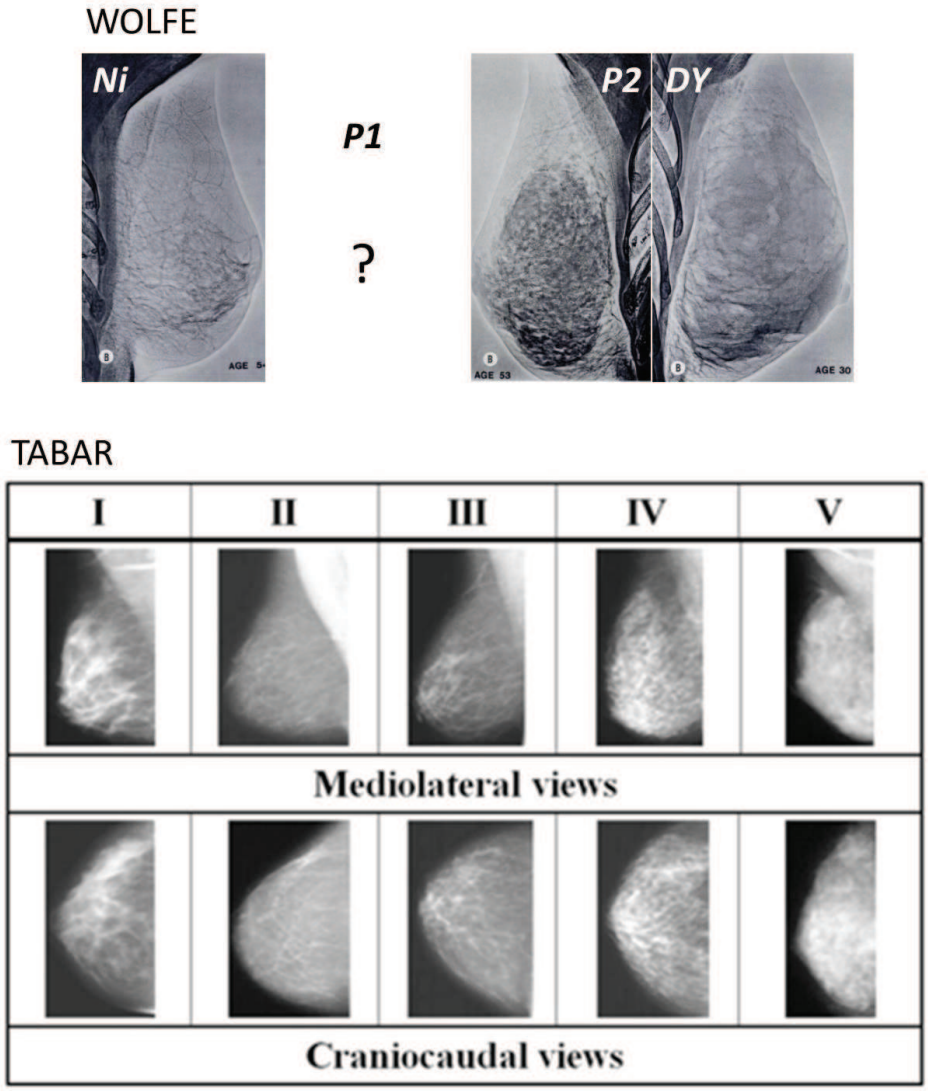

Figure 11: Voorbeelden van de categoriën van Wolfe [152] en Tabar [82]. De beelden van Wolfe werden genomen met een xerografie toestel en in de publicatie mist de tweede categorie.

classificatie [33], gebaseerd op de classificatie van Wolfe, schat de verhouding van de

fibroglandulaire zone en de totale zone van de borst in de beelden(*area-based breast density (ABD)*) zoals weergegeven in Figuur 12. De verhouding tussen het volume van fibroglandulair weefsel en het volume van de volledige borst heet volumetrische borstdensiteit (*volumetric breast density (VBD)*). De mammografietoestellen bevatten vaak een automatische exposiecontroller, die volautomatisch het meest dense gebied in de borst zoekt. De volumetrische borstdensiteit in deze zone heet *peak breast density (PBD)*. De

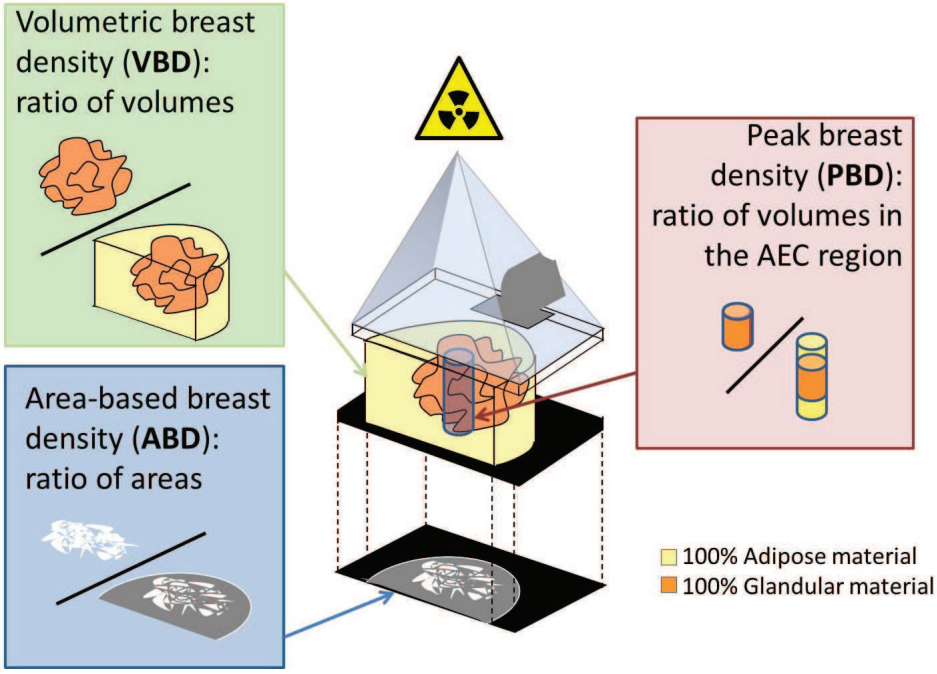

Figure 12: Schema van de verschillende types borstdensiteiten: de oppervlaktedensiteit (ABD), de volumetrische densiteit (VBD) en de piekdensiteit (PBD).

classificaties van Wolfe [152], Tabar et al. [64] en BI-RADS [33] worden visueel geschat door de radiologen. Half-automatische algoritmes werden ontwikkeld voor de schatting van de ABD, gebaseerd op een drempelwaarde voor pixelwaardes [27, 102, 160]. Zelfs bij automatische bepaling van de ABD is gebleken dat de waarden bekomen bij verschillende opnames van dezelfde borst kunnen verschillen omdat er bij compressie en projectie steeds een ander beeld van het glandulair weefsel verkregen werd. Daarom is de VBD beter geschikt om het borstweefsel te karakteriseren [95]. Het berekenen van de VBD is mogelijk via de beelden en de exposieparameters.

Het merendeel van de recente methodes voor de VBD-berekening is gebaseerd op het werk van Highnam, Brady en Shepstone in 1996 [74]. Zij digitaliseerden de mammogrammen van systemen gecalibreerd met behulp van een fantoom. De gedigitaliseerde pixelwaarden werden vervolgens vergeleken met deze van de gekende fantomen. Een dagelijkse calibratie was nodig om fluctuaties in de systemen te kunnen verwerken.
In 2002 publiceerden Kaufhold et al. [86, 87] een methode voor de berekening van de VBD in digitale mammogrammen. Ze namen hiervoor beelden van borstweefsel equivalent materiaal (0%, 50% et 100% VBD) voor diktes en buisspanningen die klinisch voorkomen. De pixelwaarden in de calibratiebeelden worden uitgezet en geïnterpoleerd als functie

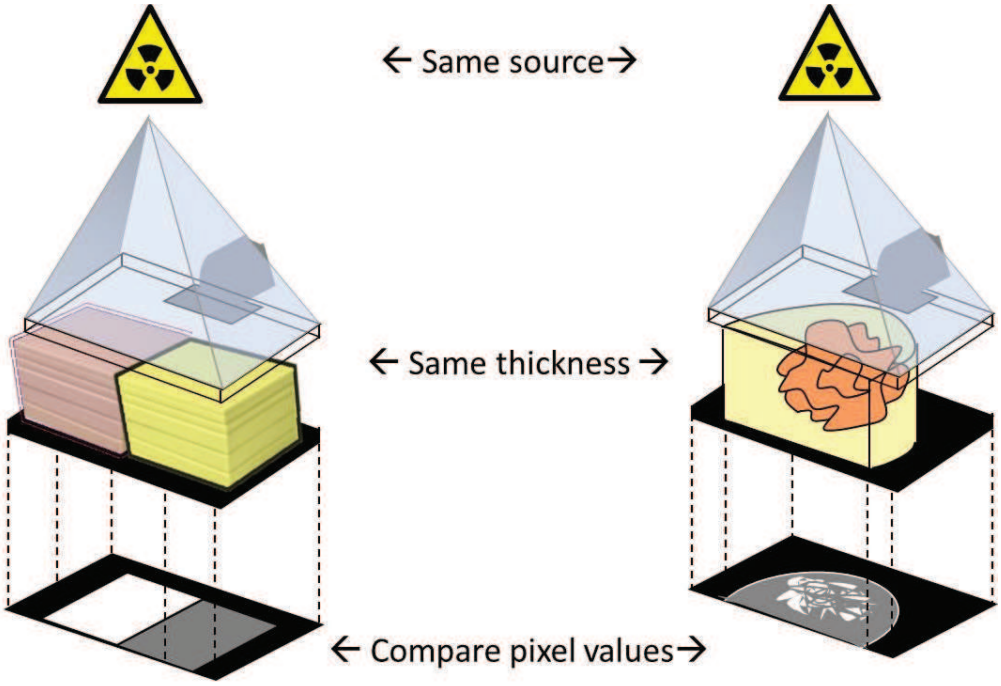

Figure 13: Schema van de methode om de VBD te berekenen, gebaseerd op de vergelijking van de pixel waardes van het onbekende object met deze van gekende objecten (fantomen) genomen met dezelde acquisitieparameters.

van de dikte voor een constante spanning, zodat de VBD berekend kan worden (zie Figuur 13). In 2006, werd de methode van Highnam, Brady et al. [76] aangepast aan de digitale systemen. De methode was ook de basis van twee commerciele producten: R2 QUANTRA™ (Hologic, Bedford, MA) en Volpara® (Matakina® Inc., Wellington, New Zealand). Het moeilijkste punt is de meting van de dikte die bij Highnam, Brady et al. gebaseerd was op de adipeuse band in het niet-samengedrukte deel aan de rand van de borst. De R2 QUANTRA™ software maakt gebruik van een diktecorrectiemethode gebaseerd op het beeld en de hoogte van de compressieplaat [69]. De Volpara® software gebruikt fasecongruentie [75]. Shepherd et al. [130] vergeleken de pixelwaardes in de mammografieën met twee referenties in het beeld. Om het dikteprobleem op te lossen met inbegrip van de oriëntatie van de compressieplaat, plaatsten ze een fantoom met loodmarkeringen op de compressieplaat [103].

Al deze methodes houden hypotheses in en bijgevolg moeten de resultaten vergeleken kunnen worden met gekende densiteiten. De hoeveelheden adipeus en fibroglandulair weefsel kunnen berekend worden gebaseerd op een 3D beeldacquisitie van dezelfde borst. De anatomische aflijningen van de borst zijn echter niet goed gedefiniëerd, waardoor het vinden van het volume moeilijk is zowel in 2D als in 3D beeldvorming. Bijgevolg is het ook moeilijk om een goede correlatie te vinden tussen volumes berekend via verschillende modaliteiten [143,147]. Ondanks deze moeilijkheid blijkt het toch mogelijk een correlatie te vinden. Voor de VBD methodes eerder beschreven (Volpara® [75], R2 QUANTRA™ [69]) vergeleken de auteurs hun resultaat met de VBD berekend uit de segmentatie van borst

en klierweefsel in magnetische resonantie (MR) beelden van eenzelfde patiente. Manuele segmentatie is nodig omwille van inhomogeniteiten die een uniforme drempel pixelwaarde verhinderen. Echter de onregelmatige en fibreuse structuren maken manuele segmentatie echter moeilijk. De MR beeldvorming werd ook niet geoptimaliseerd voor optimaal contrast tussen adipeus en klierweefsel maar om de perfusie van tumoren in het licht te stellen, vaak met constrastproduct. Ze berust ook niet op dezelfde criteria als voor X-stralen beeldvorming (relaxatie van nucleaire spins versus X-stralen attenuatie).
Alonzo-Proulx et al. [10] hebben daarna een methode voorgesteld voor de validatie, gebruik makend van een borst CT scanner. Deze methode werd eveneens door Vedantham et al. [146] gebruikt. Het grootste nadeel van deze methode is dat er slechts een paar prototype scanners ter beschikking zijn in geselecteerde centra. In januari 2014 publiceerden Salvatore et al. [125] een studie die aantoonde dat er een goede correlatie is tussen BI-RADS classificatie en de VBD berekend via manuele segmentatie van beelden van thorax scans. Daaruit kunnen we besloten wij dat thorax CT scanners een goede bron zouden kunnen zijn voor de validatie van VBD.

Onze bijdragen

We hebben een methode bestudeerd en verbeterd om de VBD te berekenen, die we vervolgens met thorax CT beelden gevalideerd hebben. We konden hiervoor rekenen op een groot aantal thorax CT scans genomen voor verschillende medische doeleinden, andere dan borstkanker screening en ter beschikking in de PACS. Deze validatie kan gemakkelijk door andere gebruikers van VBD berekeningen geimplementeerd worden.

Berekening van de VBD

De methode om de VBD te berekenen wordt schematisch weergegeven in figure 14. Vanuit de stralingsfysica [18, 25, 97] kunnen we afleiden dat

$$VBD_{MX} = \frac{ln(p/m)_A - ln(p/m)_x}{ln(p/m)_A - ln(p/m)_G} \tag{3}$$

met VBD_{MX} de volumetrische borstdensiteit berekend in de mammografie beelden, p de offset gecorrigeerde pixelwaarde in het beeld, m het stroom tijd product uitgedrukt in mAs, A het adipeus weefsel, G het glandulaire weefsel en x het onbekende weefsel. De termen $ln(p/m)_a$ en $(ln(p/m)_a - ln(p/m)_g$ worden beschreven door een polynoom van tweede orde in functie van de borstdikte en de buisspanning.

$$ln(p/m)_A = \begin{pmatrix}1 & kV & kV^2\end{pmatrix} \begin{pmatrix}a_{11} & a_{12} & a_{13}\\ a_{21} & a_{22} & a_{23}\\ a_{31} & a_{32} & a_{33}\end{pmatrix} \begin{pmatrix}1\\ T\\ T^2\end{pmatrix}$$

$$ln(p/m)_A - ln(p/m)_G = \begin{pmatrix}1 & kV & kV^2\end{pmatrix} \begin{pmatrix}b_{11} & b_{12} & b_{13}\\ b_{21} & b_{22} & b_{23}\\ b_{31} & b_{32} & b_{33}\end{pmatrix} \begin{pmatrix}1\\ T\\ T^2\end{pmatrix}$$

met kV de buisspanning en T de borstdikte. De coëfficiënten a en b worden bepaald via beelden van testobjecten met een gekende dikte en samenstelling (glandulair of adipeus). Om deze formule te verifiëren, hebben we de VBD berekend voor beelden van fantomen

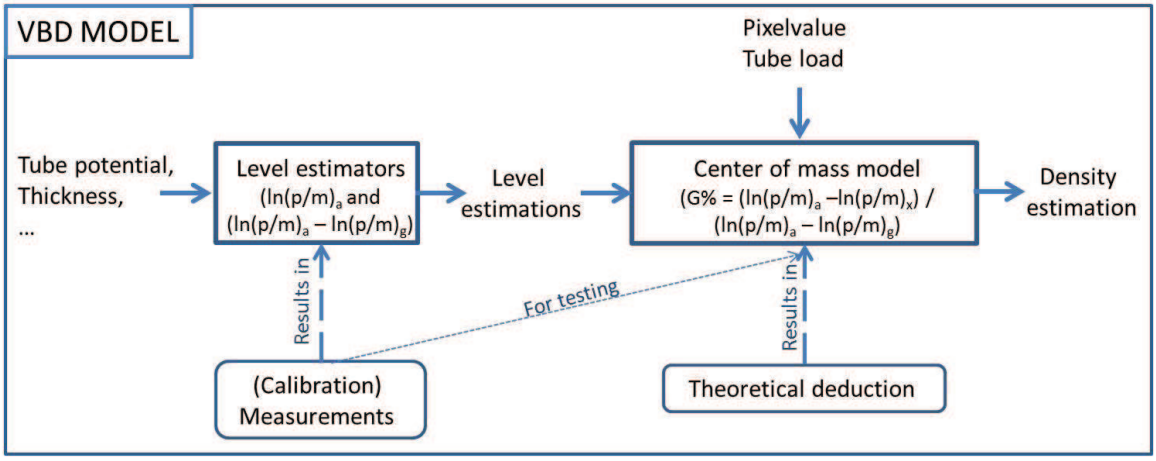

Figure 14: Overzicht van de voorgestelde methode voor de berekening van de densiteit. De parameters voor de massacentrum-vergelijking, gebaseerd op de fysische eigenschappen, zijn de modellen afgeleid van de ijkingsmetingen (de voorspelde waarden van $ln(p/m)_a$ en $(ln(p/m)_a - ln(p/m)_g)$, de acquisitieparameters en de pixel waardes.

met gekende VBD. De correlatie tussen de berekende en gekende VBD is weergegeven in figuur 15. De resultaten van de VBD berekeningen hebben een maximum verschil van 1,5

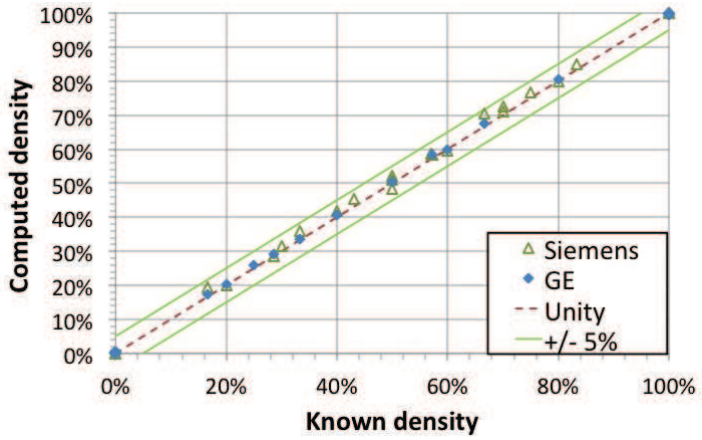

Figure 15: Verificatie van vergelijking 3 : de correlatie tussen de gekende en berekende VBD voor fantomen voor twee verschillende mammografie toestellen.

densiteitspercentages ten opzichte van de werkelijke waarde en zijn daarmee bij de beste resultaten uit de literatuur [75]. Een histogram van de verdeling van de densiteit in onze databank wordt vergeleken met de verdeling gepubliceerd door Yaffe al. [156] (figuur 16). Voor de toepassing van de methode op beelden van borsten wordt de dikte gebruikt van de samengedrukte borst zoals die ter beschikking is inde DICOM header van het beeld.

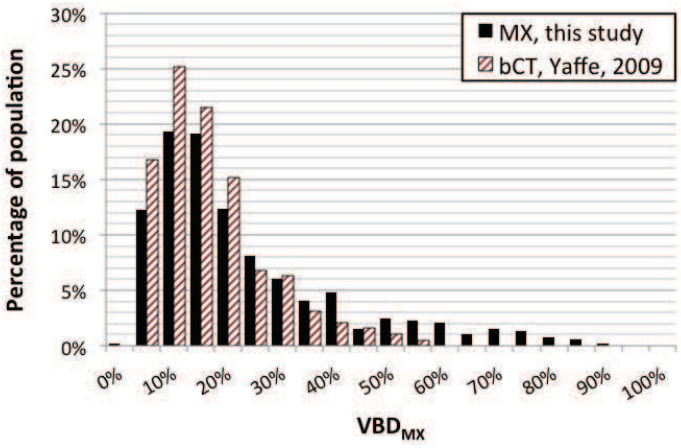

Figure 16: Verdeling van de VBD voor de screeningspopulatie. De resultaten van onze studie worden vergeleken met de resultaten van Yaffe et al. [156].

Validation methode

De validatie is gebaseerd op de definitie van de Hounsfield Unit (HU) die een lineaire functie is van de gemiddelde attenuatiecoëfficiënten van de materialen. Bijgevolg variëren de HU lineair met de lokale VBD zonder dat het nodig is om de glandulaire zones af te lijnen. De bijhorende formule is

$$VBD_{CT} = \frac{HU_X - HU_A}{HU_G - HU_A} \tag{4}$$

met VBD_{CT} de densiteit berekend met de thorax CT, HU de Hounsfield Units, A het adipeus weefsel, G het glandulair weefsel en X het onbekende weefsel. HU_A en HU_G werden bepaald vanuit de patiëntenbeelden waar puur adipeuse en glandulaire zones geïdentifiëerd werden. Deze formule is geldig, zowel lokaal als gemiddeld over het volledige borstvolume.

De VBD_{CT} hebben we vergeleken worden met de resultaten van de VBD uit de mammografie beelden. Het volstond om vrouwen te selecteren die in hetzelfde jaar een thorax CT ondergingen waarvoor de leeftijd overeenkomt met de borst kanker screeningsleeftijd. De kans dat ze een mammografie ondergingen binnen een redelijke tijdslimiet van de CT, is hoog. In totaal hebben we 87 mammografie beelden gevonden waarvoor we de VBD_{MX} en de gemiddelde HU in de CT beelden in de zone geïdentifiëerd als de borst konden vergelijken. De correlatie is weergegeven in figuur 17. De gemiddelde fouten op het geheel van de punten in onze databank, opgesteld voor dit doel, zijn 10% en 4%. De fouten kunnen verklaard worden door verschillende factoren, onder andere de positionnering van de borst door de verpleegster en de interpretatie van de rand van de borst voor de manuele segmentatie door de fysici. Opnieuw zijn de resultaten vergelijkbaar met de beste waarden in de literatuur verkregen met MR.

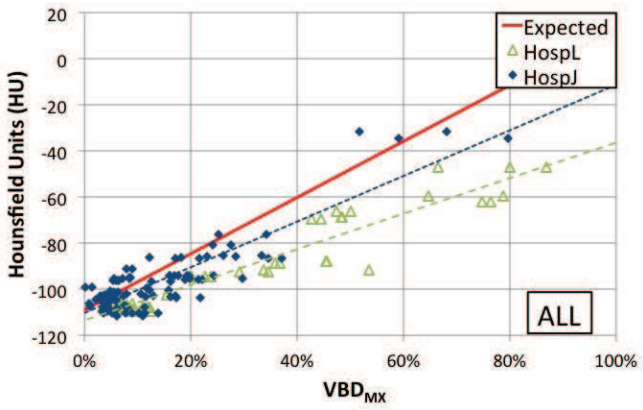

Figure 17: De gemiddelde HU van het borstvolume in thorax CT vergeleken met de VBD_{MX}. Elk punt stelt een borst voor, voor dewelke de gemiddelde HU gekend is en de VBD_{MX} geschat. Patiëntes uit twee verschillende ziekenhuizen werden afzonderlijk voorgesteld met hun overeenkomstige lineaire regressie. De volle lijn steld de verwachtte HU voor op basis van de vergelijking 4 en de bepaling van de HU_A- en de HU_G-waarden.

Energie geabsorbeerd door het klierweefsel

State of the art

Algemeen wordt aangenomen dat het stralingsrisico ten gevolge van een mammografie onderzoek beperkt blijft tot het borstweefsel zelf. Hammerstein et al. [66] bestudeerden de geabsorbeerde borstdosis en stelden voor om een grootheid te implementeren die rekening houdt met de ruimtelijke verdeling van het risicovol klierweefsel. De aandacht werd dus gevestigd op de geabsorbeerde klierdosis. Daarvoor was het echter nodig om veronderstellingen te maken over de hoeveelheid en verdeling van het klierweefsel voor de gemiddelde borst. Ze stelden de "totale energie afgezet in het klierweefsel" voor als risico-indicator en de "gemiddelde dosis voor een gemiddelde borst" voor de vergelijking van dosissen van verschillende radiografie technieken [85]. Het voordeel voor dat laatste is dat er geen kennis vereist is over de verdeling van het klierweefsel.
Meerdere auteurs ontwikkelden daarna methodes om de gemiddelde glandulaire dosis (*average glandular dose*, AGD) te berekenen [22, 39, 124, 132, 153]. De methode van Dance et al. [41] werd geïntegreerd in de nationale reguleringen en internationale aanbevelingen voor kwaliteitscontrole, zoals in Europa [116]. De methodes berekenen de AGD genormaliseerd per *air kerma* in het bovenvlak van de borst [21]. Dance et al. [39], Wu et al. [153] en Boone [22] lijstten tabellen op van genormaliseerde AGD op basis van Monte-Carlo simulaties voor een semi-circulair fantoom met variable diktes [39, 133] en inhoud [41, 153] en voor verschillende X-stralen spectra [22, 23, 41, 154].
Nochtans beantwoordt de AGD niet aan de noden van een individuele risicoindicator [35, 126]. De beperkingen van de AGD werden door Sechopoulos et al. [128] besproken. De belangrijkste beperking werd door Dance et al. [40] aangetoond: er is een verschil tot 43% tussen de AGD voor een fantoom met textuur berekend met Monte-Carlo simulaties en een homogeen fantoom met dezelfde densiteit berekend met de coëfficiënten uit de tabellen. Porras-Chaverri et al. [120] vonden eveneens belangrijke verschillen tussen fantomen met elk in totaal 50% densiteit, maar opgebouwd uit lagen van verschillende

densiteit in verschillende volgordes. De verschillen tussen de homogene en heterogene fantomen lopen op tot 50% voor fantomen van 8 cm dik met de dichtste laag onderaan. Ook Sechopoulos et al. [128] vonden een overschatting van 27% voor een gestructureerde borst, berekend met een borstscanner, in vergelijking met een homogene borst.
Een andere beperking betreft de hoeveelheid glandulair weefsel voor de gemiddelde borst. De gemiddelde dichtheid van 50% glandulair weefsel werd door Hammerstein [66] voorgesteld, omdat er geen nauwkeurigere data beschikbaar waren. Sindsdien werd aangetoond dat de gemiddelde borstdensiteit eerder 20% is [93, 146, 156] (zie figuur 16).
De verschillende auteurs van AGD tabellen integreerden de densiteitsverschillen in hun tabellen van genormaliseerde AGD. Een latent probleem met deze tabellen is het gebruik van de juiste densiteit. De densiteit voor de tabellen is de massieke densiteit met uitsluiting van de huid. Deze definitie is vaak genegeerd door de gebruikers van de genormaliseerde AGD tabellen. In onze presentatie op the RSNA Annual meeting 2013 [58] toonden we een verschil aan tot 15% voor hetzelfde fantoom met verschillende definities van de densiteit (oppervlakte, volume, piek en diktegemodeleerd). Zo overschat de oppervlaktedensiteit de massadensiteit, waardoor de AGD onderschat wordt.
Een derde probleem met de initiële Monte-Carlo simulaties is de dikte van de huid. Dance [39] en Wu [153] gebruikten respectievelijkj 5 en 4 mm adipeus weefsel. Ondertussen rapporteerden Huang et al. [78] een huiddikte van 1,45 mm bij echte patiënten. De densiteit van de huid ligt dicthter bij de glandulaire densiteit dan de adipeuse [66]. Als gevolg daarvan wordt bij het gebruik van de tabellen de dosis van echte borsten onderschat.

Onze bijdragen

De hedendaagse geneeskunde richt zich steeds meer naar individualisatie [15, 138]. Een alternatief voor de AGD, die een populatiegrootheid is, zou meer aangepast zijn als individuele risico-indicator. Wij stellen hier een methode voor niet om de "AGD te individualiseren", maar om de geabsorbeerde energie in klierweefsel (GIE) te berekenen zoals voorgesteld door Hammerstein et al. [66]. Meer bepaald moet er voor elke vrouw rekening gehouden worden met de hoeveelheid en de localizatie van verschillende borstweefsels. Pogingen werden reeds ondernomen om het klierweefsel te localizeren op basis van een densiteitskaart [119]. De opkomst van de borst tomosynthese zorgt voor een gedeeltelijke oplossing voor de localizatie van het klierweefsel in de samengedrukte borst [121, 123, 145], waardoor de geabsorbeerde energie in glandulair (GIE) en adipeus (AIE) weefsel gesplits kunnen worden. In dit werk presenteren we een methode om de localizatie van glandulair weefsel te schatten en analyseren we de geabsorbeerde energie per weefsellaag voor een poly-energetisch spectrum.

Berekening van de geabsorbeerde energie

Het doel is om de geabsorbeerde energie te berekenen in elk punt, rekening houdend met alle interactiemechanismen. We kozen om hiervoor Monte-Carlo simulaties te gebruiken. Daarvoor gebruikten we apparatuur intern beschikbaar in GE, CatSim en zijn afgeleide dosismeter CatDose [104]. Deze software werd ontwikkeld voor CT toepassingen, en wij valideerden een uitbreiding naar dosisberekeningen voor mammografie. Dit werd gedaan door de genormaliseerde AGD tabellen van Dance [41] en van Boone [23] te berekenen. Een verschil van minder dan 10% werd gevonden.

De software werd gebruikt om de geabsorbeerde energie te berekenen voor gekende geometrische fantomen, en om de invloed te bestuderen van de hoeveelheid en verdeling van respectivelijk de geabsorbeerde energie en AGD [61].

Berekening van de geabsorbeerde energie per laag

De locale GIE werd berekend met Monte-Carlo simulaties die niet mogelijk zijn voor dagelijks gebruik. Daarom is het wenselijk om over een snelle en eenvoudige methode te beschikken. Daarvoor bestudeerden we de verdeling van de geabsorbeerde energie als functie van de diepte in het weefsel, zoals ook Chan en Doi. [31] reeds deden voor lagen van water in diagnostische radiologie.
De resultaten werden berekend en genormaliseerd ten opzichte van de air kerma. De geabsorbeerde energie per laag van 1mm werd berekend voor een homogeen fantoom met dezelfde vorm als dat beschreven door Dance et al. [39] en met volledige glandulaire of volledig adipeuse samenstelling. De verkregen waarden werden eveneens genormaliseerd per oppervlakteeenheid. Het resultaat is dus de waarde van de geabsorbeerde energie per volume of ook de geabsorbeerde volumetrische energie (*Imparted Volumetric Energy*, IVE). De figuur 18 toont de resultaten van de simulaties. De energie per laag is de som van

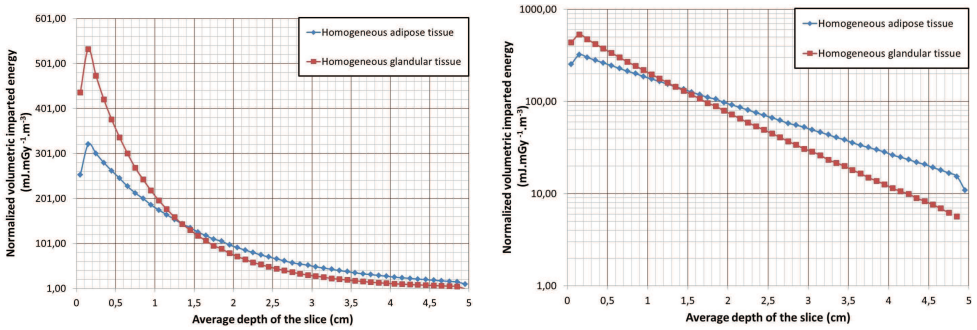

(a) (b)

Figure 18: Geabsorbeerde volumetrische energie in homogeen adipeus en glandulair weefsel per m^3 en per air kerma.

de energie afgezet door de attenuatie van de inkomende stralenbundel, de verstrooiing van de voorgaande lagen en de terug-verstrooiing van de volgende lagen. Voor de eerste lagen is de verstrooiing lager omdat voorgaande lagen ontbreken. De piek is vergelijkbaar met het *build-up* effect, gekend in radiotherapie. In een evenwichtstoestand, na 3 mm, neemt de geabsorbeerde volumetrische energie exponentieel af met de diepte. In geval van een puur glandulair volume is de waarde van de IVE geëxtrapoleed naar de oorsprong 532 $mJ.mGy^{-1}.m^{-3}$ en wordt per 7,3 mm gehalveerd (een dempinscoëfficient van 0,95 cm^{-1}). Voor een volume van puur adipeus weefsel is de geëxtrapoleerde waarde aan de oorsprong 347 $mJ.mGy^{-1}.m^{-3}$ en wordt per 10,7 mm gehalveerd (een dempingscoëfficiënt van 0,64 cm^{-1}). Beide kurves kruisen elkaar op 13 mm, de dikte waar de IVE in adipeus weefsel hoger wordt dan in glandulair weefsel. We vinden hetzelfde gedrag met lineaire attenuatie-coëfficiënten als voor de geabsorbeerde energie voor mono-energetische straling van 18 keV (adipeus weefsel) en 18,5 keV (glandulair weefsel). Een vergelijkbare methode werd reeds voorgesteld, waarbij de geabsorbeerde energie van Comptonstraling, de niet co-lineaire verstrooiing en meervoudige verstrooiing verwaarloosd werden [65]. Deze werd hier

bevestigd zonder hypothesen te moeten maken. Het is dus mogelijk om de geabsorbeerde energie te berekenen in een volume waarvan de eigenschappen en locale samenstelling gekend zijn.

Localizatie van glandulair weefsel

We stellen een methode voor om de verkregen tomosynthesebeelde te segmenteren gebruik makende van de VBD. De VBD kan berekend worden uit de 0° zoals voor een gewone mammografie. De berekening werd op punt gesteld voor het tomosynthesis toestel SenoClaire van GE. Het toestel heeft hetzelfde antisverstrooiingrooster in 2D en tomosynthese, dus een enkele kalibratie volstaat. De VBD kan geïnterpreteerd worden als het percentage van borstvoxels bestaande uit glandulair weefsel, de andere zijn dan adipeus. In tegenstelling tot bij CT scanners is de draaihoek van tomosynthese toestellen beperkt, waardoor de pixelwaarden niet gekwantifiëerd kunnen worden naar een fysische grootheid. Vooral de resolutie volgens de as van de X-stralen is zeer inferieur aan de resolutie in de vlakken parallel op deze as, waardoor artefacten zich doorheen de gereconstrueerde vlakken voortplanten en de weefselsegmentatie bemoeilijken. De door ons voorgestelde nieuwe segmentatiemethode is gebaseerd op het behoud van densiteit tussen de projectie en het gereconstrueerde volume. We stelden voor om het histogram te berekenen van het gereconstrueerde volume en stellen een drempelwaarde voor waarboven het aantal voxels ten opzichte van het totaal aantal borstvoxels gelijk is aan de VBD. De voxels boven deze drempelwaarde worden als “glandulair” geklassifiëerd, de anderen als “adipeus”.

Toepassing van de berekening van de energie geabsorbeerd in tomosynthese

Eerst definieerden we een reeks geometrische fantomen met verschillende verdelingen van glandulaire bollen. We berekenden de geabsorbeerde energie voor deze fantomen en stelden die als de juiste waarde. Daarna simuleerden we een tomosynthese en reconstrueerden het 3D volume. Een tweede berekening van geabsorbeerde energie, deze keer voor het gereconstrueerde volume, en de resultaten werden vergeleken met de eerste waarden. De waarden van de GIE zijn lager dan 5μJ/mGy voor een glandulaire massa van 32g. Voor negen van de tien fantomen zijn de verschillen tussen het echte gewicht en het gereconstrueerde gewicht tussen 8% en 13%. Voor het tiende fantoom, gekarakteriseerd door een dikte gelijk aan de diameter van de bollen, bedraagt het verschil in gewicht is 83%. Voor de helft van de fantomen is het verschil in geabsorbeerde energie kleiner dan 20%. De andere fantomen zijn het fantoom met een slecht berekend gewicht, het fantoom waar de GIE bijna nul is en het fantoom met een grote dikte waarvoor de energie van de gebruikte straling, die in deze opstelling hetzelfde was voor alle fantomen, te laag was. De werkwijze werd eveneens toegepast op een fantoom met textuur, gegenereerd volgens de methode van Carton et al. [30] met als VBD 6%. De doorsnede van het fantoom is weergegeven in figuur 19(a), een projectiebeeld in figuur 19(b) en een doorsnede van het gereconstrueerde volume in figuur 19(c).
Na de reconstructie segmenteerden we het volume op basis van het histogram. Het originele en gereconstrueerde gesegmenteerde volume worden weergegeven in figuur 20.
De totale massa van het fantoom werd met 15% overschat en de glandulaire massa met 23%. De geabsorbeerde energie in het klierweefsel werd onderschat met 25%. Deze methode werd

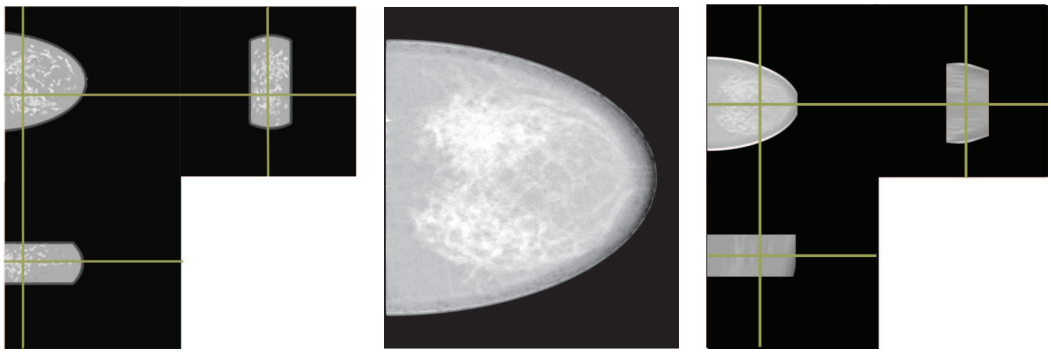

(a) (b) (c)

Figure 19: a) Fantoom met textuur, b) tomosynthese projectie en c) het gereconstrueerde volume.

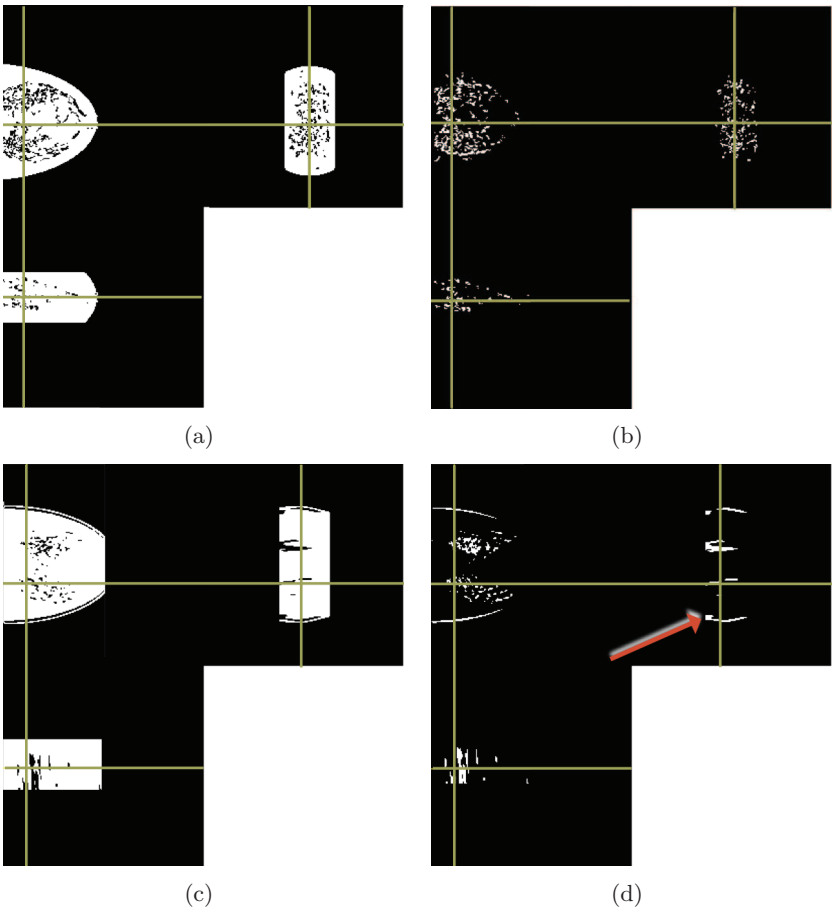

(a) (b)

(c) (d)

Figure 20: Segmentaties van a) adipeus en b) glandulair weefsel van het originele volume, en van c) adipeus en d) glandulair weefsel van het gereconstrueerde volume.

eveneens toegepast op een tomosynthese beeld van een patiente zonder dat het mogelijk was om te vergelijken met de echte waarde.

Conclusie

Dit onderzoeksproject had twee hoofddoelen: a) de implementatie en de verbetering van een methode voor de berekening van de volumetrische borstdensiteit (VBD), en b) een voorstel voor een meting van de stralingsblootstelling voor de evaluatie van individueel stralingsrisico in mammografie en een methode om die grootheid te schatten.

We ontwikkelden een meetmethode voor de VBD en pasten die toe op twee digitale mammografie toestellen. Deze methode berust op de kalibratie van het toestel met fantomen met gekende dikte en absorptie equivalent aan borstweefsel. Een densiteitskaart werd berekend op basis van een digitaal beeld en de acquisitieparameters. De bekomen precisie is 1,2%, en vergelijkbaar met de state-of-the-art [75]. We hebben eveneens een methode op punt gesteld voor de validatie van de VBD, via de vergelijking tussen de VBD_{MX} van de mammografische beelden en de VBD_{CT} berekend in de thorax CT beelden. Het verschil tussen de CT berekening en onze VBD berekeningsmethode is kleiner dan 10% gemiddeld, wat aanvaardbaar is.

In het tweede deel hebben we een alternatief gezocht voor de *average glandular dose (AGD)* zoals vandaag gebruikt, die een goede grootheid is voor de collective metingen, maar die niet voldoet aan de voorwaarden voor een individuele maatstaf voor stralingsrisico [58, 61]. Zoals Hammerstein in 1979 [66] hebben we de geabsorbeerde energie in klierweefsel (GIE) weerhouden. Deze grootheid vereist complexere berekeningen dan de AGD, want de kennis van de verdeling van het klierweefsel, gevolgd door een berekening van de lokale geabsorbeerde energie zijn nodig. De tomosynthese laat toe om de verdeling van het klierweefsel te benaderen. De voorgestelde methode is een demonstratie van de mogelijkheid om de GIE te berekenen voor een borst tomosynthese onderzoek. De segmentatie van het reconstrueerde tomosynthesevolume gebeurt met behoud van de VBD ten opzichte van de 0° projectie. Typische waarden van de GIE per air kerma zijn lager dan 20μJ/mGy. Huidige berekeningen waren gebaseerd op Monte-Carlo simulaties, maar we toonden de mogelijkheid aan om de geabsorbeerde energie eenmalig te berekenen per stralingsspectrum en voor beide borstweefsels zodat de implementatie van de methode mogelijk wordt voor borst tomosynthese onderzoeken. Dit onderzoek opent een nieuwe weg voor individuele metingen van stralingsrisico. Alvorens GIE een standaard kan worden in mammografie moet het geheel eerst nog verder grondig bestudeerd worden. Met dit doctoraat en onze publicaties droegen we bij aan de uitbreiding van informatie die berekend kan worden op basis van een mammografie beeld, in de hoop dat deze informatie kan bijdragen tot een verbetering en individualisering van borstkanker screening.

Quantitative evaluation of fibroglandular tissue for estimation of tissue-differentiated absorbed energy in breast tomosynthesis

Chapter 1

Introduction

1.1 General problem statement

The present research project resides in the field of Medical Imaging and more specifically in X-ray breast imaging, including its application to Breast Cancer Screening. Breast cancer is an important disease, accounting worldwide for 25.2% of all female cancers [7] and for 16% of cancer deaths in adult women [6]. Fortunately early detection of suspicious lesions via breast screening increases survival chances [8]. Screening is performed through mammography, the cornerstone of population-based breast cancer screening [116]. It uses X-rays to obtain 2D-projection images from the tissues inside the breast. As for all X-ray exposures, it is necessary to follow the ALARA-principle: to expose with a radiation dose that is As Low As Reasonably Achievable. This means that irradiating a targeted population is accepted if the benefits are significantly higher than the risks. In screening set-ups, justification includes that in the population more cancers are found than induced due to exposure to X-rays during screening. Although most developed countries have implemented a screening program, the debate on the benefits and risks of screening is ongoing in scientific literature [20, 94, 111, 134], as well as in public media. The quality of screening tools is strictly controlled [116] and continuously improved. A possible improvement of the current screening programs is an even more specific identification of the population to be screened, which is today based almost exclusively on age, and somehow on patient or family history [71]. Another improvement is a better estimation of the risk from the X-ray exposure. For both improvements *breast density*, a breast content measure, is a key parameter [41, 108].

The healthy breast contains mainly adipose and fibroglandular tissues, the former showing up as dark in the mammography image, the latter as white. Fibroglandular tissue differs in amount and distribution within the population. The percentage of fibroglandular tissue of the total breast is called breast density (see later for exact definitions). Breast density has been identified as an inherent risk factor for breast cancer by many studies [108]. In addition an abundant dense tissue tends to mask suspicious lesions and reduces their detection. Breasts were originally classified according to their projection images by Wolfe in 1976 [152]. The influence of breast density on the development of breast cancer is not well understood [26, 106]. Recent findings from Lisanti et al. [101] point in the direction of functional similarities between cancer cells and high density fibroblasts, especially in the case of stress response. A difficulty is that there is not yet a full consensus in

relation to breast cancer risk on how to quantify the density [54, 73], how its distribution is important [88, 100, 148], and how to include all this in risk models [32]. Different density measures and computation methods are described below.
In 1979 Hammerstein et al. [66] stated that "mammary gland" is "tissue at high risk" for radiation dammage, compared to "skin, fat and connective tissue, which are not at high risk". They concluded with the proposition of "total energy absorbed in glandular tissue as the most relevant indicator of risk in mammography" adding that "detailed information will have to be obtained on the amount and distribution of gland tissue (...) properly applied to the problem of individual risk ".
In this chapter we will first review the anatomy and histology of the breast, then the computation of the breast density from mammographic images and finally the computation of dose and radiation risk indicators. This will allow us to state more precisely our research objectives.

1.2 State of the art

1.2.1 Breast anatomy and histology

The breast is an organ dedicated to the excretion of milk and female hormones [98]. Breast tissue can be situated on a line from the armpit to the groin for women as well as men. The milk is excreted from the glandular cells via epithelial cells and finds its way out via the lactiferous ducts [13] (see Figure 1.1). The glandular tissue is organized in lobes, each lobe of the breast consisting in lobules and an extralobular terminal duct. The lobule itself consists in ductules (also named the acini) and the intralobular terminal duct. The different branches (lobes) are surrounded by dense connective tissue. The connective tissue is sometimes also called stroma. The space between the connective tissue is filled with adipose tissue for energy and nutritional storage, mechanical and thermal insulation [9]. Furthermore the breast incorporates a network of nerves, blood vessels and the lymphatic system. The ratio of the different composites depends on the woman, her age, her ethnicity, the phase of her menstrual cycle ... [68, 151].
Radiologically the tissue is separated into adipose tissue (with low attenuation coefficients) and the remaining *dense tissues* (with higher attenuation coefficients). Although dense tissue is often called fibroglandular tissue, it includes the acinar and ductal epithelium and associated connective tissue or stroma [16, 42, 113].

Breast cancers most often originate in the acini or the ductal cells: most frequent breast cancers are Ductal Carcinoma in Situ, Invasive Ductal Carcinoma and Invasive Lobular Carcinoma [1]. However, the cancer cells are not only influencing the surrounding tissue and adipose tissue, they are also influenced *by* the adipose and surrounding tissue: *in vitro* some types of adipose cells are accelerating the development of cancer. If the same breast cancer tissue is placed in another type of adipose cells, the cancer development is delayed [49]. Therefore it seems that not only the quantity of dense tissue, but also its interaction possibility with the adipose tissue must be taken into account for the determination of breast cancer risk.

1.2.2 Breast density

The classification of breast images in categories was originally developed by Wolfe in 1976 [152]. He proposed 4 categories according to the risk to develop breast cancer based on the characteristics of parenchymal patterns and on the relative tissue distributions in the mammographic images (see Figure 1.2).
Also Tabar et al. [64] developed a classification with 5 categories (see Figure 1.2) according to breast cancer risk and even more recently 6 categories were considered by Jeffreys et al. [83]. Wolfe's classification was converted to the BI-RADS classification [33], where breast density is estimated from the ratio of fibroglandular tissue to total breast tissue as observed in mammographic images. The ratio of the *area* of fibroglandular tissue to the *area* of the breast is referred to as the *area-based breast density (ABD)* (see Figure 1.3) as evaluated from mammographic images. Later, Kopans [95] proposed the *volumetric breast density (VBD)* as the ratio of the *volume* of the fibroglandular tissue to the *volume* of the breast (see Figure 1.3). The volumetric breast density limited to the region of the AEC [48] is called *peak breast density (PBD)*.
In 1982 Tabar and Dean [135] declared that Wolfe [152] had discovered a new breast cancer risk factor, but that it is "not specific enough to be used for the planning of screening programs". A systematic review and meta-analysis of publications on breast density and parenchymal patterns in relation to breast cancer risk was published in 2006 by McCormack et al. [108]. The study demonstrated that the ABD, and to a lesser extent Wolfe grades and BI-RADS classification, are strong predictors of the risk of developing breast cancers. More studies are ongoing to understand the impact of breast density on cancer prediction [129]. Van Gils et al. [144] and Ting et al. [139] also found that the speed of conversion of the glandular tissue as a function of time was indicative for the risk of developing breast cancers: the faster the changes, the higher the risk. For women who are being treated for breast cancer with Tamoxifen, the effect on the fibroglandular tissue was found indicative for survival rate [99], with a higher survival rate for women

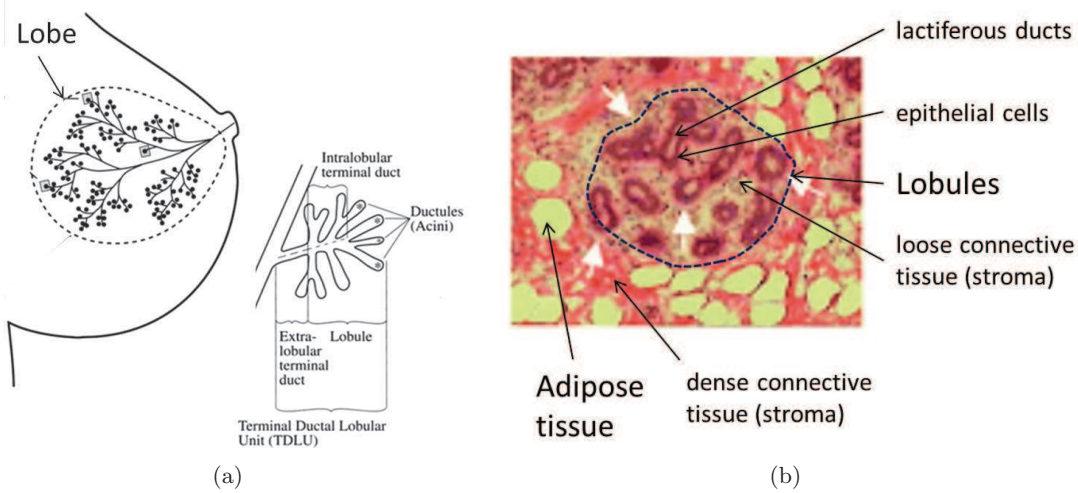

(a) (b)

Figure 1.1: The breast at macroscopic and microscopic level. a) Anatomically the breast tissue consists of several lobes, made up of lobules ending in acini. b) Histologically the breast consists of adipose tissue and functional tissue, i.e. supportive and excretion tissue [136].

whose amount of fibroglandular tissue decreases. Reproducible and consistent methods of quantification of breast density have therefore become important tools in breast cancer epidemiology.

Computation of breast density

The previously described classifications of Wolfe [152], Tabar et al. [64] and BI-RADS [33] are usually visually evaluated by radiologists, although some automated tools have been developed [54]. For visual determination of the ABD the user estimates the area of the pixels representing fibroglandular area (white) to total breast area (not completely black). To improve this estimation semi-automatic software was created, where the user chooses the threshold of the grey-value of the fibroglandular tissue per image. The total breast

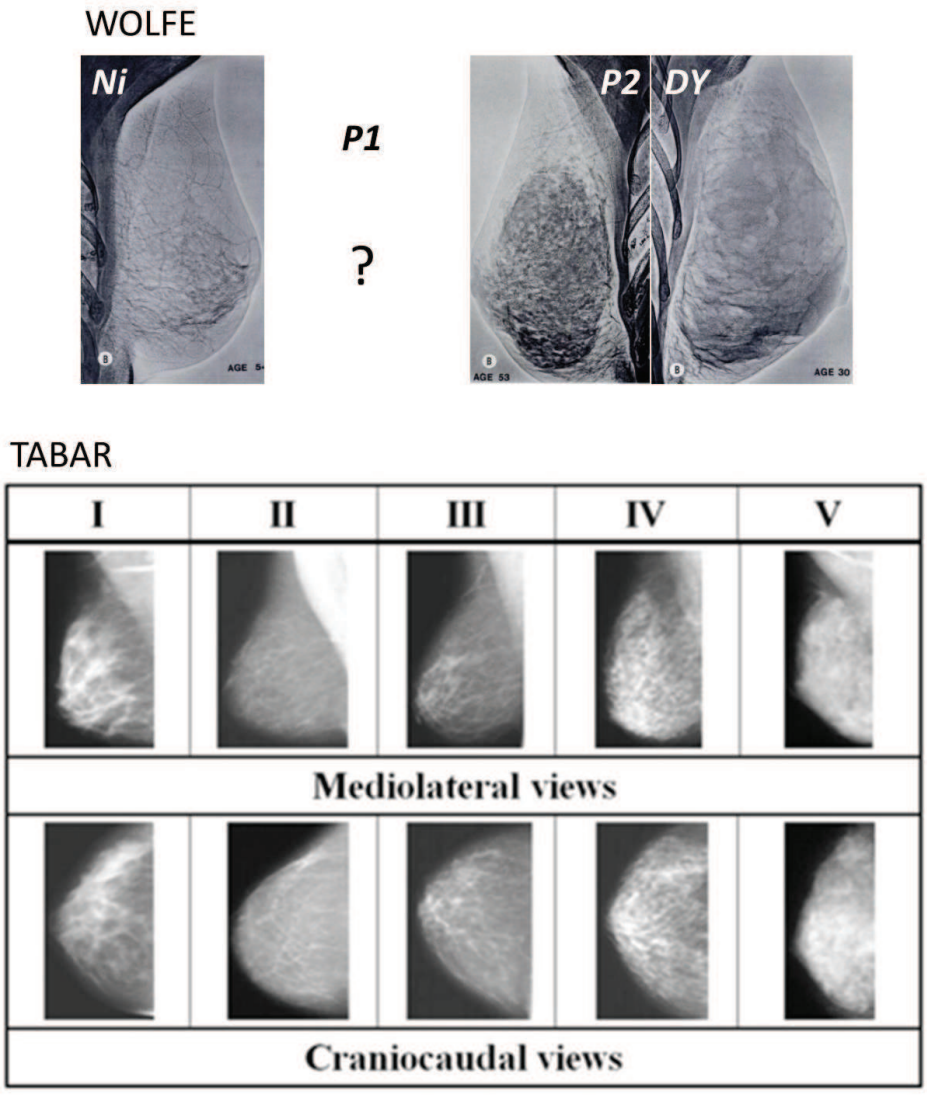

Figure 1.2: Examples of the categories of Wolfe [152] and Tabar [162]. The images from Wolfe are made with xerography and in his publication the second category is missing.

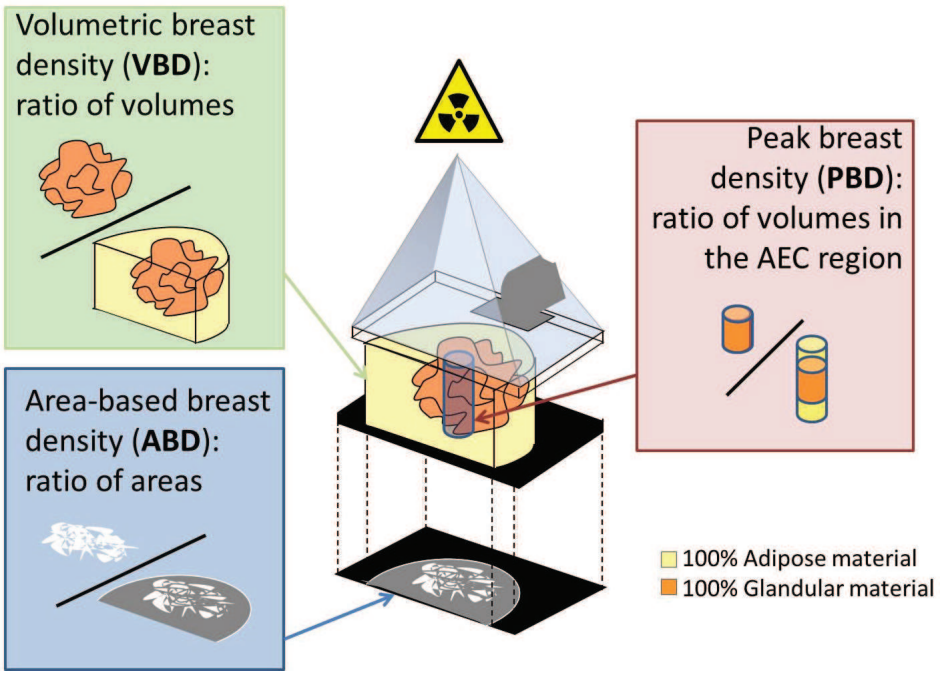

Figure 1.3: Scheme of the different breast densities: area-based breast density, volumetric breast density and peak breast density.

is subsequently segmented automatically and the integral of the histogram above the threshold, set by the user, is computed. Fully automated methods are also based on a threshold of the grey-values of the fibroglandular tissue, but set automatically to improve objectivity and reproducibility. Examples of measuring tools of ABD are Cumulus (up to version 4), an interactive thresholding method developed in Toronto [27], the Histogram Segmentation Method (HSM), the fully automated version of this method [102], and the Mammographic Density ESTimator (MDEST), a fully automated method developed in Michigan [160].
Despite automated methods, ABD values for the same breast can differ between mammographic images, mainly due to variable breast positioning and compression, generating a different area and different superpositions of fibroglandular tissue. To overcome this problem the real volume has to be taken into account [95]. This is possible via analysis of the mammographic image and its exposure parameters.

A first step in this direction of quantification was made as an improvement of the Automatic Exposure Control (AEC) of mammographic equipment. The AEC used to simply stop the exposure when a preset level was reached from the integration of the signal coming from a sensor placed below the film/screen cassette. The other parameters (anode track, filter and kV) were selected by the operator. A more refined concept had been introduced with GE Senographe DMR, where all parameters were selected automatically, based on a model calibrated on polymethylmethacrylate (PMMA) plates representing a 50% density breast. The parameters were optimized based on their PMMA-equivalent attenuation determined during a short preliminary pre-exposure [72]. However it was found later that exposing a thick fatty breast or a thinner dense breast the same way would not give

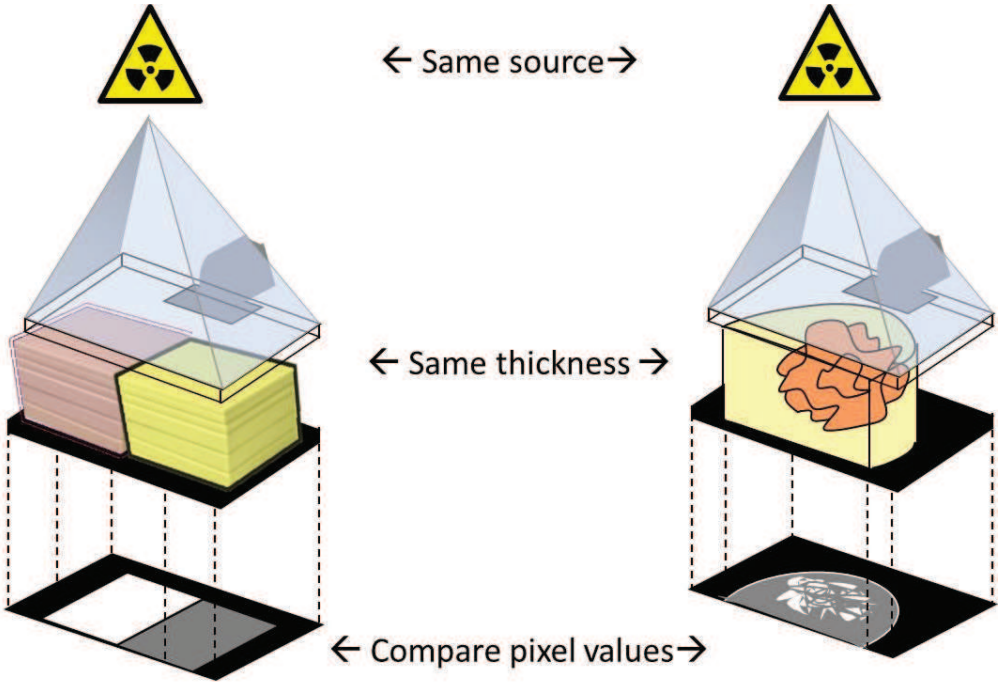

Figure 1.4: Scheme of the methods to compute VBD, based on comparing pixel values of an unknown object with those of a known object for the same exposure settings.

the same results, and radiologists were not satisfied. A solution was found, consisting in correlating the breast transmission with the compressed breast thickness. From this, a breast density was computed and used as a second input in the determination of the X-ray technique factors [48]. The operators were instructed to position the sensor in the area most susceptible to be the densest in the breast in order to minimize the risk of underexposure. For that reason the density measured was not the average but the peak breast density (PBD see Figure 1.3). Using a comparable method, Klein et al. [93] and Beckett and Kotre [16] developed a PBD estimation method based upon the exposure technique factors by correlating the AEC-determined current-time product for patient images with the AEC current-time product for breast tissue equivalent material of known composition and the same thickness.

Most of the recent methods for the VBD are based on the work of Highnam, Brady and Shepstone in 1996 [74]. They digitized mammographic images and acquired calibration images of a PMMA stepwedge. The digitized pixel values of both images were compared to transform the mammographic images into PMMA equivalent thickness images. Daily calibrations with PMMA were required to control the fluctuations of film-screen response, film processor and film digitizer.

In 2002, Kaufhold et al. [86, 87] developed a VBD computation method for digital mammography. They acquired images of breast tissue equivalent material (0%, 50% and 100% VBD) for clinically used values of tube potentials and phantom thicknesses. The pixel values from those images were plotted as a function of thickness for a fixed tube potential. The VBD for a pixel could then be obtained by interpolation from the pixel values in the images of the breast tissue equivalent material for the same tube potential. A scheme of

the method is presented in Figure 1.4. In 2006 Van Engeland et al. [143] showed that the logarithm of the ratio of beam intensity for a given spectrum and breast thickness before and after transmission through the breast has an almost linear relation with the thickness of the gland. The same year, the method of Highnam, Brady et al. [76] was adapted to digital images. This method served as the basis for two commercially available products: R2 QUANTRA™ (Hologic, Bedford, MA) and Volpara® (Matakina® Inc., Wellington, New Zealand). Whereas the thickness estimation from the method of Highnam, Brady et al. was based only on the hypothesis of a purely adipose uncompressed breast region and some image smoothness criteria, the R2 QUANTRA™ software uses an improved image-based thickness correction according to Hartmann et al. [69], with the recorded paddle height as the initial value for the compressed breast thickness. According to Highnam, Brady et al. [75] the Volpara® software is searching for a purely adipose region in the image to compute the VBD with a high precision compressed breast thickness. They used therefore phase congruency, a technique characterizing low-level image features from the frequency domain and invariant to image intensity and acquisition parameters [96]. Shepherd et al. [130] compared the pixel values of the breast with the pixel values of two references placed in the image. The method was improved to solve the problem of the compression paddle orientation by placing a phantom with lead markers on the paddle [103].

Validation of breast density computation.

All these density computation methods depend on some hypotheses. It is therefore important that they can be validated against known values. The common approach is to quantify the respective amounts of adipose and fibroglandular tissues in 3D images of the same breast. Unfortunately the anatomical limits of the breast are not well defined and determining the volume of the breast is inherently difficult. This is also the case for 2D mammography. As a consequence, it is difficult to obtain good correlations between breast volumes obtained from different modalities [143, 147]. Despite this difficulty, the correlation between VBD as obtained from different mammographic images and from different modalities is possible. For the previously described methods (Van Engeland et al. [143], Volpara® [75], R2 QUANTRA™) [69]) the authors of the publications compared the VBD from mammographic images to the VBD obtained by delineating manually the breast and the fibroglandular tissue in breast magnetic resonance (MR) images of the same patient. The comparison between the VBD computed by single X-ray absorptiometry [130], QUANTRA™ and Volpara® on the one hand, and MR on the other hand was described recently by Wang et al. [147]. Using clinical MR images has however some drawbacks. Due to in-plane inhomogeneity of the pixel values it is not possible to set a single threshold for automatic segmentation of the fibroglandular tissue and therefore more sophisticated methods are needed. Manual segmentation of the fibroglandular tissue is difficult due to its irregular borders and the presence of small fibrous structures. Whereas differentiation of fibroglandular tissue and fatty tissue would be best from 3D T1 or T2 weighted images, these types of acquisitions may not be routinely performed. Most frequently contrast enhanced breast MR sequences are performed, which are not optimal for anatomical imaging. Next, MR images provide MR-specific characteristics of the tissues, and the subsequent tissue classification may be different from that based on X-ray imaging. Finally, breast MR is not performed for the screening population but mainly for patients being suspicious for a malignant disease, and the presence of a disease may disturb the breast

density measurement. The hypothesis of the two-compartment model, with only adipose and fibroglandular tissues, may then be no longer valid.
Alonzo-Proulx et al. [10] proposed dedicated breast computed tomography (CT) images as a basis for comparison. They computed the volumes of adipose and fibroglandular tissues from breast CT by thresholding the images. Then they simulated mammographic images from the breast CT acquisitions for which they then computed the VBD with their 2D method. Also Vedantham et al. [146] showed the possibility to measure the fibroglandular tissue and the volumetric glandular fraction based on breast CT images. Breast CT seems to be a good solution to establish reliable VBD values but is only available in a small number of research centers. In January 2014 Salvatore et al. [125] published a study where the authors showed a promising agreement between BI-RADS density classifications in mammography and thorax CT of the same patients. Their work indicates a possibility to compute also the VBD from thorax CT images. Salvatore et al. [125] used a semi-automatic computer algorithm prototype to segment the breast, partitioning the resulting breast region and computing the breast density.

Our contributions

We propose a validation method based on regular thorax CT images for a VBD computation method, based on the method of Kaufhold [87]. We exploit the large number of thorax CT acquisitions performed for other indications on the breast screening population, benefitting that most of the time the complete breast is present in the image as well. The method can easily be performed by users of breast density applications. We propose to use the characteristic that the Hounsfield Units (HU) provided by CT reconstruction algorithms are a linear function of the average attenuation coefficient of the material in the corresponding location. As a consequence, this value is a direct function of the linear attenuation coefficients of the local tissue components, and the VBD can be simply computed from the average HU over the breast volume and the HU values of adipose and fibroglandular tissues, with no need for in-breast tissue segmentation. Another advantage of using CT images instead of MR images is that the common use of X-rays in CT and mammography ensures the same classification of tissues, based on X-ray attenuation properties of the materials. Thorax CT images with lesion-free breasts can be collected in a relatively short time period. For example, at the university hospital *Universitair Ziekenhuis Gasthuisberg Leuven (BE)*, with 46 000 CT exams performed yearly, over 30 women per month undergo a screening examination within the 12 months following a CT thorax exam. Therefore, acquiring these CT data does not require additional medical examinations, with no additional radiation to patients, no extra time for the radiologists and no extra cost.
A description of the VBD computation method is given in Chapter 3, the validation method is explained in Chapter 4.

1.2.3 Breast dose

It is generally accepted that radiation risk or detriment from mammographic examinations is limited to the effects of the exposure to the breast. Very little is known on the impact of low dose at cellular level. Recently studies have been performed on the effect of mammography-like irradiation on epithelial cell cultures [17,34] and the effect on DNA was measured. However this does not yet take into account the transmission chain from DNA

to the risk of cancer development and in particular the complex intercellular interaction mechanisms and the differences in radiosensitivity between individuals.
Independent from radiobiology, it is important for the radiation risk evalutation to start from adequate physical measures of the interaction between the radiation and the tissues. Hammerstein et al. [66] investigated the absorbed radiation dose to the breast in mammography. Although the main subject of his work describes dose measurements using midbreast dose, i.e. the dose halfway the paddle and the bucky, for comparison between xerography and mammography, the authors suggested that midbreast dose might not be the best risk indicator in mammography. They stated: "It would be preferable to adopt a quantity which reflects the variation of dose levels throughout the breast and which takes into account the spatial distribution of tissue at high risk" [66]. They subsequently explored the concept of total energy absorbed in the breast per unit cross sectional area of the X-ray beam proposed by Boag [21]. As stated by Hammerstein et al., this concept "includes significant amounts of energy which in the actual patient would be absorbed in skin, fat, and connective tissue, which are not at high risk. Considerations should be restricted to energy absorbed in glandular tissue". They were thus forced to make "assumptions about the amount and distribution of glandular tissue in the "average" breast. Although they propose "total energy absorbed in glandular tissue as the most relevant indicator of risk in mammography", they also propose "mean dose to gland for the "average" breast as a basis for comparing doses delivered with different radiographic techniques", a concept of Karlsson [85], to overcome the problem of determination of distribution of glandular tissue.

This concept of "mean (average) dose to the gland for the "average" breast" was further developed by several authors [22, 39, 124, 132, 153]. Amongst the different practical implementations, Monte-Carlo simulations [38] of the mean glandular dose (MGD) [39] and the average glandular dose (AGD) [153] were the most common. MGD and AGD are two different names for the same concept, but used by different authors. In this text we will use AGD independently of the original author references. These methods [41] were integrated in national and international regulations and recommendations of quality control such as the European guidelines for quality control in mammography [116]. The methods apply normalization [21] with different conversion factors from air kerma to AGD. Dance et al. [39], Wu et al. [153] and Boone [22] tabulated their conversion factors from Monte-Carlo simulations on a semi-circular breast phantom. In different papers, Dance further developed his conversion factor tables to extent them to new thickness ranges (g-factor) [39], different spectra (extended HVL range and s-factor) [41], different massic breast densities (c-factor) [41] and recently even breast tomosynthesis angulation (t-factor) [44] and CESM conditions [37]. Because assessing the quantitative massic density from mammographic images was not possible, Dance et al. [41] added a table of density as a function of breast thickness, based on measurements of PBD over local populations by Young et al. [158] and Beckett and Kotre [16]. In a study presented at the IAEA-conference in 2012 [60] we determined a comparable PBD distribution for a larger population (147 487 images) as a function of breast thickness for populations of different continents and compared this to the curves proposed by Dance et al. [41] (see Figure 1.5 and Section 6.1).
Wu et al. tabulated the normalized glandular dose, D_{gN}, as a function of HVL, tube voltage and breast thickness for breast densities 0%, 50% and 100% [153], and added tables

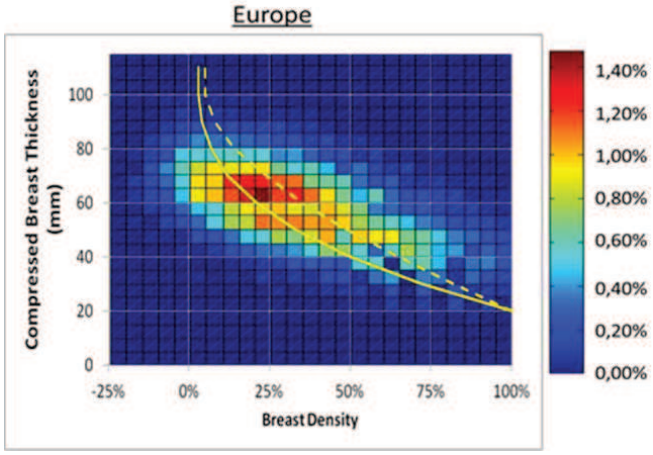

Figure 1.5: Distribution of the peak breast density as a function of compressed breast thickness for 49 847 images in Europe [60]. Estimates of "average breast composition" for different compressed breast thickness and age ranges proposed by Dance et al. [41] were plotted on top of our results [60].

for anode-filter combinations Mo-Rh and Rh-Rh [154], then the same team published a continuous model fitting the tables [133]. Boone computed tables of normalized average glandular dose for additional anode-filter combinations such as W-Rh and W-Pd and for mono-energetic beams [22], then proposed them under the form of "fit-equations" for mono-energetic beams [23] allowing to generate the normalized glandular dose for any known spectrum for 0% and 100% breast density.

However coming back to Hammerstein et al. [66], the notion of AGD is sufficient for quality control and population surveys, but is not fulfilling the requirements of an individual risk measure [35, 126]. Several limitations of this approach were highlighted by Sechopoulos et al. [128].
The main limitation of the AGD was indicated by Dance et al. [40] who showed a difference of up to 43% between the AGD for a textured phantom computed by simulations and the AGD for the same phantom computed from the tables and assuming a homogenous mixture. Also Porras-Chaverri et al. [120] found a considerable difference in computed AGD for a phantom with a total density of 50% but consisting of layers of different densities. Differences in AGD can go up to 50% for phantoms of 8 cm compressed breast thickness with the densest layer close to the bucky. On patient cases Sechopoulos et al. [128] found an overestimation of 27% on average for the AGD computed for the structured breast compared to a same amount homogeneous density.
Another limitation concerns the amount of glandular tissue in the average breast. The concept of a 50% glandular breast was introduced by Hammerstein [66] in a first attempt to approach roughly the amount and distribution of an average breast. However since then it was shown that the average breast at the age of screening population has rather a density around 20% [93, 146, 156]. The distribution we found for a population of 663 images is compared to the distribution of Yaffe et al. [156] in Figure 1.6.
The problem of the amount of glandular tissue was addressed by different authors. Wu et al. published tables for different densities (0%, 50% and 100%) [153], Dance et al.

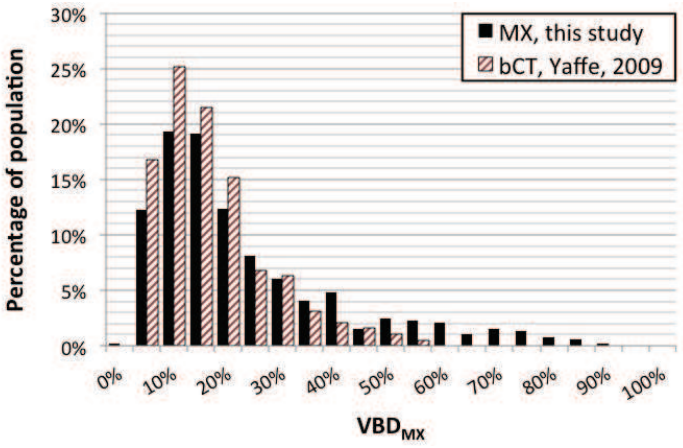

Figure 1.6: Illustration of the VBD distribution for the screening population. Results of our study are compared to the results of Yaffe et al. [156].

computed and listed an extra conversion factor (c-factor) [41]. As already mentioned, the density used to determine the conversion factor is the *intra-skin* density, i.e. the total massic density excluding the skin. Unfortunately this hypothesis seems to be neglected by most users of the conversion factor tables.
In our presentation at the RSNA-annual meeting 2013 [58] we computed the AGD with the ABD, the VBD and the PBD. We demonstrated a difference in AGD up to 15% for the different density measures of the same phantom. The density used by radiologists and physicists as input for these tables is often the ABD, or the VBD. The first case results in an overestimation of the density and thus an underestimation of the AGD. The second case results in an underestimation of the density and thus an overestimation of the AGD.
A third limitation of the phantoms used for the Monte-Carlo simulations is the thickness and composition of the skin. Dance [39] and Wu [153] used respectively 5 and 4 mm of adipose tissue, whereas for real cases Huang et al. [78] measured an average thickness of 1.45 mm and with a density and composition closer to glandular tissue than to adipose tissue [66]. This results in an underestimation of the absorbed energy when using the tables for real breasts.

Our contributions

The AGD is a dose, i.e. an absorbed energy divided by the absorbing mass, and is used as a measure for the radiation risk from mammography [42, 114]. However in [58] we showed that AGD is not correlated with the amount of tissue at risk, and as a consequence is not a good indicator for the radiation risk of a specific mammographic examination. To do so, we computed the AGD for a set of virtual breast phantoms in comparison to a reference phantom, applying the relevant normalized glandular dose coefficient. First, comparing the nominal phantom with the same phantom doubled in size, we found the same AGD, whereas the amount of glandular tissue is twice larger. When diminishing the intra-skin density, the AGD increases, the highest AGD being obtained for a totally adipose breast where no tissue at risk is present. The same problem seems to occur for thinner breasts. The heterogeneity of the energy deposition [126] makes that the AGD increases, even if

the amount of tissue at risk decreases due to decreasing breast thickness. These paradoxes are a consequence of the misuse of the AGD which is intended to be computed for the average breast but applied to the computation of the dose for an individual breast.
Today medicine is going towards individualization [15,138] and therefore a good alternative to AGD, or correction factors are needed on an individual level [128]. This lack of individualization and even more importantly the lack of uniformity between different computation methods of different vendors was also reported by Tromans et al. [140]. However we think individualization should not be done on AGD but as Hammerstein et al. already proposed on "total energy absorbed in glandular tissue as the most relevant indicator of risk in mammography" [66]. This is comparable to the imparted energy that was proposed by Huda et al. [62,79] for dosimetry in diagnostic radiology. It was proposed with some controversies as a better risk estimator than the dose equivalent [29]. In the individualized evaluation of the radiation related risk in mammography, the different radiation sensitivities of glandular and adipose tissues should be taken into account. This also requires the knowledge of the amount and localization of each of these components of the breast at an individual level. Attempts were made to estimate the localization of the different breast tissues based on the density map for conventional mammographic images [119]. Thanks to recent developments in breast imaging as breast tomosynthesis and breast CT it is possible to (partly) overcome the problem of the glandular tissue localization [121, 123, 137, 145]. It becomes thus theoretically possible to provide an individualized quantitative evaluation of the energy absorbed by glandular tissue and adipose tissue separately, based on the glandular amount and distribution. This will open the way to individual radiation risk in breast imaging, based on improved measures. In this work we go into more detail on the physical measures of imparted energy (see Figure 1.7), without addressing the biological effects and effective risk.

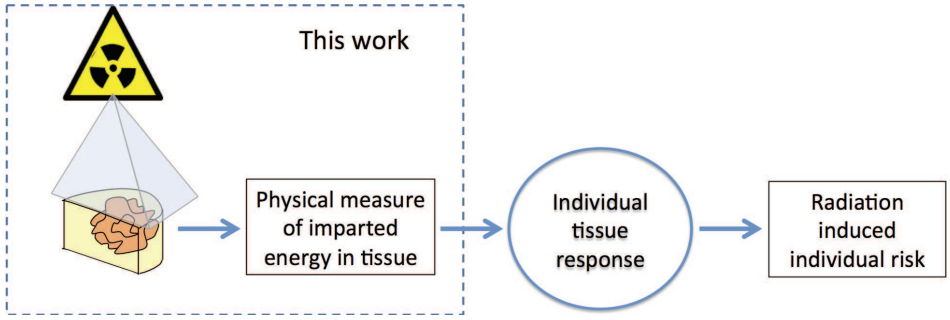

Figure 1.7: The exposure of an object has a biological impact which can be derived from physical measures. In this work we discuss only the physical measures.

1.2.4 Conclusion

Breast density is a developing subject which may find different applications.
Probably the most mediatized one is that breast density is an aggravating factor relative to breast cancer risk, mixing masking effect and correlation risk factor. Recent developments in breast imaging techniques have enlarged possibilities of density measurements, including volumetric distribution.
The breast density is also used in dosimetry. For historical reasons individual density is

being used outside its context and population metrics are mixed with individual density and radiation risk measures. We will apply our breast density measures to assess the individual risk for which we will compute the glandular imparted energy (GIE) as proposed by Hammerstein [66]. Therefore we need to know the spatial distribution of the fibroglandular tissue which becomes possible with (semi-)3D imaging methods. Our proposal of GIE and segmentation will be applied to breast tomosynthesis examination.

1.3 Research objectives

The main objective of this research is to compute the energy imparted to the different breast tissues, glandular and adipose tissues, for patients having undergone a tomosynthesis exam. The steps of this dissertation are to quantify the volumetric breast density, to deduce the distribution of the glandular tissue, to propose improved measures of the interaction between radiation and the breast tissues and to apply it to a tomosynthesis examination, as illustrated in Figure 1.8.
The two main parts of the research are:

- Design a model for the computation of the volumetric breast density,
- Design a model for the computation of locally absorbed energy.

The input is a breast tomosynthesis examination on a Senographe Essential equipped with the SenoClaire digital Tomosynthesis attachment (GE Healthcare, Chalfont,UK), using the acquisition data stored in the DICOM-header. We reconstruct the 3D planes using the SenoClaire 3D-reconstruction. Differently from CT images, the resulting voxel values have no physical meaning. For the first research objective we develop a VBD computation based on 2D-projection images and its technical acquisition parameters. This method is described in Part I. The computation method is described in Chapter 3. We developed a new validation method of the VBD computation described in Chapter 4. The computation can also be applied to the projection images of the tomosynthesis exam. The VBD computation method provides the percentage of fibroglandular tissue in the 3D breast. We investigate if the reconstructed volume can be segmented so that the VBD is matched. Then it would be possible to assign density values to the voxel values, labeling the local tissue. For the second objective we use Monte-Carlo simulations of the 2D and tomosynthesis examinations so that no hypotheses on the interactions were necessary and scatter could be taken into account. From the results of a series of simulations we will learn how to compute the energy locally imparted per voxel from a poly-energetic cone beam. This method is described in Part II. The combination of the locally absorbed energy and the labeled volume will lead to the total absorbed energy to the glandular and adipose tissues separately for the given tomosynthesis exam.

This work is supported by a three-year CIFRE-grant (N° 2011/0416) and results from a collaboration between GE Healthcare (Buc, France), Télécom ParisTech (Paris, France) and KU Leuven (Leuven, Belgium).

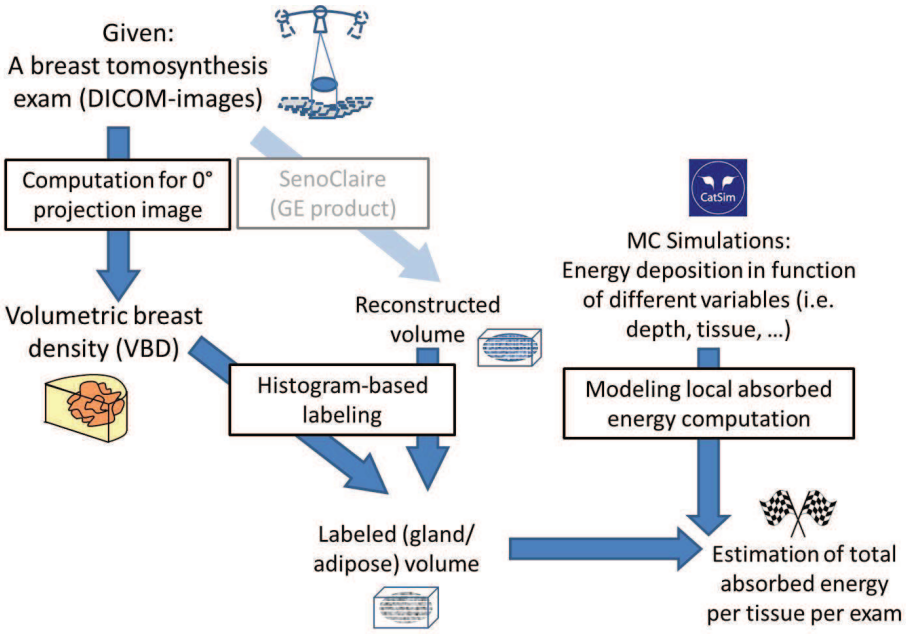

Figure 1.8: Scheme of the objectives of the thesis. The main objectives are a) a model for the computation of the volumetric breast density, and b) a model for the computation of the locally absorbed energy. The scheme shows how both parts are related to each other and which intermediate steps are needed.

Part I

BREAST DENSITY

Chapter 2

Validation of breast equivalent phantom material

A preliminary version of this chapter was presented at SPIE Medical Imaging, 2012: N. Geeraert, R. Klausz, P. Giudici, L. Cockmartin and H. Bosmans. Dual-energy CT characterization of X-ray attenuation properties of breast equivalent material plates. Vol. 8313 p. 1-7 [59].

This chapter evaluates the breast equivalent phantom that we intend to use for the volumetric breast density (VBD) computation in mammography. The material is tested on homogeneity, consistency and precision by imaging it with a dual energy CT. We discuss the use of the phantom and the need to validate it. The CT measurements are presented and the results learn us about the characteristics of the phantom. In conclusion we show how the phantom can be used for the determination of a VBD computation method.

2.1 Breast equivalent material for VBD computation

As described in Section 1.2.2, most of the VBD computation methods for mammographic projection images are based on calibrations using a breast equivalent material available from a single manufacturer following the method of White [150] and Fatouros [51] (CIRS Inc., Norfolk, VA). Consequently this breast equivalent material is the cornerstone for estimating breast densities from mammographic X-ray images. A fundamental requirement for the phantom material is a close match in attenuation properties between phantom material and real breast tissue (precision) in the energy domain of mammography (i.e. 15 keV to 30 keV). The material should in addition allow consistent measurements within the samples (homogeneity) and from sample to sample of the same nominal glandular content (consistency).
From another point of view, all breast density assessment methods should be validated on patients against available imaging modalities capable to identify the different tissues and with the possibility to measure the volume of the breast and fibroglandular tissue. CT is a 3-dimensional imaging modality with a good geometric accuracy. It can effectively distinguish fibroglandular tissue from adipose tissue, based on attenuation characteristics of both tissues and with the possibility to quantify volumes, which makes it a good candidate for the validation of breast density quantification methods [50]. We discuss this method

in Chapter 4. In the frame of our work, it was therefore of particular interest to double check the properties of the calibration phantoms using CT as well.

2.2 CT measurements of the breast equivalent phantom

The capability of CT to measure the attenuation properties of the breast equivalent phantoms must first be verified and the accuracy must be determined. The breast equivalent material generally used in mammography is available under the form of rectangular plates. The influence of the shape and configuration of these plates on the CT measurements has to be studied.
Once the use of dual energy CT is verified, we can use the voxel values, expressed in Hounsfield Units (HU), in the images of the plates. They can be used to assess the homogeneity of attenuation properties and then the consistency between different plates of the same nominal breast density equivalence. The linearity of HU to the nominal breast density equivalence can be evaluated. Finally linear attenuation coefficients can be derived from the mono-energetic HU provided by dual-energy CT as described by Wu [155] and used by Van Gompel [63] and Zhang [159]. The results for these coefficients are compared with values from the literature [66, 84].

2.2.1 CIRS

We used 24×18×2cm^3 CIRS plates (large plates) with attenuation equivalent to 0% and 100% fibroglandular tissue and $12 \times 10 \times 2$ cm^3 CIRS plates (small plates) with attenuation equivalent to 0%, 30%, 50%, 70% and 100% fibroglandular tissue. The numbers of breast equivalent material plates used for our analysis are listed in Table 2.1.

Breast density equivalence	0%	30%	50%	70%	100%
$24 \times 12 \times 2$ cm^3 (large plates)	3				3
$12 \times 10 \times 2$ cm^3 (small plates)	2	2	2	2	2

Table 2.1: Numbers of available breast equivalent plates of large and small size, with the corresponding equivalent density.

The plates were imaged using a GE Discovery CT750 (GE Healthcare, Chalfont, UK) with the dual energy option (Gemstone Spectral Imaging, GSI), in helical mode for different configurations of breast equivalent slabs, as summarized in Table 2.2 and shown in Figure 2.1. The images were analyzed using the measuring tools of the GSI viewer.
The plates were stacked together and were oriented either parallel or orthogonal to the image planes (see Figure 2.1). For configurations 1 and 2 a combination of ten small plates and four large plates were used. For configurations 3 and 4 six and four large plates respectively were used. The small plates were oriented parallel to the image planes in Configuration 1 and orthogonal to them in Configuration 2. The large plates were oriented orthogonal to the image planes in all configurations.

Configuration number	1	2	3	4
Orientation to image	In-plane	Orthogonal to plane	Orthogonal to plane	Orthogonal to plane
Surrounding material	Air	Air	Air	Water (cylinder)
Plates	Ten small Four large	Ten small Four large	Six large	Four large
Bowtie filter	Medium	Medium	Body	Medium
Slice thickness	1.25 mm	2.5 mm	2.5 mm	1.25 mm
Spacing between slices	2.0 mm	2.0 mm	2.5 mm	2.5 mm
Convolution kernel	Standard	Soft	Soft	Soft
Measured with	QC-image (140 kV)	QC-image (140 kV)	QC-image (140 kV)	QC-image (140kV)and MONO-image (40keV - 140keV)

Table 2.2: Technical parameters of the four configurations (see Figure 2.1) imaged with a dual energy CT in helical mode.

2.2.2 Configurations

In Configuration 1 (see Figure 2.1) one image plane displayed only one plate. Measurements in the same region of interest, ROI, in consecutive image planes allowed comparing HU of plates with different nominal breast density equivalences. We cannot check homogeneity with this configuration, because we did not verify the homogeneity of the images. In Configuration 2 (see Figure 2.1) each plate was displayed in all images, so homogeneity of the small plates could be verified by measuring the average HU in the same ROI in consecutive image planes. In Configuration 3 (see Figure 2.1) all large plates (alternating 0% and 100% breast density equivalence) were placed in a stack, so that the large plates could be compared on consistency of the equivalent densities between them. We wanted to investigate the influence of the shape of the configuration and of the surrounding material. Therefore in Configuration 4 the plates were placed in a cylindrical CT phantom holder for quality control (QC) of the American Association of Medical Physicists (AAPM) that was filled with water. This allowed us to compare the impact of the corners in the first configurations to the circular configuration of the same plates and the homogeneity within the large plates could be followed along the length of the phantom in the consecutive images and compared to the homogeneity in water.

Consequently the configurations were used for different tests: consistency of HU to check our method for Configurations 1 and 2, the consistency between plates of equal nominal breast density equivalence in Configuration 3, the homogeneity of large plates in Configuration 4, the linearity of HU to nominal breast density equivalence in Configuration

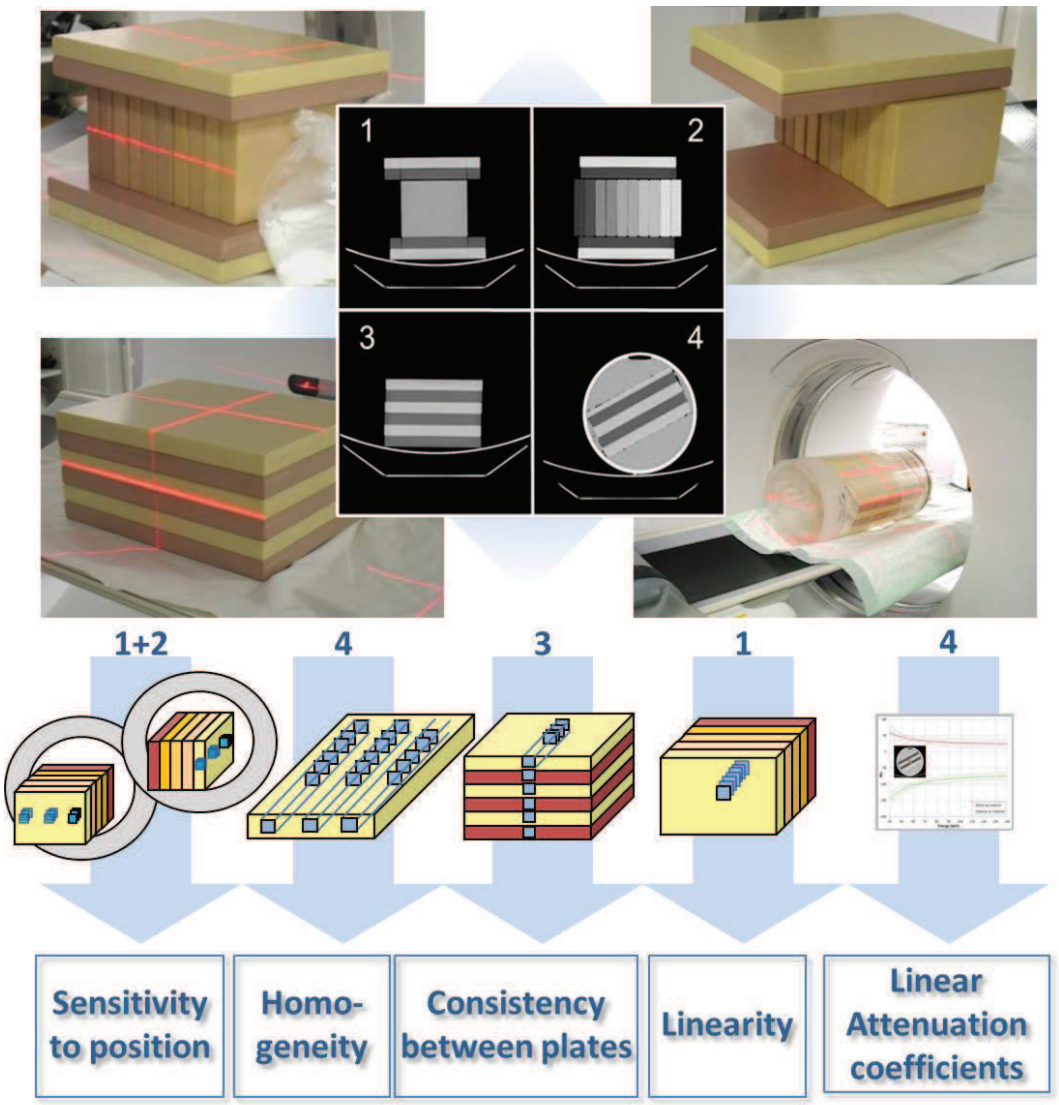

Figure 2.1: A characteristic image of a CT slice of every configuration with the corresponding photo of the set-up. Measurements in the different configurations are shown with their goals.

1, and the linear attenuation coefficients in Configuration 4.
Images of Configurations 1, 2 and 3 were displayed in the normal viewing mode at 140 kV. Images of Configuration 4 were displayed in both the normal viewing mode at 140 kV and the mono-energetic (40 keV - 140 keV) images reconstructed from the dual energy mode.

2.2.3 Measuring the CIRS characteristics

On the center line of each small plate (Configurations 1 and 2, see Figure 2.1 first arrow) physical cubic volumes ($1\times1\times1$ cm^3) were defined. The average HU per volume was computed by averaging the ROIs from corresponding image planes for Configurations 1 and 2. The difference of the average HU of the ROIs of the physical positions in the phantoms that were scanned with different orientations showed the influence of the orientation of the

plates. If the average HU for the volumes in Configurations 1 and 2 are not significantly different, it is assumed that the CT measurements are consistent with regard to orientation.

Homogeneity within the plates was checked for the large plates in Configuration 4 (see Figure 2.1 second arrow) by measuring the average HU along the imaged sequence in ROIs in the center and on the sides of each plate as seen in the 177 image planes, and computing the standard deviation over these averages. The water around the plates was homogeneous, thus measuring the standard deviation over the different planes provided us with a measure for the accuracy of the CT series.

The consistency between plates of the same nominal breast density was verified by measuring the average HU for all large plates in the ROIs in the center of the plates in all 39 image planes of Configuration 3 (see Figure 2.1 third arrow). The standard deviation was taken from the ROIs per plate. We compared HU and standard deviation of the three adipose equivalent plates and the three fibroglandular equivalent plates.

The linearity of the HU of the small plates was checked against nominal breast density equivalence in Configuration 1 (see Figure 2.1 fourth arrow). The HU values were measured in the ROIs in the center of each plate, since a good plane to plane reproducibility was found from the homogeneity measurements for water. The respective HU values were plotted as a function of the nominal glandular content. The result should follow the partial volume principle:

$$HU = \frac{VBD}{100}(HU_G - HU_F) + HU_F \tag{2.1}$$

with HU the HU of a plate with nominal breast density equivalence $'VBD'$ expressed in % and HU_G and HU_F the HU for the 100% and 0% breast density equivalent plates respectively.

The linear attenuation coefficients were computed in the mono-energetic images from Configuration 4 (see Figure 2.1 fifth arrow) generated by the GSI dual energy function. The water around the plates allowed us to accurately calibrate the HU measured in the plates. The average HU and the standard deviations within the ROIs in the center of the different plates and in the water next to the plates were computed per keV between 40 keV and 140 keV [63, 159].

From these mono-energetic HU the linear attenuation coefficient was computed using

$$\mu = \frac{HU}{1000}(\mu_{water} - \mu_{air}) + \mu_{water} \tag{2.2}$$

with μ the linear attenuation coefficient of the material and HU the average mono-energetic HU of the ROI. The values for μ_{water} and μ_{air} were taken from the National Institute of Standards and Technology (NIST) tables [19].

2.3 Breast equivalent phantom characteristics

The differences for the eight middle volumes in Configurations 1 and 2 varied between 0.1 and 1.3 HU. This must be compared to an average standard deviation of 4 HU within

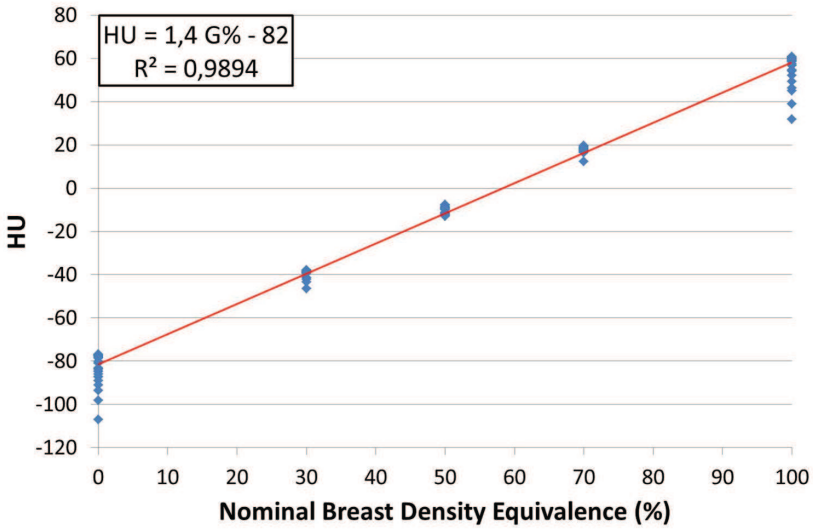

Figure 2.2: HU as a function of nominal breast density equivalence (30 measurements per breast density equivalence) and least square fit finding the expected relation ($R^2 = 0.989$).

the ROIs constituting the volumes. The standard deviation over the mean values of these ROIs is 1 HU. The difference of the average HU of the volumes of the two configurations with a different orientation is therefore not significant. The orientation of the plates can be neglected in the center of the plates and in the middle of the stack. The two outer plates of the stack of small plates differed between the Configurations 1 and 2 by 4.1 and 6.0 HU. Therefore these plates were not considered for further tests for the verification of the phantoms. The problems are caused by the sharp edges of the phantoms, so no problems are expected for patients.

The standard deviations over the ROIs respectively in water and in the plates in Configuration 4 were comparable: 0.6 in water, 0.8 and 0.6 in the two adipose equivalent plates and 0.7 and 0.7 in the two fibroglandular equivalent plates. Since the variations from ROI to ROI were not significantly different from the variations within water, the homogeneity of the plates is confirmed. Some more important moderate local deviations were observed in some image planes (maximum difference to average value of 1.5 HU within water, 2.4 HU and 5.5 HU in the two adipose equivalent plates and 2.0 HU and 2.1 HU in fibroglandular equivalent plates respectively), but do not contradict the homogeneity assessment.

The standard deviations over the ROIs of the same nominal breast density equivalence in Configuration 3, neglecting the two outer plates, were 1.7 HU for the adipose and 1.5 HU for the fibroglandular equivalent plates. Maximum differences versus the average values of the plates were 2.9 HU for the adipose and 3.2 HU for the fibroglandular equivalent plates. The average HU of the nominal breast density equivalence of 0% and 100% were respectively -67 HU (standard deviation 1.7%) and 55 HU (standard deviation 4.5%).

The measurements of the HU in the small plates in Configuration 1 were plotted against their nominal breast density equivalence (0%, 30%, 50%, 70% and 100%) in Figure 2.2.

The HU were measured in the center of the plate in 157 consecutive slices in total. The deviating values for 0% and 100% nominal breast density equivalence came from the outer plates, where the consistency of the CT measurement is not guaranteed (see above). A least square fit showed the good linear correlation between the nominal breast density equivalence and the HU as expected from Equation 2.1 ($R^2 = 0.989$).

Configuration number	1	2	3	4
Gl a	-	-	58	-
Gl b	56	49	58	61
Gl c	56	50	49	62
Gl small	55	47	-	-
Ad a	-86	-79	-68	-
Ad b	-85	-80	-66	-80
Ad c	-	-	-68	-79
Ad small	-89	-79	-	-

Table 2.3: Average HU per plate with all ROIs taken in the plates (center and sides) with Gl = glandular equivalent and Ad = adipose equivalent plates. Each column is a different configuration.

The average HU for the ROIs in the center of the plates of the 0% and 100% small plates were -83 HU and 56 HU. This was not in agreement with the HU found for the large plates in Configuration 3. The average HU for equal plates in different configurations were compared for ROIs of the entire sequence in the middle and on the side of the plate. Results are presented in Table 2.3. Variability was found between the configurations, but there was a good consistency between different plates (small and large) within one configuration even if the ROIs on the sides of the plate are taken into account. It shows that probably not only the orientation of the plates is of importance, but also the surrounding material.

The following results were measured on the GSI images, computing the HU per energy bin. Figure 2.3 shows the computed mono-energetic HU and standard deviation as a function of energy in keV for Configuration 4. HU values for adipose and glandular equivalent materials ranged from respectively -144 and 57 HU at 40 keV to -75 and 24 HU at 140 keV.
Based on these curves the linear attenuation coefficients were computed (see Figure 2.4). The linear attenuation coefficient of water was found to vary from 0.277 cm^{-1} at 40 keV to 0.152 cm^{-1} at 140 keV. When compared to the values provided by the NIST tables [19] differences ranged from 0.010 cm^{-1} to 0.001 cm^{-1} respectively.
In Figure 2.4 and Table 2.4, the linear attenuation coefficients of adipose and fibroglandular equivalent materials were compared to the linear attenuation coefficients computed by combining the atomic composition in Hammerstein et al. [66] and Poletti et al. [117] with the linear attenuation coefficients of materials from NIST [19], and to the linear attenuation coefficients measured from tissue samples [84].

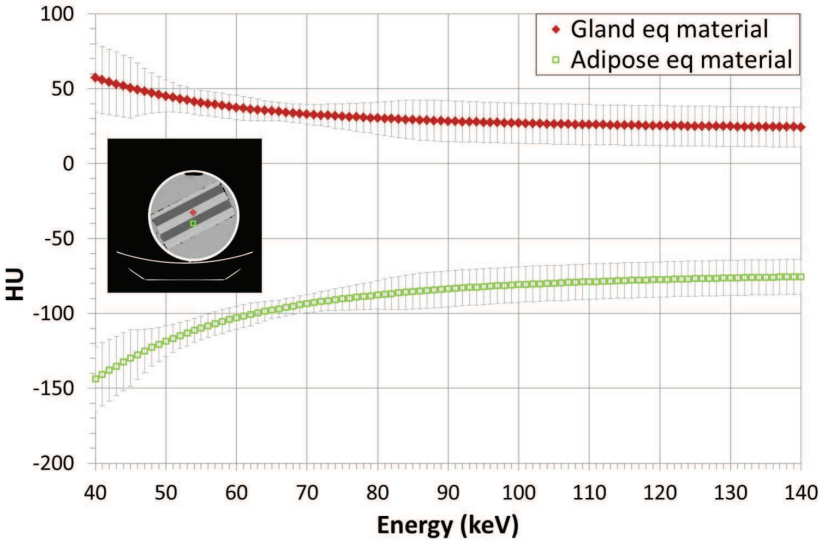

Figure 2.3: Mono-energetic HU for gland equivalent and adipose equivalent breast materials.

	source	40 keV	80 keV	140 keV
Glandular	Spectral CT	0.280 cm^{-1}	0.192 cm^{-1}	0.160 cm^{-1}
	Hammerstein [66] + NIST [19]	0.271 cm^{-1}	0.189 cm^{-1}	0.158 cm^{-1}
	Johns and Yaffe [84]	0.273 cm^{-1}	0.189 cm^{-1}	
Adipose	Spectral CT	0.248 cm^{-1}	0.170 cm^{-1}	0.142 cm^{-1}
	Hammerstein [66] + NIST [19]	0.221 cm^{-1}	0.167 cm^{-1}	0.142 cm^{-1}
	Johns and Yaffe [84]	0.215 cm^{-1}	0.167 cm^{-1}	

Table 2.4: Linear attenuation coefficients at 40 keV, 110 keV and 140 keV according to different authors.

2.4 Breast equivalent phantom in mammography

The breast equivalent phantom can be used for the calibration measurements of our model of the volumetric breast density. We used the large $24\times18\times2cm^3$ and $24\times18\times1cm^3$ plates with attenuation equivalent to 0% and 100% fibroglandular tissue. In projection mammography the density in a point is the integrated density along the path of the X-ray arriving in that point. This is an advantage for our density computation method, since a phantom with a density different from 0% or 100% can be created by combining them. To confirm this we investigated the influence of the order of the plates. We did this for a phantom with a total thickness of 4 cm and 25% density. This was reached with a 1 cm-plate of 100% density and a 1 and 2 cm-plate of 0% density. Different acquisitions were performed at the same exposure values while inverting the order of the plates. The difference in pixel values between all configurations was 0.08%. So we could

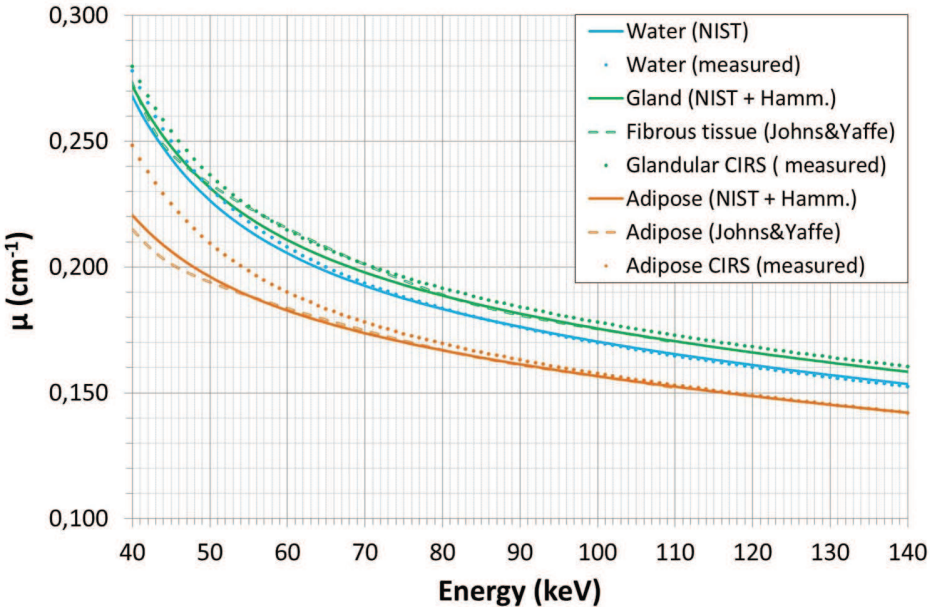

Figure 2.4: Linear attenuation coefficients for glandular tissue and equivalent material (green), water (blue) and adipose tissue and equivalent material (orange) obtained from linear attenuation of the composing elements (full lines) by sample measurements (dashed lines) and from phantom measurements (dotted line).

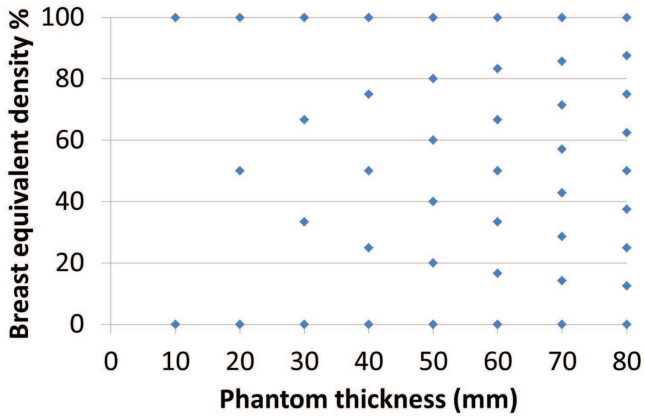

Figure 2.5: All possible combinations of equivalent density and phantom thicknesses, obtained from plates of 0% and 100% VBD of 1 cm thick.

use two separate homogeneous plates with 0% and 100% equivalent tissue to simulate a homogeneous material of an intermediate density imaged in a pixel. With the phantoms that we have at our disposition there is only a limited number of combinations and thus equivalent densities possible. The possible equivalent densities per total phantom thickness are presented in Figure 2.5.

2.5 Conclusion

In this chapter CT was found effective to study the local attenuation properties of the breast equivalent phantom plates. The homogeneity within plates was found good and the attenuation consistent between plates of the same nominal breast density equivalence. A good linear correlation ($R^2 = 0.9894$) was found between the measured HU and the breast density of the plates. This allows us to build intermediate breast densities in projection mammography by combining the plates of 0% and 100%. Spectral CT allowed us to extend the investigation to the measurement of linear attenuation coefficients of the materials, and the results found were in good agreement with those provided by independent methods. These results confirm that these breast equivalent material plates can be used for the calibration and verification of breast density estimation methods, both in 2D and 3D.

Chapter 3

Breast density computation

3.1 Volumetric breast density: introduction

Given the crucial role of breast density in the thesis project, an algorithm has been developed to calculate breast density from 2D mammographic images (VBD_{MX}). We propose a method based on the method of Kaufhold [87] for the computation of the VBD. Their method was based on calibration measurements followed by a modeling of the attenuation properties of breast equivalent material for 0% and 100% density. These attenuation properties were modeled with one polynomial per tube voltage and anode/filter combination. In our work we modeled the attenuation properties of the 0% density and of the difference between the 100% and 0% density, including the tube voltage as a parameter in the polynomials describing the attenuation properties. Breast density in a real image is then obtained by comparing pixel values of the corresponding calibration conditions using the polynomials to cope with thicknesses and tube voltages that have not been measured. The method was implemented and subsequently verified. Then we developed our own method to segment the mammographic images and to compute the local thickness in order to apply the pixel-wise VBD_{MX} computation. Finally we developed a new validation method through comparison with thorax CT breast density measurements (VBD_{CT}). The calibration, the interpolation and the application to mammographic images are described in this chapter. The validation is described in the next chapter.

3.2 VBD: from theory to practice

3.2.1 Theoretical model for the computation of VBD_{MX} from digital mammographic images

The theoretical model is based on a two-compartment model, separating breast content in only two tissues: adipose and fibroglandular tissues. The skin has approximately the same attenuation as fibroglandular tissue, and can therefore be included with the fibroglandular tissue [66].

The VBD_{MX} for a cylinder, with V_x the total volume, V_G the fibroglandular volume

and S the base of the cylinder (see Figure 3.1), can be written as:

$$VBD_{MX} = \frac{V_G}{V_x} = \frac{T_G \times S}{T_x \times S} = \frac{T_G}{T_x}.$$

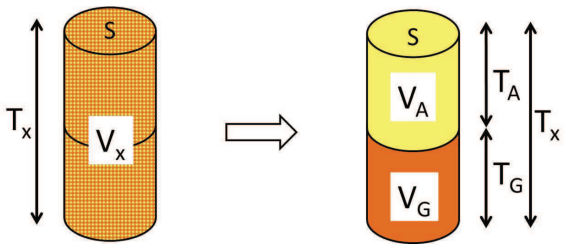

Figure 3.1: Schematic view of the content of a cylinder of breast tissue which can be separated according to the two-compartment model in a cylinder of fibroglandular tissue and one of adipose tissue. We define the total volume V_x as the sum of V_G and V_A, respectively the volumes of adipose and fibroglandular tissues. S is the area of the base, T_x is the height of the cylinder equal to the sum of T_G and T_A, respectively the heights of the fibroglandular and adipose cylinders.

Mono-energetic situation

Under the assumption of mono-energetic radiation, the product of the linear attenuation coefficient and the thickness of a composite material is equal to the sum of the products of the linear attenuation coefficients of each of the components and their respective thicknesses [47]. We can then write, with μ and T respectively the linear attenuation coefficient and the thickness of the material, with indices A for the adipose tissue, G for the fibroglandular tissue and x for the unknown composite tissue:

$$\mu_x.T_x = \mu_A.T_A + \mu_G.T_G \tag{3.1}$$

and

$$T_x = T_A + T_G.$$

From Equation 3.1, the VBD_{MX} for a mono-energetic beam can then be computed as:

$$\begin{aligned} \mu_x.T_x &= \mu_A.T_A + \mu_G.T_G \\ \mu_x.T_x &= \mu_A.(T_x - T_G) + \mu_G.T_G \\ (\mu_x - \mu_A)T_x &= (\mu_G - \mu_A)T_G \\ VBD_{MX} = \frac{T_G}{T_x} &= \frac{\mu_x - \mu_A}{\mu_G - \mu_A} \end{aligned} \tag{3.2}$$

The equation is valid as long as neither T_x nor (μ_G-μ_A) equals zero. T_x is 0 if there is no tissue, so there is no interest in computing the density. The values of μ_G and μ_A approach each other for higher energies [19, 66], but are never equal for the energies used in mammography, i.e. 15-30 keV (see Figure 3.2).

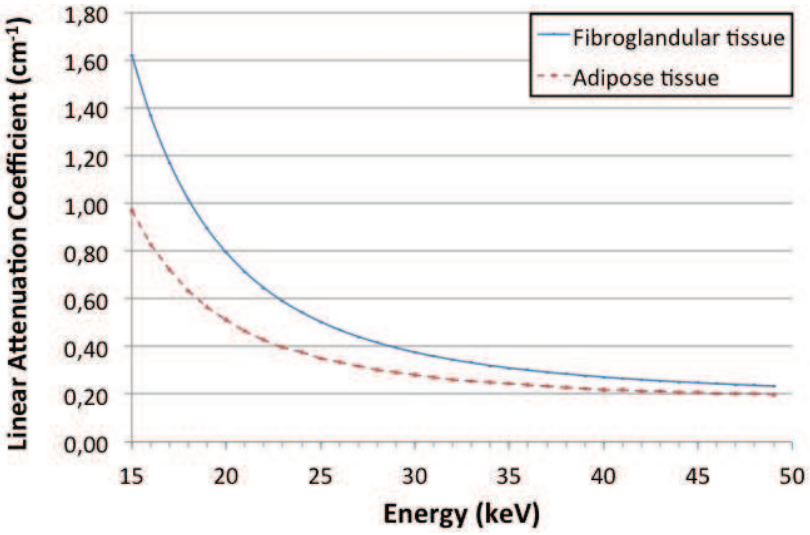

Figure 3.2: Linear attenuation coefficient for fibroglandular, μ_G, (full blue line) and adipose, μ_A, (dotted red line) breast tissues for mammographic energies (15 - 30 keV) [19,66]. The curves are not crossing each other, assuring the existence of Equation 3.2 in every point of the examined range.

The physics law of Beer-Lambert [18, 25, 97] expresses the linear attenuation coefficient, μ, of a material for a mono-energetic narrow beam as:

$$N = N_0 e^{-\mu.T}$$

or written for μ,

$$\mu = \frac{1}{T}(ln(N_0) - ln(N)), \tag{3.3}$$

with N the photon fluence behind the object, N_0 the photon fluence in front of the object, and T the thickness of the material in the direction of the beam.
Instead of using theoretical attenuation coefficients in the calculation of VBD_{MX}, we can write Equation 3.2 using the fluence N behind purely adipose and purely fibroglandular material of the same thickness as the object:

$$VBD_{MX} = \frac{ln(N_x) - ln(N_A)}{ln(N_G) - ln(N_A)} \tag{3.4}$$

Poly-energetic situation

Going from a mono-energetic to poly-energetic beam results in an integration over the energy for all energy dependant factors. The entrance photon fluence is no longer described by a simple number of photons, but as a number of photons depending on the energy over the available spectrum.

The signal provided by the image receptor is

$$I = \int N(E).E.\eta(E).\mathrm{d}E$$

with I the intensity of the signal, E the energy of a single photon, $N(E)$ the number of photons as a function of energy and $\eta(E)$ the efficiency of the detector at energy E.

The attenuation law for a poly-energetic narrow beam becomes

$$N = N_0 e^{(-\mu.T)} \rightarrow \int N(E).E.\eta(E).\mathrm{d}E = \int N_0(E).E.\eta(E).e^{-\mu(E)T}.\mathrm{d}E \tag{3.5}$$

An attenuated poly-energetic spectrum will not only change in intensity but also in shape (*beam hardening*) because low energy photons are easier attenuated than high energy photons (see Figure 3.2).

Equation 3.2 can no longer be solved analytically. However we can keep the center-of-mass principle with experimentally determined spectrum attenuation coefficients. Therefore we need to acquire poly-energetic spectrum-dependant reference measurements of purely adipose equivalent (A) and purely glandular (G) equivalent materials for the different clinical spectra.

Equation 3.2 becomes

$$VBD_{MX} \approx \frac{ln(I)_A - ln(I)_x}{ln(I)_A - ln(I)_G} \tag{3.6}$$

The equation is approximative because μ is energy dependent and thus cannot be extracted exactly from the integral in Equation 3.5. In practice, we can compute VBD_{MX} from a mammographic image if we have measured $ln(I)_A$ and $[ln(I)_A - ln(I)_G]$ for the same thicknesses and entrance spectrum. I is a linear function of pixel value (p) per current-time product (m) [90] after off-set correction.
The formula we will verify and use is thus:

$$VBD_{MX} = \frac{ln(p/m)_A - ln(p/m)_x}{ln(p/m)_A - ln(p/m)_G} \tag{3.7}$$

3.2.2 Implementation of the VBD computation

Kaufhold et al. [87] previously calibrated the values for $ln(p/m)_A$ and $ln(p/m)_G$ as a function of the thickness separately for eleven anode-filter-tube potential combinations by imaging a phantom of breast tissue equivalent material with thickness ranging from 2 to 7 cm. We have performed the calibration for a broader range of spectra (see Table 3.1) and we modeled $ln(p/m)_A$ as a second order polynomial function of both the tube potential and the thickness. In our computations we preferred to model $ln(p/m)_{G-A} = ln(p/m)_G - ln(p/m)_A$ as a single term because this gave smaller errors for VBD than modeling $ln(p/m)_G$ and $ln(p/m)_A$ separately and subtracting afterwards, i.e. 0.6% instead of 1.7% on average over intermediate points. This can be understood knowing that both terms, $ln(p/m)_G$ and $ln(p/m)_A$, depend on the incoming spectrum in the same way, which cancels out in the combined term.

For the implementation of Equation 3.7 we acquired images of breast tissue simulating phantoms (CIRS Inc, Norfolk, VA). The acquisitions were done for two Siemens

Inspiration systems in *Universitair Ziekenhuis Gasthuisberg, Leuven, Belgium*, hereafter called hosp_L, and a GE Senographe Essential in *Centre Hospitalier Jolimont-Lobbes, Entité Jolimontoise, La Louvière, Belgium*, hereafter called hosp_J.

The breast equivalent phantom was imaged with an anode/filter/tube potential combination based on the Automatic Exposure Control (AEC) settings of the different vendors. The different measurements of the imaged breast equivalent phantoms were performed with (see Figure 3.3 and Table 3.1):

- the anode/filter/tube potential combination of the AEC for the particular thickness,
- the same anode/filter combination of the AEC for the particular thickness and the tube potential ±1 kV of the tube potential of the AEC for the particular thickness,
- the anode/filter/tube potential (±1 kV) combination of the AEC for the particular thickness ±1 cm.

Experimental conditions are listed in Table 3.1. For all acquisitions the compression

System	GE Essential	Siemens Inspiration
Exposure mode	AUTOMATIC, MANUAL	AUTOMATIC, MANUAL
Anode	Molybdenum (Mo), Rhodium (Rh)	Tungsten (W)
Filter	Molybdenum (Mo), Rhodium (Rh)	Rhodium (Rh)
Tube potential (kV)	24-27 (MoMo) 25-29 (MoRh) 27-32(RhRh)	24-32 (WRh)
Thickness (mm)	10-50 (MoMo) 20-70 (MoRh) 20-80 (RhRh)	20-80 (WRh)

Table 3.1: Summary of the experimental conditions for the images of the phantoms. These data were used to implement Equation 3.7.

paddle and the anti-scatter grid were in place. Acquisitions were performed in manual exposure mode with current-time product as close as possible to the one used in automatic exposure mode for the corresponding thickness. With the manual exposure mode we extended the thickness-tube potential range of the automatic exposure mode. The values of p of the images were determined as the average of a square region of interest of 1×1 cm^2 in the middle of the plate at 6 cm from the chest wall.

The methodology with the different steps is presented in Figure 3.4.

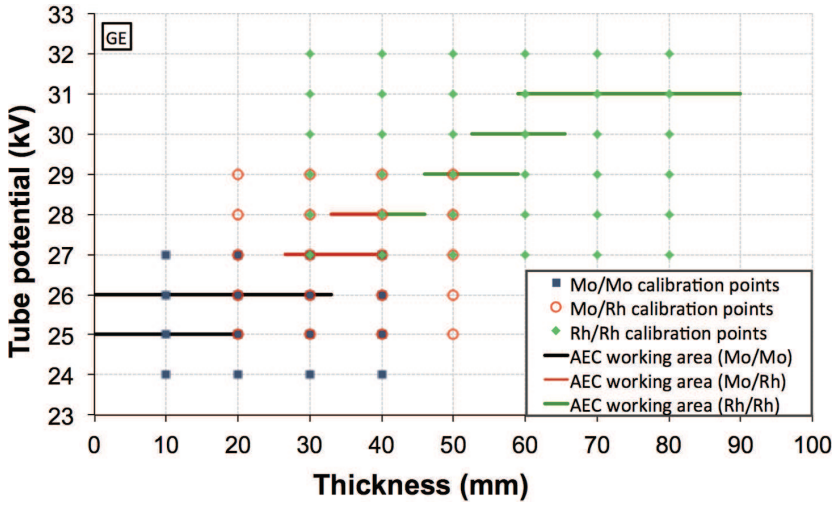

(a)

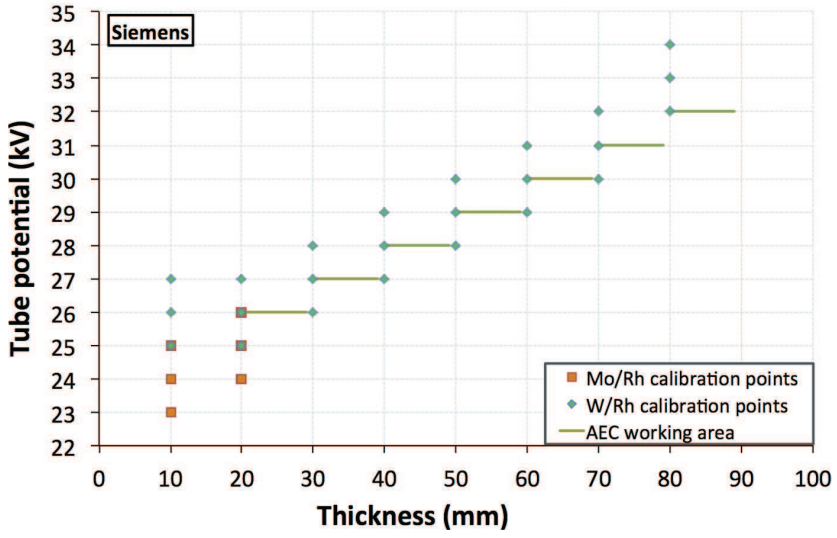

(b)

Figure 3.3: Measured tube potential/thickness combinations for GE and Siemens. The lines indicate the anode/filter/tube potential of the Automatic Exposure Control at a particular thickness for vendors GE and Siemens. The dots indicate the anode/filter/tube potential for the performed acquisitions.

The approach of using Equation 3.7, as deduced from theoretical considerations, was first verified, by using the measurements (0%, 100% and x% at a same anode/filter/tube potential) and plugging them directly in the formula and comparing the computed VBD to the known VBD. Remark that by definition the density estimation for 0% and 100% is exact since the same values are used as measurement and reference acquisitions. The density estimations of all the intermediate densities were compared to the known density values from the phantoms.
Then $ln(p/m)_A$ and $ln(p/m)_G - ln(p/m)_A$ were estimated with polynomial functions (level

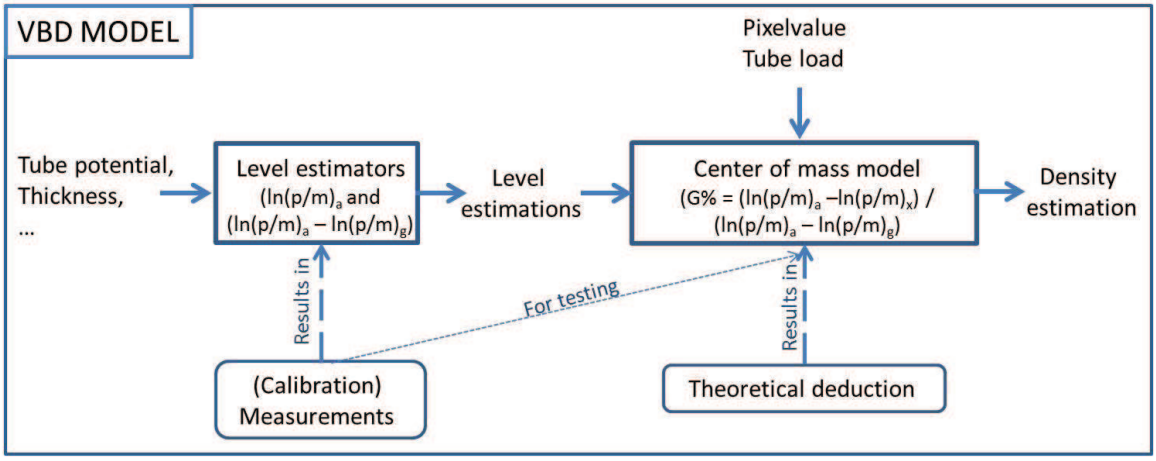

Figure 3.4: Overview of our method for the computation of the density. The center of mass model, based on the physics theory, takes as input calibration measurements or level estimators (the predicted $ln(p/m)_a$ and $(ln(p/m)_a - ln(p/m)_g)$), which take as input acquisition parameters.

estimators), dependent on tube potential and thickness, from the same measurements and per anode/filter combination. We preferred a function over a list of reference acquisitions because:

- this allows interpolation between the discrete calibration measurements to obtain more accurate level estimators for the continuous parameters;
- it is easier to transfer the level model between different systems if it is a continuous function, eventually with a limited number of calibration measurements, than to do for each system the whole set of calibration measurements.

We determined the degree of the polynomial for the level estimators relative to the tube potential and thickness by evaluation of the error on the density estimation. We evaluated the degree for the variation of the level estimator of $ln(p/m)_A$, while using the real measurements of 0% and 100% density for the denominator and vice versa for the level estimator $ln(p/m)_A - ln(p/m)_G$. Polynomials of degree two for the tube potential and for the thickness were accepted for both level models, so they $ln(p/m)_A$ and $ln(p/m)_A - ln(p/m)_G$ can be written as

$$ln(p/m)_A = \begin{pmatrix} 1 & kV & kV^2 \end{pmatrix} \begin{pmatrix} a_{11} & a_{12} & a_{13} \\ a_{21} & a_{22} & a_{23} \\ a_{31} & a_{32} & a_{33} \end{pmatrix} \begin{pmatrix} 1 \\ T \\ T^2 \end{pmatrix}$$

$$ln(p/m)_A - ln(p/m)_G = \begin{pmatrix} 1 & kV & kV^2 \end{pmatrix} \begin{pmatrix} b_{11} & b_{12} & b_{13} \\ b_{21} & b_{22} & b_{23} \\ b_{31} & b_{32} & b_{33} \end{pmatrix} \begin{pmatrix} 1 \\ T \\ T^2 \end{pmatrix}$$

with kV the tube potential, T the thickness and a and b the calibrated coefficients and depending on the anode/filter combination. More details on this choice are discussed in Appendix B as well as more details on the choice for $ln(p/m)_A - ln(p/m)_G$ instead of

$ln(p/m)_A$ and $ln(p/m)_G$ separately. This result is equivalent to a level model that was chosen earlier for GE system regulation and is described in internal documents. The accuracy of the VBD computation is measured using the estimation of $ln(p/m)_A$ and $ln(p/m)_G - ln(p/m)_A$ and the measurements for $ln(p/m)_x$, with x different from 0% and 100%.

3.2.3 Application to mammographic images

To compute the VBD of the breast from a mammographic image (VBD_{MX}), Equation 3.7 is applied to all pixels of the mammographic image. The mammographic images are all DICOM-images with as presentation intent type "FOR PROCESSING" (DICOM-tag 0008x0068). The VBD_{MX} is obtained after multiplication of the local VBD_{MX} with the local thickness, usually per pixel, integration of these values and normalization by the total volume. The anode, filter, tube potential and current-time product are retrieved from the DICOM header of the image. However, since the models for $ln(p/m)_A$ and $ln(p/m)_G - ln(p/m)_A$ are highly dependent on the total thickness, the breast thickness in every pixel must be known accurately.
For that purpose the image is segmented into three zones (see Figure 3.5): the background (outside the breast), the region where the breast under compression is in contact with the compression paddle, and the peripheral region of the breast in between these zones.

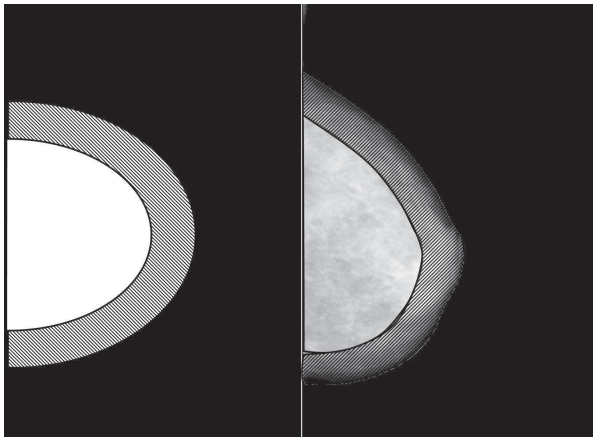

Figure 3.5: Segmentation of the mammographic image according to three thickness regions: the background (dark region), the region where the breast under compression is in contact with the compression paddle (white region), and the peripheral region (shaded region). Left: schematic view, right: patient example.

The background region is segmented by thresholding the image using a threshold value determined automatically from the histogram of the image (see Figure 3.6). The two peaks of patient information and image background can be clearly distinguished. To prevent from losing information the threshold is put closest to the peak of the pixels with image background. The region of the breast is then smoothed using a morphological closing with a circular structuring element of 8 pixels radius. Obviously the region of the background is put to 0 mm breast thickness.

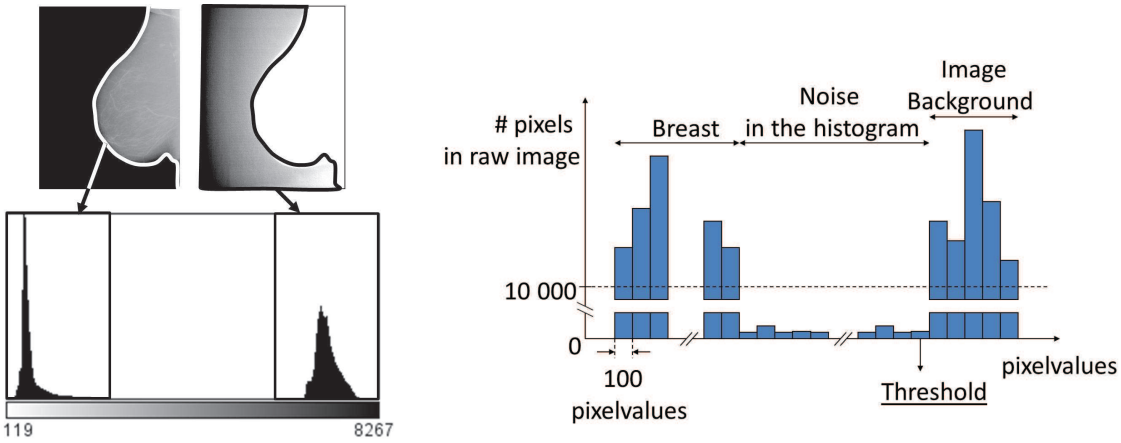

(a) (b)

Figure 3.6: Histogram of the pixel values of a "FOR PROCESSING" mammographic image. The two peaks represent the pixels in the breast (low pixel values) and the background (high pixel values). The threshold to segment the breast from the background is taken close to the background peak. a) Histogram of an example of a patient image. In the left image the upper limit of the range is put between the two peaks, showing the contrast of the low pixel values, in the right image the lower limit of the range is put between the two peaks, showing the contrast of the high pixel values. b) Scheme of the histogram and corresponding threshold.

A thickness map of the breast region is then generated. The thickness of the area in contact with the compression paddle has been considered to be constant and equal to the compressed breast thickness value, stored in the DICOM header (see Figure 3.7). The profile in Figure 3.7 shows the pixel values along a radial line, orthogonal to the breast border. From this profile we estimate the part in contact with the compression paddle, where the signal differences are caused only by differences in tissue attenuation, and the peripheral region where the signal differences are caused both by differences in tissue attenuation and breast thickness. Instead of analyzing all possible profiles to determine the peripheral region, it was set as a band parallel to the border of the breast and with a width equal to half the thickness of the breast. In this band the profiles of the thickness map are chosen to be semi-circular [143]. Again, instead of computing the thickness map based on profiles, a faster method is implemented. The method makes use of masks, one for every mm between 0 mm and the compressed breast thickness, for which the thickness map is incremented with 1 mm. The masks are generated using morphological dilations from the breast border with a circular structuring element. The computation of the size of the structuring elements and the corresponding mask is presented in Figure 3.8. On the left the thickness is represented as a semi-circle in which the structuring element for x mm is computed (chord of x mm). The distance between the chord and the circle (the sagitta of the segment, red line in Figure 3.8) is the size of the structuring element. This circular structuring element is used for the dilation of the breast border (red shaded region). The dilated image serves as a mask for the thickness map where the inner part (white part of the image) is put at x mm thickness. This is done by steps of 1 mm thickness.

The skin is excluded, from both the fibroglandular and the breast volume, by subtracting

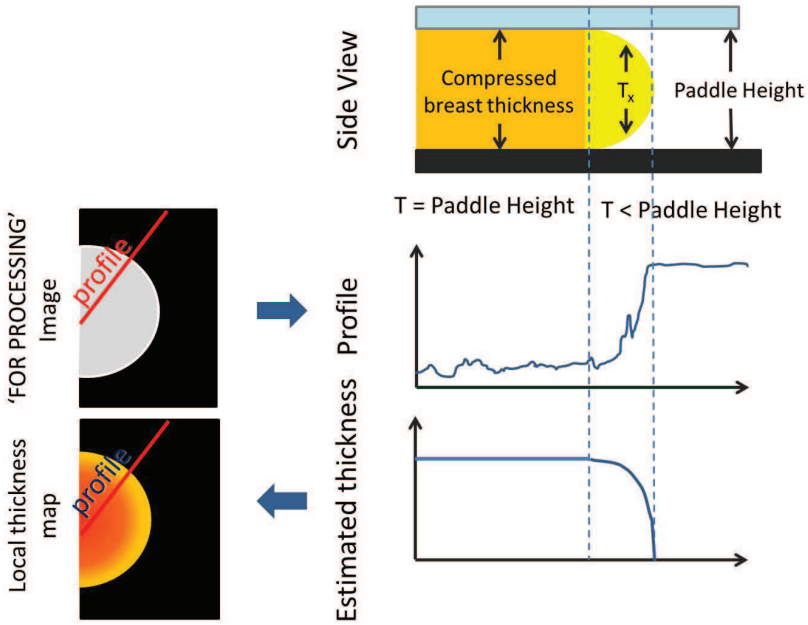

Figure 3.7: Computation of the thickness map. Up: the compressed breast seen from aside, with a region in contact with the paddle and a region not in contact. Middle: the pixel values along a profile orthogonal to the breast edge in the image. Down: thickness of the breast along the profile. The thickness map is constructed with morphological dilation of the background (see Figure 3.8).

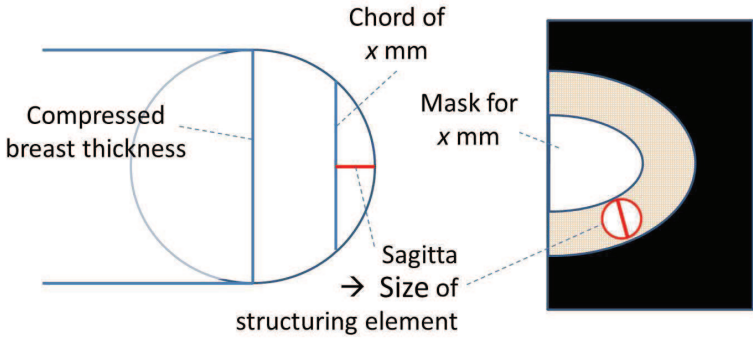

Figure 3.8: Computation of a mask of x mm compressed breast thickness. Left: the size of the structuring element is computed as the sagitta (red line), i.e. the distance from the chord of x mm to the circle. Right: the mask is computed using a dilation of the background. In the white region the thickness map is put at x mm.

a constant gland thickness of 2×1.5 mm [156] from the thickness maps. The region of the pectoral muscle is excluded. The implementation of the segmentation was kept simple by segmenting a triangle formed by the line from the middle of the breast at the long side of the image to the start of the breast at the upper short side of the image.

The knowledge of the acquisition parameters, and, for each point of the image, the

pixel value and the breast thickness, allows computing $ln(p/m)_A$, $ln(p/m)_G - ln(p/m)_A$, as a function of thickness and tube potential, and $ln(p/m)_x$. This results in a density map of the image and the VBD_{MX} of the breast. Highly attenuating objects are automatically excluded if their VBD_{MX} is over 100% and also pixels with values lower than 0%, mainly in the peripheral region, are excluded from integration for the VBD_{MX}.

3.3 Calibration of the VBD computation

3.3.1 VBD for phantoms

The VBD of the phantoms was computed using Equation 3.7 and compared to the known VBD of the phantoms (Figure 3.9(a)) on both the GE and the Siemens system. In Figure 3.9(b) the VBD_{MX} was computed with $ln(p/m)_A$ and $ln(p/m)_G - ln(p/m)_A$ directly obtained from measurements. The average errors, standard deviations and median errors expressed in points of breast density are given in Table 3.2. The maximum deviation was 3.8% on the Siemens system and 1.5% on the GE system. The average errors were 0.6% and 0.3% with standard deviations 1.2% and 0.7% respectively. The choice of Equation 3.7 as a model is therefore satisfactory.

In Figure 3.9(c) the VBD was computed with the modeled $ln(p/m)_A$ and $ln(p/m)_G - ln(p/m)_A$. The spread of the errors at 0% and 100% is larger than for the other measurements. This can be explained since the tube potential/thickness combinations for the calibration measurements at 0% and 100% were taken over a larger range than the range of the measurements of intermediate densities. The average errors, standard deviations and median errors expressed in points of breast density are given when using a level estimator for $ln(p/m)_A$ and $ln(p/m)_G - ln(p/m)_A$ separately and together in Table 3.2. Using the level estimations did not degrade and even slightly improved the density estimation. We reached the same accuracy as Highnam et al. [75], which is the best result published. We will use this VBD model, consisting of the level estimators as input for the center of mass equation as previously represented in Figure 3.4.
The model was originally built for a Senographe Essential (GE, Chalfont, UK). The model is therefore explored in more detail only with the measurements on that system.

Error distribution

In order to exclude systematic errors, we plotted the difference between the density computed with our model and the density known from the phantom as a function of the different variables thickness and tube potential (see Figure 3.10). All errors are expressed in *points of breast density*. The limits of accuracy of the center of mass equation are ±1.28%. If the errors are smaller we can not say if they are caused by the center of mass equation or by the level estimation model. Therefore from Figure 3.10 there is neither a systematic error for the tube potential nor for the thickness. There is also neither a systematic spread for the tube potential nor the thickness. Therefore we consider that it is not necessary to change the polynomial function to a higher degree.

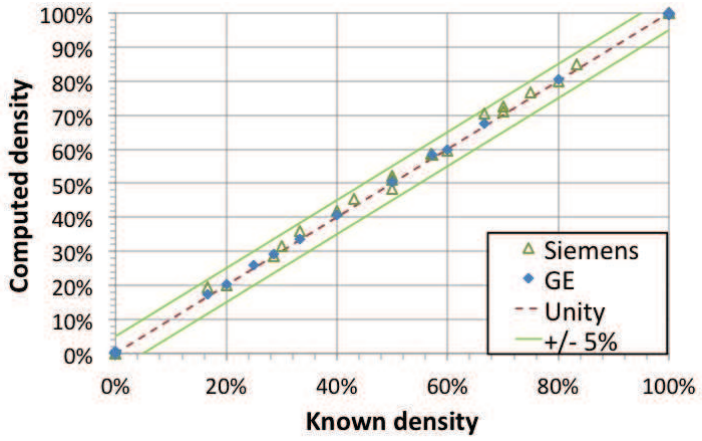

(a)

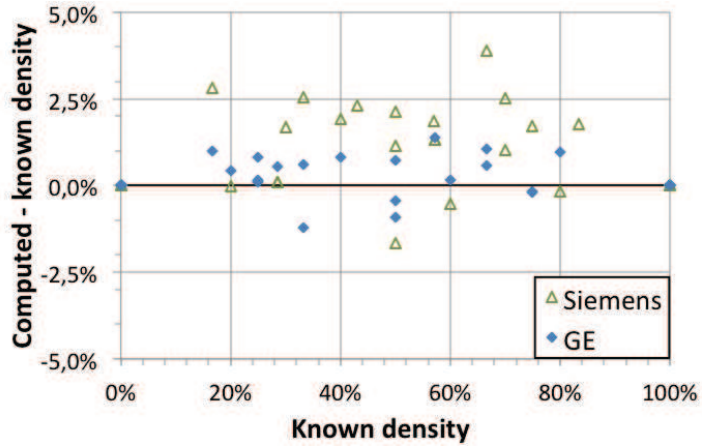

(b)

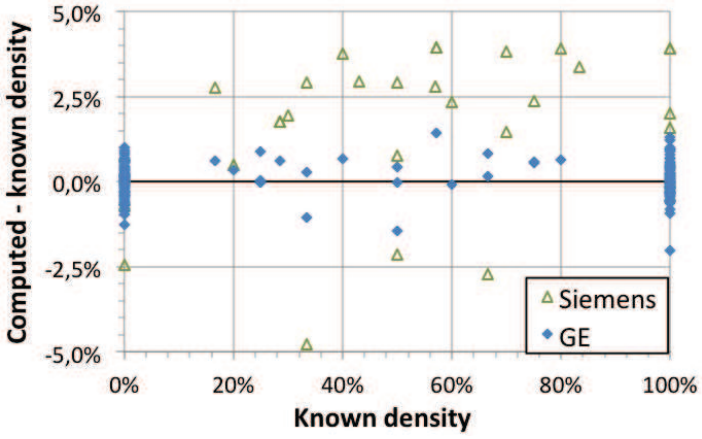

(c)

Figure 3.9: Verification of Equation 3.7. (a) The VBD_{MX} computed with the measured $ln(p/m)_A$ and $ln(p/m)_G$ as a function of the VBD of the phantom. (b) The absolute difference between the VBD_{MX} computed with the measured $ln(p/m)_A$ and $ln(p/m)_G$ and the known VBD as a function of known VBD. (c) The absolute difference between the VBD_{MX} computed with the modeled $ln(p/m)_A$ and $ln(p/m)_G - ln(p/m)_A$ and the known VBD as a function of known VBD.

Input center of mass model		Computed density minus known density (*): GE			Computed density minus known density (*): Siemens		
Denominator: $ln(p/m)_A$	Nominator: $ln(p/m)_A - ln(p/m)_G$	Average	STD	Median	Average	STD	Median
Calibration measurements ($^+$)	Calibration measurements	0.30%	0.64%	0.29%	0.6%	1.3%	0.6%
Calibration measurements (Rh/Rh only)($^+$)	Calibration measurements (Rh/Rh only)	0.77%	0.34%	0.77%	-	-	-
Level estimation	Calibration measurements	0.09%	0.42%	0.12%	0.3%	1.7%	0.8%
Calibration measurements ($^+$)	Level estimation	0.17%	0.58%	0.21%	3.2%	1.3%	3.3%
Level estimation	Level estimation	0.07%	0.40%	0.02%	2.2%	1.9%	2.6%

(*) The errors are absolute errors on the percentage of breast density. 1% of error thus means that a VBD_{MX} of 51% was found instead of 50%.

($^+$) 0% and 100% calibration measures are excluded because they are the reference values, thus resulting in an exact density estimation.

Table 3.2: Error per measurement on density estimation in *points of breast density* with different inputs to the density estimator.

Robustness

To measure the robustness, we computed the error on the density computation after introducing a relative error to one of the variables. This was done separately for the tube potential, the thickness, the pixel value and the tube load. We found that the average error on the density is slightly parabolic ($R^2 = 0.99995$) as a function of the different independent variables (see Figure 3.11).
For every variable we investigated possible deviations between the calibration of the model and when used for the VBD computation, to determine how important each variable and its errors are for the VBD computation. The deviations can occur when the calibration parameters are not the right ones, e.g. determined for another system. Other sources of deviations are long term system drift, or system recalibration by service without VBD-specific calibration [90]. Large deviations are detected thanks to regular quality control (QC)-mechanisms [116], but VBD estimation may be more demanding and require additional controls.

Tube potential

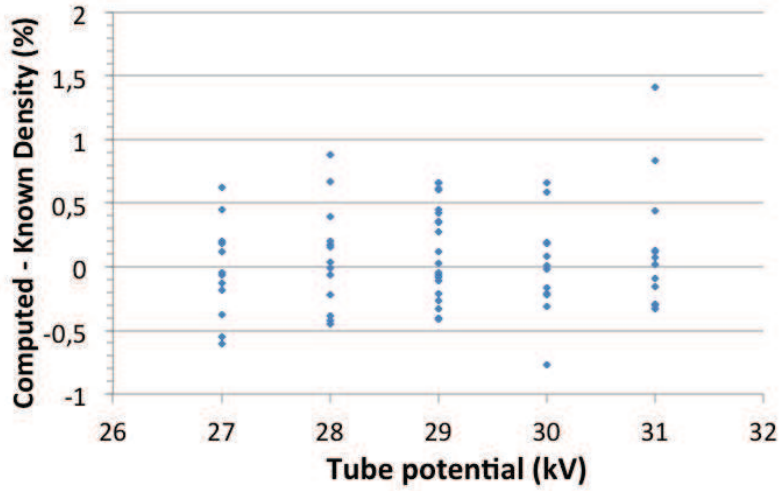

(a)

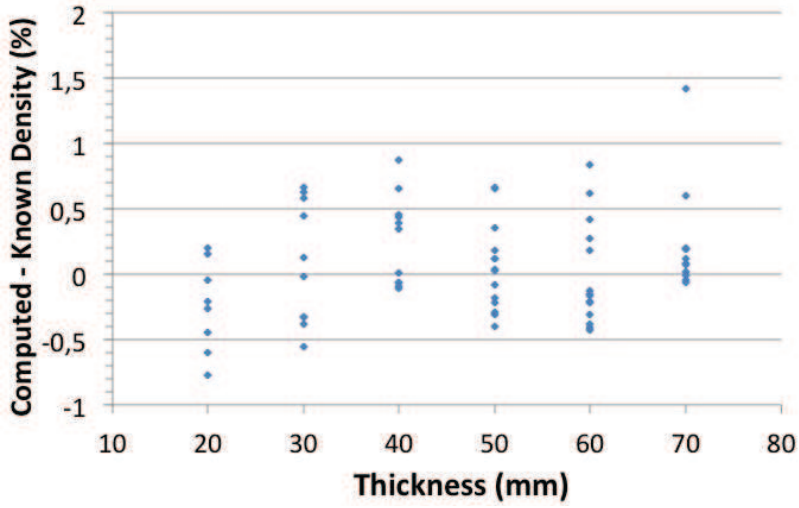

(b)

Figure 3.10: Density estimation error for variables tube potential and thickness for the measurements on the GE-system.

Errors on tube potential values are due to the calibration of the high voltage-generator. The verification on the accuracy at production is done by the manufacturer. At installation it is controlled by the QC-procedures and can be readjusted by the vendor service.

The distribution of tube potential on GE-systems at manufacturing is shown in Figure 3.12. The maximum error of the distribution on the tube potential is 1.2%, which would generate an error on the density estimation of 7.3%. The European guidelines for quality control [116] accept an error smaller than ±1 kV (or 3.5% at 28 kV), with a reproducibility better than ±0.5 kV, leading to an average error of 10.6% on the density estimation.

Thickness

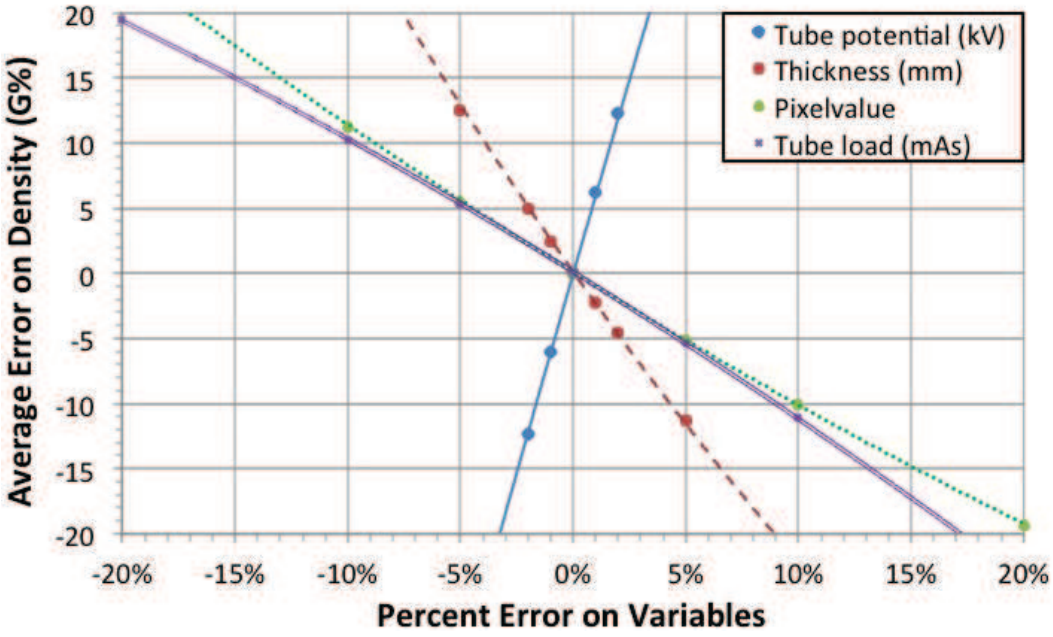

Figure 3.11: Absolute error on density estimation from Relative error on variables: tube potential (full blue line), thickness (striped red line), pixel value (dotted green line), tube load (double pink line).

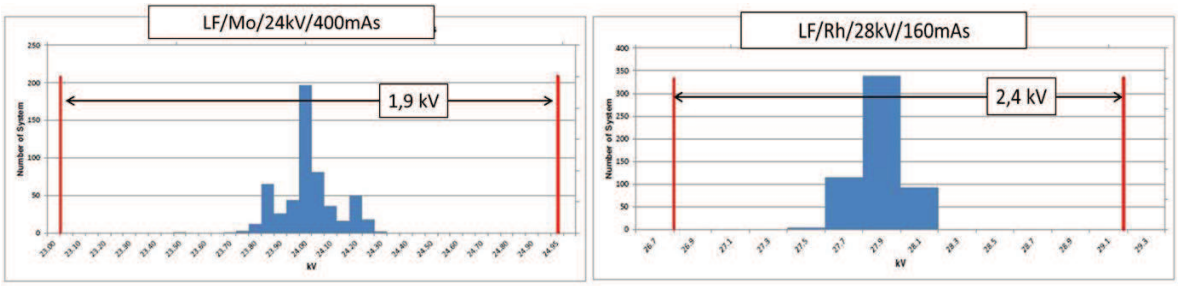

Figure 3.12: Distribution on accuracy of the tube potential at manufacturing (from GE Senographe Essential annual report to the Center for Devices and Radiological Health (CDRH), 2012).

The thickness of the phantom of our measurements was known exactly. However the thickness of a patient's breast is not known exactly and must be estimated. The estimation is based on the height of the compression paddle and the force exercised by it.

Hauge et al. [70] published the errors on the measurement of the thickness of a compressible object by the GE Essential. The rigid paddle and the small flexible paddle (18×24 cm^2) had an average thickness error of 2.8% at 60 N and 1.5% at 100 N and the large flexible paddle (24×31 cm^2) had an average error thickness of 2.9% and 3.8% respectively. These thickness errors result in almost 10% density estimation error (see Figure 3.11).

However Hauges measurements were done in one point, but for real breast measurements we need to know the thickness in every point. From Tyson et al. [141] and Mawdsley et al. [107] we know that even a rigid paddle bends up to 4.2% and that flexible paddles bent in the chestwall-nipple direction with a resulting error on the local thickness up to 9%. For future improvements, additional investigation is required in order to obtain a more accurate local breast thickness estimation [118].
Note that the density error will be more important for small breasts.

Pixel value
The detector of the system is calibrated at construction. A measured entrance dose under standardized conditions is linked to the signal at the detector and thus to the corresponding pixel value in the image.

This calibration guarantees the consistency of pixel values between systems. This statement was confirmed with a publication by Kerrison et al. [90], who found no significant changes in p/m values if there are no sudden changes in the system, i.e. maintenance.

Contrary to the other variables, the pixel value error impacts per pixel, not the entire image. It should be noticed that the gain can be decomposed in two. The average gain is calibrated using signal measurements on a large ROI in relation with an air kerma measurement. The local gain variations, e.g. differences between detector element gains, or other non-uniformities, are measured and compensated using specific flat-field calibrations. A weekly homogeneity test is recommended as part of the QC by the European guidelines for quality control [116]. However the acceptable residual errors may be different for clinical images and for VBD assessment and no numerical values of the errors at these tests are available. We can only say that 5% error on pixel values results in 5.2% error on VBD.

Tube load
The tube load value is stored in the DICOM-header of each image with a precision of 10^{-1} mAs. This variable is also measured at construction and the distribution is shown in Figure 3.13. The maximum error in the distribution of the tube load is 5% and the corresponding error on the density estimation 5.3%. There is no limit on the accuracy in the European guidelines of quality control [116].

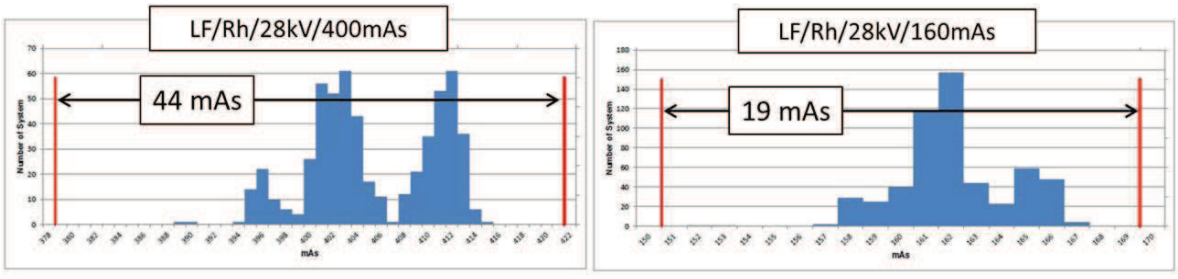

Figure 3.13: Distribution on accuracy of the tube load at manufacturing (from GE Senographe Essential annual report to CDRH, 2012).

Difference between systems

We compared two Senographe Essentials from different hospitals. They were both under quality control of the LUCMFR following the Flemish Quality Control system. No other links between the systems existed. The system on which the calibration measurements for the VBD model were acquired, is located in the hospital of Jolimont. This VBD model was applied to 52 measurements performed on a system in the hospital AZ Brugge (see Figure 3.14). The error of the density estimation compared to the known density per measurement in Brugge is shown as a function of the known density, the tube potential and the thickness. The average and the median error are -2.1% and the standard deviation is 1.04%.
The dataset covered with its 52 measurements a smaller range in the tube potential/thickness combinations, closer to the AEC-acquisition parameters, than the measurements in the hospital of Jolimont, where the model was calibrated. The larger spread of the errors at 0% and 100% density from Figure 3.9 is no longer present. From the different figures we can see that three points demonstrate a significantly higher error. They correspond to a phantom of 30 mm thickness and 100% equivalent breast density. They were acquired at 28, 29 and 30 kV. No other measurements at 30 mm were acquired with Rh/Rh and the error may be explained by the fact that this operating points deviate too much from the regular operating point of the system, which for this thickness and composition should be Mo/Rh at 27 kV.

A trend is visible in Figure 3.14(c), showing that the error on the density estimator is larger on thin phantoms than on thicker phantoms. For all measurements the object thickness was taken as the known thickness of the phantom. This shows that thin phantoms, and thus also breasts, are more sensitive to errors in any variable.

Despite the possible large errors on density estimations predicted from the robustness evaluation and the suggestions of Fowler et al. [54] to calibrate systems separately, the maximum error between these two systems is around 5% (3% without outliers). This was a rather encouraging result for the developed model, but more systems should be tested before definite conclusions can be drawn.

Comparison with the current GE model

The current GE systems Senographe DS and Essential already include a density computation used for the automatic determination of acquisition parameters. However this application does not require a very high accuracy ($< 20\%$). In Figure 3.15 we show the errors relative to the known density values for the current model versus the density model presented here. There is no correlation between the errors from both models, but the absolute value of the error is more than 10 times higher for the currently implemented model. Our density model could eventually be implemented in future GE systems.

3.3.2 VBD_{MX} for the database of mammographic images

We implemented the VBD_{MX} computation model and the segmentation method in Matlab and verified them together on a large database of mammographic images. We run the code on a database containing 663 mammographic images. 560 images were acquired on a

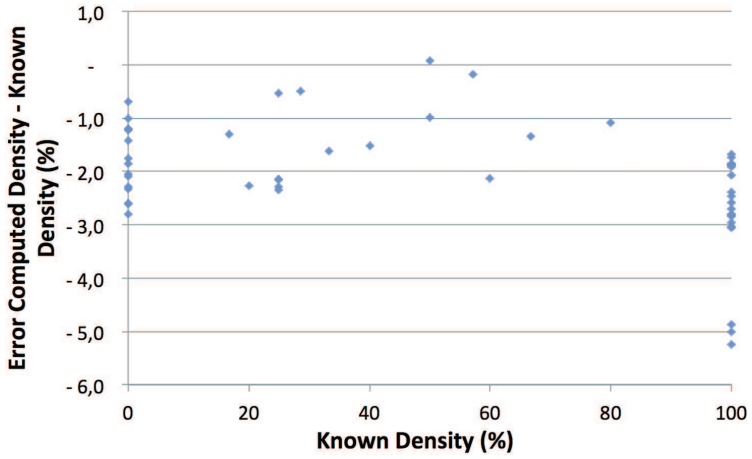

(a)

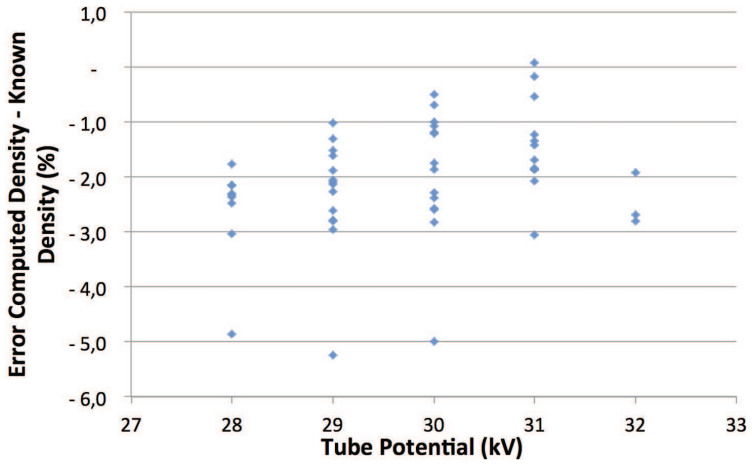

(b)

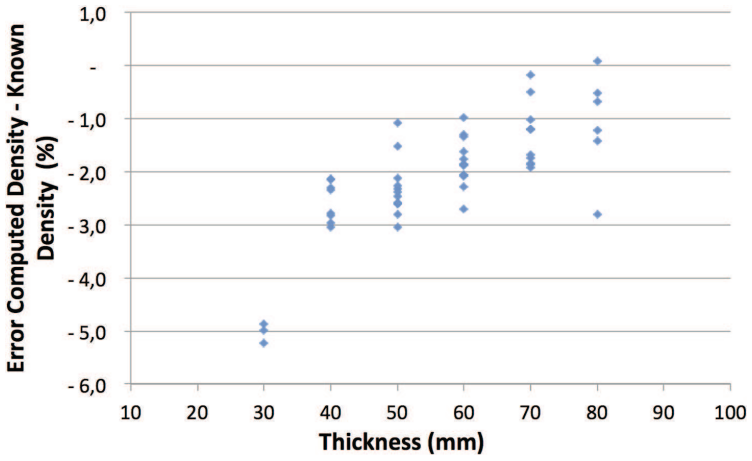

(c)

Figure 3.14: The errors of the density computation on the system in Brugge with the Jolimont calibration.

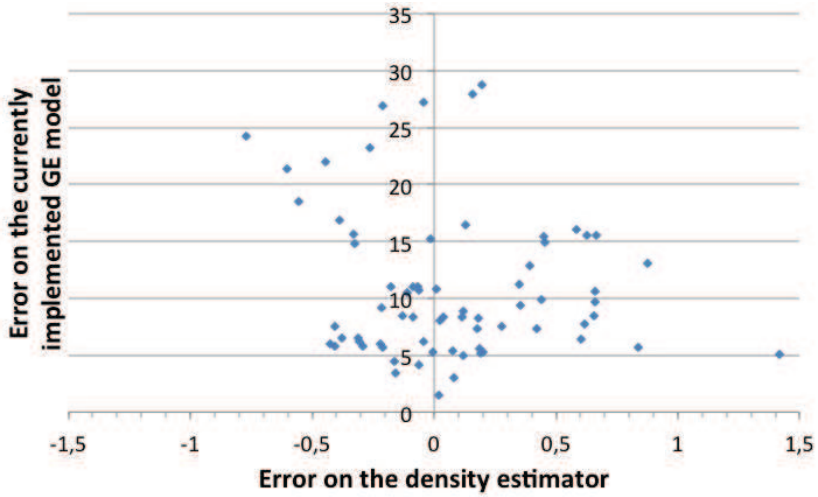

Figure 3.15: Comparison between the currently implemented GE-model and our model.

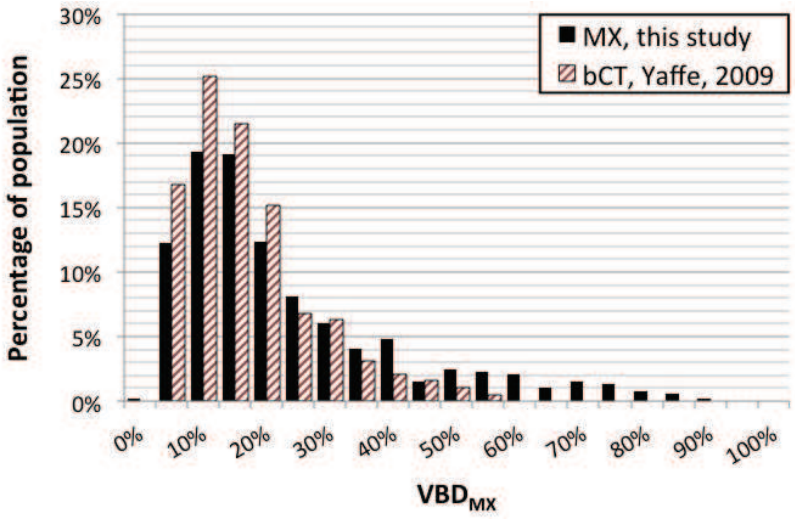

Figure 3.16: The distribution of the VBD computed for a large population of mammographic images (Siemens (560 images) and GE (103 images) compared to the distribution published by Yaffe et al. [156] based on breast CT exams. Both are skewed distributions with their maximum at 10%.

Siemens Inspiration and 103 on a GE Senographe Essential. The VBD_{MX} distribution, population mean and standard deviation were computed. Figure 3.16 represents the distribution of the VBD_{MX} for all images. The maximum of the distribution is found at 10% and the median density of the population is 14.7%. The skewness of the distribution is 1.55. Our results were compared with the results obtained by Yaffe et al. [156], who segmented automatically fibroglandular tissues in dedicated breast CT images to compute the VBD. They also found a skewed distribution with a maximum at 10% and a skewness of 1.68.
Figure 3.17 shows the average VBD_{MX} per thickness category as a function of compressed

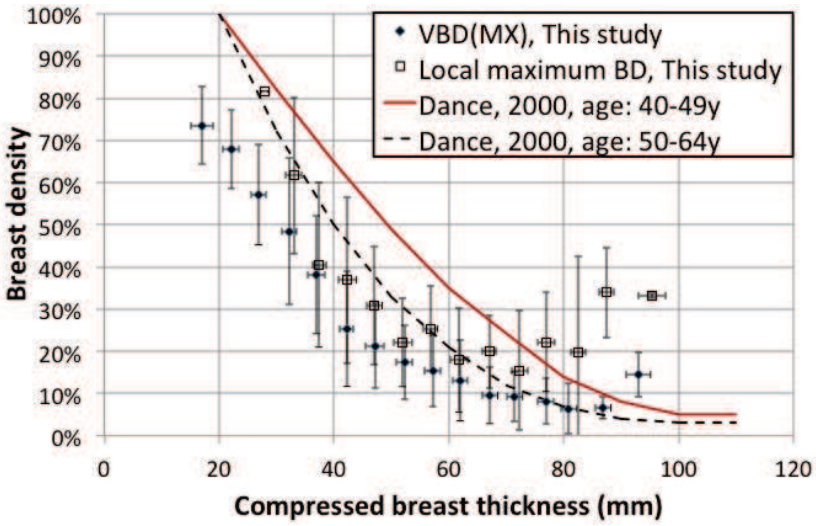

Figure 3.17: The average VBD_{MX} per thickness category computed for Database 1 (full dots), as well as the maximum local breast density for the subset of 129 GE images (empty dots), compared to the local breast density described by Dance et al. [41].

breast thickness. It is decreasing with increasing compressed breast thickness. Dance et al. [41] published this decreasing trend for the local breast density based on computations from the exposure parameters of film-screen mammographic images acquired under automatic exposure control (AEC). The AEC sensor was supposed to be manually placed over a dense region of the breast, so the resulting VBD is local and more representative of higher densities in the breast. We therefore computed the maximum local breast density, by manually selecting the densest 24×18 mm^2 region, for a subset of 129 images of Database 1 to compare to Dance's results (see Figure 3.17).
The correlations between cranio-caudal (CC) and medio-lateral oblique (MLO) images and between left and right breasts are shown in Figure 3.18 and Figure 3.19. The good correlation coefficients and the slope of the graphs close to 1 confirm the confidence in the method. In Figure 3.20 some examples of breast density maps for eight different women are shown together with their exclusion map indicating in black the pixels with density below 0% and over 100%, excluded for the VBD_{MX} computation. In Figure 3.20(b) the white lines in the density maps indicate the exclusion from the pectoral muscle estimation. Comparable findings were reported by Alonzo-Proulx et al. [10] and Zoetelief et al. [161].

3.4 Conclusion: VBD computation is possible

When applied to phantoms with known density, the accuracy of the proposed method can be compared to results obtained by Highnam et al. [75]: the authors published their method with an average error on a GE Essential of 1.11% for 25 measurements with a maximum VBD of 37.5% for Molybdenum-Rhodium 28 kV, Molybdenum-Molybdenum 26 kV and 28 kV spectra. For these spectra we obtained an average error of 0.1%.

When applied to patient images, our VBD_{MX} computation method gave results compara-

ble to other methods in terms of population statistics. The correspondence of the VBD distribution [156] was shown in Figure 3.16. Also Beckett and Kotre [16] applied their method for density estimation to large sets of patient images. They computed the VBD at the position of the AEC-sensor, manually placed by the radiographer in an area supposed to be in the fibroglandular zone of the breast behind the nipple, but constrained to remain on the axis perpendicular to the chest wall. Dance et al. [41] sorted the curves to the ages of the screening population for dosimetry purposes, and this relation between PBD versus compressed breast thickness has been retained in the European Guidelines for Quality Control [116]. Depending on the positioning of the evaluated area, an overestimation of the density versus the actual VBD should be expected. In Figure 3.17 our estimations are indeed lower than the estimations used by Dance, but follow the same trend, with the exception of the thickest breasts where we positioned the AEC more effectively on small hyperdense areas.

The assessment of VBD from mammographic images is penalized by several factors. Estimating the breast thickness in any point is the most limiting factor, even in the compressed part [70]. Secondly, we supposed a two-compartment breast with adipose and fibroglandular tissues. In order to take the skin into account, a general correction was made, with the thickness of the skin assumed to be 1.5 mm at both sides of the breast. This is however based on population averages and not on individual patient data. Thirdly, the VBD_{MX} method relies on the correspondence in attenuation coefficients between the phantoms and real breast tissue [66, 84]. This relation was verified in Chapter 2. However direct measurements of tissue composition and attenuation is limited in accuracy, resulting in large confidence intervals up to 20%. The main problems are the difficult separation of pure adipose and fibroglandular tissue and the low availability of tissue for these experiments at the time of the publications.

Although this calibration method has some limitations, it overcomes the main problem of volume measurements based on a 2D-image. The method is at the level of current

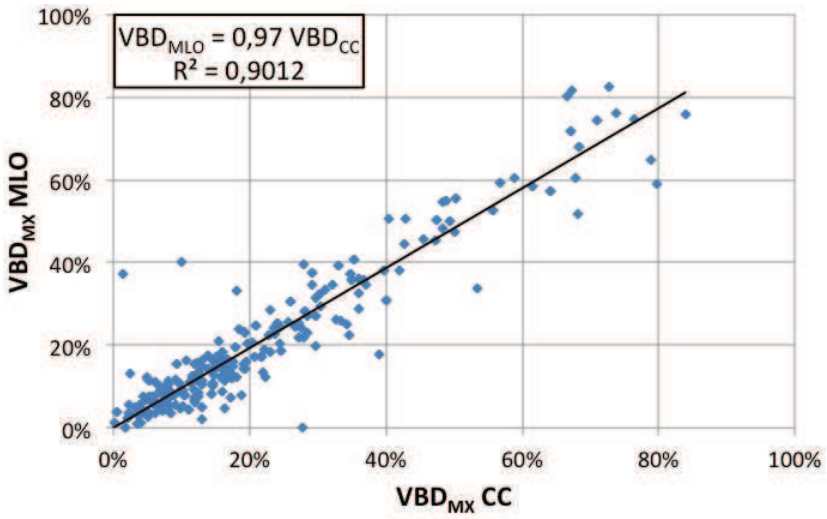

Figure 3.18: Correlation between CC and MLO VBD_{MX} for the images of Database 1.

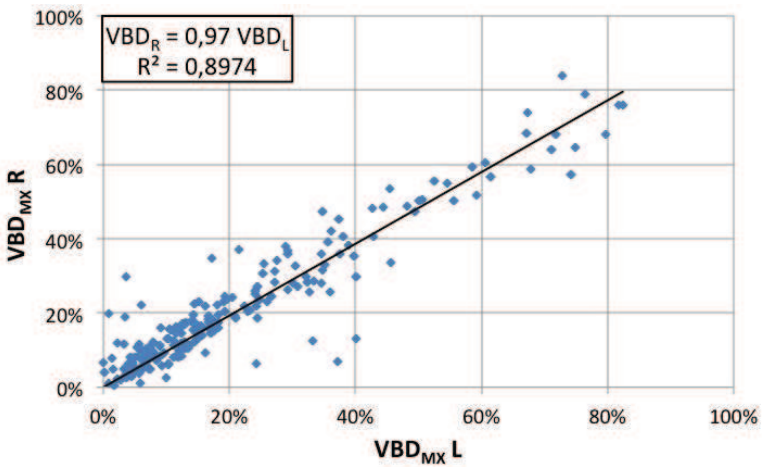

Figure 3.19: Correlation between left and right VBD_{MX} for the images of Database 1.

existing algorithms for the computation of the VBD_{MX}. In the next chapter we propose to validate the method on a patient-individual level.

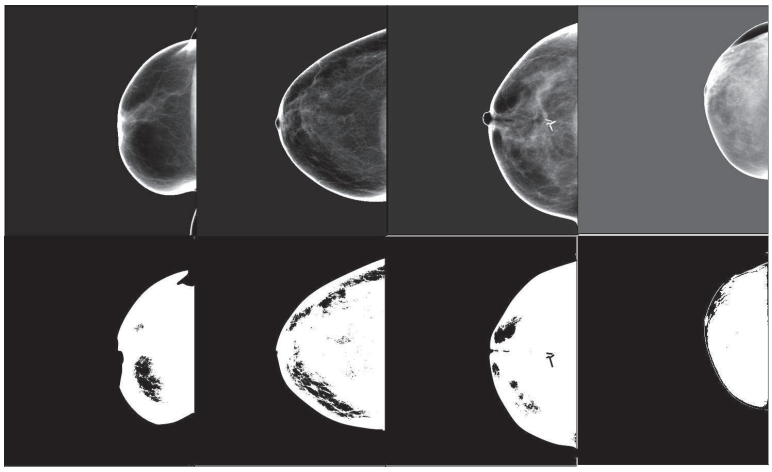

(a)

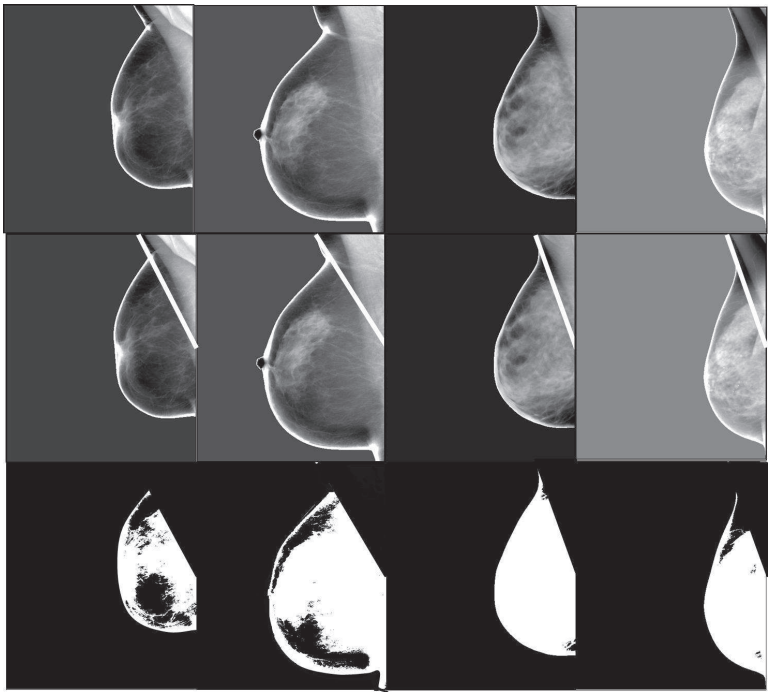

(b)

Figure 3.20: Examples of breast density maps (top row) and their corresponding exclusion maps (bottom row). a) CC b) MLO. The black areas of the exclusion maps are excluded from the VBD_{MX} computation. On the middle row of the MLO images the diagonal bars indicate the pectoral muscle delineation.

Chapter 4

New validation of the breast density computation

An adjusted version of this chapter was published as peer reviewed article: N. Geeraert, R. Klausz, L. Cockmartin, S. Muller, H. Bosmans and I. Bloch. Comparison of volumetric breast density estimations from mammography and thorax CT. *Physics in Medicine and Biology.*, 59: 4391-4409, 2014 [57].

4.1 CT versus mammography

Two methods for the computation of volumetric breast density are developed and compared, one from digital mammographic images (VBD_{MX} as described in Chapter 3) and one from thorax CT images (VBD_{CT}). VBD_{MX} is computed by applying a conversion function to the pixel values in the mammographic images, based on models determined from images of breast equivalent material. VBD_{CT} is computed from the average Hounsfield Unit (HU) over the manually delineated breast volume in the CT images. This average HU is then compared to the HU of adipose and fibroglandular tissues from patient images and phantom images. We collected images from patients who had a thorax CT and a mammography screening examination within the same year. The comparison study is described in this chapter.

4.2 VBD computation in CT

4.2.1 Theoretical derivation

The VBD was obtained from CT images (VBD_{CT}) for comparison with the VBD_{MX} from mammographic images. The voxel values in CT images are defined by:

$$HU_x = \frac{\mu_x - \mu_{water}}{\mu_{water}} \times 1000 \tag{4.1}$$

We can write VBD_{CT}, as in Equation 3.2 [47], as:

$$\begin{aligned} VBD_{CT} &= \frac{\mu_x - \mu_A}{\mu_G - \mu_A} \\ &= \frac{HU_X - HU_A}{HU_G - HU_A} \end{aligned} \tag{4.2}$$

and

$$HU_X = (HU_G - HU_A) \cdot VBD_{CT} + HU_A \tag{4.3}$$

with HU_X, HU_A and HU_G the average HU, the HU of the adipose tissue and the HU of the fibroglandular tissue, respectively [59]. Equation 4.2 can be applied per voxel, but can as well be applied to a larger volume such as the entire breast, where HU_X is the average HU over the entire volume, so only the breast and not the detailed glandular structure has to be segmented in the CT images (see Figure 4.1).

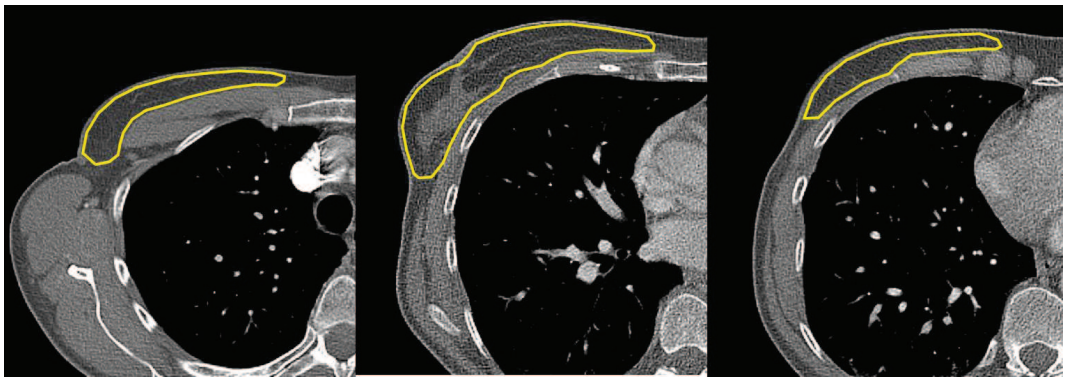

Figure 4.1: Delineation of the CT images. An upper slice (left), middle slice (middle) and lower slice (right) are presented with the delineation of the breast, determining the volume of the breast. The average HU is computed in the delineated part. In each case the skin is excluded.

As for mammography, the CT measurement method relies on the knowledge of the reference materials, adipose and fibroglandular tissues, for which the HU values must be determined in the same conditions as for the clinical images. Therefore we identified regions in the breast of the patient images that showed up as purely adipose or purely fibroglandular tissue. Ten adipose and ten fibroglandular regions were manually identified in ten patients (see Figure 4.2). HU_A and HU_G were fixed to the average HU of these regions. We applied the computation of VBD_{CT} to the database of breast images described

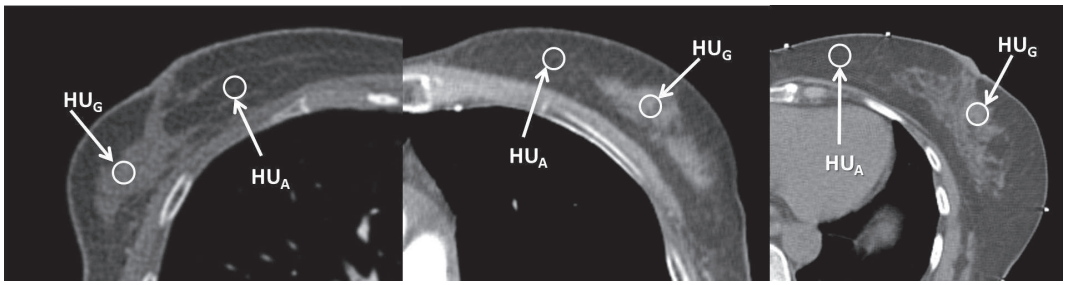

Figure 4.2: Regions of purely adipose and purely fibroglandular tissues were selected in patients images. HU_A and HU_G were set to the average HU of the regions.

in Section 4.2.2. The breast was delineated manually slice per slice for the CT acquisitions (see Figure 4.1). The skin was excluded from the volume. The pectoral muscle was taken as the chest wall border of the breast.

4.2.2 Database of mammographic and CT images

We built two databases for the validation of the VBD_{MX} computation, containing both mammographic images and CT images. All patient images were acquired for medical reasons, and no extra exams were required only for this study (Trial ID NTR3357 at *Nederlands Trial Register* according to the declaration of Helsinki, 2008). All images were collected in the two hospitals where the VBD_{MX} model was calibrated: hosp_L (database 1) and hosp_J (database 2). The databases consist of patients who underwent a standard screening mammography and a thorax CT within the same year. We generally collected one CT series and four mammographic images per patient: one CC and one MLO mammographic image for each breast. However for some CT series one breast was not fully present in the field of view (FOV) or some patients had a mastectomy, and not all patients had two mammographic images per breast. Therefore we do not always have four mammographic images per CT exam. The description of both databases is given in Table 4.1.

	Database 1	Database 2
Type of images	MX + CT	MX + CT
# of MX images	50	103
# of breasts	40	47
# of CT exams	25	27
Hospital	hosp_L	hosp_J
MX system	Siemens Inspiration	GE Senographe Essential
CT system	Siemens Sensation 64	Siemens SOMATOM Definition Flash and Definition AS
CT tube potential	120 kV	120 kV
CT slice thickness	5 mm	3 mm (22 cases), 5 mm (5 cases)
CT pixel size range	$0.63\times0.63\text{mm}^2$ to $0.89\times0.89\text{mm}^2$	$0.43\times0.43\text{mm}^2$ to $0.98\times0.98\text{mm}^2$

Table 4.1: Overview of the databases used for the computation of VBD_{MX} and VBD_{CT}.

4.3 VBD_{CT} versus VBD_{MX}

4.3.1 Calibration of the CT method

Sufficiently large homogeneous regions of both tissues could be found in the thorax CT images except for one patient for adipose tissue and two patients for fibroglandular tissue. The HU_A and HU_G values averaged over ten patients were found to be -109 and +13, with standard deviations 9.1 and 11.9 respectively.

	Our dataset		Vendantham
	$hosp_L$	$hosp_J$	et al. [146]
Mean	0.18	0.10	0.17
Minimum	0	-0.02	0.01
Median	0.14	0.07	0.14
Maximum	0.51	0.63	0.72
First quartile	0.02	0.03	0.07
Third quartile	0.33	0.12	0.24

Table 4.2: Distribution characteristics of the VBD_{CT} in comparison with the volumetric glandular fraction (VGF), published by Vedantham et al. [146].

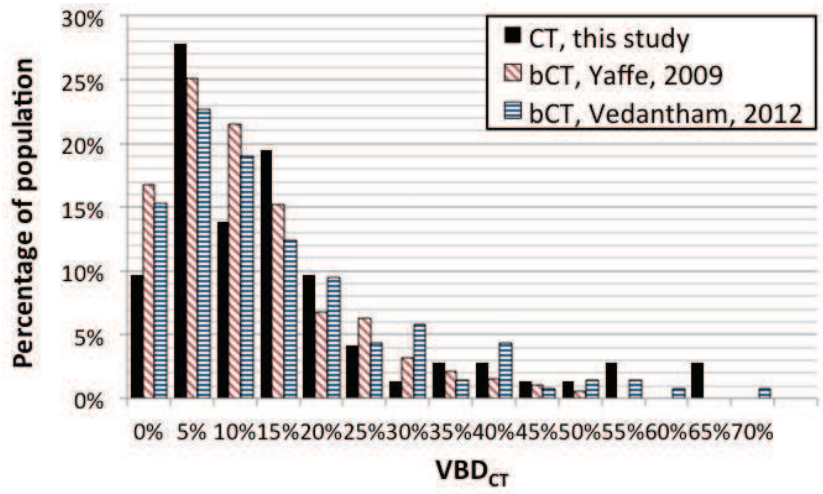

Figure 4.3: Distribution of VBD from CT measurements (our data) and breast CT (Yaffe et al. [156] and Vedantham et al. [146]), all excluding the skin.

4.3.2 VBD$_{CT}$ for the databases

We have compared our VBD_{CT} data to the results of volumetric glandular fraction (VGF) published by Vedantham et al. [146]. The characteristics of the distributions (see Table 4.2) are in good agreement, despite the small number of cases (25 for hosp$_L$ and 27 for hosp$_J$ versus 150 for Vedantham et al.). The distribution of our measurements is compared to the distributions published by Yaffe et al. [156] and Vedantham et al. [146] in Figure 4.3, all excluding the skin. The correlations between left and right breasts for VBD_{CT} are shown in Figure 4.4. The good correlation coefficients and the slope of the graphs close to 1 confirm the confidence in the method.

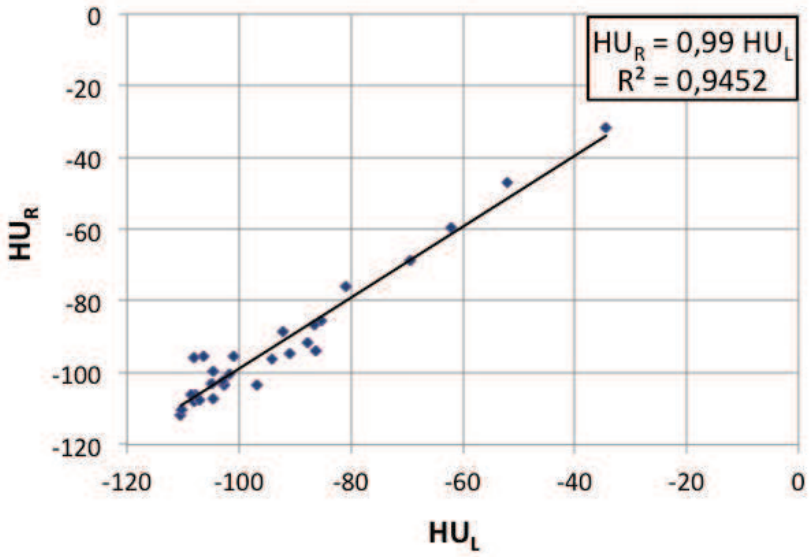

Figure 4.4: Correlation between left and right VBD_{CT} for the images of Database 2 and Database 3.

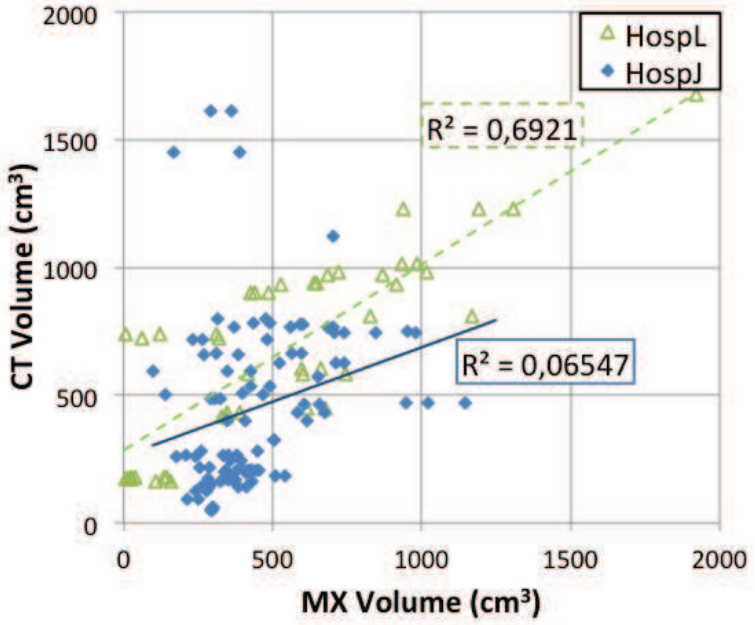

Figure 4.5: Volumes of the breast in mammographic images compared to the volumes of the same breast measured in CT images.

4.3.3 Correlation between VBD_{CT} and VBD_{MX}

We checked first how good the correlation is of the volume obtained from the mammographic images compared to the volume obtained from the delineated thorax CT images (Figure 4.5). The correlation could be improved, but we have good reasons to believe that a volume match is not critical to find a VBD correlation [14]. We thus plotted the correlation of the

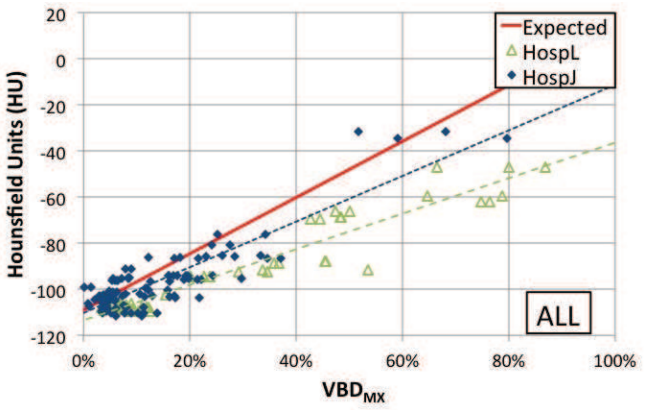

(a)

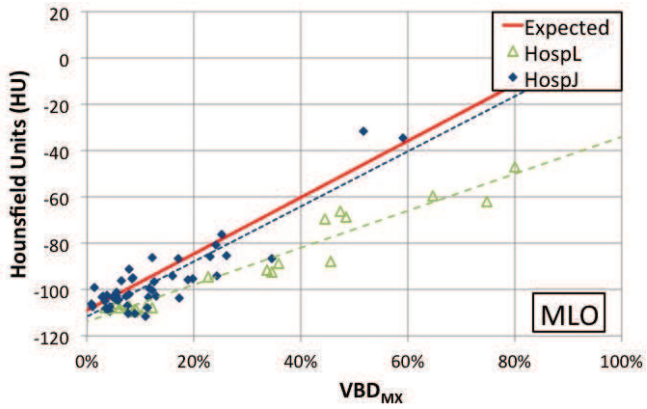

(b)

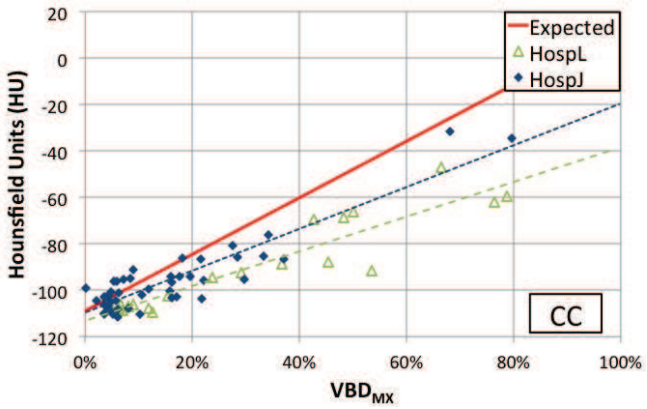

(c)

Figure 4.6: The average HU over the breast volume in thorax CT plotted versus VBD_{MX}. Each dot represents a breast for which the average HU is available (databases 2 and 3) together with a VBD_{MX} estimation. They are represented separately for the two hospitals, with the corresponding linear regressions. The solid line represents the expected HU based on Equation 4.3 and calibration values of HU_A and HU_G. a) grouped CC and MLO mammographic images, b) MLO mammographic images only, c) CC mammographic images only.

VBD_{MX} with HU in Figure 4.6, with the characteristics summarized in Table 4.3. Each dot of the graph represents a mammographic image, with on the x-axis the VBD_{MX} and on the y-axis the average HU of the corresponding breast delineated in the CT images. A linear regression is applied to the points of both databases 2 and 3 separately. The solid line represents the expected HU on the y-axis based on Equation 4.3 and the values of HU_A and HU_G measured in the thorax CT images for the given VBD on the x-axis. Figure 4.6(b) and Figure 4.6(c) show separately the MLO images, respectively the CC images. It can be seen that the linear regression in database 3 is in closer agreement with the expected curve than the linear regression in database 2, and that the linear regression on the MLO images of database 3 is in closer agreement with the expected curve than the linear regression on the CC images. The error for a point is computed as the shortest distance of the point to the expected curve. The value of Δ_1 is the average of the errors for all points per database. Table 4.3 gives an overview of the slopes, intercepts, correlation coefficients R^2 and Δ_1 for the calibration and the least square fits.

	Slope	Intercept	R^2	Δ_1
Expected curve	122	- 109	-	-
hosp_L (ALL)	77	- 113	0.91	10%
hosp_J (ALL)	99	- 110	0.78	4%
hosp_L (MLO)	80	- 113	0.93	10%
hosp_J (MLO)	119	- 112	0.80	3%
hosp_L (CC)	75	-113	0.86	10%
hosp_J (CC)	90	-110	0.83	5%

Table 4.3: Characteristics of the graphs presented in Figure 4.6.

4.4 Same breast, same VBD

The slope of the trend line for the hosp_L images in Figure 4.6 is different from the one for the hosp_J images. The trend line for the MLO images of hosp_J (Figure 4.6(b)) is in closer agreement with the expected curve than for the CC images (Figure 4.6(c)). For hosp_L there is no difference between the graphs of the MLO and CC images. There are several limitations that can cause these deviations. First of all, the CT images were delineated manually by two different physicists, which can cause a systematic bias due to a different interpretation of breast limits. Secondly, the mammographic images were acquired by two different teams of radiographers on different equipments. Due to different positioning techniques, this can cause a systematic difference in the imaged volumes between CC and MLO images. This implies a possible and different mismatch between the volumes of the breast represented in the mammographic images and the volumes delineated in the CT images (Figure 4.5). Systematic differences in positioning do not affect the correlation, but only the slope and intercept of the least square fits. Missing adipose tissue (as in CC images) in a mammographic image would increase the measured VBD_{MX} and decrease the slope of the least square curve in Figure 4.6. In CT, it was difficult to accurately

determine the limits of the breast in each slice as well as the first and last slices of series containing breast tissue.
We compared the results in Figure 4.6 to the results of the correlation between the Volpara® software and MR (Figure 2 in [75]). The range of values in their cloud of data points at 25% VBD_{MX} was between 17% and 40% VBD_{MR}. For our method, we found a range between 4% and 32% VBD_{CT}. This suggests that the comparison between VBD_{MX} and a 3D imaging method as VBD_{CT} or VBD_{MR} is limited by comparable problems.
This opens the question of the determination of the "true" breast volume and as a consequence the overall volumetric breast density. Anatomically however the limits of the breast as an organ are not clear. Radiologists tend to consider the content of the mammographic images as setting the breast limits, even if different in CC and MLO views. This problem emphasizes the limitations of the volumetric breast density as a quantitative risk factor.
We must keep in mind that the concept of breast density was originally introduced based on the appearance of film images, including the texture of the tissue [152]. The same breast density concept was used in most studies on associated risk, and formalized in the standardized reporting method [108]. It might therefore be completed with for example the absolute volume of the glandular tissue, or the texture in the unprocessed image as was explored by several groups [28, 80, 122]. For these analyses and characterisation of risk factors, quantitative images calibrated to local VBD values [54, 76] can be very useful.

With this study we demonstrated the possibility of validating VBD_{MX} computation methods by correlating them with VBD values from routine thorax CT exams. Therefore we have built a database of mammographic images of breasts for which corresponding CT series were available and showed a good correlation of the VBD_{MX}, computed with a state of the art method, to the HU measured in CT images. The correlation between the VBD computed from mammography and the VBD computed from 3D-imaging as CT, as shown in this study, shows the possibility to compute a volumetric quantity representing the dense tissue in the breast. Its 2D distribution could possibly be used for texture analysis or dose applications.

Discussion on Part I

The computation of the volumetric breast density (VBD) for digital projection mammography images is already well developed, with several academic groups having developed their own version [10, 103, 115, 143] and two commercially available products [69, 75]. However when comparing different methods for the same patients, the VBD results are not the same for all methods [147] although all methods had been validated with MRI. Our validation method with thorax CT images could be better adapted to validate new methods, thanks to the availability of a large amount of data and the nature of measured quantities (X-ray attenuation) common to both mammography and thorax CT. However also with this method some issues remain to be solved, in particular improving and standardizing the HU response versus tissue composition or mono-energetic attenuation coefficient. This is needed before thorax CT could be used as a general validation tool for VBD computations. Finally, the minimum amount of required calibration per type of equipment and per unit should be determined. The currently available products compute VBD relative to a type of equipment, with no consideration of possible deviations. It could be more practical that the density measurements (local and VBD) are integrated into the mammographic equipment, with the corresponding checks and calibrations added to the current QC.

Breast density remains an ambiguous concept. Currently it is highly visible, included in the media and among the women, following the *are you dense* movement [2] and the legal requirement made to physicians to inform woman if they have "dense breasts". A recent study demonstrated this perception by analyzing statistics obtained from "Google searches" [46]. The major concern does not reside in a subtle measurement of breast density, but in a binary classification dense/not dense probably justified by the fear of the masking effect. The sensitivity of mammography is inferior for dense breasts, which justifies further examinations (ultrasonography in particular) of dense breasts. This statement was mostly established for film/screen mammography and may not be true anymore for digital mammography. In addition, the emergence and generalization of digital breast tomosynthesis may probably change significantly this statement.
If we consider more in detail the different applications of breast density assessment, it started with the finding of a correlation between quantity and shape of dense tissue in mammographic films with the risk of developing cancer [135, 152]. The masking effect was also recognized early. In this last case it is not important to make a distinction between real glandular tissue and fibrous tissue since they produce comparable images. More recently, better metrics of the parenchymal pattern, capable of designating specified pathologies for the same VBD, were introduced [88, 89, 148], as well as large studies [77, 129, 142] designed to understand the link between breast cancer and breast density which should give more indications on how to improve the decision mechanisms for adaptive or individualized

screening.
However, concerning radiation risk, not all attenuating tissues, fibrous glandular (Cooper ligaments) and glandular have the same susceptibility to develop cancers, even if they contribute comparably to the VBD.

Another possible application is the optimization of the technique factors for each image. On the most advanced mammographic equipment not only the current-time product is adjusted automatically, but also the X-ray beam quality (anode track, filter, high voltage) as a function of the X-ray attenuation properties of the breast, measured during a short exposure preceding the main exposure. The idea of using an automatic exposure control based on this principle was described in [131]. However, for a full optimization the risk must also be evaluated. When this type of optimized AEC was first introduced, the AGD was chosen and the risk evaluated collectively using the average AGD to the population [92].
In the next part we propose the glandular imparted energy correlating with individual radiation risk taking into account the actual glandular amount and distribution of the particular patient. The only limitation resides in the fact that a digital breast tomosynthesis examination is required to obtain these characteristics of the patient breast. Since the mammographic screening examination is repeated periodically, instead of using a pre-exposure image, it is possible to use the information gathered during the previous examination, as described in [91].

Part II

BREAST DOSIMETRY

Chapter 5

Validation of the Monte-Carlo simulation tool CatDose

In the second part of this work we investigate the quantitative evaluation of irradiation (dosimetry) in X-ray mammography. We investigate the imparted energy in breast tomosynthesis through computer simulations. In this chapter we shortly present our simulation tool, CatDose, developed by GE and validate it for the functions that we want to use it for, namely to compute the imparted energy.

5.1 Monte-Carlo simulations

As described in Section 1.2.3, most dose estimation methods are based on Monte-Carlo simulations. Monte-Carlo simulations were introduced by Metropolis and Ulam [110] to "study differential equations, or more generally, integro-differential equations that occur in various branches of the natural sciences", based on statistical mechanics where "properties of sets of particles" are studied instead of individual particles. In radiation physics the stochastic nature of one interaction of a particle with its environment unit is well known. These laws are implemented in the Monte-Carlo code we used and multiple particles are simulated on multiple environment units to predict the outcome of the interaction of a large number of particles with an object, a task that is impossible by analytical computation. In X-ray imaging we are not interested in the path of a single photon but in the quantity of energy absorbed by an object and the energy crossing the object and contributing to the image. Monte-Carlo simulations are thus an appropriate tool. Simulations are an easier alternative for complex real experiments and allow a better control of the input parameters.

We used CatSim, an internal GE X-ray simulation platform software, to perform our simulations. Catsim stands for "Computer Assisted Tomography SIMulator". It was developed originally by S. Basu, B. De Man and J. Pack to simulate 3rd generation CT projections for analytical phantoms at GE Global Research Center (Niskayuna, NY, US) [104]. Since then, CatSim evolved through multiple collaborations and projects. A more complete description and most recent developments of CatSim are provided in [45]. The different elements of the imaging chain and the physical interactions are implemented as modular functions. The photoelectric effect, Compton effect and Rayleigh effect are adopted from Geant4 [3]. The settings were adapted to the mammography configuration,

as well as the spectra and detector technology [45]. We used CatSim to compute projection images in tomosynthesis. We defined the phantoms analytically and CatSim turned them into density volumes per material, defined in a separate file, in this work always with a resolution of $1\times1\times1$ mm^3. CatDose is a module in CatSim returning a volume with the imparted energy per voxel. Combining both gives the imparted energy per material.

In the next sections we propose and discuss several verification strategies to understand the strengths and limitations of the tool. We decided to verify the module of the simulation on which we are depending. Therefore we wanted to compute the half value layer (HVL) of the spectrum with the method of the TG 195 AAPM manual [127]. The HVL is the thickness of a plate of aluminum that is placed in the beam and that attenuates the beam intensity by half. It is an indication of the hardness of the spectrum and values are between 0.3 mm and 0.4 mm for the anode/filter-combination molybdenum/molybdenum [116]. Because of some technical problems this was not possible. Therefore we verified the conversion factors from air kerma to average glandular dose as described by several authors [24, 39, 154] and which are directly related to the attenuation of a spectrum in breast tissue. The measures are intended to verify that the code predicts correctly the physical phenomena known in this field.
The differences between accepted methods for the average glandular dose (AGD) computation of Dance et al. [41] and Wu et al. [154] goes up to 15% [43]. Therefore we proposed that an acceptance error level for results obtained with CatSim when compared to Dance's data is also 15%.

5.2 TG 195 AAPM manual

The task group 195 AAPM manual [127] of the American Association of Medical Physicists is the work of worldwide specialists of Monte-Carlo simulations. They recommend users of Monte-Carlo simulations in medical imaging to validate the simulation tools. The document includes complete set-up descriptions and their results with errors for the most used and commercially available tools. The report does not comment on the different commercially available code packages, but provides a "common reference for benchmarking Monte-Carlo simulations across a range of Monte-Carlo codes and simulation scenarios" and can serve as a self-teaching tool for starters in Monte-Carlo simulations. The manual was presented in March 2014 at the European Conference of Radiology (ECR).
In this manual, the computation of the HVL is described. Instead of measuring air kerma for different Al thicknesses, the authors measure the air kerma for the theoretical HVL, 0.3431 mm Al, and quarter value layer (QVL), 0.7663 mm Al, for Mo/Mo 30 kVp. The air kerma (K) in this case is computed as:

$$K = \int \psi(E) \times \frac{\mu_{en}}{\rho}(E)_{air} dE \tag{5.1}$$

with ψ the planar energy fluence and $\frac{\mu_{en}}{\rho}(E)_{air}$ the mass energy absorption coefficient of air at the given energy. The ratio of these air kermas with Al and without Al is then

computed for the theoretical HVL and QVL:

$$R_1 = \frac{K(t = HVL)}{K(t = 0)}$$
$$R_2 = \frac{K(t = QVL)}{K(t = 0)}$$

with t the thickness of the aluminum plate in the beam. The values for R_1 and R_2 are published in the TG 195 report, together with their errors for several available Monte-Carlo-platforms, so that it is possible to compare the results of new Monte-Carlo simulation tools. However CatDose allows us to compute the absorbed energy in volumes only. It is not possible to compute the energy fluence per energy bin without changing the source code, so this method could not be applied. Therefore we verified the tool by computing air kerma to dose conversion factors and by comparing them to already existent results [22,41].

5.3 Computation of dose conversion factors

5.3.1 Dance conversion factor

The set-up (see Figure 5.1) is taken from Dance et al. [38] and consisted in a 45 mm thick semi-circular cylinder with radius 80 mm of adipose tissue and inside a co-axial semi-circular cylinder with thickness 35 mm, radius 75 mm and 50% massic breast density (MBD), the ratio of the glandular mass divided by the total breast mass. The latter is called the intra-skin region, because Dance et al. [38] modeled the skin as 0.5 cm adipose tissue. The breast is compressed by a 2.7 mm polycarbonate compression paddle. We compared the conversion factors for the spectrum at Molybdenum-Molybdenum 28 kV, with a HVL of 0.3 mm Al.

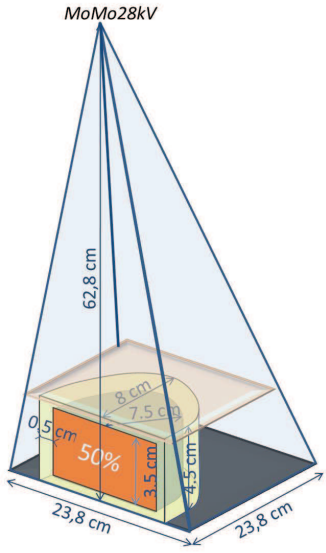

Figure 5.1: The set-up used in our measurements in accordance with the set-up of Dance et al. [41].

The conversion factors, converting air kerma into AGD, are taken from the paper of Dance [41] in the formula

$$AGD = K \times g \times c \times s \tag{5.2}$$

where K is the air kerma for the given spectrum at the entrance of the object [39], g is the general conversion factor, c is the density conversion factor and s the spectrum conversion factor.
Both g and c conversion factors were checked: the variation of the conversion factor as a function of the thickness for a density fixed at 50%, i.e. the g-factor, and the variation of the conversion factor as a function of density, i.e. the c-factor. The s conversion factor is not checked because in this work we only simulate the Molybdenum/Molybdenum anode/filter spectrum, for which the s-factor is equal to 1.
We follow the simulation set-up described by Dance et al. [39]. To obtain g the thickness of the phantom is changed, while keeping the thickness of the skin constant. The imparted energy to the intra-skin part is recorded for different phantom thicknesses between 2 and 10 cm. The results were expressed per air kerma, with the air kerma based on the results for the 4 cm phantom. Since we vary the thickness of the breast to derive the g conversion factor and knowing that the distance from the source to the breast support is constant in our simulation, the entrance air kerma changed inversely with the square of the distance to the entrance surface [39, 116].
For the dose D_x of a breast of x cm thickness, the g-factor is defined as

$$D_x = K_x \times g_x \times c_x \times s_x$$

with K_x the air kerma at the entrance surface of the breast. Since the simulations for the g-factor are performed for a phantom of 50% breast density with a beam of Molybdenum/Molybdenum both c_x and s_x are equal to 1. In our simulations we normalize the results by comparing the dose to the breast, D_x, to the air kerma obtained from the dose to the 4 cm breast D_4 and its conversion factor g_4 after distance correction:

$$\begin{aligned} D_x &= g_x \times K_x \\ D_x &= g_x \times K_4 \times (\frac{d_x}{d_4})^2 \\ D_x &= g_x \times \frac{D_4}{g_4} \times (\frac{d_x}{d_4})^2 \\ g_x &= \frac{D_x \times g_4 \times d_4^2}{D_4 \times d_x^2} \end{aligned} \tag{5.3}$$

with d_x and d_4 the distances between the source and the entrance surface of the phantom of x cm and 4 cm respectively.
The density dependence of the conversion factors is represented by the c-factor. In the simulation set-up the density was changed between 0.1% and 100%, by steps of 25% and smaller for low densities, while the breast thickness was maintained at 4.5 cm and the intra-skin thickness at 3.5 cm. As indicated by Boone [23] the percentage of the total energy imparted to the gland should be weighted per interaction and not on the total imparted energy, because the weighting factor changes with energy.

The g-factor is given in Figure 5.2. The results of the CatDose simulations are within 5% of the g-factors of Dance et al. [39] for breast thicknesses below 9 cm. The average difference is 0.4%. For 9 and 10 cm the differences are 6% and 7% respectively. CatDose finds the expected results within the preset limits of 15%, and therefore we can use it.

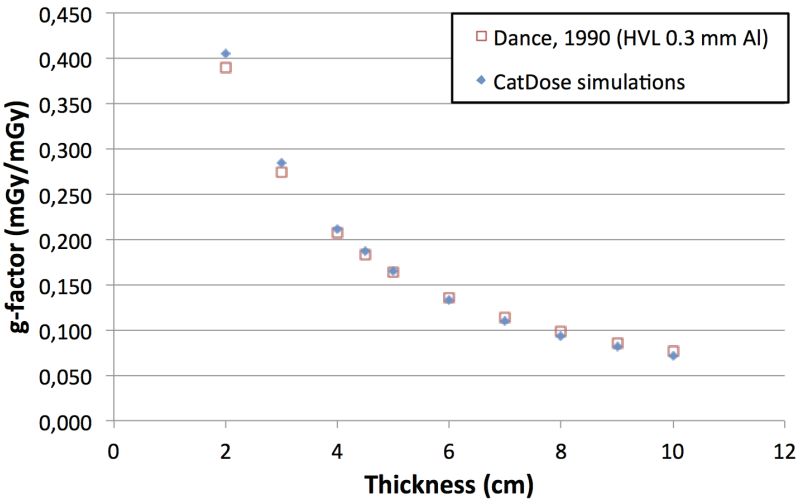

Figure 5.2: The g-factor, the conversion factor for the air kerma to dose for the "average" breast normalized to the 4 cm breast conversion factor. The results of the CatDose platform are compared to the published values in Dance [41].

The c-factors computed from the simulations are presented in Figure 5.3. As for the c-factor in Dance [41] the simulations are normalized to the simulations at 50%. The difference between the CatDose simulations and the reported values by Dance stay below 1%. This deviation can be neglected for dosimetric applications and therefore CatDose was considered to be appropriate. Also for different densities we can trust the obtained results.

5.3.2 Boone conversion factors

The conversion factors as presented in the paper of Boone et al. [22] are based on the set-up of Wu et al. [153] (see Figure 5.4). The breast is also represented by a 4.5 cm semi-cylinder of adipose tissue, but this time the intra-skin part is 3.7 cm of glandular tissue, resulting in an adipose "skin" of two times 4 mm. There is only one conversion factor called normalized glandular dose, D_{gN}, with one HVL for a given tube potential. We compared the D_{gN} for the Mo/Mo 28 kV spectrum (HVL = 0.328 mm Al). Boone et al. [22] normalized the results to "the number of photons corresponding to 1 Rontgen (R) for the entire spectrum".

In Figure 5.5 our simulations are compared to the D_{gN} of Boone [22]. The D_{gN} are normalized to the simulation at 4 cm. The difference between the results of the CatDose simulations and the D_{gN} of Boone is lower than 6% for all thicknesses. These errors are within the acceptance limit for the errors of the simulations and we can therefore use CatDose for new simulations.

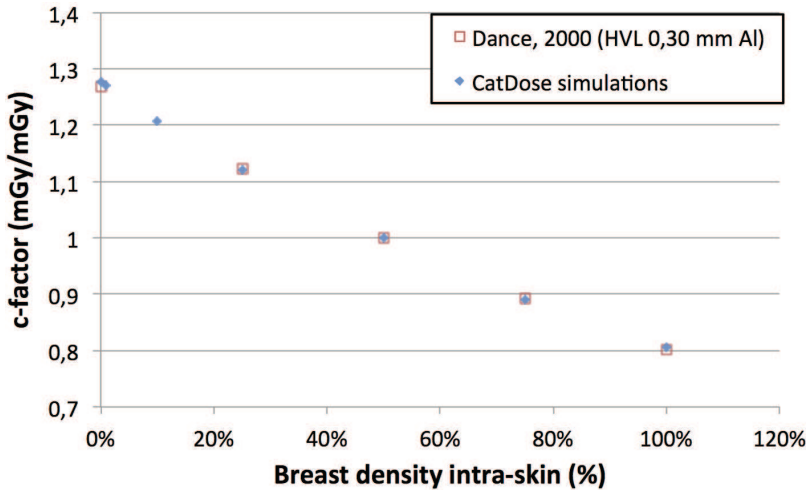

Figure 5.3: The c-factor, the conversion factor for the breast as a function of density normalized to the 4 cm breast conversion factor. The results of the CatDose platform are compared to the published values in Dance [41].

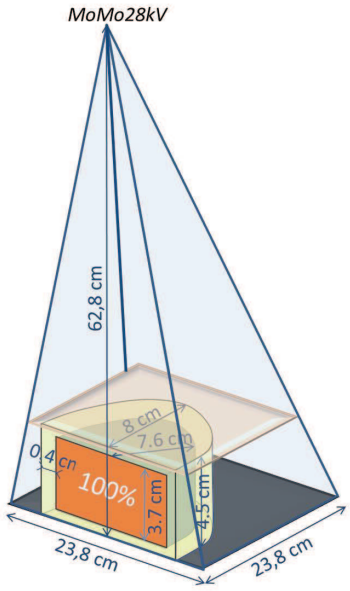

Figure 5.4: The set-up used in our measurements in accordance with the set-up in Boone et al. [22].

5.4 Limits and strengths

In this chapter, we verified the simulation tool CatDose for the computation of imparted energy per entrance air kerma. Although we need good relative values (precision), the simulations must be calibrated to a real system (accuracy), which is not our current issue. The computed conversion factors for breast tissue were in good agreement with publications [23, 39, 41] and would allow AGD calculations for typical breasts (see Appendix A).

We will use CatDose for a proof of concept of the computation of the glandular imparted energy, where we want to highlight orders of magnitude. The air kerma is difficult to determine accurately from the simulations, because of the low absorption in air. For our simulations we will compute the air kerma indirectly using the results of Dance et al. [41], i.e. deduce it from the AGD and the conversion factors.

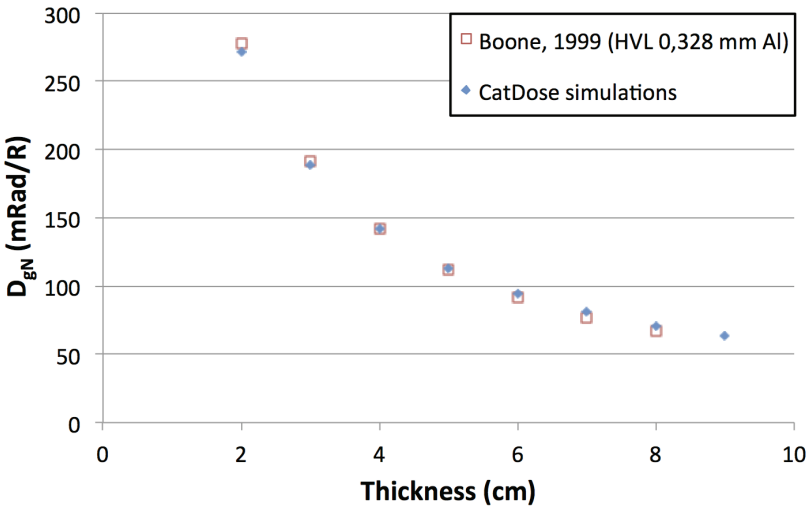

Figure 5.5: D_{gN} factors, the conversion factor of the air kerma to dose for the set-up described by Boone [22]. Simulations of CatDose are compared to the D_{gN} factors of Boone [22].

Chapter 6

Evaluation of irradiation in mammography

Different parts of this chapter were published at three conferences, with one peer reviewed article.

- Section 6.1: N. Geeraert, R. Klausz, S. Muller, I. Bloch, and H. Bosmans. Breast characteristics and dosimetric data in X-ray mammography - a large sample survey. *International Conference on Radiation Protection in Medicine - Setting the Scene for the Next Decade* Volume CN-192, page 15, Bonn, Germany, December 2012 [60].
- Section 6.2 and 6.3: N. Geeraert, R. Klausz, L. Desponds, S. Muller, I. Bloch, and H. Bosmans. Impact of breast glandular description on average glandular dose and radiation risk assessment in mammography. *Radiological Society of North America (RSNA) - Annual meeting* 2013 [58].
- Section 6.5: N. Geeraert, R. Klausz, S. Muller, I. Bloch, and H. Bosmans. Evaluation of exposure in mammography: Limitations of average glandular dose and proposal of a new quantity. *Radiation Protection Dosimetry, Special issue* In press, 2014 [61].

This chapter gives an overview of the current status of dosimetry for the population and for individuals (Section 6.1). Then the strengths and limitations of today's dosimetry are shown (Sections 6.2 and 6.3), and we propose the measures we want to add to dosimetry (Section 6.5). Finally we show how the proposed measures can be computed.

6.1 Dosimetry for individuals

Film-screen mammographic units did not provide information on delivered dose directly. Statistics have been performed by massive data collection at the price of a heavy work load [157]. With the introduction of digital mammography systems, it became easier to acquire and collect automatically large amounts of data worldwide. In our paper presented at the IAEA conference in Bonn [60] we studied the distribution of the AGD, together with the distribution of the peak breast density (PBD) computed by the equipment as a function of the compressed breast thickness, for populations from different continents. We then computed the difference between the average glandular dose (AGD) using the patient's PBD and using the population-averaged density from the method of Dance et

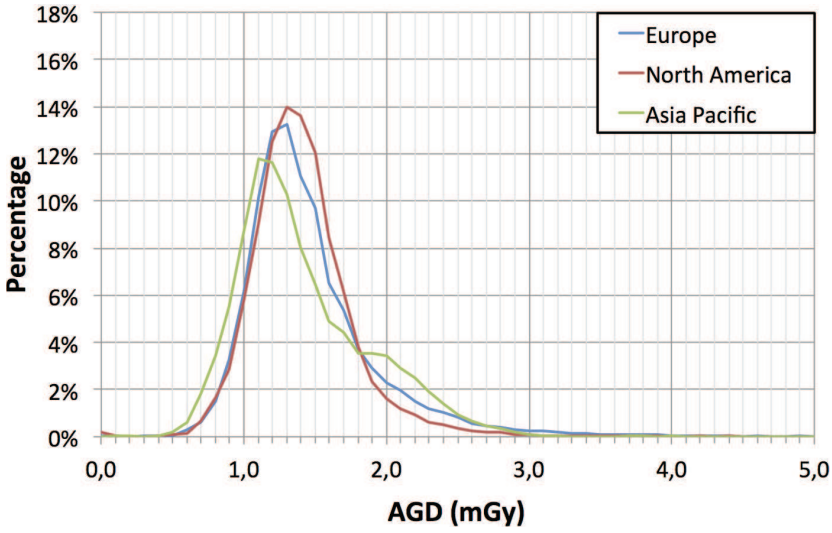

Figure 6.1: AGD distributions for the different geographical zones [60].

al. [41] for all individual exposures. We obtained the technical data and image parameters from acquisitions on Senographe DS (FOV:19×23 cm^2) and Essential (FOV: 24×31 cm^2 and 19×23 cm^2) (GE Healthcare, Chalfont, UK). The systems computed the AGD by applying the method of Wu et al. [154] with the values of D_{gN} interpolated from the published tables using the PBD as the breast glandular fraction.

The distribution of the dose per image per geographic zone computed from all the systems is presented in Figure 6.1. The median dose values found are 1.4 mGy (Europe and North-America) and 1.3 mGy (Asia-Pacific). The secondary peak around 2 mGy in the dose distribution of the Asian-Pacific population can be explained by the higher proportion of exposures taken using the contrast mode (AOP CNT, 34.30% versus 2.10% and 4.10% for Europe and North-America respectively). The histogram of compressed breast thickness as a function of PBD is shown in Figure 6.2 for the different populations with the distributions used by Dance [41] plotted on top of them (dotted line: 40-49 years, full line: 50-64 years). Negative PBD values were due to errors on the compressed breast thickness, to which the density computation used by the systems is sensitive [48] (see Section 3.3.1). The statistics on the differences in AGD, computed with the method of Dance et al. [41] or the individual PBD, are presented in Table 6.1. The average AGD over the population, computed with the PBD, was slightly higher than when using the 40-49 years population-averaged correction factor (up to 4.4%) and slightly lower than when using the 50-64 years population-averaged correction factor (up to 4.8%). For 68% of the population the difference between the dose computed by the system and the dose computed with the individual PBD is less than 10%. For 99.7% it is less than 30% (when using the 40-49 years curve) and 23% (when using the 50-64 years curve).

From these data we can say that the population-averaged correction factor is fully applicable for collective dose evaluation. However the density correction factor is not convincing for individual dose assessment. Also, in both cases, the breast density was estimated in a small area (automatic exposure control (AEC) sensor). Further improvement towards

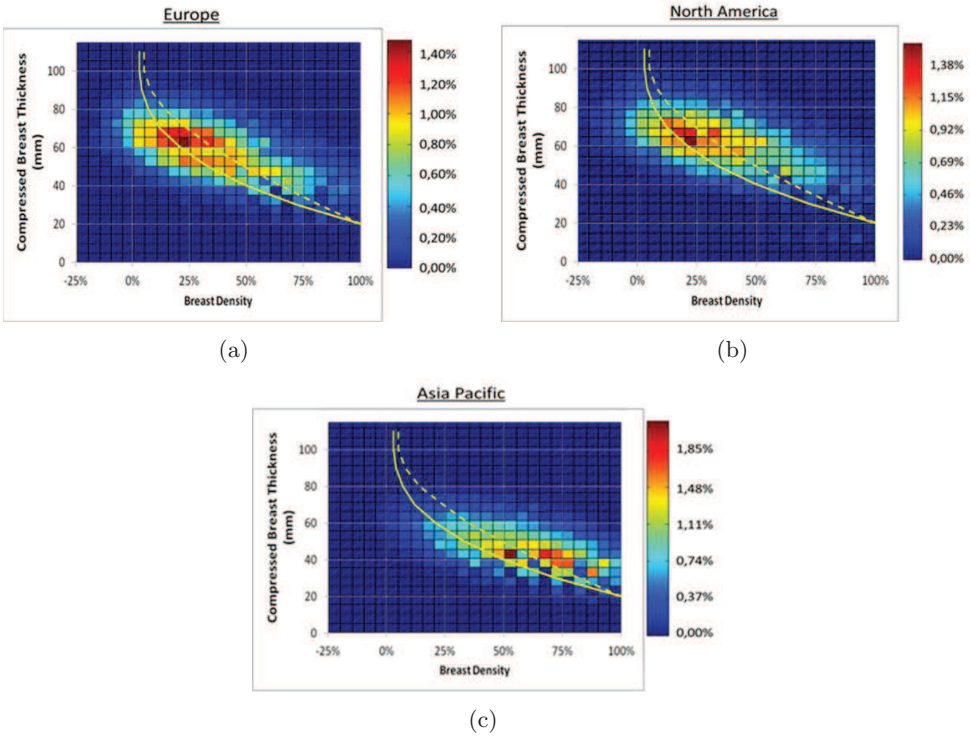

(a) (b)

(c)

Figure 6.2: Distributions of the PBD as a function of compressed breast thickness for different continents: a) Europe, b) North-America, c) Asia-Pacific. The distributions of the average PBD as a function of compressed breast thickness retained by Dance et al. [41] were plotted on top of our results (dotted line: 40-49 years, full line: 50-64 years) [60].

	40-49 years		
	Average error	Maximum error for 68% of the population (± St dev)	Maximum error for 99.7% of the population (± 3 St dev)
Europe	4.4%	11.0%	31.9%
North-America	3.3%	11.4%	30.8%
Asia-Pacific	1.1%	10.1%	26.6%
	50-64 years		
	Average error	Maximum error for 68% of the population (± St dev)	Maximum error for 99.7% of the population (± 3 St dev)
Europe	-2.1%	10.2%	23.6%
North-America	-3.0%	10.6%	23.6%
Asia-Pacific	-4.8%	9.7%	17.2%

Table 6.1: The differences between the AGD computations using the method by Dance et al. [41] with the PBD and with the population-averaged density as described by Dance et al.

patient specific dosimetry should come from a true estimation of volumetric breast density instead, and from measures appropriate for individual risk assessment.
This lack of individualization and even more important the lack of uniformity between

different computation methods of different vendors was also reported by Tromans et al. [140]. As reported by Tromans, patient specific estimates (i.e. based on individual breast density measurements) of AGD could be used to help standardize dose monitoring for patients undergoing routine screening on different X-ray systems, which meets the original goal of the AGD! However it should not be confused with patient-specific risk estimation. Therefore we propose some experiments on digital phantoms to evaluate the specific impact of the individual density evaluation and to find a good measure useful for risk estimation.

6.2 Use the right density

In order to understand the impact of using the different breast density quantities, ABD, PBD or VBD (see Figure 1.3), for the computation of the individual AGD, we set-up a study with two virtual phantoms. The first phantom (Phantom 6.3(a)), originally defined by IPSM [112] and systematically used by Dance et al. [39], is a semi-cylinder of 4.5 cm thickness with 8 cm radius. It is composed of a 50:50 mixture by weight adipose and glandular tissues and an outer shield region of adipose tissue of 0.5 cm thick mimicking the skin on all sides except the planar chest-wall side (see Figure 6.3(a)). As a consequence, Phantom 6.3(a) has an ABD of 88%, a PBD of 39% and a VBD of 34% including the skin layer. The second phantom (Phantom 6.3(b)) has the same shape (8 cm radius, 4.5 cm thick), but the inner region composition is raised to 59% glandular tissue and restricted to 75 cm^2 and 3.5 cm thick (see Figure 6.3(b)). Phantom 6.3(b) has an ABD of 75%, a PBD of 46% and a VBD of 34% including the skin layer. We want to compare the AGD values

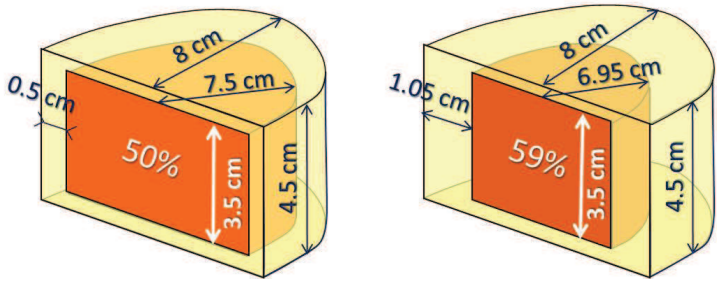

(a) (b)

Figure 6.3: Virtual phantoms: a) the regular phantom described by Dance et al. [39], b) a phantom designed to evaluate the impact of using different breast densities for the AGD computation.

computed using the different breast densities for a standard exposure: Rhodium/Rhodium target/filter, 29 kV tube potential, 0.45 mm Al HVL, and the mAs resulting in an AGD of 1 mGy for Phantom 6.3(a).
For Phantom 6.3(b) with a denser but smaller region of glandular tissue, the AGD differs according to the quantity chosen to determine the breast composition-specific c-factor. The values are listed in Table 6.2. The results show that between the different breast densities for the same phantom, there is a difference up to 18%. It is therefore mandatory to specify the proper breast density to be used following the proposed method. For the method of Dance et al. [41], the right density is the VBD excluding the skin.

6.3 New quantity used for individualized risk

In general, it is widely accepted that the radiation risk is proportional to the dose (Linear non Threshold, LNT). However, the Internationl Commission on Radiological Protection, ICRP 103 [81] explicitly states that "in radiation protection the risk is assumed to be proportional to the dose only at the population level". In our search for a measure compatible with individual risk assessment, we should not use anymore the average dose to a standard organ, since it has been recommended to evaluate the nominal risk coefficients to be applied to whole populations and not to individuals [81].
The LNT-model is based upon fundamental cellular processes coupled with dose-response data [81]. Recently, attempts have been made by Colin et al. [34] to evaluate the risk at the cellular level by measuring the effects on DNA of irradiated breast cells from breast biopsies in healthy tissue followed by in vitro radiobiological analyses. However it is neither in the scope of our work to consider the relation between the physical quantity and the biological harm, nor the possibly important variations in individual sensitivities [52, 53]. Our goal is to identify a physical quantity that can be used as input to the evaluation of the individual radiation-related risk. The *true organ* breast tissue is the fibroglandular tissue which is a tissue with a complex shape undergoing a non-uniform irradiation, thus radiation measures must take into account the amount and distribution of individual glandular tissue. Considering the dose to an individual glandular cell as the basic quantity, and supposing that all glandular cells remain independent and have an equal mass ($\mathrm{d}m$) and a location (x, y, z), the total risk (R) is proportional to the integral of the dose (D) to individual glandular cells over the complete organ ($Gland$), i.e. the risk is proportional to the total imparted energy (E) to the gland:

$$\begin{aligned} R &\propto \int_{Gland} D_{xyz}\mathrm{d}m \\ R &\propto \int_{Gland} \frac{\mathrm{d}E_{xyz}}{\mathrm{d}m}\mathrm{d}m \\ R &\propto \int_{Gland} \mathrm{d}E_{xyz} \end{aligned} \tag{6.1}$$

Using "total energy absorbed in glandular tissue as the most relevant indicator of risk in mammography" was originally proposed by Hammerstein et al. [66]. We will select the quantities allowing to estimate the individual risk and taking into account the amount and

Breast density	AGD from Dance tables [41]
ABD	0.9 mGy
PBD	1.03 mGy
VBD	1.08 mGy

Table 6.2: AGD computed for Phantom 6.3(b), using different breast densities. The air kerma is such that the AGD is 1 mGy for the Dance phantom (Phantom 6.3(a)).

distribution of individual glandular tissue. We will compute the regularly accepted AGD and two other quantities to evaluate their dependence on the amount and distribution of the glandular tissue evaluated for five virtual phantoms.

Quantities We computed three physical quantities: average glandular dose (AGD), individualized average glandular dose (iAGD) and glandular imparted energy (GIE).
AGD is used as the organ dose for collective risk evaluation. Using the method proposed by Dance et al. [41], the AGD is obtained by computing the product of the air kerma and the three conversion factors: one for the phantom thickness, one for the density, and one for the spectrum. The phantom thickness and the spectrum are the same for all phantoms and exposures in our experiment. The density to be used in the Dance tables is the massic breast density (MBD) in the central, intra-skin compartment. For the phantoms the intra-skin density was defined to be always 50% glandular - 50% adipose tissue by volume. The conversion from VBD to MBD can be computed using

$$MBD = \frac{\rho_G}{(1 - VBD)\rho_A + \rho_G VBD} \times VBD \tag{6.2}$$

with ρ_A=0.93 g/cm^3 and ρ_G=1.04 g/cm^3 the volumetric mass densities of adipose and fibroglandular tissues from Hammerstein et al. [66]. The resulting density to be used for the AGD computations is 53%.
To take into account the amount and distribution of glandular tissue, AGD was individualized (iAGD) by using phantom specific data for the computation of the AGD, i.e. by computing the imparted energy in the glandular tissue for the specific case, then dividing it by its glandular mass. If the glandular tissue is distributed over the entire breast, the iAGD remains consistent with the ICRP concept of mean value of absorbed dose averaged over the tissue.
As already proposed before (Equation 6.1) the third quantity is the total energy imparted to the glandular tissue, GIE. As GIE is the total energy imparted to the glandular tissue, it is expressed in joules (J). To facilitate computations, the GIE is normalized to the incident air kerma, to which GIE is proportional, and is then expressed in milli-joules per milli-gray (mJ/mGy).

Phantoms Simulations of exposures were performed for five semi-circular phantoms. The first phantom is again Phantom 6.3(a) designed by Dance et al. [39] as presented in Figure 6.3(a), taken as a reference. The second phantom (Phantom 6.4(a)) differs from the first by its radius of 5.8 cm. Taking into account the 0.5 cm adipose skin layer, the amount of the glandular tissue and its projected area are therefore divided by two compared to the Dance phantom. Phantoms 6.4(b), 6.4(c) and 6.4(d) have the same size and shape as Phantom 6.3(a) (8 cm radius, 4.5 cm thickness), and contain the same amount of glandular tissue (0.151 kg), but with a different distribution. All the glandular tissue is gathered into a homogeneous 1.75 cm plate of 100% glandular tissue, positioned at mid breast height for Phantom 6.4(b), in the upper part just below the skin layer for Phantom 6.4(c) and in the lower part just above the skin layer for Phantom 6.4(d).

Dose computation The energy and dose delivered to the different phantoms were computed using the dose module of the Monte-Carlo simulation platform CatDose (see

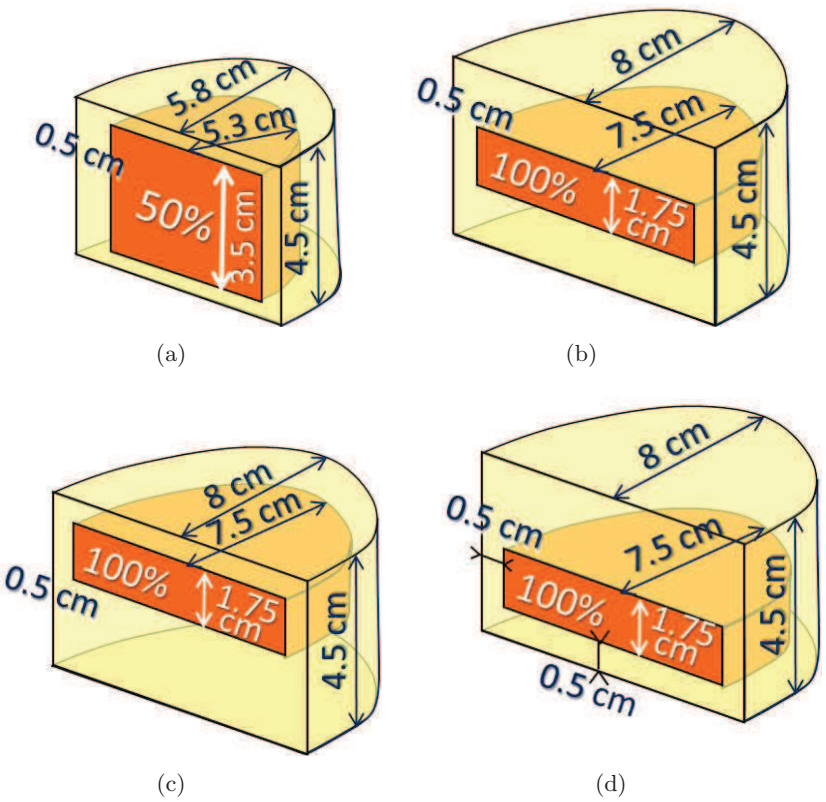

Figure 6.4: Virtual phantoms to evaluate individual risk assessment quantities: a) a smaller version of the Dance phantom, b) dense tissue concentrated at the center of the phantom, c) dense tissue concentrated at the higher part of the phantom, d) dense tissue concentrated at the lower part of the phantom.

Chapter 5). Doses normalized to an incident air kerma of 1 mGy were computed for 28 kV Molybdenum target/ Molybdenum filter. The AGD, iAGD and GIE normalized to the entrance air kerma were computed for all phantoms, as well as the ratios of the AGD, the iAGD and the GIE for Phantoms 6.4(a), 6.4(b), 6.4(c) and 6.4(d) relative to those of Phantom 6.3(a).

The results of the simulations are presented in Table 6.3.
As expected, the AGD is the same for all phantoms, since they have the same intra-skin VBD and thickness and were exposed to the same spectrum.
The iAGD of Phantoms 6.3(a) and 6.4(a) are the same, whereas the amount of glandular tissue in Phantom 6.4(a) is only half that of Phantom 6.3(a). However the iAGD takes into account the different positions of the same total amount of glandular tissue along the X-rays axis with the same projected area: the iAGD for Phantoms 6.4(b), 6.4(c) and 6.4(d) changes by almost a factor 8 between the highest values (gland close to the entrance surface, iAGD = 0.344) and the lowest values (gland close to the exit surface, iAGD =0.043) of the different phantoms. In this experiment the iAGD is sensitive to the distribution of the glandular tissue, but not to its amount.
The GIE of Phantom 6.4(a) is divided by two compared to Phantom 6.3(a), reflecting the

Phantom number	6.3(a)	6.4(a)	6.4(b)	6.4(c)	6.4(d)
AGD (mGy)	0.188	0.188	0.188	0.188	0.188
Relative AGD	1	1	1	1	1
iAGD (mGy)	0.188	0.188	0.133	0.344	0.043
Relative iAGD	1	1	0.71	1.83	0.23
GIE (mJ)	0.0285	0.0142	0.0202	0.0522	0.0065
Relative GIE	1	0.50	0.71	1.83	0.23

Table 6.3: AGD, iAGD and GIE computed for the phantoms in Figure 6.4. The air kerma is 1 mGy for all exposures. The relative values are always compared to the value of Phantom 6.3(a).

ratio of the glandular contents. The GIE for Phantoms 6.3(a), 6.4(b), 6.4(c) and 6.4(d) are quite varying (0.23 to 1.83 times that of Phantom 6.3(a)), in spite of having the same glandular mass. The GIE thus expresses the energy effectively received by the glandular tissue, the same way as iAGD does, but takes also into account differences in amount of tissue.
These results are expected from the different distributions. However the notion of imparted energy from Hammerstein et al. [66] has never been practically implemented, probably because it was impossible to compute it at that time. We would like to re-establish Hammerstein's quantity as the best approach to individual risk assessment in the frame of the LNT-model.

6.4 Computation of the local GIE

The GIE was computed so far with Monte-Carlo simulations. However making use of conversion factors could fasten this computation. Therefore we investigate the possibility to compute local conversion factors as a function of depth in the breast tissue for poly-energetic spectra. We define again four phantoms. They are semi-circular with a radius of 8 cm and a thickness of 4.5 cm. One phantom is made of homogeneous adipose tissue (Phantom 6.5(a)), another one of homogeneous glandular tissue (Phantom 6.5(b)), both defined by layers of 1 mm thickness in the Monte-Carlo simulation. The third and fourth phantom are composed of alternate layers of adipose and glandular tissues of 1 mm thickness, with the top and bottom layer being glandular tissue for Phantom 6.5(c) and with the top and bottom layer being adipose tissue for Phantom 6.5(d).
A rectangular plate of polycarbonate ($C_{15}H_{16}O_2$) of 2.7 mm thickness, representing the compression paddle, was put on top of the phantoms. The breast support was not modeled, because it impacts the imparted energy only via backscatter, which can be neglected at this place. The phantoms were exposed to a poly-energetic beam of a Molybdenum/Molybdenum-target/filter at 28 kV. The spectrum was generated with an in-house tool called SpecGene, using data from Cranley et al. (SRS) [36].
The imparted energy was computed for Phantom 6.5(b) per layer of 10 mm, 5 mm and 1 mm, to verify the impact of the slice thickness. For the other phantoms (Phantoms 6.5(a), 6.5(c) and 6.5(d)) it was computed per layer of 1 mm. For Phantom 6.5(b)

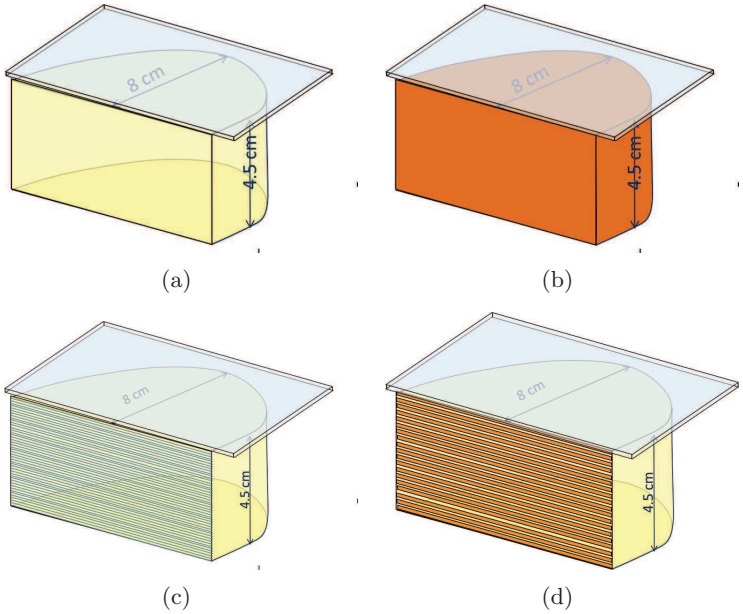

Figure 6.5: Phantoms designed to explore the local energy absorption from poly-energetic beams.

we simulated the situation without compression paddle for layers of 5 mm.
All data are again normalized to the entrance air kerma. As a consequence the sum of the layer conversion factors equals the conversion factor for the entire breast. It must be noticed that the conversion factors are also a function of the impact surface. This was shown in the previous section when comparing Phantom 6.3(a) and 6.4(a): the AGD does not change with impact surface, while the GIE does. Therefore the local GIE conversion factors should be scaled to the voxel values cross section. In this section we used the cross section of the phantom, i.e. 101 cm^2.

The impact of the slice thickness is shown in Figure 6.6. The data for the slices of 10 mm and 5 mm thickness were normalized, divided by 10 and 5 respectively, to be comparable to the data for 1 mm.
Several remarks can be made. First of all, there is an increase in imparted energy between 1 and 2 mm, which is only detectable if we simulate the imparted energy for slices of < 1 mm thickness. The increase of imparted energy at the entrance of the tissue by poly-energetic spectra is an effect, known for higher energies in radiotherapy, called *build-up*. This can be understood from photon scattering: in addition to the incident radiation, the first slice gets scattered photons from interactions in the first slice and the second slice (supposing that the scattered photon range is one slice), the second slice gets scattered photons from the first, the second and the third slice. The height and depth of the increase of imparted energy depend on the energy of the scatter range of photons in the tissue, and thus of their energy.
Secondly when comparing the results of different slice thicknesses, an error is caused by the normalization to 1 mm. This is expected because we normalized by dividing by 5 and 10 for respectively slices of 5 and 10 mm, although we know that the attenuation has an exponential behavior and not linear as supposed by this normalization. Even with this

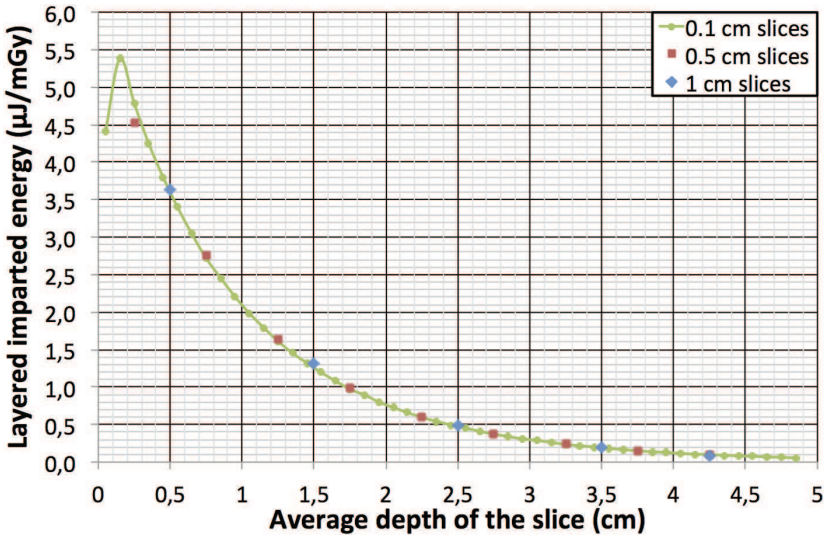

Figure 6.6: Impact of the slice thickness on the simulation results for the homogeneous glandular phantom 6.5(b). All data are normalized to the entrance air kerma of the phantom.

approximation, the values agree reasonably well (maximum difference 5.6%).
In Figure 6.7 the results of the homogeneous adipose and glandular tissues are shown and compared, normalized to the entrance air kerma. Again we find the increase of imparted energy to the first 5 mm of the tissue. The glandular tissue absorbs more energy at the entrance of the breast due to its higher linear absorption coefficient. After 13 mm the energy delivered to the adipose tissue is higher, because the fluence of the beam was less attenuated in the previous layers. After 30 mm both tissues absorbed per mm less than 1% of the total imparted energy. After 50 mm the imparted energy to both tissues is less than 5% of the first 1 mm slice of adipose tissue and less than 0.2% of the total imparted energy. The effective attenuation coefficients of the poly-energetic spectra for the Molybdenum/Molybdenum anode/filter-combination at 28 kV tube voltage are 0.64 cm^{-1} for adipose tissue and 0.95 cm^{-1} for glandular tissue. These are close to the mono-energetic attenuation coefficients for 18 keV: 0.68 cm^{-1} and 0.98 cm^{-1} respectively.
In Figure 6.8 the results of the layered phantoms (dots) are compared with those of the homogeneous phantoms (full lines) for adipose and glandular tissues respectively. With these phantoms we want to investigate the impact of the *history* of the X-ray beam before it reaches the layer for which we compute the imparted energy. The adipose odd layers result from phantom 6.5(c), the even layers from phantom 6.5(d). For the glandular layers, even layers result from phantom 6.5(c), odd layers from phantom 6.5(d). The curve that would link the dots is less smooth because the spectra for the consecutive slices in both phantoms are changed differently by the alternate tissues. The difference in imparted energy between the homogeneous and layered phantoms, or the error if we neglect the beam's *history*, is on average 13% for the adipose tissue and 35% for the glandular tissue. In absolute values these are 0.01μJ/mGy and 0.07μJ/mGy per layer of 1 mm. From Figure 6.8 we can confirm that the imparted energy to mixed adipose and glandular tissues stays within the borders of the homogeneous adipose and glandular tissues. We can compare these errors to differences between computation methods of current dosimetry (AGD) in literature which go up to 15% [42] for the entire breast. For individualized

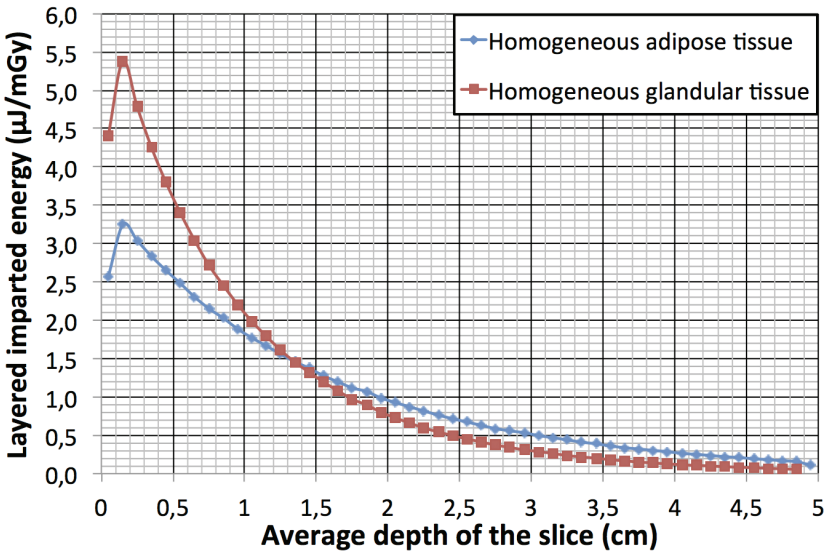

Figure 6.7: Imparted energy to homogeneous adipose tissue and glandular tissue for slices of 1 mm thickness normalized to the entrance air kerma.

dosimetry we did not find error ranges in literature. Our results suggest that it would be better to take into account the *history* of the beam for the computation of the local imparted energy.
The impact of the compression paddle is shown in Figure 6.9. The presence of a compression paddle hardens the beam, but the paddle also absorbs a part of the energy, leaving less energy in the tissue. Differences are small and do not exceed 3.2%. The simulations are not precise enough to see the increase in imparted energy to the first millimeters.

6.5 Discussion and conclusion on individual risk assessment

The AGD has been originally introduced for comparing doses delivered with different radiographic techniques [38, 39]. It was therefore computed for a standard breast, as expected for a non-individual radiation protection quantity. It was further extended in its use to assess the quantity of radiation received by patients during mammography on a collective basis and the significant influence of the glandular content was taken into account [41, 153, 154]. For that purpose, it is acceptable to use compositions obtained by correlation with the thickness, as discussed above [16]. When going to individual dose statements, it looks obvious to try reaching an individual measurement of the breast glandular content. Amongst the discussed density measures, the VBD is the most stable one, independent of positioning of the breast, and originally used in the computation of normalized average glandular dose values. The VBD is the best suited density measure for the individualized AGD and the VBD can be computed using different methods, such as described in Chapter 3. This is what is proposed e.g. by the Volpara Dose product, claiming to use "patient-specific volumetric density (...) for a patient-specific assessment of the mean glandular dose (MGD)" [4]. However this method only consists in using the patient VBD to select the appropriate values in the normalized average glandular dose tables of [41].

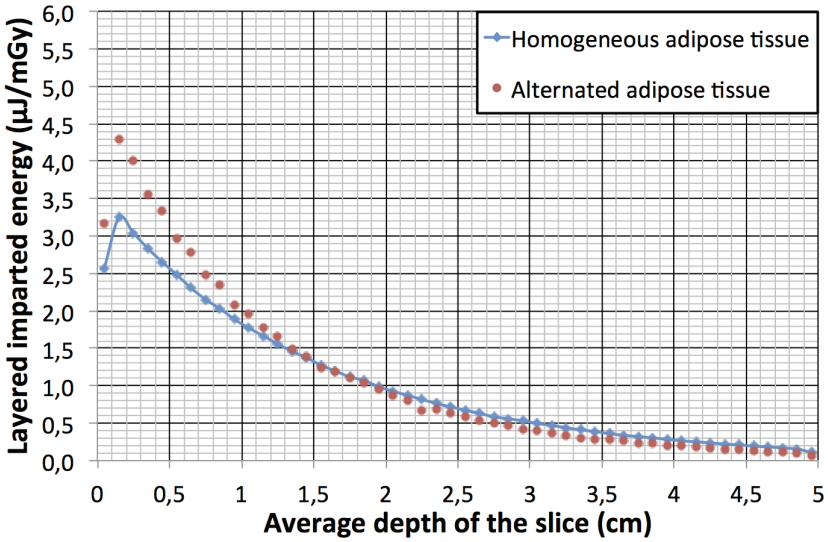

(a)

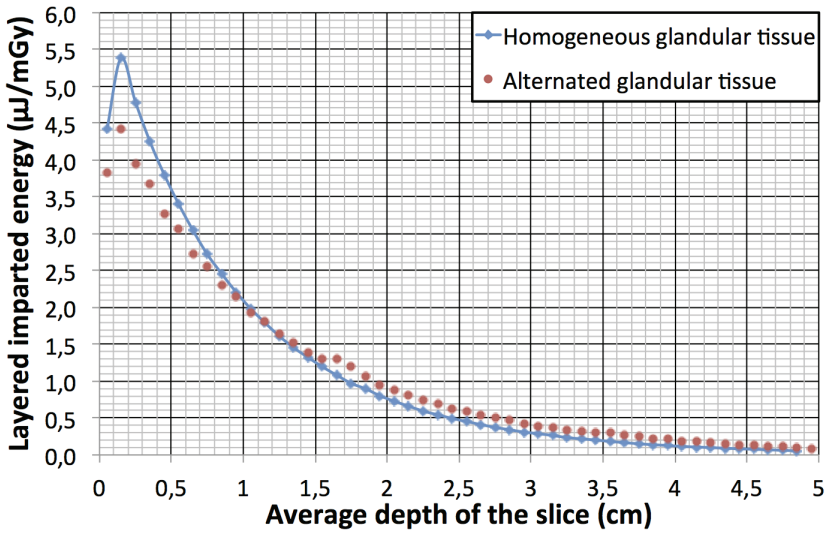

(b)

Figure 6.8: Imparted energy to the layers of adipose tissue (a) and of glandular tissue (b) of 5 mm thickness normalized to the energy imparted to the the homogeneous adipose phantom. a) The odd slices are computed from Phantom 6.5(c), the even ones from Phantom 6.5(d). b) The odd slices are computed from Phantom 6.5(d), the even ones from Phantom 6.5(c).

The results of the simulations in Section 6.3 demonstrate the limitations of the AGD for individualized risk assessment since it does not take into account the individual glandular amount and distribution. Individualizing the AGD by taking into account the glandular amount and distribution allows us to effectively compute the delivered energy to the gland in each point and thus to differentiate the risks of the breasts represented by the different phantoms. Introducing the computation of the GIE requires the 3D-localization of the glandular tissue within the breast. Emerging 3D imaging techniques such as tomosynthesis and breast CT became available only recently, making it possible to obtain information on

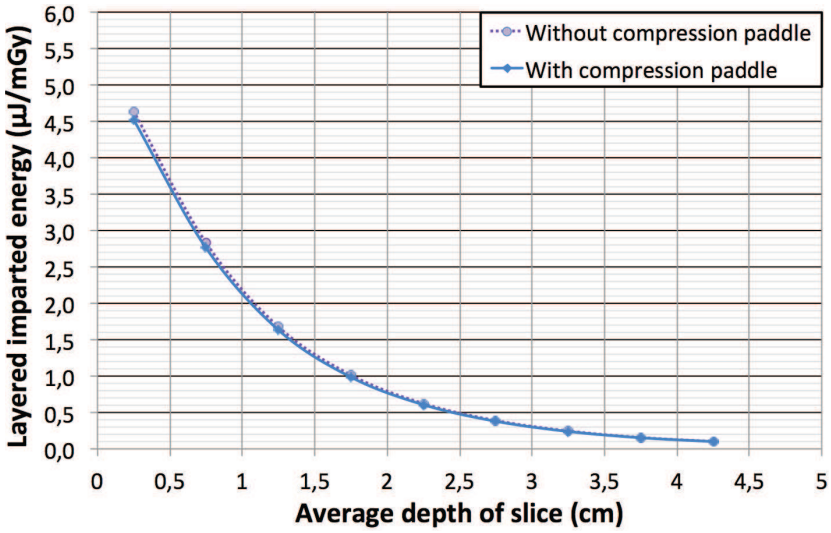

Figure 6.9: Imparted energy to homogeneous adipose tissue for slices of 5 mm thickness with and without compression paddle, normalized to the energy imparted to the homogeneous adipose phantom.

the glandular tissue distribution.
The iAGD converts the delivered energy to the gland into a dose in the usual way and takes into account the glandular distribution. However its low sensitivity to the amount of tissue at risk demonstrates that it is not sufficiently effective for individual risk assessment. Therefore GIE is a better alternative. Introducing the GIE in clinical practice might cause some discomfort to users compared to the current AGD, in particular due to the change in nature and units. Since GIE depends on glandular position, there is no easy way to "convert" AGD to GIE. For the simple case of Phantom 6.3(a) the conversion can be done by multiplying AGD and the glandular mass: 0.188 mGy/mGy$\times$0.151 kg = 0.0285 mJ/mGy, but this method does not work for the other phantoms.
Finally, even if it would have been possible to compute all quantities using a Monte-Carlo simulation, this is hardly compatible with daily clinical practice. Therefore we were looking for a formalism to compute local imparted energy of a poly-energetic beam, based on depth in the tissue. We showed the possibility to find a model describing the local imparted energy as a function of depth per beam quality, which was shown in this chapter for a Mo/Mo 28 kV-beam. To make this method suitable for a daily clinical use, these functions must be investigated for the different spectra used by the different systems. Conversion factors, converting entrance energy to local imparted energy, can be derived from those functions. The *history* of the beam should be taken into account, but its impact is less important than the impact of the depth of the tissue. Also the impact surface of the local volume should be taken into account, contrary to the use of the AGD.

Of the three evaluated quantities, the GIE responds best to the needs for an individualized quantification of the radiation induced risk in mammography, depending on both the amount and distribution of the glandular tissue. This measure could be computed using models of local imparted energy as a function of beam quality and depth in the tissue.

Chapter 7

Segmentation of glandular tissue from tomosynthesis

We assume that the radiation risk in mammography is proportional to the energy imparted to the gland. In the previous chapter we showed the possibility to compute where the energy is absorbed. In this chapter we discuss the possibility to obtain the location of the glandular tissue based on tomosynthesis images. We used the currently available reconstruction algorithm of GE SenoClaire. The study of the reconstruction algorithm is out of the scope of this thesis. We propose a segmentation of the reconstructed volume, based on the voxel values, then investigate the accuracy of our newly introduced VBD-based segmentation method applied to the imparted energy computation.

7.1 Brief introduction to tomosynthesis

Digital breast tomosynthesis (dBT) is an emerging breast imaging technique. The system is comparable to a standard mammographic system, but acquires projection images of the compressed breast under different angles (see Figure 7.1) from which tomographic planes are reconstructed. The limited angular aperture generates a non-isotropic resolution, in-plane compared to inter-plane.
The equipment manufacturers implemented this technique in different ways. The rest of this text considers only the configuration of the GE HC tomosynthesis system, SenoClaire, for which the angular range is [-12.5°, +12.5°], symmetrical around the position orthogonal to the image receptor. The tube moves from one angular position to another and stops for the next image acquisition (step-and-shoot principle). Nine projections are acquired in total. The tomographic system is an add-on to the Senographe Essential and therefore uses its detector (CSi scintillator plus amorphous silicon matrix). The reconstruction algorithm is a simultaneous algebraic reconstruction technique (SART) method [11], implemented on a dedicated PC, nicknamed ReconBox. However, in order to explain the origin of the challenges associated with the segmentation, we will use the simple back-projection (SBP) reconstruction algorithm.

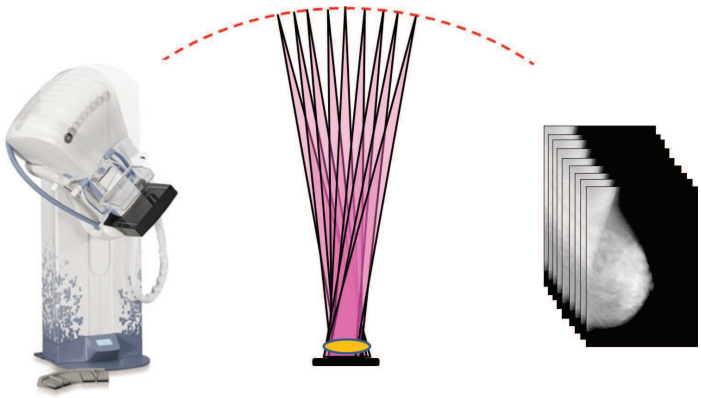

Figure 7.1: Principle of tomosynthesis: acquire projection images of the compressed breast under different angles and reconstruct the 3D-structure.

7.2 Tomosynthesis limitations

In Chapter 4 we already showed the possibility to quantify the amount of glandular tissue using thorax CT images. The advantage of breast tomosynthesis over thorax CT is the high in-plane resolution at a much lower dose. Conversely, the main disadvantage of tomosynthesis is a very anisotropic spatial resolution due to the limited sweep angle in tomosynthesis. The origin of the limited depth resolution is illustrated in Figure 7.2: Consider two images of a sphere, one taken at -12.5° and one at +12.5°, or 25° between each other (see Figure 7.2(a)), i.e. the maximum angles for a GE tomosynthesis system. The sphere attenuates the X-rays, so the signal is lower in the pixels of the projection images according to the position of the sphere, and this is different for the two images. If we back-project the two images (SBP reconstruction), all possible solutions of the projected object are contained within the diamond (yellow dashed line). We cannot be more specific or distinguish the different solutions based on the projection images. If not two but nine images are considered the artifact is more complex with voxels being included in some but not all projections (see Figure 7.2(b)). However the central region as described in Figure 7.2(a) remains undistinguishable. So far we considered a binary image. In the real images the projected circle will vary in intensity according to the thickness of the object. The voxel values of the diamond will also vary, but the diamond shape will remain. The size of the diamond in the X-ray directions is a function of the size of the object and the sweep angle [105].
An example of an in-plane artifact is represented in Figure 7.3. In this figure the object consists of four plates, two of adipose tissue and two of glandular tissue. They are placed so that the phantom has a constant thickness and a uniform density in the 0° projection image. On the left side of the phantom the adipose tissue is on top, on the right side of the phantom the glandular tissue is on top. The first image is acquired with a leftward angulation, and as the adipose tissue is less attenuating, the signal is reduced in the center of the image, where the percentage glandular tissue along the X-ray path is lower. The second image is acquired with a rightward angulation, resulting in a higher percentage of glandular tissue along the X-ray path in the center of the image. Again we suppose SBP to reconstruct the planes at different heights. The result for a given plane is the sum of the shifted projection images, with the shift depending on the height of the plane [149]. If

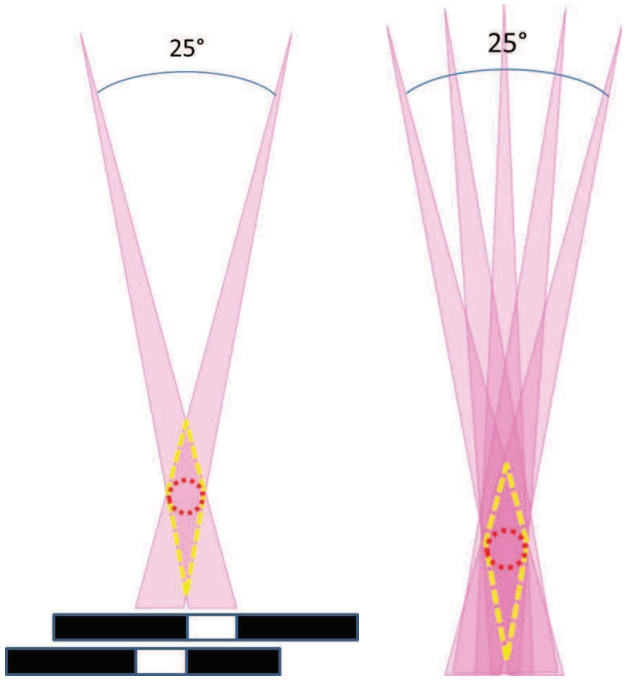

Figure 7.2: The limited angulation of the tomosynthesis examination implies artifacts with the characteristic form of a diamond. No distinction can be made, based on the pixel values, for all forms between the circle (red dashed line) and the diamond (yellow dashed line).

we number the X-ray paths at the bending points in Image 1 from 1 to 3 and in Image 2 from 4 to 6, we can find the shift of the projection images for a given plane. In the highest plane represented in Figure 7.3 on the right, X-ray 2 coincides with X-ray 4 and X-ray 3 coincides with X-ray 5. The plane is then the sum of the shifted projection images. In the plane halfway the phantom, X-ray 1 coincides with 4, 2 with 5 and 3 with 6. The resulting plane is a flat image.
From the different planes we can see that the intersection between the adipose and glandular tissues for this phantom is not representative for the object, and depends on the plane and the angle between the projection images. Also, the in-plane values of the adipose plate and the glandular plate are the same. This shows that the value in the reconstructed planes is not guaranteed to be representative of the tissue composition.

So far we discussed SBP, where the signal was not filtered before back-projection. However a more accurate solution consists in applying a ramp filter to the projections or the planar images in application of the Radon transform [109]. The effect is represented in Figure 7.4: the high-pass filter creates an under- and overshoot at the interfaces between different materials. Combining images as we did already in Figure 7.3 shows that a halo is formed around the objects of a more attenuating material. This effect is influenced by the size of the object and by the difference in density between the object and the surrounding material. We need to take this into account for glandular structures representative of real breast tissue.

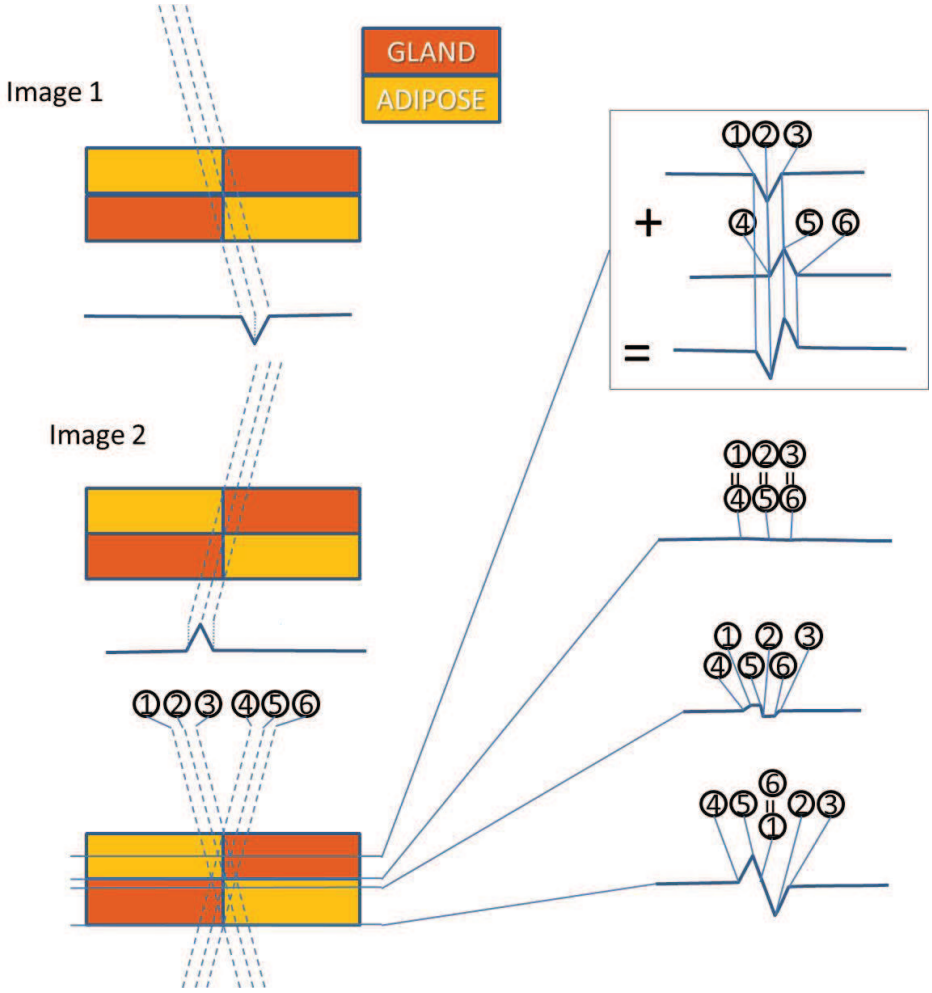

Figure 7.3: The limited angulation of the tomosynthesis examination implies in-plane artifacts. Left) the phantom for which two projection images are acquired. Right) in-plane reconstructions of the signal, formed by adding the projection images with a shift depending on the height of the plane.

7.3 Segmentation method

We propose a segmentation method based on the VBD. The VBD can be computed for the 0° projection image with the method proposed in Section 3.2. Since the GE tomosynthesis system incorporates an anti-scatter grid, a single VBD system calibration can be used for both the regular 2D projection images and for the 0° tomosynthesis projections. We presume that after some corrections, mainly for the thickness, the VBD can be computed as well for the other angles as a verification or improvement of the $0°VBD$. The VBD can be interpreted as the percentage of voxels of the breast containing fibroglandular tissue, the others being adipose tissue., Although the limited angle of tomosynthesis does not guarantee quantitative voxel values as for CT (see previous section), we can determine, from the histogram of the voxel values of the breast (see an example in Figure 7.5), a threshold for which the number of voxels with a higher voxel value is $VBD\%$ of the total

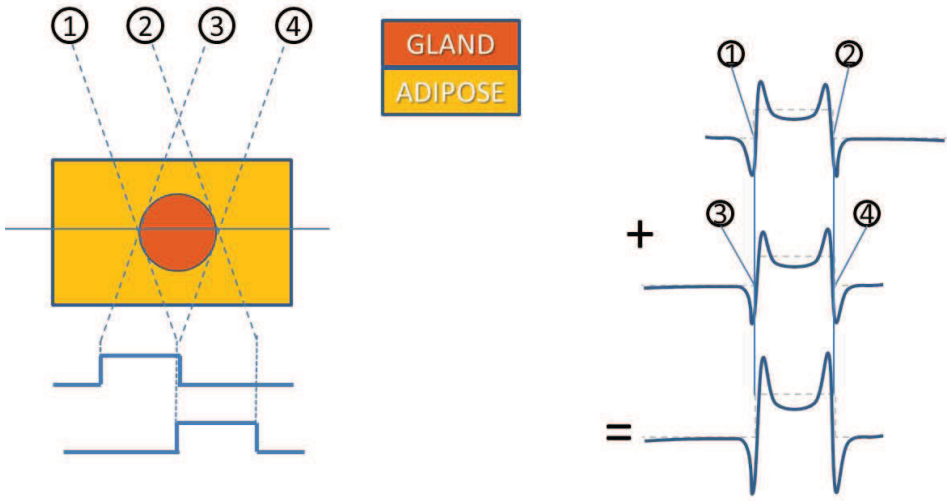

Figure 7.4: The limited angulation of the tomosynthesis exam, combined with a high-pass filter, creates a halo around dense objects. Left) the phantom for which two projection images are acquired. Right) in-plane reconstructions of the signal, formed by adding the projection images with a shift depending on the height of the plane.

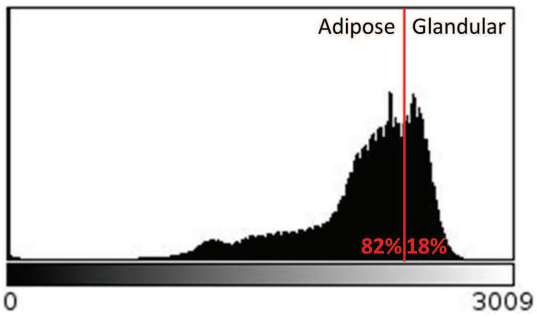

Figure 7.5: Example of the histogram of a patient reconstructed volume ($VBD = 18\%$).

amount of voxels of the breast. Therefore we classify the voxels with a binary label: the "$VBD\%$" densest voxels are classified as "glandular", and the "$(100 - VBD)\%$" voxels of lower density as being "adipose". In this section we want to explore how good the relative voxel values are in the reconstructed volume and thus if it is justified to use the histogram of the voxel values, thresholded by the VBD, to classify the reconstructed voxels.
In order to vary different parameters influencing the voxel values, we designed different phantoms represented in Figure 7.6, with characteristics precised in Table 7.1. All phantoms consist of semi-cylinders of adipose tissue containing coplanar spheres of glandular tissue. They vary by phantom thickness, height of the sphere centers, sphere sizes and distance between sphere centers. Phantom (j) is the same as Phantom (a), but with a compression paddle of 2.7 mm polycarbonate.
The phantoms were described analytically, then voxelized by the CatSim simulation tool (see Chapter 5). We use these phantoms and the segmentation of their reconstructed tomosynthesis volume to verify the proposed segmentation method. For each phantom of Figure 7.6 we first compute the energy imparted to adipose and fibroglandular tissues using

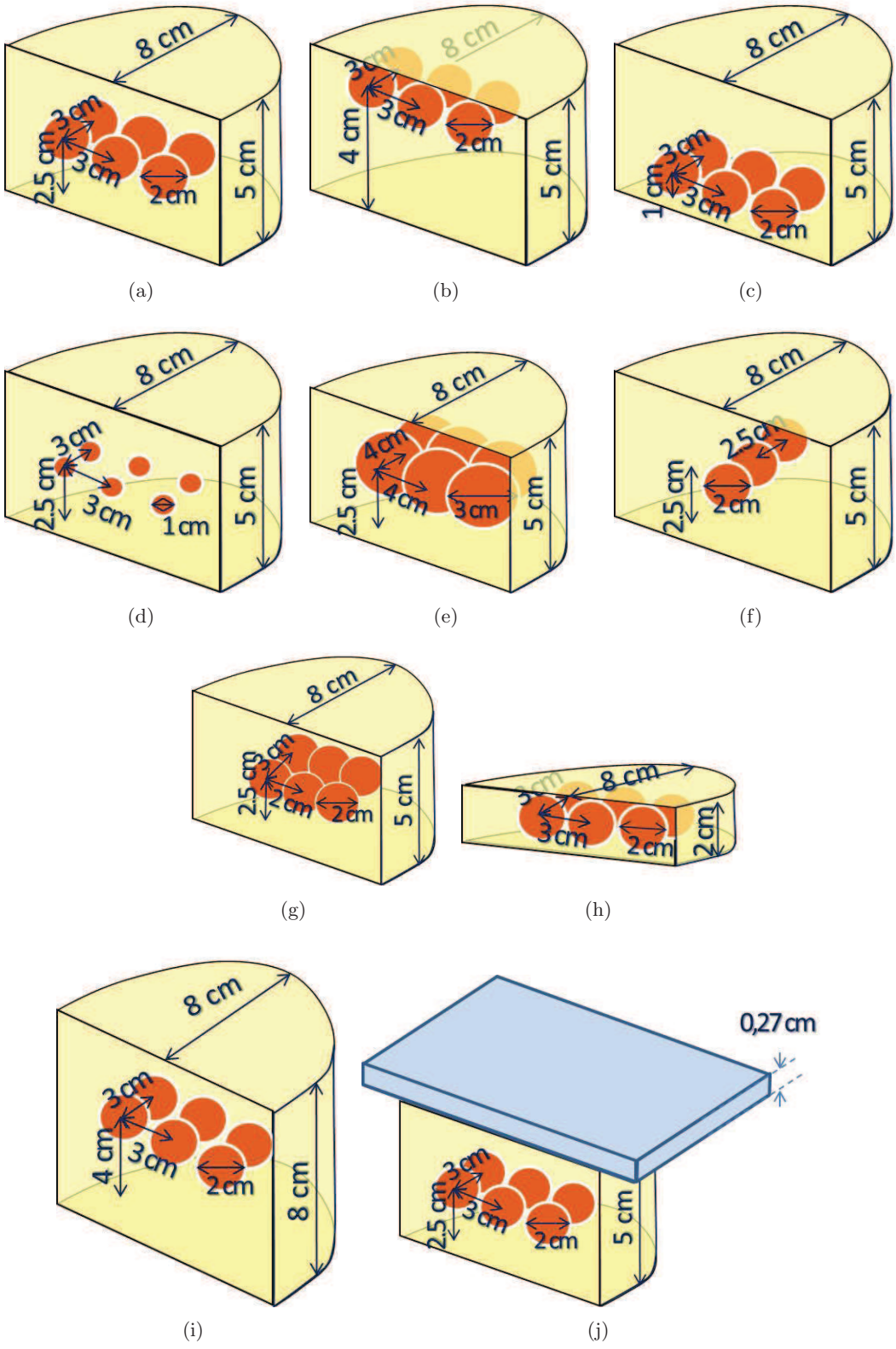

Figure 7.6: Phantoms to investigate limitations of segmentation of glandular tissue in reconstructed tomosynthesis volumes based on voxel values.

Phantom	Phantom thickness	Glandular spheres size	Distance between sphere centers	Sphere centers height above the base
Phantom 7.6(a)	5 cm	1 cm	3 cm	2.5 cm
Phantom 7.6(b)	5 cm	1 cm	3 cm	1 cm
Phantom 7.6(c)	5 cm	1 cm	3 cm	4 cm
Phantom 7.6(d)	5 cm	0.5 cm	3 cm	2.5 cm
Phantom 7.6(e)	5 cm	1.5 cm	4 cm	2.5 cm
Phantom 7.6(f)	5 cm	1 cm	2.5 cm	2.5 cm
Phantom 7.6(g)	5 cm	1 cm	2 cm	2.5 cm
Phantom 7.6(h)	2 cm	1 cm	3 cm	2.5 cm
Phantom 7.6(i)	8 cm	1 cm	3 cm	1 cm
Phantom 7.6(j)	5 cm	1 cm	3 cm	4 cm

Table 7.1: Characteristics of the phantoms in Figure 7.6.

CatDose MC software (see Chapter 5). These energies will be considered as the truth (see Figure 7.7). Then we generate projection images of the phantoms for the same conditions as for the GE breast tomosynthesis acquisition, using CatSim, and reconstruct the volume using the regular reconstruction algorithm, ReconBox. The ReconBox reconstructs a volume that is 5 mm thicker than the compressed thickness indicated in the DICOM-header to avoid missing tissue due to small errors in thickness. We left out these slices for the dose simulations. The reconstructed volume is segmented based on the VBD as described before and the imparted energy to each of the two compartments is computed with CatDose for the segmented volume. This result is compared with the "truth" for the local imparted energy. This whole simulation chain of exposures is computed for a spectrum generated with a Mo/Mo anode-filter combination at 28 kV.

7.4 Reconstructions

The method is first demonstrated graphically for Phantom 7.6(a). Figure 7.8 shows three orthogonal cross-sections through the glandular spheres. Every voxel is represented according to the tissue present. Here grey corresponds to the adipose tissue, white to the glandular tissue, and black to air. After projection and reconstruction, the same cross-sections of Phantom 7.6(a) are represented in continuous gray shades in Figure 7.9. We see that the plane parallel to the breast support in Figure 7.9 shows little alteration compared to the original shape of the phantom in Figure 7.8. This is quite different for the side and front views where the impact of the effect described in Figure 7.2(a) of Section 7.2 is clearly visible. We can also see that the cones generated around the spheres are circular in the center, but elliptical on the top, with the long side as expected in the direction orthogonal to the plane of the tomographic sweep. From the top view, as well as in the front view, we can see the halo effect as described in Figure 7.4 in Section 7.2.

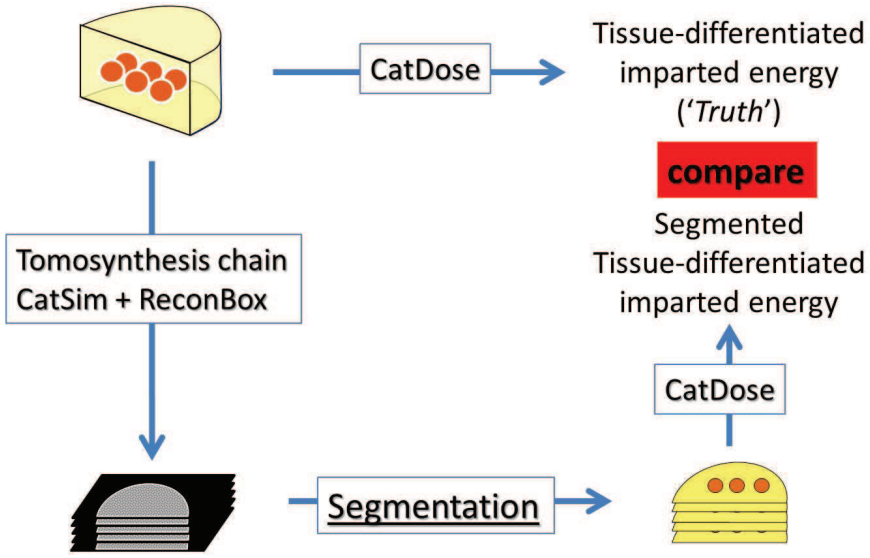

Figure 7.7: Method to verify the accuracy of the tissue segmentation.

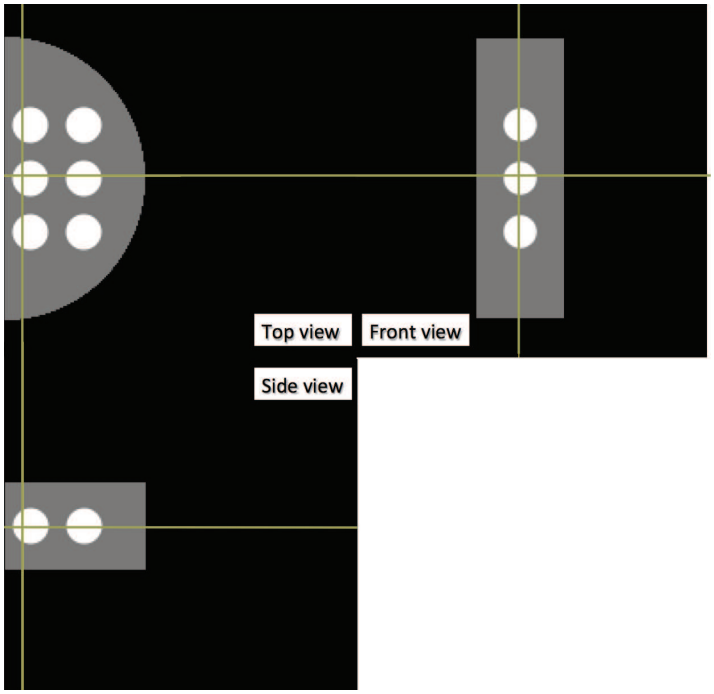

Figure 7.8: Phantom 7.6(a) as seen by CatSim and CatDose: side, front and top view.

The side view and front view also show that the reconstructed volume is no longer semi-cylindrical (see red arrows): on the "nipple"-side (seen in the side view) the upper corner is missing. This missing part decreases on the left and right sides of the breast (seen in the front view), i.e. in the direction of the tube motion. This is a problem related to the shape of the phantoms and the reconstruction algorithm which is adapted specifically to breast shapes. We should check the importance of this issue for breast shaped phantoms.

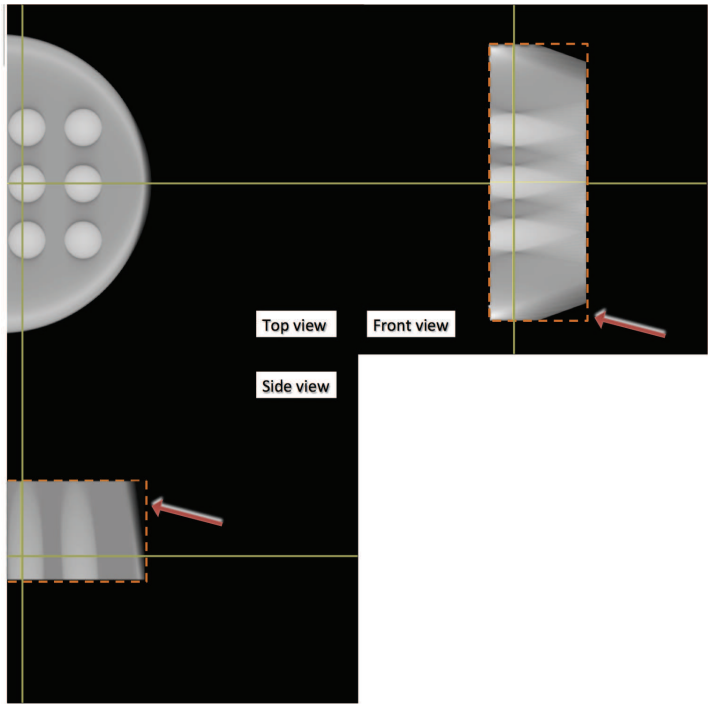

Figure 7.9: Phantom 7.6(a) reconstructed by the ReconBox from the mammographic system, based on the projection images generated with CatSim: side, front and top view.

The VBD value of 5.8% computed from the voxelized phantom in Figure 7.8 is used for the segmentation of the reconstructed images of Figure 7.9. The result of this segmentation is represented in Figure 7.10(a) for the adipose tissue and in Figure 7.10(b) for the glandular tissue. The results show that it is possible to segment the reconstructed volume and to find the glandular objects in the adipose phantom and to get rid of the halo artifact. However the shape of the glandular spheres is not preserved, and becomes elliptical, i.e. longer in the vertical direction and smaller in-plane as a consequence of the volume conservation for each of the components imposed by the VBD segmentation method. The ellipsoid is not symmetrical in the vertical direction, but larger on the lower side. On the other hand, the cross sections of the cones are more circular than expected visually from the reconstructed volume, while in the side view the conical shape is only guessed. An artifact on the lower side of the phantom is misinterpreted as glandular tissue (see red arrow in Figure 7.10(b)). This object is present all along the border of the phantom and more distinct on the left and right sides than on the "nipple"-side. This is again the region where there is no compressed breast, so this artifact should also be verified for breast shaped phantoms, instead of rectangular phantoms. For this exercise, the impact is minor, because the voxels are on the lower side of the phantom, where the dose is low.
We computed the mass and the imparted energy for both adipose and glandular tissues. The results are presented in Tables 7.2 and 7.3. The masses are expressed in grams, the imparted energies normalized to the air kerma in the entrance plane of the phantoms in μJ/mGy. We also computed the energy imparted to the glandular tissue as a percentage of the total imparted energy to each phantom. First of all we notice that the masses of the reconstructed phantoms are smaller than the actual values for each phantom, ranging from

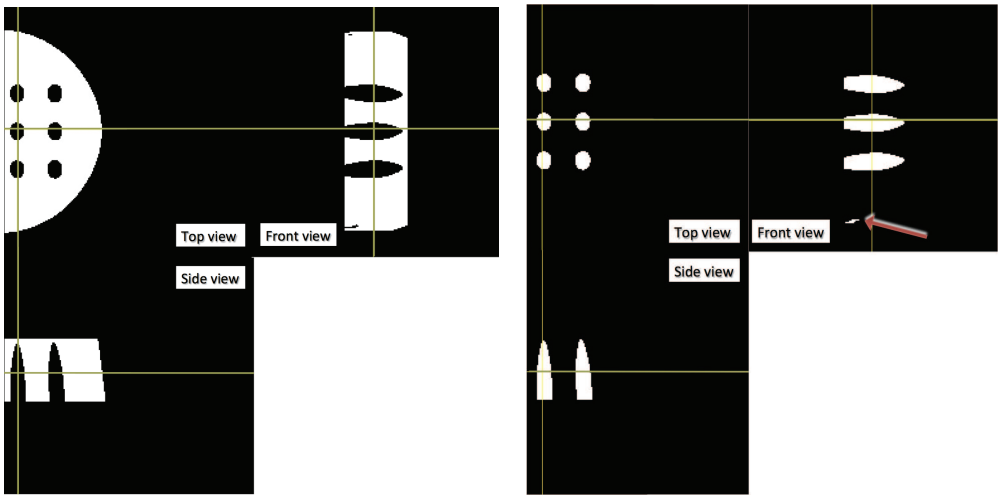

(a) (b)

Figure 7.10: The labeled a) adipose and b) glandular volumes based on thresholding of the reconstructed volume of Phantom 7.6(a).

Phantom	Original phantom		Reconstructed phantom		Relative difference	
	Adipose	Glandular	Adipose	Glandular	Adipose	Glandular
Phantom 7.6(a)	469.4	32.6	403.0	28.2	14%	13%
Phantom 7.6(b)	469.4	32.6	414.9	28.2	12%	13%
Phantom 7.6(c)	469.4	32.6	414.7	29.0	12%	11%
Phantom 7.6(d)	488.1	0.74	440.1	0.65	10%	12%
Phantom 7.6(e)	420.1	101.1	361.3	88.7	14%	12%
Phantom 7.6(f)	478.8	16.2	427.7	14.5	11%	10%
Phantom 7.6(g)	469.4	32.4	414.8	28.9	12%	11%
Phantom 7.6(h)	182.2	32.6	31.1	5.6	83%	83%
Phantom 7.6(i)	756.6	32.6	689.3	29.9	9%	8%
Phantom 7.6(j)	469.4	32.5	417.3	29.1	11%	10%

Table 7.2: Adipose and glandular mass (g) of the original and reconstructed phantoms of Figure 7.6. All are computed from the phantoms voxelized by CatDose.

48 g to 70 g, i.e. 9% to 14%, and 178 g, i.e. 83%, for Phantom 7.6(i). This was expected from the images in Figure 7.9 where the upper corner of the phantom is missing (see red arrows). As the segmentation is based on the percentage of voxels, this underestimation of volume is proportionally distributed over the adipose and glandular tissues. As a consequence the total imparted energy is higher in the original phantoms than in the reconstructed phantoms, i.e. maximum 9 μJ/mGy or 11%, distributed over both adipose and glandular tissues. The correlation between the mass of the original pantoms and the

Phantom	Original phantom			Reconstructed phantom			Relative difference	
	AIE	GIE	GIE/TIE*	AIE	GIE	GIE/TIE*	AIE	GIE
Phantom 7.6(a)	84	4.2	4.7%	78	1.7	2.2%	7%	58%
Phantom 7.6(b)	75	11	13%	73	10	12%	2%	9%
Phantom 7.6(c)	84	1.6	1.8%	81	2.0	2.4%	4%	-25%
Phantom 7.6(d)	85	0.1	0.8%	82	0	0%	3%	64%
Phantom 7.6(e)	72	14	17%	71	13	15%	2%	11%
Phantom 7.6(f)	83	2.0	2.3%	81	1.6	1.9%	3%	21%
Phantom 7.6(g)	81	4.0	4.7%	79	4.0	4.8%	3%	1%
Phantom 7.6(h)	87	1.6	1.8%	94	0.3	0.4%	-8%	79%
Phantom 7.6(i)	56	11	16%	11	1.7	14%	81%	84%
Phantom 7.6(j)	71	3.5	4.7%	80	3.5	4.9%	-12%	2%

* % of the total imparted energy (TIE) in each phantom.

Table 7.3: Adipose (AIE) and glandular (GIE) imparted energy per air kerma (μJ/mGy) for the original and reconstructed phantoms of Figure 7.6.

mass of the reconstructed phantoms is shown in Figure 7.11(a). The correlation of the GIE of the original phantoms and the reconstructed phantoms normalized to the entrance air kerma is shown in Figure 7.11(b). There is a range of GIE for a same mass, because the same mass can receive different amounts of energy according to the localization of the tissue. From the table we compute the imparted energy difference for the glandular tissue between the original and the reconstructed phantoms to determine the impact of the different phantom configurations. The maximum difference is very large, i.e. up to 84% for Phantom 7.6(h). However if we look at the GIE as a percentage of the total imparted energy, the difference between the original phantom and the reconstructed phantom is only 2.5%. For the total reconstructed volume, and thus absolute imparted energy values, an important error was observed, however a good approximation was obtained for the ratio of the tissue-differentiated imparted energies. Hence it could be a better option to compute the percentage of GIE from the reconstructed volume, but to compute the total imparted energy in another way. This might be performed from the projections and system models, as is the case for the AGD in several systems today.
The error in terms of percentage of total imparted energy for the glandular spheres in the center of the phantom (Phantom 7.6(a)) is larger (2.5%) than for the spheres located in the upper and lower part of the phantom (0.8% and 0.6% respectively). This can be understood from the smaller artifacts, who are cropped at the borders of the reconstructed volume (see Figure 7.12). The error for the small spheres (Phantom 7.6(d)) is smaller (0.05%) than for the large spheres (Phantom 7.6(e), 1.7%). From Figure 7.12 Phantom 7.6(d) we can see that the glandular spheres are missed. Only the artifact at the border is picked up as "gland". The impact of the "nipple - chest wall" direction (Phantom 7.6(f)), the "left-right" distance between the spheres (Phantom 7.6(g)) and the compression paddle

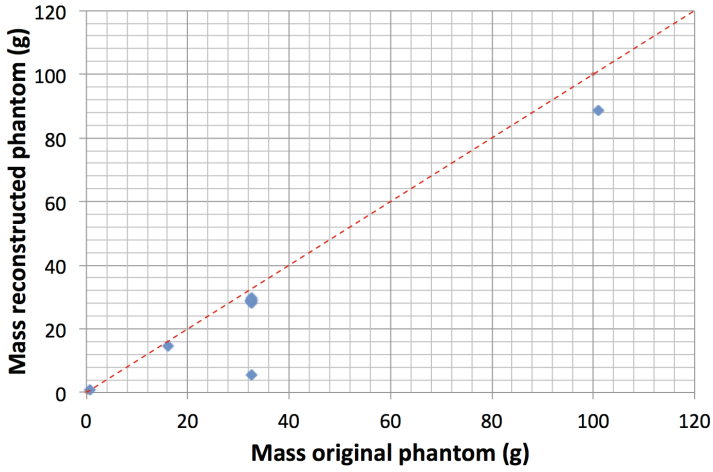

(a)

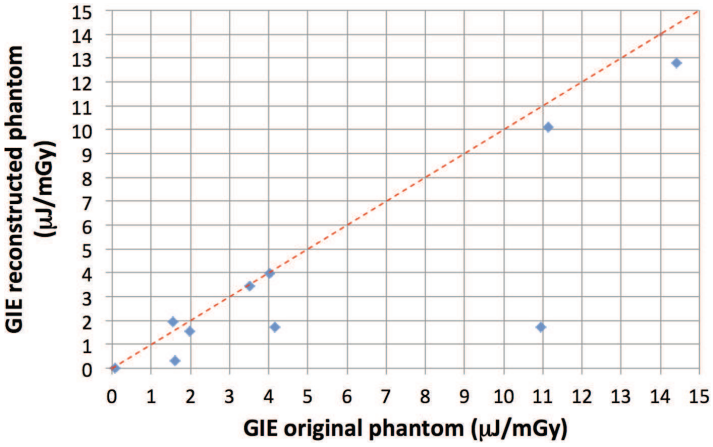

(b)

Figure 7.11: Correlation between a) the original phantom mass (g) and the reconstructed phantom mass (g) and b) the original phantom GIE (μJ/mGy) and the reconstructed phantom GIE (μJ/mGy) of Figure 7.6.

(Phantom 7.6(j)) have little impact on the segmentation and thus on the error of the imparted energy. The largest errors (79% and 84% respectively) are for the small and the large phantoms (Phantoms 7.6(h) and 7.6(i)). Surprisingly the segmentation method did not find the glandular spheres in the large phantom and instead labeled the border artifact as glandular tissue (see Figure 7.12). This can be explained since for Phantom 7.6(i) the VBD is low, limiting the number of glandular voxels, and the artifacts having the highest voxel values. In the next sections we apply and evaluate the segmentation method and the computation of the GIE to a textured phantom and to a patient acquisition in order to evaluate the segmentation for realistic glandular structures.

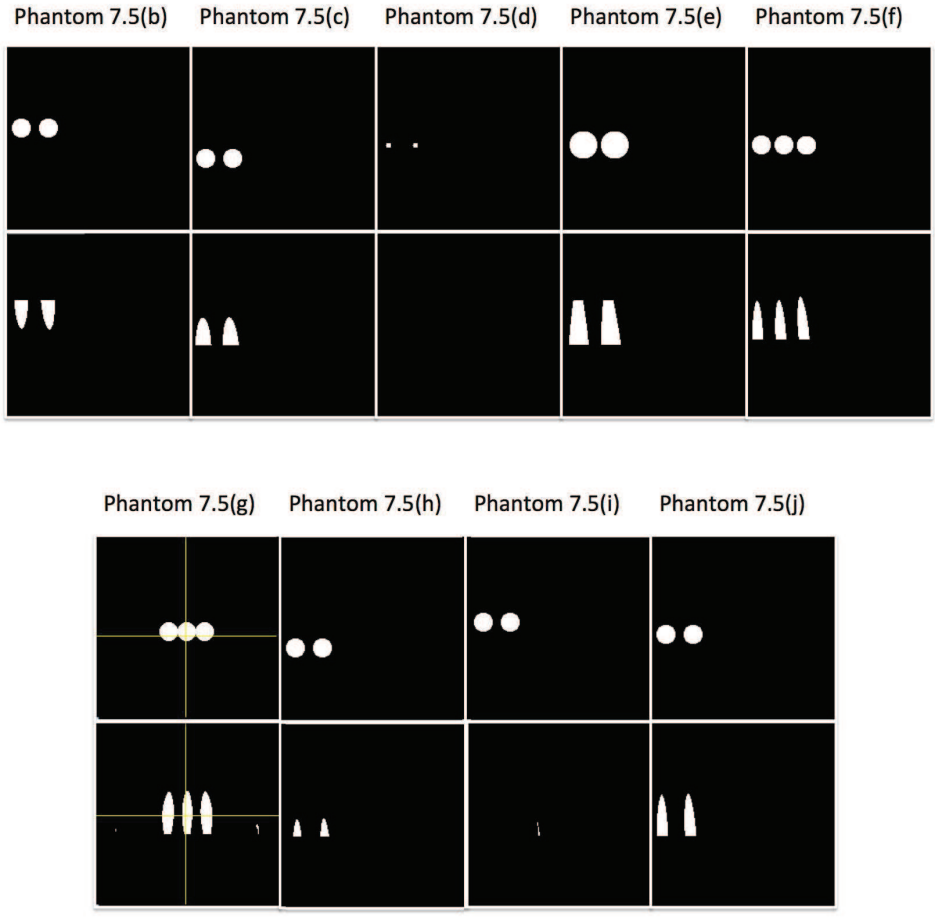

Figure 7.12: Side view of the original and reconstructed phantoms and front view for Phantom 7.6(g).

7.5 Textured phantom

The segmentation chain is applied to the textured phantom proposed by Carton et al. [30] with cross-sections represented in Figure 7.13(a) and a projection image in Figure 7.13(b). The phantom is based on the knowledge of the organization of breast tissue. The interplane distance of the reconstructed volume is 1 mm (see Figure 7.13(c)). The glandular texture is visible in-plane, but very fuzzy in the orthogonal planes. Also the shape of the phantom in the direction of the X-rays is less rounded than we expected from the conception of the phantom. However this is how the reconstruction algorithm is conceived.
Despite the fuzzy orthogonal views we applied the same VBD-based segmentation as described above. The VBD was computed from the voxelized phantom and found to be 6%. The original volumes and segmented volumes are represented in Figure 7.14. The segmented tissue has the shape that we expected from the reconstructed volumes and the examples of the analytical phantoms: fibrous appearance in the direction of the X-rays. The hyperintense artifact at the bottom is still present (see red arrow in Figure 7.14(d)), though much less prominent. Since the borders of this phantom are slightly rounded, we expect that for patient images these artifacts will not be present (see Section 7.6).

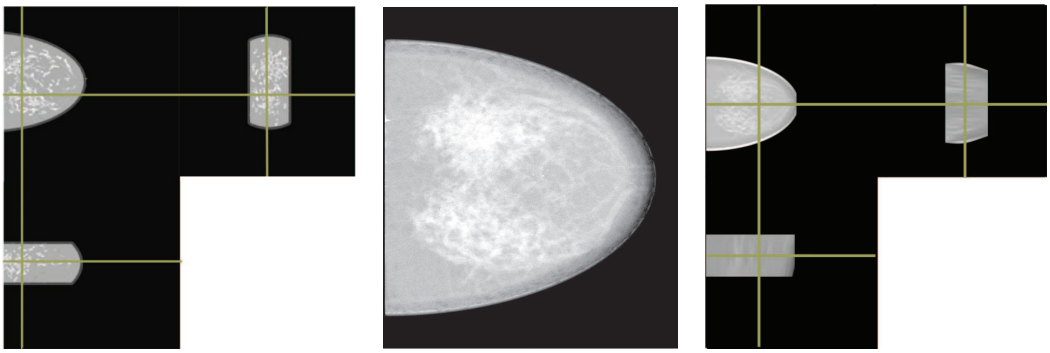

(a) (b) (c)

Figure 7.13: a) Textured phantom, b) one of its nine projections and c) the reconstructed volume.

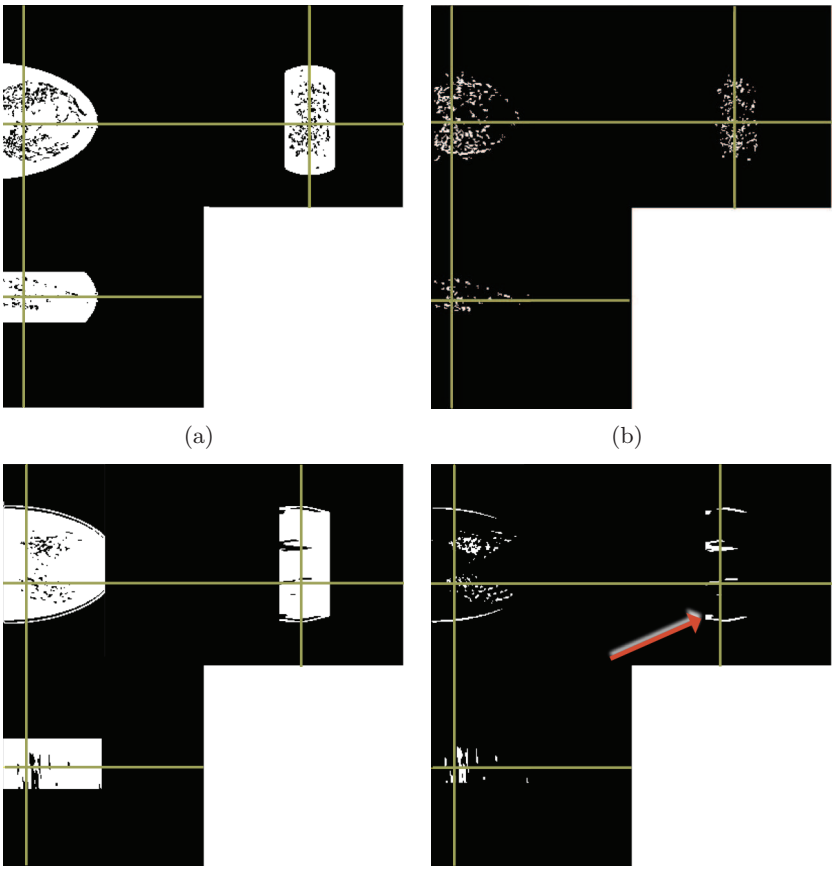

(a) (b)

(c) (d)

Figure 7.14: Segmentations of a) the adipose and b) the glandular tissues of the original volume and c) the adipose and d) the glandular tissues of the reconstructed volume.

The numerical values are given in Table 7.4. This time the reconstructed phantom is overestimating the mass of both adipose and glandular tissues. However, the artifact at the bottom of the phantom causes still an underestimation of the GIE and of its percentage to the total imparted energy.

Phantom	Mass (g)		Imparted energy (μJ/mGy)		
	Adipose	Glandular	AIE	GIE	GIE/TIE*
Original phantom	372.8	24.8	64	5.6	8.0%
Reconstructed phantom	426.3	30.6	82	4.2	4.9%
Relative error	-14%	-23%	-28%	25%	

* % of the total imparted energy in each phantom.

Table 7.4: Mass (g) and imparted energy per air kerma (μJ/mGy) for the original and segmented textured phantom.

7.6 Real patient cases

To illustrate the method, the segmentation chain and the GIE computation have been applied to the left and right breast tomosynthesis images of a patient. The images are amongst the first ones acquired just after intallation of the SenoClaire tomosynthesis system at the *Centre Hospitalier Jolimont-Lobbes, Entité Jolimontoise, La Louvière, Belgium*. Figure 7.15 shows one of the nine projection images ("FOR PROCESSING") of the left and right breast.

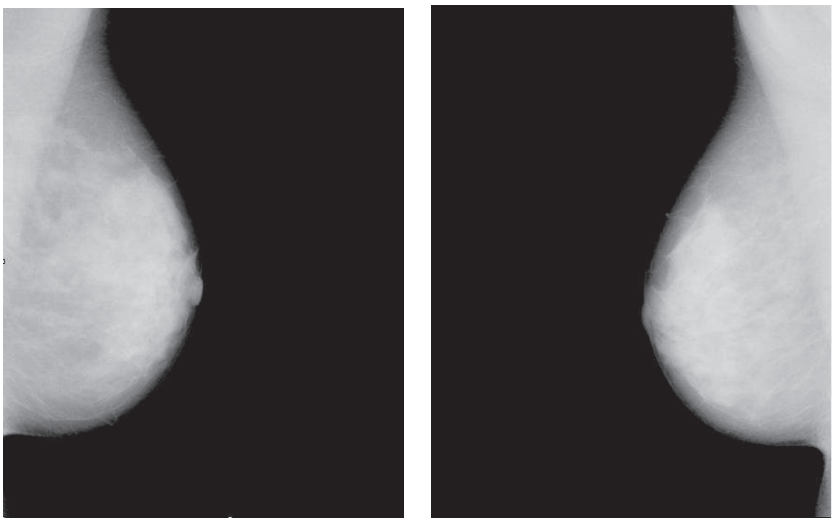

(a) (b)

Figure 7.15: Projection images of a a) left and b) right breasts.

The images are reconstructed with the standard ReconBox reconstruction algorithm, with a slice thickness of 1 mm in Figures 7.16. Again the shape of the breast is not what we expect from the real breast and comparable to what we found for the phantoms. This indicates that some corrections might be useful to compensate for the volume difference. The hyperintense artifact on the bottom is no longer present.
For both breasts the VBD was estimated at 18%. The segmented adipose and glandular volumes for the left and right breasts are shown in Figure 7.17. Also for the patient images the elongated shapes of the glandular tissue are found in the segmented volumes.

Phantom	Mass (g)		Imparted energy (μJ/mGy)		
	Adipose	Glandular	AIE	GIE	GIE/TIE$^+$
Left patient breast	387	95.1	72	19	20%
Right patient breast	363.8	89.4	75	18	19%

$^+$ % of the total imparted energy per air kerma in each phantom.

Table 7.5: Mass (g) and imparted energy per air kerma (μJ/mGy) for the reconstructed and segmented real breast images, for which the AGD is 1.49 mGy, and the entrance dose 0.57 mGy per view.

For this trial we did not exclude the pectoral muscle of the volume and included it with the glandular tissue. As for the computation of the VBD we find again the problem of poorly defined breast borders.
To compute the imparted energy for an examination everything in the image should be taken into account since it is all irradiated. To compute tissue-differentiated imparted energy the tissues with different radiation sensitivity should be distinguished. It might therefore be useful to label a third class, "muscle", and separate the voxels based on location, voxel value and connectivity. After labeling, one could then compute the GIE, the adipose imparted energy (AIE) and the muscular imparted energy (MIE). We propose this approach, even if, until now, the adipose and muscular tissues are considered to be without radiation risk in mammography.
We do not have the truth for these breasts, for which the acquisitions were part of a regular medical exam, so no other 3D imaging was performed. Table 7.5 lists the mass and GIE of the reconstruction.

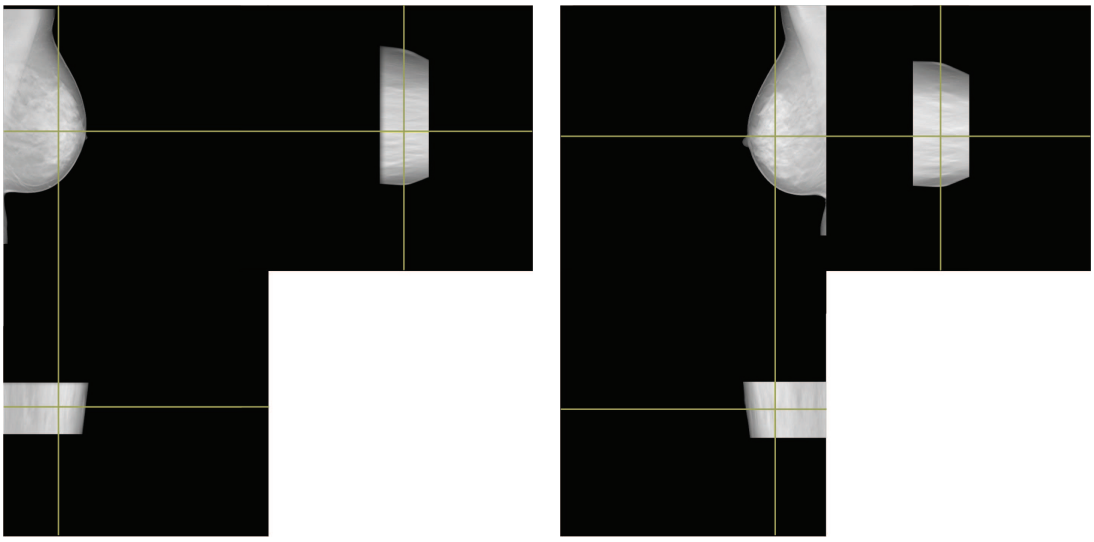

(a) (b)

Figure 7.16: Reconstructed volumes with a slice thickness of 1 mm of a) the left and b) right breast of Figure 7.15.

7.7 Conclusion on tomosynthesis segmentation

In this section we verified the possibility to label the voxels of a reconstructed tomosynthesis acquisition. The main limitation of the acquisition is the limited angular range, which has a non-negligible impact on the voxel values of the reconstructed volume. The required accuracy of the segmentation is evaluated through the difference between the GIE for the original phantom and for the reconstructed volume. The differences compared to the imparted energy of an adipose reference phantom are non-negligible (up to 84%). The segmentation for these simple objects could partially be corrected. However for real patient cases the artifacts are less distinct and thus less easy to correct.
A distinction must be made between the accuracy of the total GIE and the local GIE. The extensions of the objects average out the over- and underestimation of the energy to the

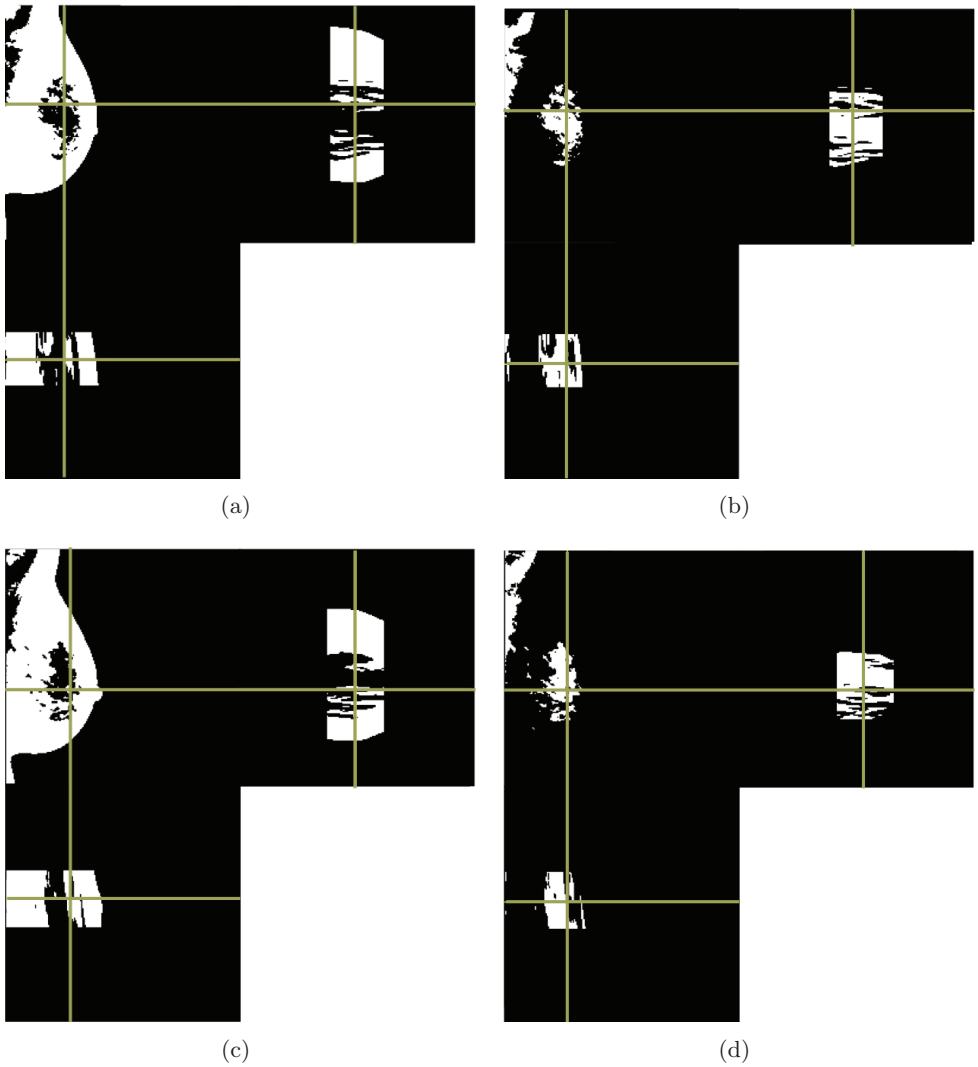

Figure 7.17: Segmented adipose volumes with a slice thickness of 1 mm of a) the left and c) right breasts and segmented glandular volume with a slice thickness of 1 mm of b) the left and d) the right breasts of Figure 7.15.

real object, resulting in an acceptable percentage of GIE as compared to the total imparted energy (less than 2.5% difference). With the current method it is thus not possible to obtain an accurate distribution of the energy imparted per glandular voxel. However it is possible to segment the reconstructed volumes and to compute the tissue-differentiated imparted energy of the entire volume, based on voxel values and an *a priori* knowledge of the VBD.

Discussion on Part II

Complements to the simulations

This part is a proof of concept so we limited the investigation to a single spectrum. As a consequence a more detailed evaluation is needed before the method can be implemented for routine use.

In our GIE computation we only used digital breast tomosynthesis (dBT) (generation of the projections followed by the dBT reconstruction) to determine the 3D distribution of the fibroglandular tissue. Once the volume was reconstructed, we computed the GIE only for the 0° projection and not for the complete dBT acquisition sequence. If we want to compute the corresponding GIE we have to run the MC computation again for each of the angulations, taking into account the different X-ray paths and their local imparted energy in every point for each projections. The VBD can also be computed for each projection but should obviously provide the same value whatever the angle.
Since the complete GIE computation chain includes the specificities of the equipment (geometry, step and shoot or continuous movement, beam quality, reconstruction algorithm), the same computation should be performed and validated for systems from the different vendors. In particular, due to the different sweep angles and reconstruction algorithms, the segmentation of the glandular tissue might be different or even not possible with an acceptable accuracy and therefore limit the possibility to localize the different tissue components and compute the GIE.

Complements to the segmentation

The segmentation as presented in this work relies on the computation of the VBD and a tomosynthesis acquisition. This is currently a strong limitation since dBT is neither generalized yet, nor accepted for breast screening in most countries. In dBT some of the 3D information is available as discussed in this work. Further improvements will result from the progress in reconstruction algorithms [67]. Some image processing can also be used to compensate for the known artifacts. In projection mammography no 3D information is available at all, making the proposed method not applicable. However the structure of the glandular tissue can be estimated based on some hypotheses. One of the possible hypotheses is that before the compression the structure of the fibroglandular tissue is locally isotropic. This would mean that the glandular structure in the z-direction (the direction of the X-rays) can be estimated from the local texture analysis [56] in the projection image, taking into account the deformation induced by the compression, the amount of tissue computed from the VBD and using some *a priori* knowledge of tissue such as tissue orientation [122].

Understanding GIE

Introducing the GIE in clinical practice will pose some difficulties. Mainly medical doctors and technologists, and even medical physicists, might be uncomfortable with the unusual units for "dose" and with the lack of reference values. However this situation is not new since medical users have really become familiar with the dose concepts, units, and orders of magnitude, for the last few years only, following the laws transcribing the Euratom Directive [5].

As a rule of thumb we can remind that the GIE for a homogenously distributed gland in a breast corresponding to the Dance model can be easily deduced from the AGD. As an example: for an AGD of 1 mGy = 1 mJ/kg, and a gland of 0.1 kg, the GIE will be 1 mJ/kg x 0.1 kg= 0.1 mJ = 100 μJ. For a thick breast, the AGD can reach 5 mGy, but corresponding to a breast mass of 2 kg, and for a conventional glandularity of 5%, giving the same 0.1 kg of gland, the GIE would be about 5 mGy x 0.1 kg = 0.5 mJ = 500μJ.

In real cases, for a same mass of glandular tissue additional differences in GIE are provoked by the differences in the glandular distributions. For example in the previous case, the gland is probably far from the skin, and a self-shielding effect occurs as for the previously described phantoms, generating further reduction of GIE, e.g. by 2 or more.

A direct application of this is the determination of the operating points of the mammographic equipment. Currently the AGD increases with breast thickness. One factor for that increase is the fact that when taking the conventional composition [16, 116] the glandularity of equivalent breast decreases with thickness, which increases the DgN (or c factor). Using GIE for radiation risk evaluation in the determination of the operating point of the automatic exposure controls would go the opposite way: less glandular content means less risk, and there would be less restriction increasing the dose for thick breasts, and therefore preserve image quality.

Chapter 8

General conclusions and perspectives

In this research project the main goals were a) to implement a method for the computation of the volumetric breast density (VBD), as described in the first part, and b) to propose an improved quantity for the assessment of individual radiation-induced risk, in particular during mammography, together with a method to quantify it, as described in the second part.

Different methods for the computation of the VBD had already been published when we started this thesis. We first studied them, then we selected the method which we considered as the most appropriate for our application, improved it and implemented it for the systems that we had access to. This method is based on the calibration of the mammography system acquisition chain with breast equivalent phantoms. Based on acquisition parameters, pixel values and the computation of a local thickness map, we are able to compute a breast density map and integrate it to obtain the VBD. We obtained an accuracy of 1.2%, which is comparable to the state-of-the-art [75]. The method is ready to be implemented in a product. A remaining question is the model calibration which has yet to be performed entirely on each system. However, a single test consisting in using the calibration of one system for another one provided acceptable results (see Figure 3.14). Our most important contribution in Part I resides in a new validation method applicable to *any* VBD computation, consisting in comparing its results with the VBD obtained from a thorax CT examination for the same patient. This validation method was applied to our VBD computation. We found an average deviation from the expected VBD_{MX} in comparison to the VBD_{CT} of less then 10%. Also this results are comparable to the state-of-the-art results for other validation methods [75].

Usually the VBD is computed as a breast cancer risk factor. Here in Part II we used it to compute the glandular dose and the imparted energy to the tissues during mammography. In X-ray imaging dosimetry there are new research possibilities for the individual measurements of absorbed dose and imparted energy, opening the way to the evaluation of the individual response, from the cellular level to that of the individual. Our contributions to this domain are more fundamental and question currently accepted measures. We believe that the average glandular dose is useful for some, but not all the applications for which it is currently used. In particular trying to make it more individual for the radiation risk assessment of each patient is, according to us, not a good direction. This was illustrated by the phantom with half the glandular incident surface, and thus a lower radiation risk,

having the same AGD. Therefore we proposed to replace AGD for that specific usage by the quantity Glandular Imparted Energy (GIE), which is the total energy imparted to the glandular tissue. This quantity is different from the known dose concepts and requires more complex computations. The local imparted energy has to be computed for all the places where glandular tissue is present. Therefore a volume reconstruction of the compressed breast indicating the localization of the glandular tissue is required. We showed in this work a proof of concept for the 3D segmentation of the glandular tissue for tomosynthesis images, based on the previously computed VBD computed from the 0° projection image, and allowing further computation of the local imparted energy with Monte-Carlo computations. Typical values of the GIE per entrance air kerma are below 20μJ/mGy. Our work is only at the start of a new era in individual radiation risk assessment and much work has still to be done before this metric can be computed easily and accurately before it can become a new standard. In particular the GIE computation must be extended to all clinical spectra and the segmentation of glandular tissue be worked out for the different tomosynthesis manufacturers. These developments around individualization are in agreement with international opinions as proved by the acceptance of our paper at the international conference on Radiation Protection in Medicine [61].

With this work and our publications on these topics we enlarged the amount of information that can be obtained from mammographic images and hope so to contribute to the discussion on the improvement of (individualized) breast cancer screening. The VBD plays an important role in the improvement of the efficiency of breast cancer screening by individualizing further the balance between risk and benefit [26, 71, 152], e.g. adjusting the frequency of examinations or the choice of "dose" levels.
The computation of the VBD is investigated by many groups and only minor improvements still can be made. However the interpretation of the VBD in the breast cancer risk models remains vague [32, 55] and the way of how the breast density impacts the inherent breast cancer risk is not yet well understood. Since the development of the robust VBD computation methods large studies can be set up [77, 129, 142] to integrate the VBD in risk models or to indicate eventual adjustments to the determination of the VBD inherent risk factor [88, 89, 148].
On the other side of the ALARA balance the (radiation) risk must be evaluated. Distinctions should be made between decisions concerning a whole population, such as breast cancer screening policy, where AGD is a good measure and those concerning individuals, such as acquiring extra examinations. Even though we suggested, in agreement to Hammerstein [66] to use the glandular imparted energy for individual radiation risk evaluation, additional measures can be considered too, such as the adipose imparted energy. Adipose tissue is not generally considered to be radiosensitive in the sense that cancers are developed within this tissue, but radiation can cause inflammation which can move glandular cells to develop a cancer [12]. Iterative interactions between radiobiologists, analyzing the cellular responses, and physicists, providing the most appropriate radiation measurements, will lead to the right measures for both collective and individual radiation risk assessment where individual sensitivity should also be taken into account. This debate is larger than mammography and concerns the entire medical X-ray imaging community.

Appendix A

Breast statistics

The data presented in this annex, were published at three conferences: N.Geeraert, R.Klausz, M.Lemuhot, D.Sundermann and S.Muller.Contribution of compression paddle flexibility to estimation of breast glandularity. ECR2011, Vienna, oral presentation. N. Geeraert, R. Klausz, D.Sundermann, S. Muller and H.Bosmans. Breast Size and Exposure Control Sensing Area Position A Large Sample Study. ECR2012, Vienna, eposter presentation. N.Geeraert, R.Klausz, M.Lemuhot, D.Sundermann and S.Muller. Comparing consequences of rigid and flexible compression paddles on the automatic optimization of parameters in mammography. Empec2011, Dublin, oral presentation.

In this chapter we present the statistical data of the three studies, discussing distributions of breast characteristics. The data were obtained via remote access to the technical data for each exposure. Neither patient data other than the breast thickness, obtained from the height of the compression paddle, nor any image according these data, were available. The data were retrieved for 60859 acquisitions worldwide and were sorted according to the size of the field of view (FOV), the angulation (ECR2011, ECR2012) and the paddle type (EMPEC2011).

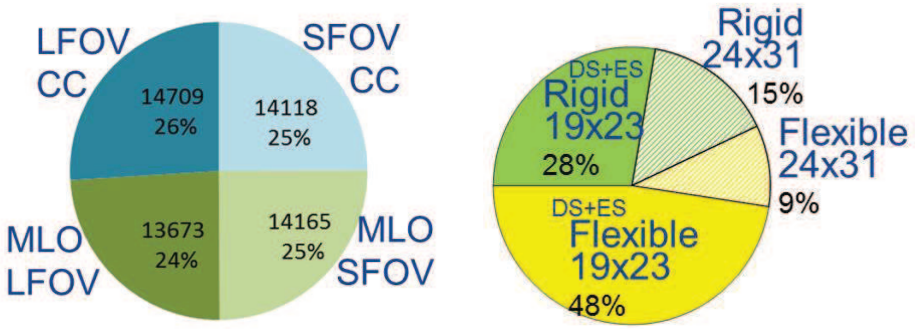

(a) (b)

Figure A.1: Distribution of the acquisitions worldwide over a) the FOV-angulation possibilities and b) the paddle type rigid versus flexible.

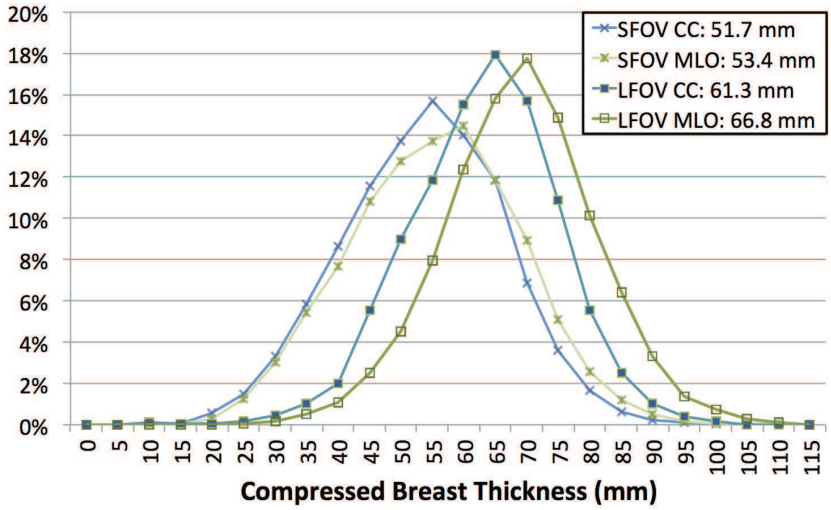

(a)

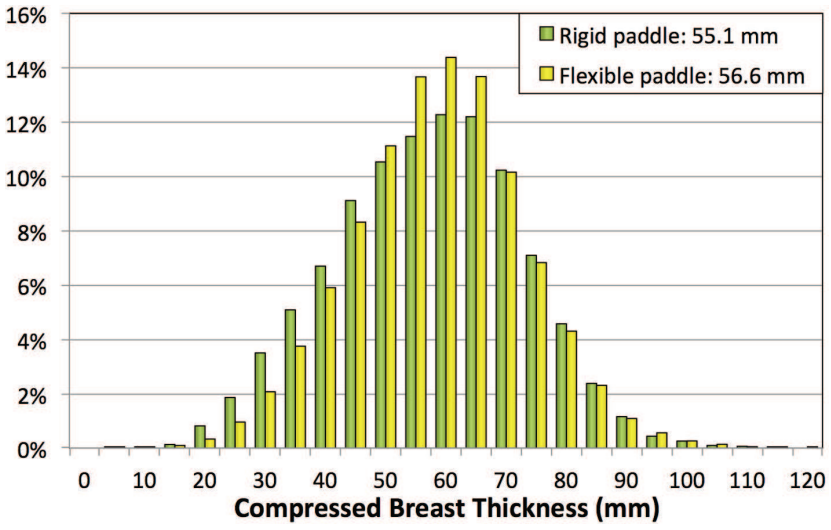

(b)

Figure A.2: Breast thickness distribution as a function of a) field of view (FOV) size, and cranio-caudal versus medio-lateral oblique angulation and b) rigid versus flexible paddle.

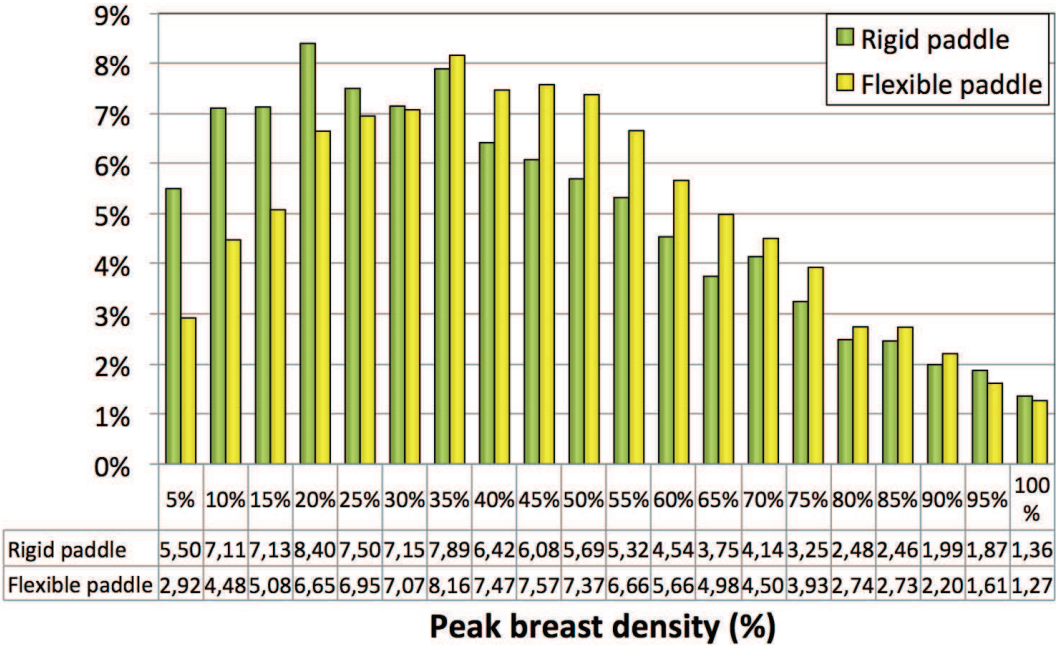

	5%	10%	15%	20%	25%	30%	35%	40%	45%	50%	55%	60%	65%	70%	75%	80%	85%	90%	95%	100 %
Rigid paddle	5,50	7,11	7,13	8,40	7,50	7,15	7,89	6,42	6,08	5,69	5,32	4,54	3,75	4,14	3,25	2,48	2,46	1,99	1,87	1,36
Flexible paddle	2,92	4,48	5,08	6,65	6,95	7,07	8,16	7,47	7,57	7,37	6,66	5,66	4,98	4,50	3,93	2,74	2,73	2,20	1,61	1,27

Figure A.3: Peak breast density distribution as a function of rigid versus flexible paddle.

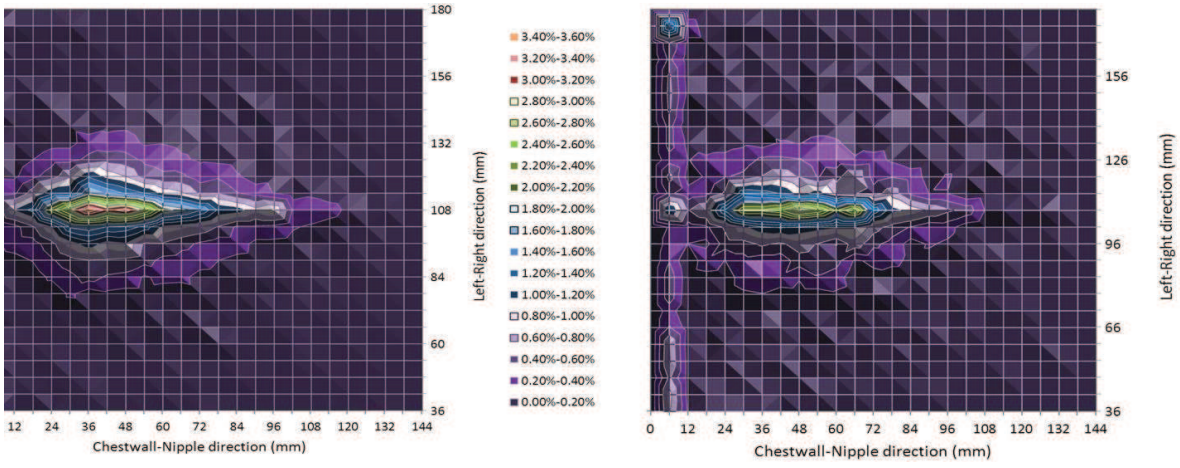

Figure A.4: Location of the AEC sensor, automatically placed at the densest region of the breast for rigid versus flexible paddle. Left: rigid paddle, right: flexible paddle.

Appendix B

Level estimators

Figure 14 gives an overview of the statistics of the errors of the density estimation for different level estimators discussed in Chapter 3. All estimators are polynomials but of different degrees in thickness and tube potential, expressed in the second part of the table. The statistics of the errors are expressed for all measurements together (fourth part), for measurements of 0% density only (fifth part), for measurements of 100% density only (sixth part) and for the measurements with density between 0% and 100% (seventh part). The first line of results evaluates the density model using the calibration measurements as reference acquisition. The last line is the selected best level model.

Comparing lines 2 to 13 with lines 14 and 15 of the table shows that a first degree in thickness or in tube potential is not sufficient to reach the aimed limits. Comparing the two last lines shows that a simple model for the level estimator $[ln(p/m)_A - ln(p/m)_G]$ is slightly better than the difference of two separately calibrated level models for $ln(p/m)_A$ and $ln(p/m)_G$.

	order of kV ln(I)a estimator	order of kv ln(I)g estimator	order of kV ln(i)a-ln(I)g estimator	order of T ln(I)a estimator	order of T ln(I)g estimator	order of T ln(i)a-ln(I)g estimator	number of calibration points for estimator ln(I)a	number of calibration points for estimator ln(I)g	number of calibration points for estimator ln(I)a-ln(I)g	number of points for validation	max min error density	max error density	stdev error density	median error density	average error density
RhRh	--	-	-	-	-	-	-	-	-	69	-3,3E-13	1,374514	0,311747	0	0,122747
RhRh	1	1	-	1	1	-	29	29	-	69	-14,8026	6,54672	5,073536	-0,90636	-1,15997
RhRh	1	-	1	1	-	1	29	-	29	69	-15,6345	6,335385	6,178899	-2,77323	-2,77832
RhRh	1	-	1	1	-	2	29	-	21	69	-11,9528	13,94795	4,437026	5,215809	4,524483
RhRh	1	-	1	1	-	2	29	-	21	32	2,151356	9,65267	1,977095	5,200489	5,494347
RhRh	1	1	-	2	1	-	34	29	-	69	-14,605	3,149109	3,564053	-2,28875	-3,19657
RhRh	1	1	-	2	2	-	34	29	-	69	-5,06738	3,315848	1,956696	-1,96663	-1,70809
RhRh	1	-	1	2	-	1	34	-	29	69	-13,4495	3,057457	4,53256	-4,66508	-4,94587
RhRh	1	-	1	2	-	2	34	-	29	69	-4,95798	3,326542	1,941804	-1,92348	-1,60464
RhRh	2	1	-	1	1	-	29	29	-	69	-14,7543	0,424628	3,44113	-2,5953	-3,45134
RhRh	2	2	-	1	1	-	29	29	-	69	-19,2518	0,398607	6,240922	-5,86982	-7,15696
RhRh	2	-	2	1	-	1	29	-	29	69	-6,24416	10,29943	4,435243	0,856426	2,332505
RhRh	2	-	2	2	-	1	29	-	29	69	-0,78572	10,63273	3,779496	2,946049	3,716553
RhRh	2	2	-	2	2	-	29	29	-	69	-0,78744	3,142515	1,211622	1,479852	1,278726
RhRh	2	-	2	2	-	2	29	-	29	69	-0,77016	1,416724	0,403084	0,0186	0,073457

min error on 0%	max error on 0%	st dev on error 0%	median on error 0%	average on error 0%	number of 0% points	min error on 100%	max error on 100%	st dev on error 100%	median on error 100%	average on error 100%	number of 100% points	min error on non 0 non 100 points	max error on non 0 non 100 points	st dev on error non 0 non 100 points	median on error non 0 non 100 points	average on error non 0 non 100 points	number of non 0 non 100 points	image number
0	0	0	0	0	29	0	0	0	0	0	29	0,147073	1,374514	0,335713	0,810971	0,769961	11	1
-4,41699	6,54672	2,758825	3,270698	3,03474	29	-14,8026	0,394268	3,644601	-5,26096	-5,76014	29	-2,58742	2,734751	1,6973	-0,40219	-0,09105	11	2
-4,68214	6,335385	2,75014	3,11327	2,875495	29	-15,6345	-2,13152	3,902031	-8,14617	-8,48932	29	-6,31352	1,956446	2,9148	-2,64845	-2,62754	11	3
-4,88935	7,421041	3,083371	3,701968	3,40882	29	-11,9528	13,94795	5,894243	6,463567	5,183955	29	3,747232	9,503427	1,87431	5,185169	5,72717	11	4
2,151356	5,966646	1,12259	3,701968	3,845301	11	5,478038	9,65267	1,440122	6,936793	7,052193	10	3,747232	9,503427	1,87431	5,185169	5,72717	11	5
-3,02299	3,149109	1,621253	-0,99856	-0,55974	29	-14,605	0,415278	3,607105	-5,50889	-5,91799	29	-3,96898	-1,03903	0,94336	-3,34233	-2,97355	11	6
-3,42408	3,315848	1,700934	-1,04116	-0,59141	29	-5,06738	1,543366	1,94904	-2,83708	-2,61987	29	-3,63933	-0,89999	0,974354	-2,4051	-2,24826	11	7
-3,06389	3,057457	1,576294	-0,96462	-0,54148	29	-13,4495	-4,66508	2,507685	-9,4253	-9,33636	29	-7,7565	-2,2282	1,725077	-4,76293	-4,98248	11	8
-3,40535	3,326542	1,70459	-1,04693	-0,58959	29	-4,95798	2,299745	2,031159	-2,63104	-2,40619	29	-3,41062	-0,76053	0,86775	-2,25253	-2,21675	11	9
-5,52617	0,424628	1,647932	-1,15491	-1,33215	29	-14,7543	0,417738	3,687571	-5,48966	-5,97472	29	-4,34916	0,363794	1,450573	-2,78108	-2,38575	11	10
-5,25201	0,398607	1,558453	-1,05884	-1,23418	29	-19,2518	-7,98437	3,010628	-13,5291	-13,5472	29	-10,6972	-1,19045	3,294378	-5,86982	-5,92462	11	11
-6,24416	0,478703	1,838273	-1,26607	-1,495	29	-3,65507	10,29943	3,857647	6,465071	5,70472	29	-0,23497	7,827272	2,363877	3,593831	3,532813	11	12
-0,78572	0,713591	0,371436	0,02724	-0,01326	29	1,24423	10,63273	2,423799	7,514576	7,186463	29	1,991017	7,816701	2,126727	4,270054	4,401741	11	13
-0,78744	0,680161	0,360069	0,02564	-0,01549	29	1,616496	3,142515	0,352285	2,347241	2,398381	29	0,861284	3,084645	0,738956	1,479852	1,738943	11	14
-0,77016	0,665212	0,351957	0,025019	-0,01518	29	-0,55407	0,659327	0,294414	-0,06189	-0,0388	29	-0,0864	1,416724	0,383907	0,618402	0,603101	11	15

Figure B.1: Statistics of the errors for different polynomials as level model.

List of publications

Peer reviewed scientific articles

1. N. Geeraert, R. Klausz, L. Cockmartin, S. Muller, I. Bloch, H. Bosmans. Comparison of Volumetric Breast Density Estimations from Mammography and Thorax CT. *Physics in Medicine and Biology* 59:4391-4409, 2014.

2. N. Geeraert, R. Klausz, S. Muller, I. Bloch, H. Bosmans. Evaluation of exposure in mammography: limitations of average glandular dose and proposal of a new quantity. *Radiation Protection Dosimetry* In press, Special Issue December 2014.

Conference proceedings

1. N.Geeraert, R.Klausz, S.Muller, I.Bloch, H.Bosmans. Breast characteristics and dosimetric data in X-ray mammography a large sample survey. *International conference on Radiation Protection in Medicine (IAEA) Setting the scene for next decade* CN-192, 3-7/12/2012, Bonn, Germany

2. N.Geeraert, R.Klausz, P. Giudici, L.Cockmartin, H.Bosmans. Dual-energy CT characterization of X-ray attenuation properties of breast equivalent material plates. *Society of Photographic Instrumentation Engineers, Medical Imaging* Volume 8313, 4V, 4-9/02/2012, San Diego, CA

3. E. Shaheen, F. Bemelmans, C. Van Ongeval, F. De keyzer, N. Geeraert and H. Bosmans. The investigation of different factors to optimize the simulation of 3D mass models in breast tomosynthesis. *International Workshop on Breast Imaging proceedings* 7/2014, Japan, p.528-535

4. L.Vancamberg, N.Geeraert, R.Iordache, G.Palma, S.Muller, R.Klausz. 3D density estimation in digital breast tomosynthesis: application to needle path planning for breast biopsy. *Society of Photographic Instrumentation Engineers, Medical Imaging* Volume 7964, 0D, 12-17/02/2011, Orlando, Fl

Oral presentations

1. N. Geeraert, R. Klausz, S. Muller, I. Bloch, H. Bosmans. Evaluation of exposure in mammography: limitations of average glandular dose and proposal of a new quantity. *International conference on Radiation Protection in Medicine.* 30/05-2/06/2014, Varna, Bulgaria

2. N.Geeraert, R.Klausz, I.Bloch, S.Muller, H.Bosmans. Accuracy of Breast Density Estimation from Mammographic Images. *Belgian Hospital Physicist Association Annual meeting.* 1-2/02/2013, Mechelen, Belgium

3. N.Geeraert, R.Klausz, M.Lemuhot, D.Sundermann, S.Muller. Comparing consequences of rigid and flexible compression paddles on the Automatic Optimization of Parameters in mammography. *European Medical Physicist and Engineering Conference.* 1-3/09/2011, Dublin, Ireland

4. N. Geeraert, R. Klausz, M. Lemuhot, D. Sundermann, S. Muller. Contribution of compression paddle flexibility to estimation of breast glandularity. *European Congress of Radiology.* 3-7/03/2011, Vienna, Austria

Poster presentations

1. N. Geeraert, R. Klausz, D. Sundermann, S. Muller, H. Bosmans. Breast size and exposure control sensing area position: a large sample study. *European Congress of Radiology.* 1-5/03/2012, Vienna, Austria

2. N.Geeraert, R.Klausz, L.Desponds, S.Muller, I.Bloch, H.Bosmans. Impact of breast glandular description on average glandular dose and radiation risk assessment in mammography. *Radiological Society of North America Annual meeting.* 1-7/12/2013, Chicago, Il

Bibliography

[1] http://www.medicinenet.com/breast-cancer/article.htm, (July 30, 2012).

[2] http://www.areyoudense.org (March 24 , 2010).

[3] http://cern.ch/geant4.

[4] http://volparasolutions.com/solutions/volparadose/, (December 4, 2013).

[5] COUNCIL DIRECTIVE 97/43/EURATOM of 30 June 1997 on health protection of individuals against the dangers of ionizing radiation in relation to medical exposure, and repealing Directive 84/466/Euratom Official Journal of EU, L180, July 1997.

[6] Part 1: ten highlights in health statistics. http://www.who.int/whosis/whostat/enwhs08-part1.pdf, World Health Organisation, 2008.

[7] GLOBOCAN 2012: Estimated cancer incidence, mortality and prevalence worldwide in 2012. http://globocan.iarc.fr/pages/fact-sheets-population.aspx (february 16, 2014), International Agency for Research on Cancer - World Health Organisation, 2012.

[8] Breast cancer screening (Physician Data Query®). http://www.cancer.gov/cancertopics/pdq/screening/breast/healthprofessional/page1 (february 16, 2014), National Cancer Insitute - National Health Institute, 2014.

[9] A.L. Albright and J.S. Stern. *Adipose tissue.* Encyclopedia of Sports Medicine and Science. T.D. Fahey, 1998.

[10] O. Alonzo-Proulx, N. Packard, J.M. Boone, A. Al-Mayah, K.K. Brock, S.Z. Shen, and M.J. Yaffe. Validation of a method for measuring the volumetric breast density from digital mammograms. *Physics in Medicine and Biology*, 55:3027–3044, 2010.

[11] A.H. Andersen and A.C. Kak. Simultaneous algebraic reconstruction technique (SART): A superior implementation of the ART algorithm. *Ultrasonic Imaging*, 6(1):81–94, 1984.

[12] S. Baatout. Private communication, 2012.

[13] F.R. Bailey, W.M. Copenhaver, and D.D. Johnson. *Bailey's Textbook of Histology.* Williams and Wilkins, Fourteenth edition, 1958.

[14] P.R. Bakic, AK. Carton, D. Kontos, C. Zhang, A.B. Troxel, and A.D.A. Maidment. Breast percent density: Estimation on digital mammograms and central tomosynthesis projections. *Radiology*, 252:40–49, 2009.

[15] M. Becich. Pathology: why the future of medicine's gold standard is to go digital. Invited lecture at *SPIE Medical Imaging*, 2012.

[16] J.R. Beckett and C.J. Kotre. Dosimetric implications of age related glandular changes in screening mammography. *Physics in Medicine and Biology*, 45:801–813, 2000.

[17] L. Beels. *DNA double-strand breaks induced by low-dose exposure to X-rays used in medical diagnostics*. PhD thesis, Universiteit Gent, 2011.

[18] A. Beer. Bestimmung der absorption des rothen lichts in farbigen flussigkeiten. *Annalen der Physik und Chemie*, 86:78–88, 1852.

[19] J. Berger, J.H. Hubbell, S.M. Seltzer, J. Chang, J.S. Coursey, R. Sukumar, D.S. Zucker, and K. Olsen. Xcom: Photon cross sections database, national institute of standards and technology. *National Institute of Standards and Technology*, 1990.

[20] A. Bleyer and H.G. Welch. Effect of three decades of screening mammography on breast-cancer incidence. *The New England Journal of Medicine*, 367:1998–2005, 2012.

[21] J.W. Boag, A.J. Stacey, and R. Davis. Radiation exposure to the patient in xeroradiography. *British journal of radiology*, 49:253–261, 1976.

[22] J.M. Boone. Glandular breast dose for mono-energetic and high-energy X-ray beams: Monte Carlo assessment. *Radiology*, 213:23–37, 1999.

[23] J.M. Boone. Normalized glandular dose (DgN) coefficients for arbitrary X-ray spectra in mammography: computer-fit values of Monte Carlo derived data. *Medical Physics*, 29:869–875, 2002.

[24] J.M. Boone, T.R. Nelson, K.K. Lindfors, and J.A. Seibert. Dedicated breast CT: radiation dose and image quality evaluation. *Radiology*, (3):657–667, december 2001.

[25] P. Bouguer. *Essai d'Optique, sur la gradation de la lumière*. 1729.

[26] N.F. Boyd, L.J. Martin, M.J. Yaffe, and S. Minkin. Mammographic density and breast cancer risk: current understanding and future prospects. *Breast Cancer Research*, 13:223–235, 2011.

[27] J.W. Byng, N.F. Boyd, E. Fishell, R.A. Jong, and M.J. Yaffe. The quantitative analysis of mammographic densities. *Physics in Medicine and Biology*, 39:1629–1638, 1994.

[28] J.W. Byng, N.F. Boyd, E. Fishell, R.A. Jong, and M.J. Yaffe. Automated analysis of mammographic densities. *Physics in Medicine and Biology*, 41:909–923, 1996.

[29] J. Cameron. Dose equivalent out - imparted energy in. *Health Physics Society (HPS) Newsletter*, 1992.

[30] A.K. Carton, A. Grisey, P. Milioni de Carvalho, C. Dromain, and S. Muller. A virtual human breast phantom using surface meshes and geometric internal structures. In H. Fujita et al., editor, *International Workshop on Breast Imaging*, volume 8539, pages 356–363, 2014.

[31] H. Chan and K. Doi. Radiation dose in diagnostic radiology: Monte Carlo simulation studies. *Medical Physics*, 11:480–490, 1984.

[32] J. Chen, D. Pee, R. Ayyagari, B. Graubard, C. Schairer, C. Byrne, J. Benichou, and M.H. Gail. Projecting absolute invasive breast cancer risk in white women with a model that includes mammographic density. *Journal of National Cancer Institute*, 98:1215–1226, 2006.

[33] C.J. D'Orsi, L.W. Bassett, W.A. Berg et al. *BI-RADS: Mammography*, pages 179–180. C.J. D'Orsi, E.B. Mendelson, D.M. Ikeda, et al: Breast Imaging Reporting and Data System: ACR BI-RADS - Breast Imaging Atlas, Reston, VA, American College of Radiology, Fourth edition, 2003.

[34] C. Colin, C. Devic, A. Nol, M. Rabilloud, M.-T. Zabot, S. Pinet-Isaac, S. Giraud, B. Riche, P.-J. Valette, C. Rodriguez-Lafrasse, and N. Foray. DNA double-strand breaks induced by mammographic screening procedures in human mammary epithelial cells. *International Journal of Radiation Biology*, 87:1103–1112, 2011.

[35] Y.S. Cordoliani. La dose efficace n'existe pas... pourtant elle augmente! *Journal de Radiology*, 91:449–450, 2010.

[36] K. Cranley, B.J. Gilmore, G.W.A. Fogarty, and L. Desponds. Ipem-report 78: Catalogue of diagnostic X-ray spectra and other data. *The institute of physics and engineering in medicine (IPEM)*, York (UK), 1997.

[37] D. Dance and K.C. Young. Estimation of mean glandular dose for contrast enhanced digital mammography: factors for use with the UK, European and IAEA breast dosimetry protocols. *Physics in Medicine and Biology*, 59:2127–2137, 2014.

[38] D.R. Dance. The Monte Carlo calculation of integral radiation dose in xeromammography. *Physics in Medicine and Biology*, 25:25–37, 1980.

[39] D.R. Dance. Monte Carlo calculation of conversion factors for the estimation of mean glandular breast dose. *Physics in Medicine and Biology*, 35:1211–1219, 1990.

[40] D.R. Dance, R.A. Hunt, P.R. Bakic, A.D.A. Maidment, M. Sandborg, G. Ullman, and G.A. Carlsson. Breast dosimetry using high-resolution voxel phantoms. *Radiation protection dosimetry*, 114:359–363, 2005.

[41] D.R. Dance, C.L. Skinner, K.C. Young, J.R. Beckett, and C.J. Kotre. Additional factors for the estimation of mean glandular breast dose using the UK mammography dosimetry protocol. *Physics in Medicine and Biology*, 45:3225–3240, 2000.

[42] D.R. Dance, D.L. Skinner, and G.A. Carlsson. Breast dosimetry. *Applied Radiation and Isotopes*, 50:185–203, 1999.

[43] D.R. Dance, K.C. Young, and R.E. van Engen. Further factors for the estimation of mean glandular dose using the United Kingdom, European and IAEA breast dosimetry protocols. *Physics in Medicine and Biology*, 54:4361–4372, 2009.

[44] D.R. Dance, K.C. Young, and R.E. van Engen. Estimation of mean glandular dose for breast tomosynthesis: factors for use with the UK, European and IAEA breast dosimetry protocols. *Physics in Medicine and Biology*, 56:453–471, 2011.

[45] P. Milioni de Carvalho. *Low-Dose 3D Quantitative Vascular X-ray Imaging of the Breast*. PhD thesis, Université Paris Sud, 2014.

[46] S.F. Dehkordy, R.C. Carlos, K.S. Hall, and V.K. Dalton. Novel data sources for women's health research: Mapping breast screening online information seeking through google trends. *Academic Radiology*, In press, 2014.

[47] R.D. Deslattes. Estimates of X-ray attenuation coefficients for the elements and their compounds. *Acta Crystallographica*, A25:89–93, 1969.

[48] L. Desponds and R. Klausz. Automatic estimation of breast composition with mammographic X-ray systems. *Radiological Society of North America (RSNA) - Annual meeting*, 1994.

[49] B. Dirat, L. Bochet, M. Dabek, D. Daviaud, S. Dauvillier, B. Majed, Y.Y. Wang, A. Meulle, B. Salles, S. Le Gonidec, I. Garrido, G. Escourrou, P. Valet, and C. Muller. Cancer-associated adipocytes exhibit an activated phenotype and contribute to breast cancer invasion. *Cancer research*, 71:2455–2465, 2011.

[50] M. Durnez. Comparison of density estimates from (3D) chest CT and 2D mammography. Master-thesis, KU Leuven, 2011.

[51] P.P. Fatouros, S.E. Skubic, and H. Goodman. The development and use of realistically shaped, tissue- equivalent phantoms for assessing the mammographic process. *Radiology*, 157:32, 1985.

[52] N. Foray and C. Colin. Relationship between radiosensitivity, initial DNA damage, apoptosis and gen expression: between reproducible works and technical artefacts. *Breast*, 22:185, 2013.

[53] N. Foray, C. Colin, and M. Bourguignon. 100 years of individual radiosensitivity: How we have forgotten the evidence. *Radiology*, 264, 2012.

[54] E.E. Fowler, T.A. Sellers, B. Lu, and J.J. Heine. Breast Imaging Reporting and Data System (BI-RADS) breast composition descriptors: automated measurement development for full field digital mammography. *Medical Physics*, 40:113502, 2013.

[55] M.H. Gail, W.F. Anderson, M. Garcia-Closas, and M.E. Sherman. Absolute risk models for subtypes of breast cancer. *Journal of National Cancer Institute*, 22:1657–1659, 2007.

[56] B. Galerne, Y. Gousseau, and J.M. Morel. Random phase textures: Theory and synthesis. 20:257–267, 2011.

[57] N. Geeraert, R. Klausz, L. Cockmartin, S. Muller, H. Bosmans, and I. Bloch. Comparison of volumetric breast density estimations from mammography and thorax CT. *Physics in Medicine and Biology*, 59:4391–4409, 2014.

[58] N. Geeraert, R. Klausz, L. Desponds, S. Muller, I. Bloch, and H. Bosmans. Impact of breast glandular description on average glandular dose and radiation risk assessment in mammography. *Radiological Society of North America (RSNA) - Annual meeting*, 2013.

[59] N. Geeraert, R. Klausz, P. Giudici, L. Cockmartin, and H. Bosmans. Dual-energy CT characterization of X-ray attenuation properties of breast equivalent material plates. In *SPIE Medical Imaging*, volume 8313 of *Physics of Medical Imaging*, 2012.

[60] N. Geeraert, R. Klausz, S. Muller, I. Bloch, and H. Bosmans. Breast characteristics and dosimetric data in X-ray mammography - a large sample survey. In *International Conference on Radiation Protection in Medicine - Setting the Scene for the Next Decade*, volume CN-192, page 15, Bonn, Germany, December 2012.

[61] N. Geeraert, R. Klausz, S. Muller, I. Bloch, and H. Bosmans. Evaluation of exposure in mammography: Limitations of average glandular dose and proposal of a new quantity. *Radiation Protection Dosimetry*, Special issue, *In press*, 2014.

[62] N.A. Gkanatios and W. Huda. Computation of energy imparted in diagnostic radiology. *Medical Physics*, 24:571–579, 1997.

[63] G. Van Gompel, N. Buls, K. Nieboer, and J. de Mey. Accuracy estimation of spectral attenuation curves obtained by Dual Energy CT. *European Conference on Radiology - Annual meeting*, 2011.

[64] I.T. Gram, E. Funkhouser, and L. Tabar. The Tabar classification of mammographic parenchymal patterns. *European journal of radiology*, 24:131–136, 1997.

[65] B. Grosjean. *Lesion Detectability in Digital Mammography: Impact of Texture*. PhD thesis, Ecole Centrale Paris, 2007.

[66] G.R. Hammerstein, D.W. Miller, D.R. White, M.E. Masterson, H.Q. Woodard, and J.S. Laughlin. Absorbed radiation dose in mammography. *Radiology*, 130:485–491, 1979.

[67] E. Haneda, E. Tkaczyk, G. Palma, R. Iordache, S. Zelakiewicz, S. Muller, and B. De Man. Towards a dose reduction strategy using model-based reconstruction with limited-angle tomosynthesis. In *SPIE Medical Imaging*, volume 9033 of *Physics of Medical Imaging*, 2014.

[68] B.L. Hart, R.T. Steinbock, F.A. Mettler Jr., D.R. Pathak, and S.A. Bartow. Age and race related changes in mammographic parenchymal patterns. *Cancer*, 63:2537–2539, 1989.

[69] K. Hartman, R. Highnam, R. Warren, and V. Jackson. Volumetric assessment of breast tissue composition from FFDM images. In E.A. Krupinski, editor, *International Workshop on Digital Mammography*, volume 5116, pages 33–39, 2008.

[70] I.H.R. Hauge, P. Hogg, K. Szczepura, P. Connolly, G. McGill, and C. Mercer. The readout thickness versus the measured thickness for a range of screen film mammography and full-field digital mammography units. *Medical Physics*, 39:263–271, 2012.

[71] Dépistage du cancer du sein en France Haute Autorité de Santé. Identification des femmes à haut risque et modalité de dépistage, volet 2, recommendations de santé publique, Mars 2014.

[72] R. Heidsieck. FR 2648229 (A1) - Procédé d'étalonnage d'un système radiologique et de mesure de l'épaisseur équivalente d'un objet. *Patent*, june 1989.

[73] J.J. Heine, E.E. Fowler, and C.I. Flowers. Full field digital mammography and breast density: Comparison of calibrated and non-calibrated measurements. *Academic Radiology*, 18:1430–1436, 2012.

[74] R. Highnam, M. Brady, and B. Shepstone. A representation for mammographic image processing. *Medical Imaging Analysis*, 1:1–18, 1996.

[75] R. Highnam, S.M. Brady, M.J. Yaffe, N. Karssemeijer, and J. Harvey. Robust breast composition measurement - Volpara. In J. Marti et al., editor, *International Workshop on Digital Mammography*, volume 6136, page 342, 2010.

[76] R. Highnam, X. Pan, R. Warren, M. Jeffreys, G.D. Smith, and M. Brady. Breast composition measurements using retrospective standard mammogram form (SMF). *Physics in Medicine and Biology*, 51:2695–2713, 2006.

[77] University hospital of South Manchester. PROCAS study. http://www.uhsm.nhs.uk/research/Pages/PROCASstudy.aspx, 2010.

[78] S.Y. Huang, J.M. Boone, K. Yang, A.L.C. Kwan, and N.J. Packard. The effect of skin thickness determined using breast CT on mammographic dosimetry. *Medical Physics*, 35:1199–1206, 2008.

[79] W. Huda, J. McLellan, and Y. McLellan. How will the new definition of 'effective dose' modify estimates of dose in diagnostic radiology? *Journal of Radiological Protection*, 11:241–247, 1991.

[80] Z. Huo, M.L. Giger, D.E. Wolverton, W. Zhong, S.Cumming, and O.I. Olopade. Computerized analysis of mammographic parenchymal patterns for breast cancer risk assessment: Feature selection. *Medical Physics*, 27:4–12, 2000.

[81] ICRP. The 2007 recommendations of the international commission on radiological protection. ICRP Publication 103. Ann. ICRP 37 (2-4), 2007.

[82] R.W. Jakes, S.W. Duffy, F.C. Ng, F. Gao, and E.H. Ng. Mammographic parenchymal patterns and risk of breast cancer at and after a prevalence screen in Singaporean women. *International Journal of Epidemiology*, 29:11–19, 2000.

[83] M. Jeffreys, R. Warren, R. Highnam, and G.D. Smith. Breast cancer risk factors and a novel measure of volumetric breast density: cross-sectional study. *British journal of cancer*, 98:210–216, 2007.

[84] P.C. Johns and M.J. Yaffe. X-ray characterisation of normal and neoplastic breast tissues. *Physics in Medicine and Biology*, 32:675–695, 1986.

[85] M. Karlsson, K. Nygren, G. Wickman, and G. Hettinger. Absorbed dose in mammary radiography. *Acta Radiologica Therapy Physics Biology*, 15:252–258, 1976.

[86] J. Kaufhold, J.A. Thomas, and J.W. Eberhard. Longitudinal retrospective study of breast tissue composition. In H.O. Peitgen et al., editor, *International Workshop on Digital Mammography*, pages 486–490, 2002.

[87] J. Kaufhold, J.A. Thomas, J.W. Eberhard, C.E. Galbo, and D.E.G. Trotter. A calibration approach to glandular tissue composition estimation in digital mammography. *Medical Physics*, 29:1867–1880, 2002.

[88] B.M. Keller, J. Chen, E. Conant, and D. Kontos. Breast density and parenchymal texture measures as potential risk factors for estrogen-receptor positive breast cancer. In *SPIE Medical Imaging*, volume 9035 of *Medical Imaging*, 2013.

[89] B.M. Keller, E.F. Conant, H.Oh, and D. Kontos. Breast cancer risk prediction via area and volumetric estimates of breast density. In A.D.A. Maidment et al., editor, *Breast Imaging*, volume 11, pages 236–243, 2012.

[90] C. Kerrison, O. Putt, J.C. Sergeant, T. Dunn, J. Diffey, S.M. Astley, and A. Hufton. Breast density measurement in full-field digital mammography: system calibration and stability. In A.D.A. Maidment et al., editor, *Breast Imaging*, volume 7361, page 545, 2012.

[91] R. Klausz. FR 2939200 (B1) - Procédé et dispositif d'acquisition d'images médicales. *Patent*, july 2013.

[92] R. Klausz and N. Shramchenko. Dose to population as a metric in the design of optimised exposure control in digital mammography. *Radiation protection dosimetry*, 114:369–74, 2005.

[93] R. Klein, H. Aichinger, J. Dierker, J.T.M. Jansen, S. Joite-Barfu, M. Sabel, R. Schulz-Wendtland, and J. Zoetelief. Determination of average glandular dose with modern mammography units for two large groups of patients. *Physics in Medicine and Biology*, 42:651–671, 1997.

[94] D. Kopans. Arguments against mammography screening continue to be based on faulty science. *The Oncologist*, 19:107–112, 2014.

[95] D.B. Kopans. Basic physics and doubts about relationship between mammographically determined tissue density and breast cancer risk. *Radiology*, 246:348–353, 2008.

[96] P. Kovesi. *Image Features from Phase Congruency*. Videre. MIT Press, Cambridge, 1999.

[97] J.H. Lambert. *Photometria sive de mensura et gradibus luminis, colorum et umbrae*. 1760.

[98] R.J. Last. *Anatomy: regional and applied*. Churchill Livingstone-Edinburgh London Melbourn and New York, Seventh edition, 1984.

[99] J. Li, K. Humphreys, L. Eriksson, G. Edgren, K. Czene, and P. Hall. Mammographic density reduction is a prognostic marker of response to adjuvant tamoxifen therapy in postmenopausal patients with breast cancer. *Journal of Clinical Oncology*, 31:1–10, 2013.

[100] X.Z. Li, S. Williams, and M.J. Bottema. Texture and region dependent breast cancer risk assessment from screening mammograms. *Pattern recognition letters*, 36:117–124, 2014.

[101] M.P. Lisanti, A. Tsirigos, S. Pavlides, K.J. Reeves, M. Peiris-Pags, A.L. Chadwick, R. Sanchez-Alvarez, R. Lamb, A. Howell, U.E. Martinez-Outschoorn, and F. Sotgia. JNK1 stress signaling is hyper-activated in high breast density and the tumor stroma: Connecting fibrosis, inflammation, and stemness for cancer prevention. *Cell Cycle*, 13:580–599, 2014.

[102] L.W. Lu, T.K. Nishino, T. Khamapirad, J.J. Grady, M.H. Leonard Jr., and D.G. Brunder. Computing mammographic density from a multiple regression model constructed with image-acquisition parameters from a full-field digital mammographic unit. *Physics in Medicine and Biology*, 52:4905–4921, 2007.

[103] S. Malkov, J. Wang, and J. Shepherd. Improvements to single energy absorptiometry. Method for digital mammography to quantify breast tissue density. In E.A. Krupinski et al., editor, *International Workshop on Digital Mammography*, volume 5116, pages 1–8, 2008.

[104] B. De Man, S. Basu, N. Chandra, B. Dunham, P. Edic, and M. Iatrou. Catsim: a new computer assisted tomography simulation environment. In *SPIE Medical Imaging*, volume 6510, pages 1–8, 2007.

[105] N.W. Marshall and H. Bosmans. Measurements of system sharpness for two digital breast tomosynthesis systems. *Physics in Medicine and Biology*, 57:7629–7650, 2012.

[106] L.J. Martin and N.F. Boyd. Mammographic density: potential mechanisms of breast cancer risk associated with mammographic density hypotheses based on epidemiological evidence. *Breast Cancer Research*, 10:201–214, 2008.

[107] G.E. Mawdsley, A.H. Tyson, C.L. Peressotti, R.A. Jong, and M.J. Yaffe. Accurate estimation of compressed breast thickness in mammography. *Medical Physics*, 36:577–586, 2009.

[108] V.A. McCormack and I. dos Santos Silva. Breast density and parenchymal patterns as markers of breast cancer risk: A meta-analysis. *Cancer Epidemiology, Biomarkers and Prevention*, 15:1159–1169, 2006.

[109] T. Mertelmeier, J. Orman, W. Haerer, and M.K. Dudam. Optimizing filtered backprojection reconstruction for a breast tomosynthesis prototype device. In *SPIE Medical Imaging*, volume 6142, page 0F, 2006.

[110] N. Metropolis and S. Ulam. The Monte Carlo Method. *Journal of the American Statistical Association*, 44:335–341, 1949.

[111] A.B. Miller, C. Wall, C. Baines, P. Sun, T. To, and S.A. Narod. Twenty five year follow-up for breast cancer incidence and mortality of the canadian national breast screening study: randomised screening trial. *British Medical Journal*, 348:g366, 2014.

[112] Institute of Physical Sciences in medicine. The commissioning and routine testing of mammographic X-ray systems. Topic group report 59, 1989.

[113] D.L. Page and A.C. Winfield. The dense mammogram. *American Journal of Roentgenology*, 147:487–489, 1986.

[114] V. Patel, R. Highnam, C. Tromans, R.J. Pizzutiello, and S. Destounis. Patient specific average glandular dose in mammogrpaphy. In *The international journal of medical physics research and practice*, volume 40, page 96. American Association of Physicists in Medicine, 2013.

[115] O. Pawluczyk, B.J. Augustine, M.J. Yaffe, D. Rico, J. Yang, G.E. Mawdsley, and N.F. Boyd. A volumetric method for estimation of breast density on digitized screen-film mammograms. *Medical physics*, 30:352–364, 2003.

[116] N. Perry, M. Broeders, C. de Wolf, S. Törnberg, R. Holland, and L. von Karsa. *European guidelines for quality assurance in breast cancer screening and diagnosis*. Fourth edition, 2006.

[117] M.E. Poletti, O.D. Goncalves, and I. Mazzaro. X-ray scattering from human breast tissues and breast-equivalent materials. *Physics in Medicine and Biology*, 47:47–63, 2002.

[118] S.T.L. Polhmann, J. Hewes, A.I. Williamson, J.C. Sergeant, A. Hufton, A.Gandhi, C.J. Taylor, and S.M. Astley. Breast volume measurements using a games console input device. In H. Fujita et al., editor, *International Workshop on Digital Mammography*, volume 8539, pages 666–673, 2014.

[119] M. Porras-Chaverri, J. Vetter, and R. Highnam. Retrospective determination of personalized mean glandular dose coefficients for conventional mammography using heterogeneously layered breast models. *Medical Physics*, 40:511, 2013.

[120] M.A. Porras-Chaverri, J.R. Vetter, and R. Highnam. Personalizing mammographyic dosimetry using multilayered anatomy-based breast models. In A.D.A. Maidment et al., editor, *Breast Imaging*, pages 134–140, 2012.

[121] X. Qin, G. Lu, I. Sechopoulos, and B. Fei. Breast tissue classification in digital breast tomosynthesis images based on global gradient minimization and texture features. In *SPIE Medical Imaging*, volume 9034 of *Classification and texture*, 2014.

[122] I. Reiser, S. Lee, and R.M. Nishikawa. On the orientation of mammographic structure. *Medical Physics*, 38:5303–5306, 2011.

[123] B. Ren, A. Smith, and Z. Jing. Measurement of breast density with digital breast tomosynthesis. In *SPIE Medical Imaging*, volume 8313 of *Physics of Medical Imaging*, page 173, 2012.

[124] M. Rosenstein. *HANDBOOK of Selected Tissue Doses for Projections Common In Diagnostic Radiology*. Center for Devices and Radiological Health, Rockville, Maryland 20857, 1988.

[125] M. Salvatore, L. Margolies, M. Kale, J. Wisnivesky, S. Kotkin, C.I. Henschke, and D.F. Yankelevitz. Breast density: Comparison of chest CT with mammography. *Radiology*, 270:67–73, 2014.

[126] E. Samei, X. Li, B. Chen, and R. Reiman. The effect of dose heterogeneity on radiation risk in medical imaging. *Radiation Protection Dosimetry*, 155:42–58, 2013.

[127] I. Sechopoulos, E.S.M. Ali, A. Badal, A. Badano, J.M. Boone, I.S. Kyprianou, E. Mainegra-Hing, M.F. McNitt-Gray, K.L. McMillan, D.W.O. Rogers, E. Samei, and A.C. Turner. Monte Carlo reference data sets for imaging research. Task group 195, *American Association of Physicists in Medicine*, 2014.

[128] I. Sechopoulos, K. Bliznakova, X. Qin, B. Fei, and S.S.J. Feng. Characterization of the homogeneous tissue mixture approximation in breast imaging dosimetry. *Medical Physics*, 39:5050–5059, 2012.

[129] J.C. Sergeant, J. Warwick, D.G. Evans, A. Howell, M. Berks, P. Stavrinos, S. Sahin, M. Wilson, A. Hufton, I. Buchan, and S.M. Astley. Volumetric and area-based breast density measurement in the Predicting Risk of Cancer at Screening (PROCAS) study. In A.D.A. Maidment et al., editor, *Breast Imaging*, volume 7361, pages 228–235, 2012.

[130] J.A. Shepherd, L. Herve, J. Landau, B. Fan, K. Kerlikowske, and S.R. Cummings. Novel use of Single X-ray Absorptiometry for measuring breast density. *Technology in Cancer Research and Treatment*, 4:173–182, 2005.

[131] N. Shramchenko, P. Blin, C. Mathey, and R. Klausz. Optimized exposure control in digital mammography. In *SPIE Medical Imaging*, volume 5368 of *Physics of Medical Imaging*, 2004.

[132] S.E. Skubic and P.P. Fatouros. The effect of breast composition on absorbed dose and image contrast. *Medical Physics*, 16:544–542, 1989.

[133] W.T. Sobol and X. Wu. Parametrization of mammography normalized average glandular dose tables. *Medical Physics*, 24:547–554, 1997.

[134] L. Tabar and T.H. Chen. We do not want to go back to the dark ages of breast screening. *Auntminnie*, 2014.

[135] L. Tabar and P.B. Dean. Mammographic parenchymal patterns: Risk indicator for breast cancer? *The Journal of the American Medical Association*, 247:185–189, 1982.

[136] L. Tabar and P.B. Dean. *Teaching atlas of mammography*. Thieme, Third edition, 2001.

[137] A. Tagliafico, G. Tagliafico, D. Astengo, F. Cavagnetto, R. Rosasco, G. Rescinito, F. Monetti, and M. Calabrese. Mammographic density estimation: one-to-one comparison of digital mammography and digital breast tomosynthesis using fully automated software. *European Radiology*, 22:1265–1270, 2012.

[138] A. Tagliafico, G. Tagliafico, and N. Houssami. Differences in breast density assessment using mammography, tomosynthesis and MRI and their implications for practice. *British Journal of Radiology*, 86:20130528, 2013.

[139] C. Ting, S.M. Astley, J. Morris, P. Stavrinos, M. Wilson, N. Barr, C. Boggies, and J.C. Sergeant. Longitudinal change in mammographic density and association with breast cancer risk: a case-control study. In A.D.A. Maidment et al., editor, *Breast Imaging*, volume 7361, pages 205–211, 2012.

[140] C. Tromans, A. Chan, and R. Highnam. Comparing personalized mean glandular dose estimates between X-ray systems over time in mammography. In *European Congress on Radiology*, pages C–0360, 2014.

[141] A.H. Tyson, G.E. Mawdsley, and M.J. Yaffe. Measurement of compressed breast thickness by optical stereoscopic photogrammetry. *Medical Physics*, 36:569–576, 2009.

[142] A university of Califoria program. Athena breast health network. http://athenacarenetwork.org, 2014.

[143] S. van Engeland, P.R. Snoeren, H. Huisman, C. Boetes, and N. Karssemeijer. Volumetric breast density estimation from full-field digital mammograms. *Institute of Electrical and Electronics Engineers*, 25:273–282, 2006.

[144] C.H. van Gils, J.H.C.L. Hendriks, R. Holland, N. Karssemeijer, J.D.M. Otten, H. Straatman, and A.L.M. Verbeek. Changes in mammographic breast density and concomitant changes in breast cancer risk. *European Journal of Cancer Prevention*, 8:509–515, 1999.

[145] L. Vancamberg, N. Geeraert, R. Iordache, G. Palma, R. Klausz, and S. Muller. 3D density estimation in digital breast tomosynthesis: application to needle path planning for breast biopsy. In *SPIE Medical Imaging*, volume 7964 of *Visualization, Image-Guided Procedures, and Modeling*, 2011.

[146] S. Vedantham, L. Shi, A. Karellas, and A.M. O'Connell. Dedicated breast CT: fibroglandular volume measurements in a diagnostic population. *Medical Physics*, 39:7317–7328, 2012.

[147] J. Wang, A. Azziz, B. Fan, S. Malkov, C. Klifa, D. Newitt, S. Yitta, N. Hylton, K. Kerlikowske, and J.A. Shepherd. Agreement of mammographic measures of volumetric breast density to MRI. *PLoS ONE*, 8:e81653, 2013.

[148] Y. Wang, B.M. Keller, Y. Zheng, R.J. Acciavatti, J.C. Gee, A.D.A. Maidment, and D. Kontos. Texture feature standardization in digital mammography for improving generalizability across devices. In *SPIE Medical Imaging*, volume 8670 of *Computer-Aided Diagnosis*, 2013.

[149] S. Webb. *From watching of shadows: The origins of radiological tomography*, chapter 1. Tomography - history, page 11. IOP Publishing, 1948.

[150] D.R. White, R.J. Martin, and R. Darlison. Epoxy resin based tissue substitutes. *British Journal of Radiology*, 5:814–821, 1977.

[151] E. White, P. Velentgas, M.T. Mandelson, C.D. Lehman, J.G. Elmore, P. Porter, Y. Yasui, and S.H. Taplin. Variation in mammographic breast density by time in menstrual cycle among women aged 40-49 years. *Journal of National Cancer Institute*, 90:906–910, 1998.

[152] N.J. Wolfe. Breast patterns as an index of risk for developing breast cancer. *American Journal of Radiology*, 126:1130–1139, 1976.

[153] X. Wu, G.T. Barnes, and D.M. Tucker. Spectral dependence of glandular tissue dose in screen-film mammography. *Radiology*, 179:143–148, 1991.

[154] X. Wu, E.L. Gingold, G.T. Barnes, and D.M. Tucker. Normalized average glandular dose in Molybdenum target-Rhodium filter and Rhodium target-Rhodium filter mammography. *Radiology*, 193:83–89, 1994.

[155] X. Wu, D.A. Langan, D. Xu, T.M. Benson, J.D. Pack, A.M. Schmitz, J.E. Tkaczyk, J. Leverentz, and P. Licato. Monochromatic CT image representation via fast switching dual kVp. In *SPIE Medical Imaging*, volume 7258 of *Physics of Medical Imaging*, 2009.

[156] M.J. Yaffe, J.M. Boone, N. Packard, O. Alonzo-Proulx, S.-Y. Huang, C.L. Peressotti, A. Al-Mayah, and K. Brock. The myth of the 50-50 breast. *Medical physics*, 36:5437–5443, 2009.

[157] K.C. Young and A. Burch. Radiation doses received in the UK breast screening programme in 1997 and 1998. *The British journal of radiology*, 73:278–287, 2000.

[158] K.C. Young, M.L. Ramsdale, and F. Bignell. Review of dosimetric methods for mammography in the UK breast screening programme. *Radiation Protection Dosimetry*, 80:186–187, 1998.

[159] D. Zhang, X. Li, and B. Liua. Objective characterization of GE Discovery CT750 HD scanner: Gemstone spectral imaging mode. *Medical Physics*, 38:1178–1188, 2011.

[160] C. Zhou, H. Chan, N. Petrick, M.A. Helvie, M.M. Goodsitt, B. Sahiner, and L.M. Hadjiiski. Computerized image analysis: estimation of breast density on mammograms. *Medical Physics*, 28:1056–1069, 2001.

[161] J. Zoetelief, W. J. H. Veldkamp, M. A. O. Thijssen, and J. T. M. Jansen. Glandularity and mean glandular dose determined for individual women at four regional breast cancer screening units in The Netherlands. *Physics in Medicine and Biology*, 51:1807–1817, 2006.

[162] M. Zulfiqar, I. Rohazly, and M. Rahmah. Do the majority of malaysian women have dense breasts on mammogram. *Biomedical Imaging and Intervention Journal*, 7(2):e14, 2011.

Quantitative evaluation of fibroglandular tissue for estimation of tissue-differentiated absorbed energy in breast tomosynthesis

Nausikaä GEERAERT

ABSTRACT : The breast density is known as a breast cancer risk factor. The objective quantification of the volumetric breast density was developed, based on already published methods, and improved computing a breast density map. Our most important contribution resides in a new validation method applicable to any VBD computation, consisting in comparing its results with the VBD obtained from a thorax CT examination for the same patient.
For the individual radiation risk, we proposed to replace the average glandular dose by the imparted energy, which depends on the quantity and distribution of the glandular tissue, which is the tissue at risk. Simulations allow the computation of the imparted energy by VBD-based segmented tissues.

KEY-WORDS : Mammography, breast density, glandular tissue, thorax CT, breast tomosynthesis, tissue segmentation, glandular imparted energy

RESUME : La densité du sein est connue comme indicateur de risque du cancer. Une méthode de quantification objective de la VBD a été développée, à partir d'approches existantes, et améliorée. Une carte de densité est calculée. La contribution majeure de la thèse consiste en une nouvelle méthode de validation, applicable à tout calcul de VBD d'image de mammographie. Elle consiste à comparer les résultats aux valeurs de densité obtenues par des scanners thoraciques pour la même patiente.
Pour le risque d'irradiation individuel, nous proposons de remplacer la dose glandulaire moyenne par l'énergie déposée, qui dépend de la quantité et de la distribution du tissu glandulaire, qui est le tissu à risque. Des simulations permettent de calculer l'énergie impartie par les tissus segmentés à l'aide la densité du sein.

MOTS-CLEFS : Mammographie, densité du sein, tissu glandulaire, scanner thoracic, tomosynthèse du sein, segmentation de glande, énergie impartie à la glande

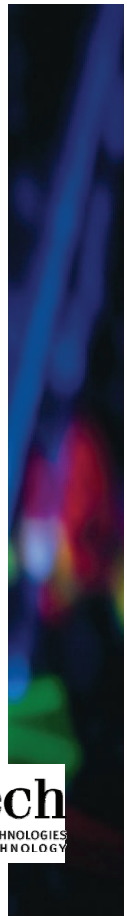

KU LEUVEN
DOCTORAL SCHOOL BIOMEDICAL SCIENCES

TELECOM ParisTech

EDiTE

ParisTech
INSTITUT DES SCIENCES ET TECHNOLOGIES
PARIS INSTITUTE OF TECHNOLOGY